

MICROSTRUCTURAL EVOLUTION OF TiAl₃ AND TiAl₃ - BASE COMPOUNDS FORMED BY REACTION SYNTHESIS

by
M. Sujata

CS

7/1
2/2/1996/TD
SU 4-12

MME

1996

D
SUJ
MIC



Department of Materials and Metallurgical Engineering

INDIAN INSTITUTE OF TECHNOLOGY KANPUR

FEBRUARY, 1996

MICROSTRUCTURAL EVOLUTION OF TiAl₃ AND TiAl₃ BASED COMPOUNDS FORMED BY REACTION SYNTHESIS

A Thesis Submitted
in Partial Fulfilment of the Requirements
for the Degree of
DOCTOR OF PHILOSOPHY

by

M. SUJATA

to the

 **DEPARTMENT OF MATERIALS AND METALLURGICAL
ENGINEERING**

**INDIAN INSTITUTE OF TECHNOLOGY
KANPUR**

FEBRUARY 1996

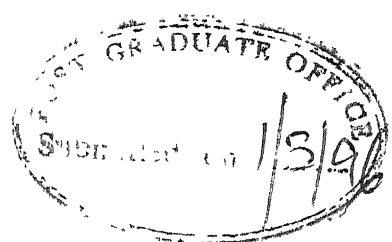
- 8 JUL 1997 / Metallurgical E.

CENTRAL LIBRARY
I.I.T. KANPUR

Reg No. **A 123583**

MME-1996-D-SUJ-MIC

Certificate



It is certified that the work contained in the thesis entitled "**Microstructural Evolution of $TiAl_3$ and $TiAl_3$ Based Compounds Formed by Reaction Synthesis**", submitted by M.Sujata has been carried out under our supervision and that this work has not been submitted elsewhere for a degree.


(Dr. S. Bhargava)
(Dr. S. Sangal)

Department of Materials and Metallurgical Engineering
Indian Institute of Technology
Kanpur-208016
India

to
Shri V. P. Guptaji

...for his selfless contributions in my development

Acknowledgements

I express my deep sense of gratitude to my supervisors Dr. S.Bhargava and Dr. S.Sangal for their inspiring guidance and cooperation throughout the tenure of this work. I feel myself lucky to work in such a friendly atmosphere.

I also express my sincere gratitude to Prof. G.S.Upadhyaya for his constant encouragement and moral support throughout the tenure of this work.

I am thankful to Prof. Jitendra Kumar and Prof. C.Venkobachar for extending their lab facilities to me without which it would have been difficult to complete this work. I am indebted to Prof. K.P.Gupta, Prof. A.Ghosh, Prof. R.K.Dube, Prof. R.K.Ray, Dr.V.S.R.Murthy and Dr.R.Balasubramaniam for their help extended to me at various stages of this study.

Helps of various kind rendered by Messrs. S.C.Soni, G.S.Sharma, P.K.Paul, Umashankar Singh, K.P.Mukherjee, B.K.Jain, S.C.Barthwal, U.S.Lal, R.P.Singh, P.P.Singh, A.K.Verma, G.P.Bajpeyi, K.S.Bhamra, H.C.Srivastava, B.S.Deshwal, S.D.Singh, C.L.Sachan, S.B.Shukla and V.Kumar are gratefully acknowledged.

Among my senior colleagues and friends who were always helpful to me are Dr.(Mrs.) M.Umadevi, Dr.R.R.Nagrajan, Dr.M.N.Mungole, Dr.S.K.Chowdhuri, Niloyada, Tapasda, GG, Sudipto Ghosh Chowdhury, Basudev, Sudipto, KK and Daniel.

Thanks are owed to to Mr.Subhash Chand for his sincere help and cooperation, without which this work would not have been completed in time.

The constant help and encouragement received from Ligy is greatly acknowledged. In addition, I would like to thank Gracius Sir and Nitin for their help at several stages of this work.

Affection, respect and support received from Rakshit, Manas, Kallol, Sonu, Arvind and Vidya is really memorable. I do not find words to express my feelings for them. I also express my thanks to my friends K.S.Rao, Thakurji, Babu, Santanu, Anirban, Bidisha, Shailja, Shobha and Betadidi.

The homely atmosphere provided by the families of Mr.S.C.Soni and Mr.V.P.Gupta is immemorable.

The help received from Mr.R.N.Srivastava during the preparation of this thesis is highly acknowledged.

Lastly, the painstaking help of Dr.S.Bhargava in the last stages of this work is beyond any word of acknowledgement.

Sujata

Contents

	page
Acknowledgement	iv
List of Figures	xiii
List of Tables	xxiii
SYNOPSIS	xxvi
Chapter 1: Introduction	1
Chapter 2: Literature Review	10
2.1 : The Ti-Al System	11
2.2 : Ti-Al-X System	20
2.2.1 Ti-Al-Mo System	20
2.2.2 Ti-Al-V System	21
2.2.3 Ti-Al-Zr System	21
2.2.4 Ti-Al-Si System	22
2.3 : Physical Metallurgy and Mechanical Behaviour of $TiAl_3$ Based Aluminides	24
2.3.1 Deformation Behaviour of Binary $TiAl_3$ Based Aluminides	27
2.3.2 Mechanical Properties of $TiAl_3$	28
2.4 : $L1_2$ Titanium Trialuminides	28
2.5 : Physical Metallurgy and Mechanical Behaviour of Titanium Aluminides other than $TiAl_3$	33
2.5.1 Ti_3Al Based Intermetallics	33
2.5.2 $TiAl$ Based Intermetallics	38

2.6 : Reaction Synthesis Technique-Application to Aluminide Systems	39
2.6.1 Research Activities In The Reaction Synthesis Systems	41
2.6.2 Reaction Synthesis Processes in General	41
2.6.3 Thermodynamics of Combustion/Reaction Synthesis	48
2.6.4 Modes of Combustion Synthesis	52
2.6.5 Combustion Synthesis of Aluminide Intermetallics	55
2.6.5.1 Reaction Synthesis of Titanium Aluminides	56
2.6.5.2 Reaction Synthesis of Ni-Al Intermetallics	61
2.6.5.3 Reaction Synthesis of Fe-Al Based Intermetallics	63
2.6.5.4 Reactive Synthesis of NbAl_3	63
2.6.5.5 Reaction Synthesis of Cu-Al Intermetallics	64
2.7 : TiAl_3 Formation During Interaction of Ti with Liquid Al	64
2.7.1 Nature of Samples Used for Studies on TiAl_3 Formation	65
2.7.2 Chemical Composition and Microstructures of the Aluminides Formed	67
2.7.3 Growth Kinetics of TiAl_3 Formation	69
2.7.4 Effect of Alloying Elements on the Growth Kinetics of TiAl_3	77

Chapter 3:	Aims of the Present Study	80
Chapter 4:	Experimental Procedures	82
4.1 :	Preparation of Pure Ti/Al and Ti alloy/Al Reaction Couples	82
4.2 :	Experimental Set-Up and Conditions of Reaction Synthesis	86
4.3 :	Characterization of the Reaction Product	91
4.3.1	X-ray Diffraction Analysis	94
4.3.2	Microstructural Examination	95
4.3.2.1	Optical Microscopy	95
4.3.2.2	Scanning Electron Microscopy	95
4.3.2.3	Electron Probe Microanalysis	96
4.3.2.4	Transmission Electron Microscopy	96
4.4 :	Quantitative Metallography	98
4.4.1	Measurement of Reaction Zone Thickness	99
4.4.2	Measurement of Volume Fraction of the Reaction Product as a Function of Distance from the Reaction Interface	99
4.4.3	Determination of Average Volume Fraction of the Reaction Product in the Reaction Zone	101
4.4.4	Estimation of Reaction Product Formed Per Unit Area of the Reaction Interface	103
4.4.5	Measurement of Aluminide Particle Size and Its Distribution in the Reaction Zone	105

4.4.6	Analysis of Morphology of the Reaction Product	107
4.4.7	Microhardness Measurements	107
Chapter 5: Results		109
5.1 :	Formation of Titanium Aluminide(s) as the Reaction Synthesis Product	109
5.1.1	General Microstructural Features of the Reaction Couples	109
5.1.2	Variation of Reaction Zone Thickness as a Function of Reaction Conditions	111
5.1.3.	Compositional Analysis of Phases Presented in the Partially Reacted Couples	118
5.2 :	Structural Analysis of Phases Present in the Reaction Product	128
5.2.1	Aluminide Formation in Ti/Al Couples In the Temperature Range of 973K-1273K	129
5.2.2	Aluminide Formation in Ti/Al Couples at the Reaction Temperature of 1373K	136
5.2.3	Aluminide Formation In the Ti-Al-V alloy/Al and Ti-Al-Mo-Zr-Si alloy/Al Couples	143
5.3 :	Variation of Reaction Zone Microstructural Features in Partially Reacted Couples	150
5.3.1	Morphological Features of the Reaction Interface	151

5.3.2	Morphological Features and Microstructural Details of the Reaction Layer	154
5.3.3	Morphological Features and Microstrucural Details of the Dispersed Reaction Domain	155
5.3.3.1	Sub-structural Features of Titanium Aluminide Particles	155
5.3.3.2	Cracking and Fissuring in Titanium Aluminide Particles	158
5.3.3.3	Particle Shape Changes in Pure Ti/Al Couples	160
5.3.3.4	Particle Shape in Ti-Al-V alloy/Al and Ti-Al-Mo-Zr-Si alloy/Al Reaction Couples	167
5.3.3.5	Volume Fraction of Aluminide Particles in the Dispersed Reaction Domain as a Function of Distance From the Reaction Interface	175
5.3.3.6	Variation of Average Volume Fraction of Aluminide Particles as a Function of Reaction Conditions	183
5.3.3.7	Particle Size Distribution in the Dispersed Reaction Domain	185
5.3.4	Hardness Variation in Ti/Al Couples	202
Chapter 6:	Discussion	207
6.1 :	TiAl ₃ Foramtion in the Temperature Range of 973K-1273K	207

6.2	: Mechanism of $TiAl_3$ Formation	214
6.2.1	Formation of $TiAl_3$ by Chemical Reaction	214
6.2.2	Growth of the Reaction Layer	220
6.3	: Physical Phenomena Occurring in the Reaction Zone	223
6.3.1	Exothermic Heat Evolution and Rise in the Reaction Interface Temperature	226
6.3.2	Build-up of Thermal Gradients and Convective Currents in Liquid Al	231
6.3.3	Smoothening of $TiAl_3$ Particles Surfaces by Selective Dissolution	237
6.3.4	Reprecipitation of $TiAl_3$ Particles from the Al Melt	238
6.3.5	Neck Formation by Solid State Sintering	240
6.4	: Microstructural Variations Observed in the Dispersed Reaction Domain	242
6.4.1	Effect of Reaction Time and Temperature on the Reaction zone Thickness and the Amount of Reaction Product	242
6.4.2	Variations of Volume Fraction of $TiAl_3$ Particles With Distance From the Reaction Interface	245
6.4.3	Variation of Particle Shape in the Dispersed Reaction Domain	250
6.4.4	Variation of Particle Size Distribution and Mean Particle Size with Distance from the Reaction Interface	252

6.4.5	Variation of Average Particle Size With Reaction Temperature and Time	254
6.4.6	Particle Coarsening in Fully Reacted Couples	254
6.5	: Formation of Ti_9Al_{23} in Pure Ti/Al Couples at the Reaction Temperature of 1373K	255
6.5.1	Mechanism of Formation of Ti_9Al_{23}	255
6.5.2	Effect of Reaction Conditions on the Morphology of the Aluminide Particles	264
6.6	: Kinetics of $TiAl_3$ Formation	265
Chapter 7:	Conclusions	274
References		279
Appendix		287

LIST OF FIGURES

	page
Figure 2.1	Binary Ti-Al phase diagram according to Murray 12 [23].
Figure 2.2	Binary Ti-Al phase diagram according to 14 McCullough et al. [47].
Figure 2.3	Binary Ti-Al phase diagram according to 15 Schuster and Ipser [24].
Figure 2.4	Crystal structure of the titanium aluminides; 18 (a) Ti_3Al , (b) $TiAl$ and (c) $TiAl_3$.
Figure 2.5	Compressive yield strength of polycrystalline 29 $TiAl_3$ as a function of test temperature [51].
Figure 2.6	Slip systems in the lattices of Ti_3Al , $TiAl$ 34 and $TiAl_3$; (a) DO_{19} base Ti_3Al , (b) $L1_0$ base $TiAl$ and (c) DO_{22} base $TiAl_3$.
Figure 2.7	Effect of B2 volume fraction on the yield 37 strength of various Ti_3Al -Nb alloys [76].
Figure 2.8	A schematic diagram showing the reaction 42 synthesis system.
Figure 2.9	A schematic diagram explaining the calculation 50 of T_{ad} .
Figure 2.10	A schematic SHS diagram. 53
Figure 2.11	Results obtained on reactive powder processing 58 of $TiAl$ alloys [114].
Figure 2.12	Process maps for the formation of $TiAl_3$ and 60 $TiAl$ intermetallics [117].

Figure 2.13	Nature of specimens used for studies on $TiAl_3$ formation [119] (a) cuboidal shape samples used by Mackowiak and Shreir (b) Ti/Ti weld samples [126] (c) samples used for laser surface alloying [124].	66
Figure 2.14	Decrease in thickness of Ti specimens due to dissolution in liquid Al; (a) 99.75 wt.% Ti and (b) 99.00 wt.% Ti.	70
Figure 2.15	Arrhenius plots of $\log (k)$ versus $\frac{1}{T}$ for the dissolution of Ti in liquid Al; A: 99.00 wt.% Ti and B: 99.75 wt.% Ti.	71
Figure 2.16	Variation of interaction layer thickness with time; (a) 99.75 wt.% Ti and (b) 99.00 wt.% Ti.	73
Figure 2.17	(a) Arrhenius plots of growth rate constant (k) as a function of $1/T$ obtained on the thickness of $TiAl_3$ [126]. (b) Coating layer thickness obtained at different dipping times	76
Figure 4.1	Schematic diagram of reaction couples used in the present study.	83
Figure 4.2	Microstructures of the as-received Ti and Ti alloys.	87
Figure 4.3	Schematic diagram of the set-up used for reaction synthesis experiments.	88
Figure 4.4	Stainless steel trolley and sample holder assembly used for reaction synthesis experiments.	90
Figure 4.5	(a) Longitudinally sectioned partially reacted couple showing the unreacted Ti/Ti alloy, unreacted Al and the reaction zone (b) Schematic view of a typical reaction zone.	93
Figure 4.6	Schematic diagram showing the non-uniform nature of reaction zone thickness.	100

		page
Figure 4.7	Schematic diagram showing the regions at which 102 volume fraction measurements were made.	102
Figure 4.8	Schematic diagram of a partially reacted couple.	104
Figure 5.1	SEM micrograph of the longitudinal section of 112 the reaction couple showing the reaction zone and the adjacent unreacted Ti and Al layers; (a) Low magnification micrograph (b) High magnification micrograph sample reacted at 973 K (700°C) for 7200 s (2 hr).	112
Figure 5.2	Variation of average thickness of the reaction zone with reaction time for different reaction temperatures in pure Ti/Al couples .	114
Figure 5.3	Comparison of reaction zone thickness obtained 116 in Ti alloy/Al and pure Ti/Al couples reacted at different temperatures; (a) reacted for 3600 s (1 hr) and (b) reacted for 7200 s (2 hr).	116
Figure 5.4	(a) SEM micrograph showing phases present 119 adjacent to the reaction interface of Ti/Al couple reacted at 1073 K (800°C) for 3600 s (1 hr); (b), (c) X-ray dot mapping for the element, Ti _y (b) and Al (c) on the region shown in (a).	119
Figure 5.5	SEM micrograph of Ti/Al couple reacted at 1073 123 K (800°C) for 3600 s (1 hr) showing the presence of thin TiAl ₃ reaction layer adjacent to the unreacted Ti and concentration profile of Ti (a) and concentration profile of Al (b) in the phases present adjacent to the reaction interface.	123
Figure 5.6	(a) SEM micrograph of the reaction zone 125 formed in Ti/Al couple reacted at 973 K (700°C) for 3600s (1 hr) (b), (c) X-ray dot mapping for element Ti (b) and Al (c) for the region shown in (a)	125
Figure 5.7	(a) SEM micrograph of the reaction zone 126 formed in Ti/Al couple reacted at 1173 K (900°C) for 3600 s (1 hr); (b), (c) X-ray dot mapping for element Ti (b) and Al (c) for the region shown in (a).	126

Figure 5.8 (a) SEM micrograph of the reacted zone formed 127 in $(\text{Ti}-\text{Al}-\text{V})/\text{Al}$ couple reacted at 1073 K (800°C) for 3600 s (1 hr);
 (b), (c) X-ray dot mapping for the element Ti_y(b) and Al (c) for the region shown in (a). 130

Figure 5.9 X-ray diffraction patterns obtained from the couples reacted for 3600 s (1 hr) at (a) 973 K (700°C), (b) 1073 K (800°C), (c) 1173 K (900°C) and (d) 1273 K (1000°C). 130

Figure 5.10 X-ray diffraction patterns from the Ti/Al couples reacted at 1073 K (800°C) for different time intervals; Reacted for (a) 3600 s (1 hr), (b) 7200 s (2 hr) and (c) 14400 s (4 hr). 132

Figure 5.11 (a) Bright field electron micrograph of the dispersed reaction domain from Ti/Al couples reacted at 1073 K (800°C) for 7200 s (2 hr); selected area diffraction patterns corresponding to the regions A, (b) and region C, (c), (d) and (e) are indexed patterns corresponding to the regions A and C. 134

Figure 5.12 X-ray diffraction patterns from the Ti/Al couples reacted for 3600 s (1 hr) at (a) 973 K (700°C), (b) 1173 K (700°C) and (c) 1373 K (1100°C). 138

Figure 5.13 (a) Selected area diffraction pattern of aluminide formed in Ti/Al couple reacted at 1373 K (1100°C) for 3600 s (1 hr)
 (b) Indexed pattern of Figure - 5.13(a). 144

Figure 5.14 X-ray diffraction patterns from couples reacted at 1073 K (800°C) for 7200 s (2 hr); (a) Ti/Al couple, (b) Ti-Al-V alloy/Al and (c) Ti-Al-Mo-Zr-Si alloy/Al.
 (Ti_a and Ti_b represent the peaks corresponding to the Ti-Al-V and Ti-Al-Mo-Zr-Si alloys used respectively). 145

Figure 5.15 Bright field transmission electron micrograph of TiAl_3 base particles in (a) Ti-Al-V alloy/Al reaction couple and (b) Ti-Al-Mo-Zr-Si alloy/Al reaction couple; Couples reacted at 1073 K (800°C) for 7200 s (2 hr). 148

		page
Figure 5.16	Selected area diffraction patterns from $TiAl_3$ 149 base particles shown in (a) Figure - 5.16(a) and (b) Figure - 5.16(b); Indexed diffraction patterns of (c): Figure - 5.16(a) and (d): Figure - 5.16(b).	
Figure 5.17	SEM micrographs showing the nature of reaction 152 interface and reaction layer in $TiAl_3$ base compound with increase in distance from the reaction interface; (a) Ti/Al couple reacted at 973 K ($700^\circ C$) for 7200 s (2 hr) (b) Ti-Al-V alloy/Al couple reacted at 973 K ($700^\circ C$) for 7200 s (2 hr) (c) Ti-Al-Mo-Zr-Si alloy/Al couple reacted at 1073K ($800^\circ C$ for 3600s (1hr).	
Figure 5.18	(a) Phases present adjacent to the reaction 153 interface in Ti/Al couple reacted at 1073 K ($800^\circ C$) for 3600 s (1 hr) showing the presence of Ti islands inside the reaction zone ahead of the reaction interface. (b) X-ray dot mapping of the element Ti on the region shown in Figure - 5.18(a) (c) X-ray dot mapping of the element Al on the region shown in Figure - 5.18(a).	
Figure 5.19	SEM micrographs showing the reaction layers of 156 couples reacted at (a) 973 K ($700^\circ C$) for 14400 s (4 hr) and (b) 1073 K ($800^\circ C$) for 7200 s (2 hr); Figures (a) and (b) show the nature of cracking inside the reaction layer leading to its decohesion from Ti.	
Figure 5.20	Bright field transmission electron micrograph 157 of a region of the reaction layer formed in Ti/Al couples reacted at 1073 K ($800^\circ C$) for 7200 s (2 hr).	
Figure 5.21	Bright field TEM micrographs of $TiAl_3$ 159 particles of the dispersed reaction domain showing (a) heavily dislocated regions, (b)ystacking faults and (c) dislocations originating at a grain boundary.	
Figure 5.22	SEM micrographs showing the nature of cracking 161 inside the $TiAl_3$ base particles in the reaction zones of (a) Ti/Al, (b) Ti-Al-V alloy/Al and (c) Ti-Al-Mo-Zr-Si alloy/Al couples reacted at 1073 K ($800^\circ C$) for 7200 s (2 hr).	

Figure 5.23 Bright field TEM micrographs of $TiAl_3$ 162 particles inside the reaction zones showing the substructural features adjacent to cracked regions in Ti/Al couples reacted at 1073 K ($800^\circ C$) for 7200 s (2 hr);
(a) long straight edge dislocations regions A and B
(b) and (c) dislocation arrays and network configurations inside $TiAl_3$
(c) crack configuration.

Figure 5.24 SEM microstructures showing changes in the 164 particle size and morphology of $TiAl_3$ base particles at varying distances from the reaction interface in Ti/Al couples reacted at 1073 K ($800^\circ C$) for 3600 s (1 hr).

Figure 5.25 SEM micrographs showing the effect of reaction 166 temperature on the particle size and morphology of $TiAl_3$ formed in Ti/Al couples reacted for 3600 s (1 hr) at (a) 973 K ($700^\circ C$), (b) 1073 K ($800^\circ C$), (c) 1173 K ($900^\circ C$), (d) 1273 K ($1000^\circ C$) and (e) 1373 K ($1100^\circ C$).

Figure 5.26 SEM micrograph showing the variation in 168 particle size and morphology of vanadium containing $TiAl_3$ based compound formed in Ti-Al-V alloy/Al couple as a function of distance from the interface in couples reacted at 1073 K ($800^\circ C$) for 7200 s (2 hr);
(a) adjacent to the interface, (b) 0.4 mm and (c) 1.6 mm from the reaction interface.

Figure 5.27 SEM micrograph showing the variation in 169 particle size and morphology of molybdenum, zirconium and silicon containing $TiAl_3$ based compound formed in Ti-Al-Mo-Zr-Si alloy/Al couple as a function of distance from the reaction interface in couples reacted at 1073 K ($800^\circ C$) for 7200 s (2 hr);
(a) adjacent to the interface, (b) 0.2 mm, (c) 0.4 mm, (d) 0.8 mm, (e) 1.6 mm, (f) 2.4 mm and (g) 2.8 mm.

Figure 5.28 Optical micrographs of the dispersed reaction 171 domain reaction zones formed in Ti alloy/Al couples reacted at 1073 K (800°C) for 7200 s (2 hr); Near the reaction interface: (a) and (b) Ti-Al-V alloy/Al couple and (b) Ti-Al-Mo-Zr-Si alloy/Al; Away from the reaction interface: (c) Ti-Al-V alloy/Al couple and (c) Ti-Al-Mo-Zr-Si alloy/Al couple.

Figure 5.29 Variation of aspect ratio of $TiAl_3$ base 173 particles formed in Ti-Al-V alloy/Al and Ti-Al-Mo-Zr-Si alloy/Al couples with distance from the reaction interface of couples reacted at 1073 K (800°C) for 7200 s (2 hr).

Figure 5.30 SEM micrographs showing the effect of reaction 174 temperature on the particle size of $TiAl_3$ base compound formed in Ti-Al-Mo-Zr-Si alloy/Al couples; (a) reacted at 973 K (700°C) for 7200 s (2 hr) and (b) reacted at 1073 K (800°C) for 7200 s (2 hr).

Figure 5.31 Variation of volume fraction of $TiAl_3$ in the 176 reaction zone as a function of distance from the reaction interface in Ti/Al couples reacted for 3600 s at (a) 973 K (700°C), (b) 1073 K (800°C) and (c) 1173 K (900°C).

Figure 5.32 Variation of volume fraction of $TiAl_3$ base 177 compounds in the reaction zone as a function of distance from the reaction interface in couples reacted at 1073 K (800°C) for 7200 s (2 hr) in (a) Ti/Al, (b) Ti-Al-V alloy/Al and (c) Ti-Al-Mo-Zr-Si alloy/Al.

Figure 5.33 Variation of maximum and minimum volume 182 fractions of aluminide particles as a function of reaction temperature and reaction time in pure Ti/Al couples.

Figure 5.34 Effect of reaction temperature and time on the 184 distance at the peak volume fraction of aluminide particles.

Figure 5.35 Variation of average volume fraction of 187 aluminide particles in the dispersed reaction domain with reaction temperature and time in pure Ti/Al couples.

		page
Figure 5.36	SEM microstructures showing the changes in the particle size and morphology of $TiAl_3$ base particles at increasing distance from the reaction interface in Ti/Al couples reacted at 973 K (700°C) for 7200 s (2 hr)	190 (a) 0.4 mm, (b) 1.2 mm and (c) 2.0 mm.
Figure 5.37	Optical microstructures of the reaction zones formed in Ti/Al couples reacted for 3600 s (1 hr) at (a) 973 K (700°C), (b) 1073 K (800°C), (c) 1173 K (900°C) and (d) 1373 K (1100°C).	191
Figure 5.38	SEM micrographs showing the effect of reaction time on the morphology and particle size of $TiAl_3$ in Ti/Al couples reacted at 1073 K (800°C) for (a) 3600 s (1 hr), (b) 7200 s (2 hr) and (c) 14400 s (4 hr).	192
Figure 5.39	SEM micrographs showing the effect of alloying elements on the particle size and morphology of Ti_3Al based compounds formed in couples reacted at 973 K (700°C) for 7200 s (2 hr); (a) Ti/Al, (b) Ti-Al-V alloy/Al and (c) Ti-Al-Mo-Zr-Si alloy/Al.	194
Figure 5.40	Variation of particle size distribution of $TiAl_3$ in the dispersed reaction domain of pure Ti/Al couples reacted for 3600 s (1 hr) at (a) 973 K (700°C), (b) 1073 K (800°C) and (c) 1173 K (900°C).	195
Figure 5.41	Variation of particle size distribution as a function of reaction time in pure Ti/Al couples reacted at 1073 K (800°C) for (a) 3600 s (1 hr), (b) 7200 s (2 hr) and (c) 14400 s (4 hr).	197
Figure 5.42	Particle size distribution of $TiAl_3$ at different distances from the reaction interface in pure Ti/Al couples reacted at 1073 K (800°C) for 7200 s (2 hr); (a) 0.2 mm, (b) 0.4 mm, (c) 0.8 mm and (d) 1.6 mm.	198
Figure 5.43	Variation of average particle size of $TiAl_3$ with reaction time in Ti/Al couples reacted at 1073 K (800°C); A: for the size range of 0-24 mm B: for the size range of 4-24 mm.	200

	page
Figure 5.44 .	201
Variation of average particle size of $TiAl_3$ with reaction temperature in Ti/Al couples reacted for 3600 s (1 hr);	
A: for the size range of 0-24 mm	
B: for the size range of 4-24 mm.	
Figure 5.45	203
Variation of average particle size of aluminide with reaction temperature in pure Ti/Al couples reacted for 3600 s (1 hr).	
Figure 5.46	204
Variation of mean particle size of $TiAl_3$ with distance from the reaction interface in pure Ti/Al couples reacted at 1073 K (800°C) for 7200 s (2 hr).	
Figure 6.1	213
Free energies of formation of various Ti-Al compounds as a function of temperature obtained from [49].	
Figure 6.2	218
(a) The dihedral angle between intersecting grains, (b) nature of liquid shape at different dihedral angles and (c) liquid Al penetration through grain boundaries leading to $TiAl_3$ formation.	
Figure 6.3	219
SEM micrographs of the separated Ti islands showing an envelope of $TiAl_3$ around them (a): Compositions of the regions marked (b) 100.0 at. % Ti, (c) Ti-74.68 at. % Al and (d) Ti-99.46 at. % Al.	
Figure 6.4	224
Schematic diagram showing the reaction layer formation, its fragmentation and formation of the fresh reaction layer.	
Figure 6.5	232
Schematic diagram showing the temperature profiles at the reaction interface and the adjacent Ti and liquid Al.	
Figure 6.6	234
Schematic diagram showing the nature of the velocity profiles ahead of a hot solid particle (which is at a temperature of T_I) inside the fluid (initial fluid temperature is T_R).	
Figure 6.7	236
Schematic diagram showing the nature of the circulating loops, thermal currents inside the dispersed reaction domain.	

Figure 6.8 The Al-rich portion of the Ti-Al phase diagram 239 showing the variation of solubilities of Ti in liquid Al.

Figure 6.9 Schematic diagram showing the particle 241 disintegration along the pre-existing cracks.

Figure 6.10 Variation of total amount of reaction product 243 formed per unit area of the reaction interface with time at different reaction temperatures.

Figure 6.11 Variation of normalized distance of peak 249 volume fraction with reaction time at different reaction temperature.

Figure 6.12 Bright field TEM micrographs showing the 251 process of particle disintegration leading to formation of sharp edged particles.

Figure 6.13 SEM microstructures of $TiAl_3$ particles in 256 fully reacted couples; reacted at (a) 1073 K ($800^{\circ}C$) for 14400 sec (4 hour), (b) 1173 K ($900^{\circ}C$) for 7200 sec (2 hour) and (c) 1273 K ($1000^{\circ}C$) for 3600 sec (1 hour).

Figure 6.14 Schematic variation of reaction interface 259 temperature for various starting reaction temperature.

Figure 6.15 The Al-rich portion of the Ti-Al phase diagram 262 [60].

Figure 6.16 Nature of separation of $TiAl_3$ layer from Ti 266 surface due to incipient melting of $TiAl_3$ at higher reaction temperature.

Figure 6.17 $\ln k$ vs. $1/T$ for the data obtained on total 270 amount of reaction product per unit area of the reaction interface.

Figure 6.18 $\ln k$ vs. $1/T$ for the data obtained from the 270 variation of reaction zone thickness with time.

LIST OF TABLES

	page	
Table 1.1	Properties of Ni, Fe and Ti aluminides for high temperature applications	4
Table 1.2	Important properties of Ti_3Al , $TiAl$ and $TiAl_3$	6
Table 2.1	Various reactions occurring in binary Ti-Al system [49]	17
Table 2.2	Crystal structure, Pearson symbol and the respective phototype structures and lattice parameters of various Ti-Al compounds	19
Table 2.3	Compositional dependence of lattice parameters of solid solutions of $ZrAl_3$ - $TiAl_3$ [38]	23
Table 2.4	Elastic constants of $TiAl_3$ obtained from first principle calculations and experimental measurements.	26
Table 2.5	Lattice parameters and mechanical properties of various $L1_2$ base $TiAl_3$ intermetallics [58]	32
Table 2.6	Mechanical properties of various Ti_3Al base alloys [2]	36
Table 2.7	Constants of growth rate of $(TiAl_3 + Al)$ layer (K_C) and formation of $TiAl_3$ phase (K) [128]	74
Table 2.8	Effect of alloying elements on the coating layer thickness formed on Ti [127]	79
Table 4.1	Chemical compositions of the alloys used for the reaction couple preparation	84
Table 5.1	The minimum reaction time (t_{min}) at which complete consumption of liquid Al occurs	110
Table 5.2	Effect of reaction temperature on the average thickness of the reaction zone in Ti/Al reaction couples	110
Table 5.3	Effect of reaction temperature and time on the thickness of the reaction zone in Ti alloy/Al couples	117

Table 5.4a	Composition of the unreacted Ti in the Ti/Al couples reacted at 1073 K for 7200 s	120
Table 5.4b	Composition of the unreacted Al in the Ti/Al couple reacted at 1073 K for 7200 s	120
Table 5.4c	Composition of the TiAl_3 layer formed at the reaction interface (analysis done by EDS and WDS)	121
Table 5.4d	Composition of the TiAl_3 particles present in the two phase mixture of the reaction zone of couples reacted at 1073 K for 7200 s	122
Table 5.4e	Composition of the Al-rich matrix of the reaction zone in Ti/Al couples reacted at 1073 K for 7200 s	122
Table 5.5	Peaks positions (2θ) of the various phases present in Ti/Al couples reacted at 1373 K (1100°C) for 3600 s (1 hr)	139
Table 5.6	Standard X-ray diffraction data from powder diffraction cards for the compounds TiAl_3 , $\text{Ti}_8\text{Al}_{24}$ and $\text{Ti}_9\text{Al}_{23}$	141
Table 5.7	Lattice parameters of TiAl_3 base compounds formed in pure Ti/Al and Ti alloy/Al couples by reaction synthesis at 1073 K for 7200 s	147
Table 5.8	Reaction zone thickness, maximum and minimum values of aluminide particle volume fractions in the dispersed reaction particle and the distance at maximum volume fraction for different reaction couples	179
Table 5.9a	Polynomial expressions for volume fraction of TiAl_3 particles (V_v) as a function of distance from the reaction interface (x) in pure Ti/Al couples.	180
Table 5.9b	Polynomial expressions representing the variation in volume fraction (V_v) of TiAl_3 base particles with distance from the reaction interface in Ti-Al-V alloy/Al and Ti-Al-Mo-Zr-Si alloy/Al couples	181

Table 5.10	Effect of reaction temperature and time on the average volume fraction of $TiAl_3$ in the two phase (Al + $TiAl_3$) dispersed reaction domain of Ti/Al couples	186
Table 5.11	Effect of reaction temperature and time on the average volume fraction of $TiAl_3$ base compound in the reaction zone of Ti-Al-V alloy/Al and Ti-Al-Mo-Zr-Si alloy/Al couples	188
Table 5.12	Mean values of the microhardness of different phases in the reaction zone along with those of unreacted Ti and Al (mean value with confidence interval for 95% confidence level are shown)	205
Table 6.1	Temperature dependence of free energy of formation of various Ti-Al compounds as reported by Kattner et al. [49]	212
Table 6.2	Adiabatic temperatures recorded at reaction temperatures during reaction synthesis studies of different aluminide intermetallics and ceramic materials.	227
Table 6.3	Variation of the reaction interface (T_{ad}) with reaction temperature (T_R)	230
Table 6.4	Reactions occurring in the Al-rich portion of the Ti-Al phase diagram according to Raman and Schubert [60].	263
Table 6.5	Effect of reaction temperature and time on the amount of $TiAl_3$ formed per unit area of the reaction interface in Ti/Al couples.	269
Table 6.6	Activation energy obtained during studies on interaction of Ti with liquid Al.	272

SYNOPSIS

Aluminides of titanium have drawn considerable amount of attention of researchers in view of their attractive properties such as low density, high specific strength at room as well as elevated temperatures and good oxidation resistance. These properties indicate that titanium aluminides can be considered as potential materials for high-temperature structural applications. Among various intermetallic compounds existing in the Ti-Al phase diagram, the three aluminides based on compositions of Ti_3Al (alpha 2), $TiAl$ (gamma) and $TiAl_3$, respectively are of current interest. Of these three intermetallics, the compounds based on the composition of $TiAl_3$, are of special interest because they possess a superior oxidation resistance compared to the other two at temperatures as high as 1273K. In addition, $TiAl_3$ based compounds exhibit a higher specific hardness as compared to those of Ti_3Al and $TiAl$ base compounds. Due to these superior attributes of $TiAl_3$ base compounds over Ti_3Al and $TiAl$, an interest has recently been generated in developing $TiAl_3$ based alloys as low-density materials for high-temperature structural applications..

In spite of their many attractive properties the aluminides of titanium, in general, and $TiAl_3$, in particular suffer from poor room as well as elevated temperature ductilities. This poor ductility limits their fabricability by the conventional ingot metallurgy route(s). One way of circumventing this problem is to

develop net or near-net shape methods as alternative processing routes for the manufacturing of components from titanium aluminides. Among various alternative routes for making net shape components, the processing routes based on powder metallurgy (P/M) have been shown to be technologically feasible and economically viable. Reaction synthesis is one of the P/M based methods which has recently been adopted for producing aluminides of various metals such as Ni, Fe, Ti, Nb etc. P/M base reaction synthesis processes for synthesizing aluminides, in general, involve (a) blending of elemental powders in proportion to the stoichiometric composition of the compound, (b) carrying out the compound forming chemical reaction at a suitable temperature with or without a simultaneously applied external pressure on the powder mass or compact. The reaction temperature is generally kept above the melting point of aluminium and the aluminide of the metal is thus produced by a reaction between liquid aluminium and solid metal.

Though several investigations have been reported on the nature of the reaction between solid titanium and liquid aluminium, very little work has been done to understand the steps involved in the formation of intermetallic compound(s) and the mechanism(s) involved therein. The role of various processing parameters in understanding the evolution of microstructure in the synthesized product also remains unexplored. Therefore, the present work was undertaken to study the formation of $TiAl_3$ and $TiAl_2$ base alloys by the reaction synthesis with the objectives of understanding the

effect of processing parameters on (a) mechanism(s) responsible for the formation of titanium aluminide(s), (b) the kinetics of aluminide formation reaction and (c) the evolution of microstructure and its variation in the reaction product.

In order to meet these objectives, studies were carried out on reaction couples made from (i) pure titanium and pure aluminium and (ii) Ti-6Al-4V alloy and pure aluminium and (iii) Ti-6.5Al-3.2Mo-1.8Zr-0.3Si and pure aluminium respectively. Reaction couples were prepared from cylindrical samples of 20.0 mm height and 20.0 mm diameter machined from pure Ti or Ti alloy bars. A blind hole of 8.0 mm diameter and about 10.0 mm height was drilled in each sample along its cylindrical axis and after its cleaning with distilled water, acetone and hydrofluoric acid respectively a solid piece of high purity aluminium was inserted in it. Couples thus prepared were reacted isothermally under a flowing argon atmosphere in a specially designed horizontal tubular furnace at temperatures ranging between 973 K and 1373 K for time intervals from 0.9 ks to 14.4 ks.

Reacted samples were subsequently cut along their longitudinal axis and were subjected to different characterization techniques for the identification of phases formed and the analysis of microstructural features as evolved with respect to reaction time, reaction temperature and alloy chemistry. These techniques included x-ray diffraction analysis, optical, scanning and

transmission electron microscopy, energy dispersive spectroscopy (EDS), electron probe microanalysis and micro-hardness measurements. Since the reaction product of partially reacted couples was in the form of aluminide particles dispersed in an Al-rich matrix, quantitative metallography techniques were employed to estimate their (i) volume fraction, (ii) particle size distribution and (iii) morphology.

The metallographic examination of partially reacted products formed under all reaction conditions revealed the presence of (i) a reaction interface, (ii) a thin continuous $TiAl_3$ reaction layer adjacent to the reaction interface and (iii) a dispersed reaction domain in front of the reaction layer. The dispersed reaction domain consisted of fine aluminide particles of different sizes and morphologies in an Al-rich matrix. The zone consisting of thin continuous reaction layer of $TiAl_3$ and the dispersed reaction domain containing aluminide particles in Al-rich matrix was termed as the reaction zone. The reaction interface was the interface between unreacted Ti and the reaction layer. It was generally observed that both, the reaction layer as well as aluminide particle in the dispersed reaction domain, contained numerous cracks.

In couples partially reacted at a given temperature for a given time, the reaction layer as well as the entire reaction zone, though microscopically not planar, were found to be of more

or less a uniform thickness. Both, the mass of the total reaction product per unit area of the reaction interface and the reaction zone thickness, increased linearly with reaction time at reaction temperatures of 973K, 1073K and 1173K. Activation energy calculations based on such data gave its value to be lying in the range of 14.9 - 15.7 kcal/mole.

X-ray diffraction studies on pure Ti/Al reaction couples showed that while $TiAl_3$ was the only reaction product formed in the temperature range of 973K to 1273K, $TiAl_3$, as well as Ti_3Al_{23} formed at the reaction temperature of 1373K. The formation of $TiAl_3$ was also confirmed by the analysis of selected area diffraction patterns obtained under TEM. Even in the case of Ti-Al-V/Al and Ti-Al-Mo-Zr-Si/Al reaction couples $TiAl_3$ base compounds formed in the temperature range of 973 K to 1173 K. From the micro-probe analysis of the $TiAl_3$ base compounds formed in Ti-Al-V alloy/Al and Ti-Al-Mo-Zr-Si alloy/Al reaction couples, their chemical compositions were found to be Ti-62.8Al-1.6V and Ti-62.8Al-1.4Mo-0.7Zr-0.1Si (all in wt%) respectively. Results of the present study showed that a decrease in the lattice parameters of $TiAl_3$, i.e. a and c , occurred as a result of its alloying with V as well as (Mo + Zr + Si).

The x-ray dot mapping of the unreacted Ti adjacent to the continuous $TiAl_3$ layer did not show any enrichment by Al. Similarly, no significant amount of Ti was found to be present in

the Al matrix of the reaction zone. Further, regions of titanium/titanium alloy adjacent to the reaction interface did not show any variation in micro-hardness with distance from the reaction interface implying no solid-solution strengthening of titanium/titanium alloy adjacent to the reaction interface by its alloying with Al. From these findings it was concluded that the synthesis of $TiAl_3$ occurred by chemical reaction between solid Ti/ Ti alloy and liquid Al without any significant role of diffusion in it. However, once direct contact between solid titanium and liquid aluminium ceased further growth of the reaction layer occurred by diffusion, mainly that of Al through the lattice of $TiAl_3$.

The formation of $TiAl_3$ in preference to other Ti-Al aluminides in the reaction temperature range of 973K - 1273 K range could be explained in terms of its lowest free energy of formation among those of Ti_3Al , $TiAl$ and $TiAl_3$. The formation of $TiAl_3$, as well as Ti_3Al_{23} at the reaction temperature of 1373K could be explained in terms of (i) heat evolution at the reaction interface due to highly exothermic nature of the chemical reaction associated with $TiAl_3$ formation and (ii) incipient melting of $TiAl_3$, subsequently formed on the Ti side of the reaction layer. The formation of Ti_3Al_{23} at the reaction temperature of 1373K could thus be explained in terms of (i) the reaction between solid Ti and liquid $TiAl_3$, leading to the formation of Ti_5Al_{11} , (ii) decomposition of Ti_5Al_{11} giving $TiAl_2$ and $TiAl_3$ by the eutectic reaction and (iii) formation of Ti_3Al_{23} by a peritectic reaction between $TiAl_2$ and $TiAl_3$.

As observed under TEM, sub-structural features of the reaction layer as well as TiAl₃ particles present in the reaction layer revealed that the reaction product formed comprised heavily dislocated regions possessing planar defects such as stacking faults and superdislocations and also had numerous cracks along well defined orientations.

Results of the quantitative metallographic measurements made on dispersed reaction domains of partially reacted pure Ti/Al couples showed some general microstructural features. These features revealed that (i) the aluminide particles in the dispersed reaction domain had numerous cracks and possessed more-or-less equiaxed morphology, (ii) the degree of particle smoothness decreased and the extent of micro-cracking/ fissuring increased with increase in distance from the reaction interface, (iii) the particle size increased with increase in distance from the reaction interface and (iv) the volume fraction of particles in the reaction zone varied with distance from the reaction interface and went through a maximum in each case. The distance at which maxima occurred increased with increasing reaction time as well as reaction temperature. However, the distance at which the peak in the volume fraction occurred, when normalized with respect to the reaction zone thickness, initially decreased and then increased with increase in reaction time.

The particle size distribution in the dispersed reaction domain was also found to vary with distance from the reaction interface. The number of particles in the size range of 0 - 4 μm was found to be the largest near the reaction interface and it gradually decreased as the distance from the reaction interface increased. On the other hand, coarse particles were almost non-existent near the reaction interface and their number gradually increased with increasing the distance from the reaction interface. Increase in reaction temperature as well as reaction time resulted in an increase in the number of coarser particles with a corresponding decrease in the that of finer ones. With an increase in reaction time and temperature, particles initially exhibited a bimodal distribution and then attained a more or less uniform size distribution.

These general trends of microstructural distributions were found to be similar in the TiAl_3 base compound particles containing either ($\text{Mo} + \text{Zr} + \text{Si}$) or V formed in Ti-Al-Mo-Zr-Si alloy/Al and Ti-Al-V alloy/ Al reaction couples. The shape of these aluminide particles, however, varied considerably from that formed in pure Ti/ Al reaction couples. The TiAl_3 base alloy particles, in general, had more severe micro-cracking/fissurring in them and a majority of them had sharp and angular surfaces with a elongated morphology. The extent of particle angularity and their non-equiaxed nature increased with increasing the distance from the reaction interface. Also, the aspect ratio of particles in the

dispersed reaction domain increased as the distance from the reaction interface increased.

Microstructural features observed in dispersed reaction domains of reaction couples could be explained in terms of (i) convective currents which were set up in liquid ahead of the reaction interface due to the build-up of a thermal gradient arising from the exothermic nature of the chemical reaction, (ii) primary formation of aluminide particles from the reaction layer by processes of its fragmentation and separation, (iii) secondary formation of aluminide particles by disintegration of primary particles during their transportation under the influence of convective currents, (iv) smoothening of particle surfaces by their dissolution in the surrounding liquid, (v) reprecipitation of particles from super-saturated liquid and (vi) particle coarsening by Ostwald ripening.

Chapter 1

Introduction

Since weight saving by using lighter components at a given service temperature is one of the major objectives of aircraft engine design, the usage of titanium alloys for high-pressure compressor components in engines designed in early sixties had an important role to play in improving the performance of the gas turbine engines [1]. However, due to the limitations of their inferior strength, lower creep resistance and poor oxidation resistance at higher temperatures the application of even the most advanced titanium alloys is limited to approximately 850 K [2]. The usage of special steels and superalloys for engine components operating at higher service temperatures, therefore, has continued in spite of their densities being higher.

The demand for improving the performance of gas turbine engines, however, has been continuously increasing. Since such a goal can be made realistic by developing lighter high-strength high-temperature materials, the race for developing newer materials for elevated temperature applications has been going on at an ever increasing pace. Similarly, there is a widespread need for materials for other high-temperature aerospace applications also. Obviously, the requirements from these materials are low density, high strength, good creep resistance and microstructural stability at elevated service temperatures and a good oxidation resistance.

Since the capacity to improve these properties in metallic materials seems to have almost been exhausted by developing several alternative nickel- and iron-base superalloys, and no major breakthrough in the development of advanced metallic alloys has been reported in the literature during the last decade, the attention of researchers has shifted for the search of alternative advanced materials from among other generic groups such as ceramics and intermetallics. Intermetallics are compounds of two or more metals. These compounds can be either stoichiometric or may exist over a composition range, but are generally represented by a chemical formula. Intermetallic compounds crystallize in ordered structures which can be represented as interpenetration of two sublattices [3]. Ordered intermetallics have been found to have many of the desirable properties needed in high-temperature materials [4] and hence are considered as potential candidate materials for several high temperature structural applications [5]. From the point of view of their applications in aircraft gas turbine engines aluminides of nickel and titanium hold a considerable amount of promise [6]. In recent years the alloy development work in the area of structural intermetallics has remained focussed mainly on the aluminides based on Ni, Fe and Ti [5, 7].

Aluminides generally contain sufficient amount of Al so that they possess lower densities. Also, due to the presence of aluminium in them a thin protective layer of alumina forms when they are exposed to oxidizing environments at high temperatures [7]. This thin alumina layer as well as the covalent bonding

between constituent elements make them highly oxidation and corrosion resistant [4]. Further, since atoms in the ordered crystal structures of aluminides have specific neighbours and inter-atomic distances, activation barriers against plastic flow processes in them are high [2]. Obviously, these factors provide them high yield strengths. Moreover, for most of these aluminides the critical ordering temperature, i.e. the temperature above which the material becomes disordered, is equal to their melting point, their structure and strength are retained even at elevated temperatures [5]. However, in spite of having several important and useful properties, aluminides generally suffer from their room temperature brittleness which limits their use.

Properties of some of these aluminides which are important from the point of view of their high temperature applications have been shown in Table-1.1. Among various aluminides discussed above aluminides of titanium have drawn considerable attention because they possess low density and high specific strength at room as well as elevated temperatures [8, 9]. From the point of view of their potential as high-temperature low-density materials, three important titanium aluminides have been identified in the binary Ti-Al system. These aluminides are based on the compositions of Ti_3Al (commonly referred to as α_2), $TiAl$ (commonly referred to as γ) and $TiAl_3$.

Initially the research activities in the area of titanium aluminides were focussed mainly on the development of Ti_3Al , $TiAl$ and their alloys. However, several recent studies on

Table 1.1 : Important properties of aluminides of Ni, Fe and Ti

Alloy	Crystal structure	Melting Point (°C)	Density (g/cm ³)	Yield strength (MPa)	Room temp. ductility	Creep limit
Ni ₃ Al	L1 ₂	1,390	7.50	250-500*	2-50†	760
NiAl	B2	1,640	5.86	250-475	2	~1,200‡
Fe ₃ Al	DO ₃	1,540	6.72	385-392	2-12§	~700
FeAl	B2	1,250	5.56	360-380	2-17§	~827
TiAl	L1 ₀	1,460	3.91	400-650	1-4	1,000
Ti ₃ Al	DO ₁₉	1,600	4.20	700-900	2-10	760

* 0.2 wt. % B

† 0.1 wt. % B

‡ Alloyed with Nb

§ Depends on atmosphere.

TiAl_3 and its alloys have shown that these aluminides exhibit better oxidation resistance and superior specific strength at elevated temperatures [10]. Some of the important properties of these three aluminides have been summarized in Table-1.2. As far as the oxidation resistance of TiAl_3 is concerned, it has been reported that among Al rich compounds, i.e. TiAl and TiAl_3 , TiAl has poor oxidation resistance when compared to that of TiAl_3 at temperatures above 1073 K (800°C). This observation has been attributed to the chemical composition of the external layer formed in the two compounds when they are exposed to high temperatures. While in the case of TiAl base compounds the protective layer has been found to consisting of either TiO_2 or a mixture of TiO_2 and Al_2O_3 , the protective layer in the case of TiAl_3 has been found to be consisting of mainly Al_2O_3 . Thus TiAl_3 based alloys have been found to possess excellent oxidation resistance even at 1273K (1000°C) [10]. Further, owing to a higher Al content in TiAl_3 its density is lower than the other two aluminides which is mainly responsible for its high specific strength. Such attractive properties make TiAl_3 based compounds potential candidate materials for low-density high-temperature structural applications.

However, like most other intermetallic compounds titanium aluminides, and specially TiAl_3 , have poor room temperature ductility which makes them inferior in their fabricability as well as machinability [11]. Various approaches are therefore being adopted to improve their fabricability. These approaches include

Table-1.2 Properties of Ti_3Al , $TiAl$, and $TiAl_3$ Intermetallic Compounds

Property	Ti_3Al based α_2 alloys	$TiAl$ base γ alloys	$TiAl_3$ base alloys	Ref
Crystal Structure	DO_{19}	$L1_0$	DO_{22}	11
Mode of Deformation	Slip of $\frac{1}{6}<12\bar{1}0>$ on (i) (0001) , (ii) (1010) , (iii) (0221) Slip of $\frac{a}{6}<1210>$ + $c<0001>$ on (i) (1211) (ii) (0221)	Slip of $\frac{1}{2}<110>$ on $\{111\}$ Slip of $<011>$ on $\{111\}$ Slip of $\frac{1}{2}<112>$	Twinning of $(111)[11\bar{2}]$ Slip of $[110]$ on $\{001\}$ at 11	11
Critical Ordering Temperature ($^{\circ}C$)	1100	1460	1350	11
Melting Point ($^{\circ}C$)	1600	1460	1350	11
Density (g/cm^3)	4.1- 4.7	3.7- 3.9	3.4	11
Yield Strength (MPa)	700 - 990	400 - 650	-	11
Tensile Strength (MPa)	800 - 1100	450 - 700	-	11
Young's Modulus (GPa)	120 - 145	160 - 176	192*	11
Vickers Microhardness (kg/mm^2)	180 - 350	180 - 450	465-670	13
Oxidation Resistance ($^{\circ}C$)	650	800	1000	13

* $L1_2$ based $Ti_{25}Al_{67}Fe_8$

- (a) changing the alloy chemistry by micro- or macro-alloying with the aim of changing their room temperature ductility [5],
- (b) engineering the grain-boundary structure by thermo-mechanical processing so that an enhanced room temperature ductility is obtained in them [5]
- (c) development of near-net shape technologies so that the number of fabricating steps in the processing are minimized [12].

Powder metallurgical (P/M) processes have been thought of as commercially viable near-net shape manufacturing processes for several of these intermetallic compounds. Though fabrication of intermetallics can be undertaken by most of the conventional P/M processes, several unconventional processes based on the principles of *reaction synthesis* have drawn the attention of several researchers in the recent past [12-21]. These processes, classified here as a generic group of processes based on the principles of reaction synthesis, include reactive sintering (RS), reactive hot pressing (RHP), reactive hot isostatic pressing (RHIP), shock induced explosive formation (SIEF) and self propagating high temperature synthesis (SHS). In essence, all these processes involve (a) blending of elemental powders in proportion to the stoichiometric composition of the intermetallic compound and (b) carrying out the compound forming reaction at high temperature with or without the use of an externally applied pressure on the powder mass/compact. The key factor in all these

processes is the principle of reaction synthesis of intermetallic compounds which occurs due to the reaction between the constituent elements.

Though, several investigations have been reported on the synthesis of various titanium aluminides by reaction synthesis, very little work has been done to understand (i) the kinetic steps associated with the formation of intermetallic compounds and the mechanism(s) involved therein and (b) microstructural evolution in the reaction synthesized product and its variation with processing parameters. The present thesis deals with these aspects of reactive synthesis for the formation of $TiAl_3$ and its alloys. For this purpose, studies were made on reaction couples prepared from pure Al and pure Ti, pure Al and Ti-Al-V alloy and pure Al and Ti-Al-Mo-Zr-Si alloys which were subjected to reaction synthesis conditions at various temperatures for different time intervals.

This document deals with the literature review of the above mentioned problem in the area of intermetallics, the experimental procedures adopted, the results obtained and the conclusions drawn. Detailed literature review on (a) physical metallurgy and mechanical behaviour of $TiAl_3$ based aluminides and other Ti-Al intermetallics including those of Ti_3Al , $TiAl$ alloys, (b) reaction synthesis processes as applied to aluminide based intermetallics, in general, and Ti-Al based aluminides in particular and (c) $TiAl_3$ formation by solid-state diffusion between Ti and Al has been presented in Chapter-2. While objectives/scope of the present work has been given in Chapter-3,

the materials used and the detailed experimental procedures followed have been described in Chapter-4. The results obtained and discussion on them have been presented in Chapter-5 and Chapter-6 respectively. Finally, the conclusions drawn from the present study are enlisted in Chapter-7. Some suggestions which can be undertaken for further studies have been given in Chapter-8.

Chapter 2

Literature Review

Reaction synthesis of aluminides is generally done by carrying out the compound forming reaction within a stoichiometric powder compact prepared from elemental powder mixture. The exothermic energy released as a result of high heat of formation of the compounds gives rise to extremely high temperatures within the compact and thus helps in sintering it. Attainment of high temperatures at the reaction interface and relatively rapid cooling rates which may occur subsequently suggest that different non-equilibrium phases may form during reaction synthesis. Formation of several metastable phases, apart from equilibrium products, has in fact been reported during reaction synthesis of several aluminides. For example, during the reaction sintering of aluminides belonging to the compositions of Fe_3Al and $NiAl$, some amounts of other intermetallics ($FeAl_3$ and Fe_2Al_5 in the case of Fe_3Al and $NiAl_3$ and Ni_2Al_3 in the case of $NiAl$) were reported to have been formed [12, 20].

In order to explain the additional presence of these metastable/non-equilibrium phases in the reaction product knowledge of the phase equilibria in the corresponding temperature range is essential. It is therefore, relevant to discuss the different phases present in the Ti-Al and other ternary Ti-Al-X systems. This chapter deals first with (a) a brief overview of the

binary Ti-Al system and some of the ternary Ti-Al-X systems, (b) various intermetallics present in the Ti-Al system, their crystal structures and other relevant physical metallurgical aspects and (c) the reaction synthesis aspects of Ti-Al and other aluminide intermetallics of interest.

2.1 THE Ti-Al SYSTEM:

The binary Ti-Al phase diagram, as evaluated by Murray [22, 23], has been shown in Figure-2.1. It can be seen from this figure that the major equilibrium phases in the Ti-Al system are high- as well as low-temperature allotriomorphs of titanium, i.e. body center cubic (BCC) β -Ti and hexagonal close packed (HCP) α -Ti, their solid solutions with Al, Al and its solid-solution with Ti, liquid TiAl and the ordered intermetallic compounds - Ti_3Al (α_2), TiAl (γ), TiAl_2 and TiAl_3 [24]. In addition to these major phases, some other long period cubic super structures have been found to exist in the 25at.% Ti - 50at.% range of Ti of the Ti-Al phase diagram. However, they are still under discussions in the literature [24].

The interest in developing various titanium aluminide based intermetallic compounds for futuristic high- temperature structural applications has triggered a considerable amount of research activity in understanding the binary Ti-Al system and ternary systems with alloying additions such as Nb, Mo, V, Zr etc., [25-46]. For example, McCullough et al. have recently conducted more systematic studies on the high temperature phase

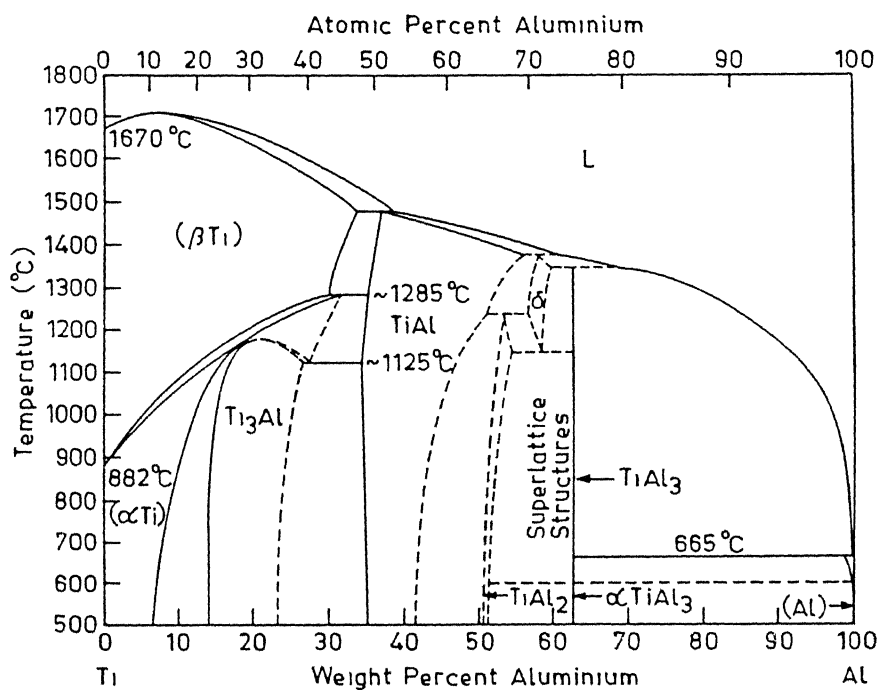
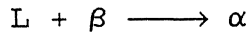
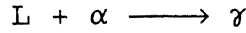


Figure 2.1 Binary Ti-Al phase diagram according to Murray [23].

equilibria in the Ti-Al system [47] and have shown that the hexagonal close packed (HCP) α -phase exists in the range of 46-50 at% Al at temperatures close to the melting point. It was also observed by them that in alloys containing < 44 at% Al the body center cubic (BCC) β -phase remains stable at similar temperatures. On the basis of these findings, McCullough et al. have proposed a modified binary Ti-Al phase diagram which has been shown in Figure-2.2. This revised phase diagram includes the two following peritectic reactions;



and



Similarly, several investigations have been carried out on phase equilibria studies in the Al-rich portion of the Ti-Al system [24, 48]. According to the studies of Schuster and Ipser [24], seven intermetallic phases are observed in the composition range of 24 - 42 at% Ti at above 1000°C [1]. TiAl_3 was found to melt incongruently at 1387°C decomposing into $\text{Ti}_5\text{Al}_{11}$ and liquid [48]. TiAl_3 co-exists with r- TiAl_2 up to 970°C and with Ti_2Al_5 in the range $970-1215^{\circ}\text{C}$. Above 1215°C , TiAl_3 coexists with $\text{Ti}_5\text{Al}_{11}$. $\text{Ti}_5\text{Al}_{11}$ forms from Ti_2Al_5 and r- TiAl_2 upon heating at 1206°C and decomposes peritectically at 1416°C into h- TiAl_2 + liquid [24]. h- TiAl_2 melts incongruently at 1433°C decomposing into h- $\text{Ti}_{1-x}\text{Al}_{1+x}$ and liquid. The Al-rich portion of the Ti-Al phase diagram as calculated by Schuster and Ipser [24] has been shown in Figure-2.3.

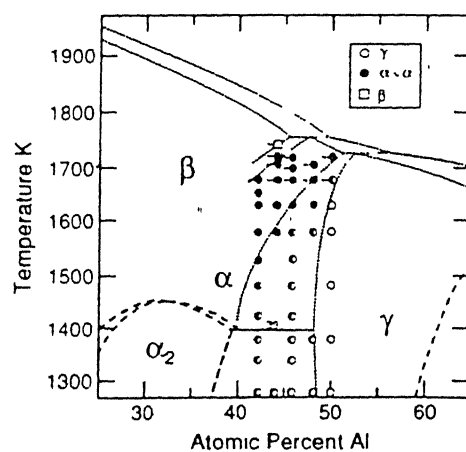


Figure 2.2 Binary Ti-Al phase diagram according to McCullough et al. [47].

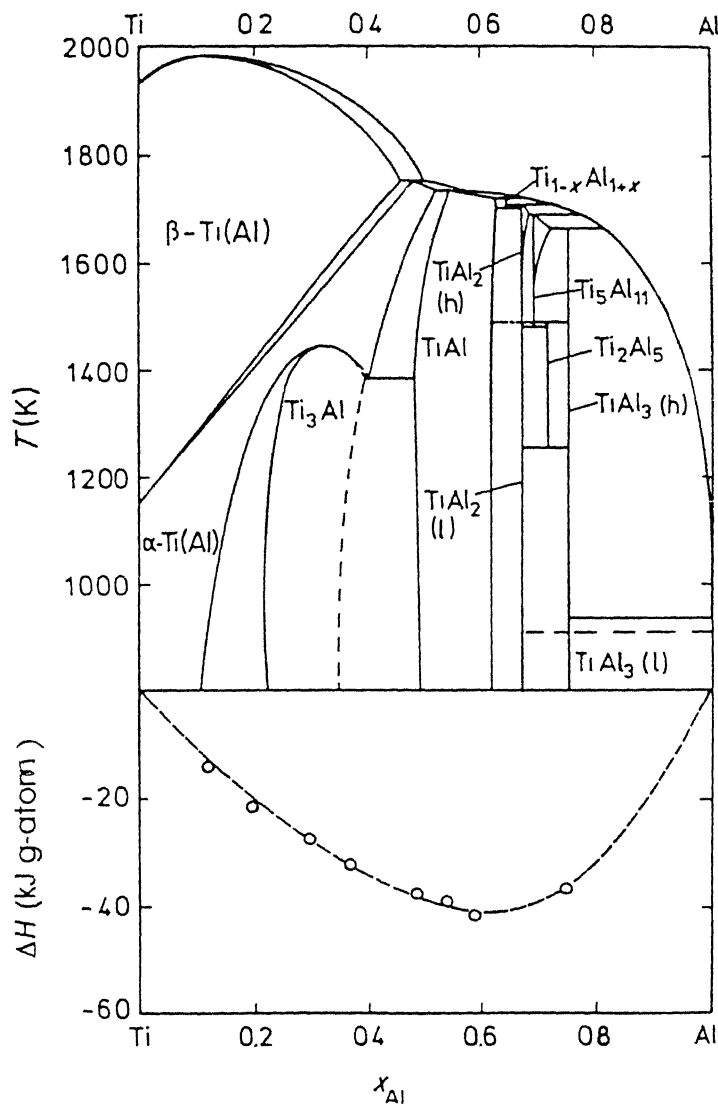


Figure 2.3 Binary Ti-Al phase diagram according to Schuster and Ipsen [24].

Kattner et al. have recently reviewed these developments on binary Ti-Al system as studied by various researchers [49]. Various invariant reactions in the binary Ti-Al phase diagram, as reviewed by Kattner et al., have been summarized in Table-2.1.

Thus several intermetallic compounds, such as Ti_3Al , $TiAl$, $TiAl_2$, Ti_2Al_5 , Ti_5Al_{11} , Ti_9Al_{23} and $TiAl_3$ exist in the Ti-Al system. Among these compounds Ti rich compounds Ti_3Al and $TiAl$ exist over a range of composition. As shown in Figure-2.4(a), Ti_3Al crystallizes in an ordered hexagonal DO_{19} crystal structure. Similarly, $TiAl$ also exists over a range of composition and crystallizes in face centered tetragonal $L1_0$ structure [Figure-2.4(b)]. In contrast to Ti_3Al which undergoes an order-disorder transformation, $TiAl$ remains ordered up to its melting point ($1450^{\circ}C$). In contrast to these two compounds, $TiAl_3$ phase exists as a line compound and crystallizes in tetragonal DO_{22} unit cell [Figure 2.4(c)]. Lattice parameters of $TiAl_3$ are $a = 0.03848\text{nm}$; and $c = 0.08596\text{nm}$. In addition to $TiAl_3$, Ti_9Al_{23} , Ti_2Al_5 and Ti_5Al_{11} also crystallize in the tetragonal ordered lattice. The compound $TiAl_2$ exists in two different crystal structures. It exists in the tetragonal ordered structure of the $HfGa_2$ type from room temperature to $\sim 1216^{\circ}C$. At temperatures above $1216^{\circ}C$, it transforms to an orthorhombic crystal structure and it remains in this structure up to $1433^{\circ}C$. Crystal structure, Pearson symbols and their respective prototype structures and the lattice parameters of these Ti-Al compounds are summarized in Table-2.2.

Table 2.1 Calculated and experimental invariant equilibria of the Ti-Al system as summarized by Kattner et al. [49]

Reaction	Composition of the respective phase (at. % Al)			Temperature (°C)
$L + \beta - Ti \rightarrow \alpha-Ti$	49.4	44.8	47.3	1490.0
	49	46.5	47	1495.0
$L + \alpha - Ti \rightarrow TiAl$	55.1	51.4	55.0	1462.8
	56	51	-	1462.0
$L + TiAl \rightarrow Ti_2Al_5$	72.5	66.5	71.4	1415.9
	68	-	-	1415.0
	~76	~64	-	1416.0
	~73	-	-	1425.0
$L + Ti_2Al_5 \rightarrow TiAl_3$	79.1	71.4	74.6	1392.9
	~78	-	-	1395.0
$L + TiAl_3 \rightarrow Al$	99.9	75.0	99.4	664.2
$\beta-Ti + \alpha-Ti \rightarrow Ti_3Al$	~29	35	30	~1200
$\beta-Ti + Ti_3Al \rightarrow \alpha-Ti$	~24	~26	25	~1150
$\alpha-Ti \rightarrow Ti_3Al + TiAl$	39.6	38.2	46.7	1118.5
	-	-	-	1120.0
	-	37	48	1107.0
$TiAl + Ti_2Al_5 \rightarrow TiAl_2$	64.5	71.4	66.7	1199.4
	-	-	-	1175.0
	-	-	-	1215.0
$Ti_2Al_5 \rightarrow TiAl_2 + TiAl_3$	71.4	66.7	74.2	990.0
	-	-	-	990.0

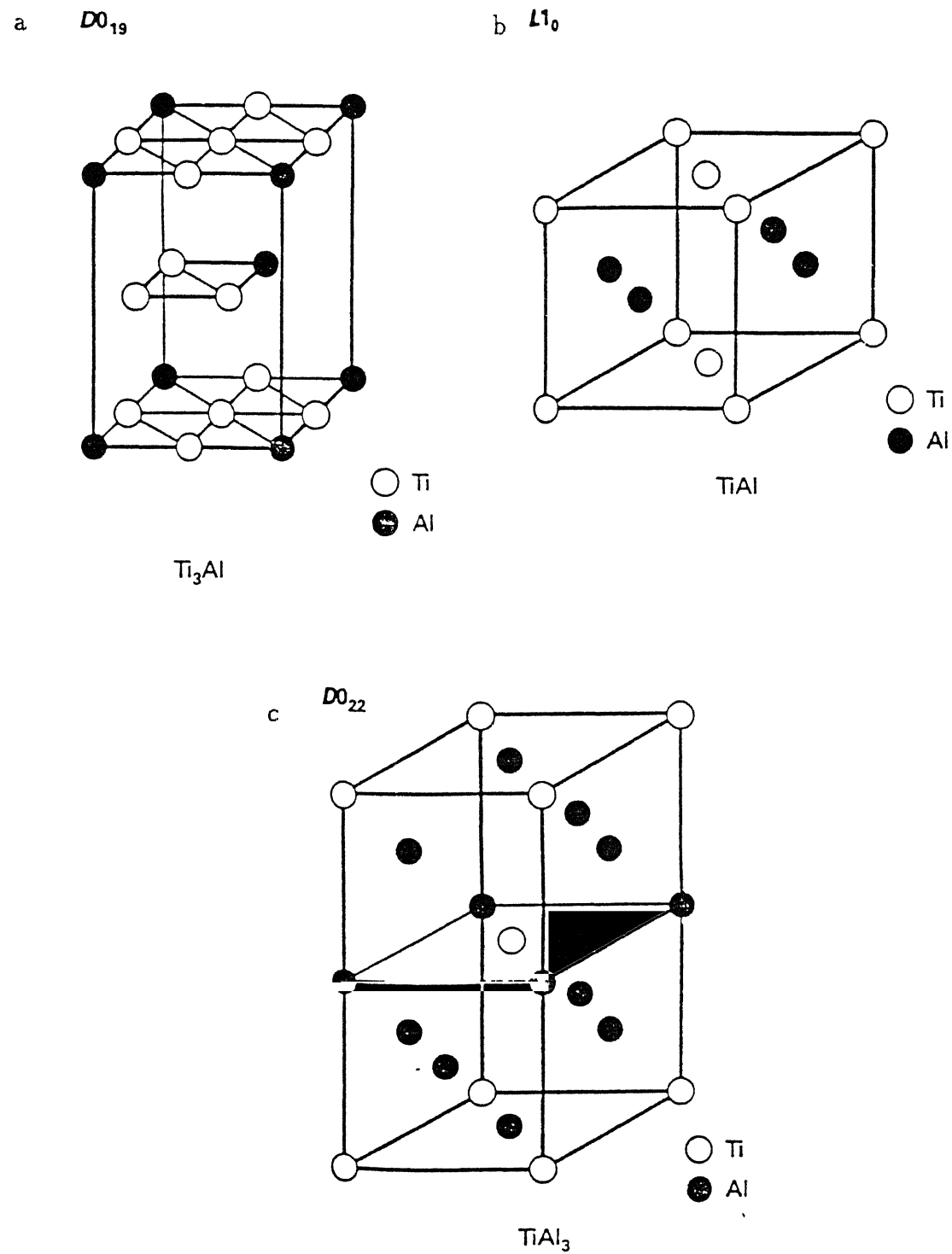


Figure 2.4 Crystal structure of the titanium aluminides;
 (a) Ti_3Al , (b) $TiAl$ and (c) $TiAl_3$.

Table 2.2 : Crystallographic data of the intermetallic compounds present in the Ti-Al system

Phase/temp. range (°C)	Pearson symbol/ crystal structure (Prototype)	Lattice parameter (pm)	Comments
Al < 660.45	cF4/fcc (Cu)	a=404.96	Pure Al at 25°C
β Ti (h)	c12/bcc (W)	a=330.65	Pure Ti at 900°C
α Ti (r) < 882	hP2/hcp (Mg)	a=295.06 c=468.35	Pure Ti at 25°C
Ti ₂ Al ₅ ~1215-985	tI28/tetragonal (Ti ₂ Al ₅)	a=390.53 c=291.96	
ξ Ti ₅ Al ₁₁ 1416-1206	tI16/tetragonal (ZrAl ₃)	a=392.30-393.81 c=1653.49-1649.69	29.1% to 31.5 at % Ti
TiAl ₂ (h) 1433-1214	oC12/tetragonal (ZrGa ₂)	a=1208.84 b=394.61 c=402.95	33-34 at % Ti
TiAl ₂ (r) < 1216	tI24/tetragonal (HfGa ₂)	a=396.7 c=2429.68	
Ti _{1-x} Al _{1+x}	oP4/tetragonal	a=402.62 b=396.17 c=402.62	x=0.28
γ TiAl < 1460	tP4/L1 ₀ (AuCuI)	a=398.69 c=405.39 a=401 c=407	at 38.5 at % Ti 1000°C at 50 at % Ti
α ₂ , Ti ₃ Al < 1180	hP8/DO ₁₉ (Ni ₃ Sn)	a=580.6 c=465.5 a=574.6 c=462.4	at 78 at % Ti at 62 at % Ti
TiAl ₃	tI8/DO ₂₂ (TiAl ₃)	a=384.8 c=859.6	at 75 at % Ti

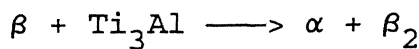
2.2 Ti-Al-X SYSTEMS:

In addition to binary Ti-Al phase diagram a number of ternary Ti-Al-X phase equilibria have been studied [25 - 46]. Phase equilibria in some of the important Ti-Al-X systems relevant to the present work are briefly reviewed in this section.

2.2.1 Ti-Al-Mo System:

The Ti-Al-Mo ternary system has been evaluated by several workers [27, 32]. The data on solid phases has revealed two ternary phases, β_2 and σ , which were identified as Ti_2MoAl and $Ti_3Mo_3Al_4$ respectively. The former one has been reported to have formed as a result of ordering of the BCC β solid solution of TiAl-MoTi and has the superlattice structure of CsCl type [30]. On the other hand, the second ternary phase σ , exists in equilibrium with the solid solutions based on the binary compounds TiAl, $TiAl_3$ and Mo_3Al . A significant mutual solubility of some binary phases has been observed in this system. For instance, the solubility of Mo in TiAl and $TiAl_3$ is 8 and 20 at.% respectively, whereas, the solubility of Ti in Mo_3Al is more than 20 at.%. In this ternary system, both Mo and Ti (up to 10 at.%) are soluble in $TiAl_3$ in comparison with the binary stoichiometric phase which exists as a line compound [31, 32].

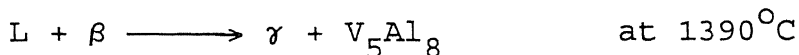
In addition to the above mentioned phases, a four phase invariant equilibrium exists at $550^{\circ}C$



where β_2 is the ordered phase of the Ti_2MoAl composition.

2.2.2 Ti-Al-V System:

The ternary Ti-Al-V system has been investigated extensively by a number of researchers [33 - 36]. However, the interest in this system has been focussed mainly on the Ti-rich corner due to the combined use of Al and V as major alloying additions to Ti. Among the solid phases, no ternary phases have been reported in this system. $TiAl_3$ and VAL_3 form a complete series of solid solutions below about $1100^{\circ}C$. As large as 8 ternary invariant reactions have been predicted in the Ti-Al-V system. Of these, only the following reaction has been detected experimentally by Volkova et al. [33];



Continuous series of solid solutions between $TiAl_3$ and VAL_3 has been reported to exist [34 - 36]. However, each of these studies have been carried out at different temperatures ($800-1100^{\circ}C$).

2.2.3. Ti-Al-Zr System:

Like Ti-Al-V, the Ti-Al-Zr system has also been investigated mainly in the Ti-rich corner at temperatures below $1200^{\circ}C$. In this system, the existence of two intermetallic compounds, ϵ and ϕ has been reported by Sandlin and Klung [37] in the composition ranges $0 < x_{Ti} < 0.55$ and $0.45 < x_{Al} < 0.60$. However, their crystal structures have not been reported. Among the pseudo-binary systems, the lattice parameters of $(Ti_xZr_{1-x})Al_3$

have been measured in the Al + 2(Zr + Ti) alloys. Two ranges of solid solutions exist for $ZrAl_3$ and $TiAl_3$. The two phase region lies between 2.75 and 6.25 at.% Zr. The compositional dependence of lattice parameters of these solutions is given in Table-2.3. In addition, the solubility limit of Al in α -Ti has been found to be constant (11.5 at.%) in the presence of 0-15 at.% Zr [38]. However, at higher Zr contents, it has not been investigated.

2.2.4 Ti-Al-Si System:

The Ti-rich corner of this system has been determined at several temperatures (in the range of 600-1200°C) up to 13 at.% Al and 3 at.% Si. Al was found to have very little effect on the solubility of Si in the HCP α -Ti phase, though it significantly decreases the solubility of Si in the BCC β -Ti [39, 40]. The precipitation of a ternary compound on addition of Ti to Al-Si eutectic alloy has been reported. This was identified to be $Ti(Al_xSi_{1-x})_2$ ($0.15 \leq x \leq 0.30$). The solubility of Si in $TiAl_3$ has been found to be up to the composition $Ti(Al_{\sim 0.85}Si_{0.15})_3$ at 1200°C [41]. Below 900°C, another ternary phase designated as $Ti_7Al_5Si_{12}$ has been found be stable [42]. However, at 700°C, a solubility range from $TiAl_3$ to $Ti(Al_{0.8}Si_{0.2})_3$ has been reported [43]. Two ternary phases one with the composition Ti_2AlSi_3 and other with undetermined compositions have been identified at this temperature. At room temperature also, a ternary compound $TiSi_2Al$ has been found to be in equilibrium with Al [44]. The invariant reaction

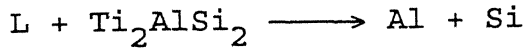
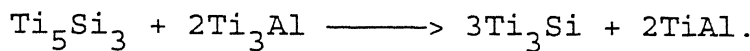


Table 2.3 : Compositional dependence of lattice parameters of solid solutions of $ZrAl_3$ - $TiAl_3$ [38]

Phase/ temperature range ($^{\circ}C$)	Pearson symbol/ prototype	Lattice parameters (pm)	Comments
β , (βTi , βZr) (h) βTi (h) 1670-882	CI2 W	$a = 330.65$ at $900^{\circ}C$	
βZr (h) 1855-863		$a = 356.8$	
α , (αTi , αZr) (r) αTi (r) <882	hP2 Mg	$a = 295.08$ at $27^{\circ}C$	
αZr (r) <863		$c = 468.55$ $a = 323.2$ $c = 514.7$	
α_2 , $Ti_3 Al$ <1180	hP8 $Ni_3 Sn$	$a = 578.2$ $c = 462.9$	22-39 at. % Al
$(Ti_{1-x}Zr_x)Al_3$ $TiAl_3$ <1387	TI8 $TiAl_3$	$0 \leq x \leq 0.11$ $a = 384.88$ at $x = 0$ $c = 859.82$ $a \approx 386$ at $x = 0.11$ (2.75 at. % Zr) $c \approx 863$	
$(Ti_xZr_{1-x})Al_3$ $ZrAl_3$ <1580	TI16 $ZrAl_3$	$0 \leq x \leq 0.75$ $a = 401.4$ at $x = 0$ $c = 1732$ $a = 393.6$ at $x = 0.75$ (6.25 at. % Zr) $c = 1685$	

is reported to occur at 579°C [46]. Another invariant equilibrium reaction is found to occur at 1067°C [46]



2.3 PHYSICAL METALLURGY AND MECHANICAL BEHAVIOUR OF TiAl_3 BASED ALUMINIDES:

In contrast to the work done on many other intermetallic compounds, very little attention has yet been paid to study the aspects of physical metallurgy, processing and the mechanical behaviour of TiAl_3 . However, the information which has been generated in the recent past on this intermetallic compound has been summarized in this section.

The binary Ti-Al phase diagram (Figure-2.1) shows that TiAl_3 intermetallic compound exists as a stoichiometric compound and has little or no off-stoichiometry. Recent *ab initio* quantum mechanical calculations have shown that, for the transition metal trialuminides dominated by the hybridized bonding between *d* electrons of the transition metal and *p* electrons of aluminium, the stable crystal structure will be one which has the maximum band-filling of the bonding states [50]. Thus the compound crystallizes in the structure for which the Fermi level lies in a deep valley separating the bonding and non-bonding states in the electronic density of states (DOS) distribution. As described in the previous section and shown in Figure-2.4(c), TiAl_3 crystallizes in the tetragonal DO_{22} (tI8) crystal structure. It can be shown that DO_{22} structure is derived from the Li_2 based fcc

ordered structure by introducing an antiphase boundary with a displacement vector of the type $\frac{1}{2} [110]$ on every (001) plane [51].

The elastic constants of TiAl_3 obtained from the first principle calculations are shown in Table-2.4 along with those measured experimentally. It was observed that the calculated values of TiAl_3 , as measured using first principle approach [52], are in good agreement with those obtained through experiments [53]. Both experimental and theoretical values of E and G for TiAl_3 are approximately three and half times those of pure Al and two and half times those of pure Ti. In addition, the density of TiAl_3 is only 24% higher than that of pure Al. The resulting specific Young's and shear modulus of TiAl_3 are thus much higher than those of the constituent elements Al and Ti. TiAl_3 is thus a material with an excellent strength to weight ratio. This tendency of 'high strength has also been observed in the other transition metal trialuminides, namely ZrAl_3 and NbAl_3 [53].

Based on the first principle calculations it was proposed that the high stiffness observed in these trialuminides is due to the strong hybridization between the aluminium 'p' orbitals and the transition metal 'd' orbitals [52]. However, the bulk modulus of TiAl_3 is only 44% higher than that of pure Al [53], giving rise to smaller $\frac{K}{G}$ values. Smaller $\frac{K}{G}$ values result in brittleness of these aluminides as suggested by Pugh [54].

Table 2.4 : Elastic constants of TiAl_3 in units of 10^2 GPa [55]

	C_{11}	C_{33}	C_{44}	C_{66}	C_{12}	C_{13}
TiAl_3 (experimental data) [53]	2.117	2.175	0.920	1.165	0.577	0.455
TiAl_3 (theoretical data) [52]	2.02	2.43	1.45	1.00	0.88	0.60

	Bulk modulus K	Young's modulus E	Shear modulus G	Poisson's ratio ν
TiAl_3 (experimental data) [53]	1.056	2.157	0.930	0.16
TiAl_3 (theoretical data) [52]	1.22	2.30	0.97	0.19

2.3.1. Deformation behaviour of binary $TiAl_3$ based aluminides:

Not much work has been carried out on the deformation behaviour of binary $TiAl_3$ based aluminides except that of Yamaguchi et al. [51,55], Vasudevan et al. [56], Morris and Lerf [57] and some studies by Nic et al. [58]. In order to identify the various deformation modes in this material. Yamaguchi et al. [51,55] studied the deformation behaviour of single crystal and polycrystalline $TiAl_3$ samples under compression.

There is a general agreement that the major mode of deformation in $TiAl_3$ is twinning of the type $(111) (11\bar{2})$ at low temperatures. However, at high temperatures, four twinning systems of the type $(111) (11\bar{2})$ augmented by slip of the types [100], [010] and [110] have been reported [51,55-58]. Further, it has been observed that significant amount of deformation occurs by slip on $(001)<110]$ at temperatures higher than $600^{\circ}C$. Vasudevan et al. [56] have suggested that the perfect dislocations with $b = \frac{1}{2}<112]$ dissociate as $\frac{1}{2}<112] + \frac{1}{3}<112]$, giving an SISF. The energy of this SISF has been measured to be $91-107 \text{mJm}^{-2}$. However, this high value of SISF energy does not justify the abundant ordered twins observed in deformed samples of $TiAl_3$ [57]. In this connection, Morris and Lerf [57] have suggested that the extensive twinning observed in $TiAl_3$ might be the result of difficulty in dislocation propagation rather than easy twinning. This proposition of Morris and Lerf is in agreement with the results of Khantha et al. [59] on the atomistic studies of screw dislocation cores in a DO_{22} crystal.

2.3.2. Mechanical properties of $TiAl_3$:

Deformation behaviour of $TiAl_3$ under compression has been reported by Yamaguchi et al. [51] and the yield strength as a function of test temperature in the range $25-860^0C$ has been obtained. The data obtained by them is shown in figure-2.5. These results show that the yield stress decreases with increase in test temperature till 620^0C . It has also been observed that room temperature fracture precedes yielding. Above 620^0C , it was observed that the yield stress decreases gradually with increase in test temperature with the resultant improved ductilities. This has been attributed to the additional operative modes of deformation by slip of the types [110], [100] and [010] at these temperatures. On the otherhand, studies on binary $TiAl_3$ alloys in the as-cast and HIP'ed conditions by Nic et al. [58] have shown no plastic strains in both compression and bending.

2.4. $L1_2$ TITANIUM TRIALUMINIDES:

As mentioned in the earlier sections, studies on DO_{22} based $TiAl_3$ by Yamaguchi et al. [51] have shown that the tetragonal $TiAl_3$ with the DO_{22} crystal structure is brittle near room temperature and deforms by ordered twinning. Brittleness in $TiAl_3$ has initially been explained to be due to the lack of sufficient slip or twin systems [51,55]. In addition, the brittleness of DO_{22} $TiAl_3$ has also been attributed to the sessile configuration of dislocation cores [59].

Therefore, efforts have been made in the direction of

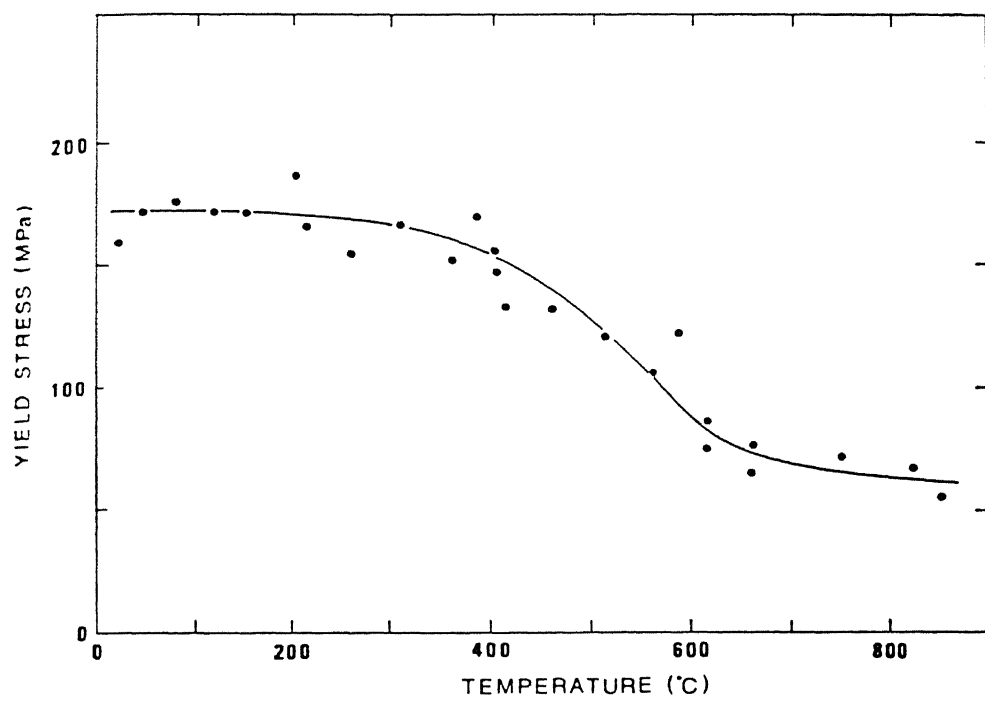


Figure 2.5 Compressive yield strength of polycrystalline TiAl_3 as a function of test temperature [51].

ductilizing these $TiAl_3$ based aluminides by transforming the tetragonal DO_{22} structure to cubic $L1_2$ structure with the expectation of inducing sufficient number of slip systems. The possibility of cubic transformation of DO_{22} to $L1_2$ crystal structure of $TiAl_3$ by the substitution of Ni, Cu and Zn for Al in DO_{22} superlattice was first reported by Raman and Schubert [60]. Similarly the formation of ternary Fe modified $L1_2$ compound $Ti_{25}Al_{66}Fe_9$ with a lattice parameter of 3.98\AA^0 was observed by Markiv and co workers [61]. More recent observations on $L1_2$ modifications of $TiAl_3$ has been reported by Seibold [62] by the substitution of Fe for Al. A series of cubic ternary alloys have been produced by alloying $TiAl_3$ with the elements of the 4th period from Cr to Cu [58]. The limits of $L1_2$ phase field at 1473K has been evaluated for arc melted Cr and Mn modified $L1_2$ alloys by Nic et al. [58].

In order to predict the DO_{22} to $L1_2$ transformations in various Al_3X ($X = Nb, Ta, V$) type of aluminides, several workers have developed the first principle calculations for electronic models [59]. Attempts have also been made to understand the relative phase stability of A_3B compounds by developing structural stability maps. Such an A_3B map has been used to explain DO_{22} to $L1_2$ transformation in the trialuminides [63]. Also, Nicholson et al. [64] have explained the DO_{22} to $L1_2$ transformation in $TiAl_3$ based compounds in terms of tetragonal distortion in stabilizing the DO_{22} structure of $TiAl_3$. Eberhart et al. [65] have used electronic models based on cluster calculations to explain the

DO_{22} to $L1_2$ phase transformation. This has been attributed to the 'd' character provided in the Al sp-bonding region by the transition metal substitution.

Effect of these elements on the microstructure, crystal structure, dislocation configurations and deformation behaviour has been reviewed by several authors [66-69]. Lattice parameters and mechanical properties of various $L1_2$ base compounds developed in the recent past have been given in Table-2.5 [58].

Though macro alloying approach has been adopted in order to ductilize $TiAl_3$ by changing the crystal structure to one which has more number of slip systems (DO_{22} -to- $L1_2$), results obtained on various transition element modified $TiAl_3$ have shown that even though they are more ductile than the DO_{22} base $TiAl_3$ in compression, they still remain brittle when tested in bending or tension [66-69]. However, some amount of tensile ductility has been observed in the Cr and Mn modified $TiAl_3$ alloys [66, 70-74].

Most of these $L1_2$ aluminides are, in general, brittle and have been found to fail by cleavage mode of fracture. Attempts were made to explain these properties in terms of crack tip blunting based on Rice-Thomson criterion [75]. Based on this model, different alloying additions have been used to modify the DO_{22} structure to $L1_2$ with the expectation of inducing sufficient number of slip systems in the structure [75].

Table 2.5 : Properties and lattice parameters of some $L1_2$ base $TiAl_3$ intermetallics [58]

Alloy	Lattice parameter a (nm)	Hardness HDP	Crack load (kg)	Young's modulus 10^6 psi
$Al_{67}Cr_8Ti_{25}$	0.3958	151 ± 2	>50	24.4
$Al_{67}Mn_8Ti_{25}$	0.3958	149 ± 5	>50	25.8
$Al_{22}Fe_3Ti_8$	0.3942	179 ± 6	10	26.0
$Al_{67}Co_8Ti_{25}$	0.3942	209 ± 10	1	
$Al_{67}Ni_8Ti_{25}$	0.3934	220 ± 10	5	26.0
Al_5CuTi_2	0.3931	300	3	
$Al_{66}Zn_9Ti_{25}$	0.392			

The results obtained on tetragonal DO_{22} to cubic $L1_2$ transformation and the effect of various alloying elements on factors such as the microstructure, deformation behaviour, mechanical properties and micro cracking of various $L1_2$ based $TiAl_3$ intermetallics have been reviewed.

2.5. PHYSICAL METALLURGY AND MECHANICAL BEHAVIOUR OF TITANIUM ALUMINIDES OTHER THAN $TiAl_3$:

As it has been discussed in section-2.1, several intermetallic Ti-Al compounds exist in binary Ti-Al system. Among these compounds the major three intermetallics which are of current interest and have been studied are Ti_3Al , $TiAl$ and $TiAl_3$. Aspects of physical metallurgy and mechanical behaviour of Ti_3Al and $TiAl$ intermetallics are reviewed in this section.

2.5.1. Ti_3Al Based Intermetallics:

As shown in the Ti-Al phase diagram (Figure-2.1) the Ti_3Al phase exists over a wide range of composition from 22-39 at% Al. Ti_3Al is represented in the Ti-Al phase diagram as α_2 . The stoichiometric compound Ti_3Al is stable upto $\sim 1090^0C$ [23].

As shown in Figure-2.6(a), it contains 3 linearly independant slip systems. These are $\frac{a}{6} <12\bar{1}0>$ type dislocation motion on the basal (0001), prismatic (1010) and pyramidal (0221) planes [8,9]. In addition to these, two (c+a) type of systems, which are related to the movement of $\frac{a}{6} <1210> + c <0001>$ dislocations on (1211) and (0221) planes, also give rise to slip

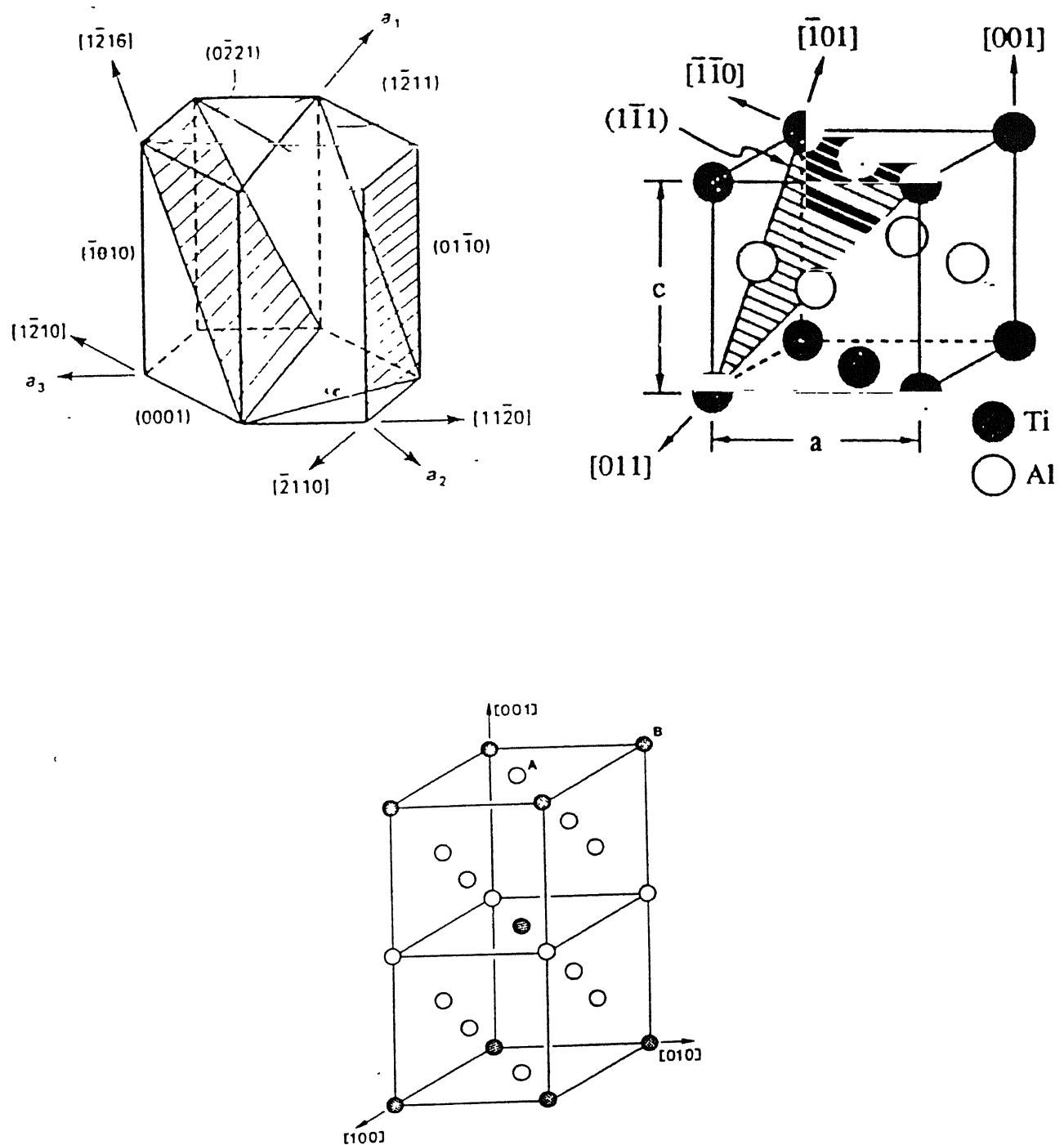


Figure 2.6 Slip systems in the lattices of Ti_3Al , $TiAl$ and $TiAl_3$;
 (a) DO_{19} base Ti_3Al , (b) $L1_0$ base $TiAl$ and (c) DO_{22} base $TiAl_3$.

in this DO_{19} structure thus amounting to a total of five independant slip systems. Stoichiometric Ti_3Al shows very little tensile ductility, upto a maximum of 0.5% at 600^0C . Above 600^0C , some improvement in ductility has been reported which has been attributed to the increase in the density of (c+a) dislocations at these temperatures [8, 9].

The mechanical properties of Ti_3Al based alloys have been reported in a review by Kim and Froes [2]. It was reported that addition of β stabilizers such as Nb, Mo and V results in twofold increase in the fracture strength (Table-2.6). Compared to the alloys with coarse widmanst tten microstructure, the fine widmanst tten microstructure containing alloys have shown better ductility. However, fracture toughness was observed to depend more on the alloying elements present rather than the microstructure. With increase in Nb content the fracture toughness was observed to increase due to an increase in the amount of β phase.

On the other hand, addition of Mo decreases the fracture toughness due to improvement in strength and a corresponding reduction in the ductility of the alloy. The ductility and toughness, are therefore found to raise sharply with increase in the β /B2 volume fraction. Effect of B2 volume fraction on the yield strength of various Ti_3Al-Nb alloys has been studied by Banerjee and Gogia [25, 76-78] and the results obtained in their studies are shown in Figure-2.7. The role of B2 phase on the mechanical properties of several Nb containing alloys can be seen

Table 2.6 : Mechanical properties of various Ti_3Al base alloys [2]

Alloys	TMP	Micro ^a	YS, MPa	UTS, MPa	El., %	K_{IC} , MPa \sqrt{m}	Creep rupture ^b
Ti-25Al	Ext	EG	538	538	0.3		
Ti-24Al-11Nb	1	W	787	825	0.7		44.7
	1A	W	510		2.0	20.7	
	4	FW	761	967	4.8		
Ti-24Al-14Nb	2	W	831	977	2.1		59.5
	1A	W	790		3.3	15.8	60.4
Ti-25Al-10Nb-3V-1Mo	3	W	825	1042	2.2	13.5	>360
	4	FW	823	950	0.8		
	5	C+P	745	907	1.1		
	5	W+P	759	963	2.6		
	6	FW+P	942	1097	2.7		
	1	W	952	1010	5.8	28.3	62
Ti-24.5Al-17Nb	7	W+P	705	940	10.0		
	3	FW	989	1133	3.4	20.9	476

^aTypical microstructure

^b H_r at $650^{\circ}C/380MPa$.

Ext = Extruded; EG = Equiaxed alpha-2 grains; W = Widmanstatten; FW = Fine Widmanstatten; FP = Fine primary alpha-2 grains; C = Colony with aligned alpha-2 plates; P = Primary alpha-2 grains.

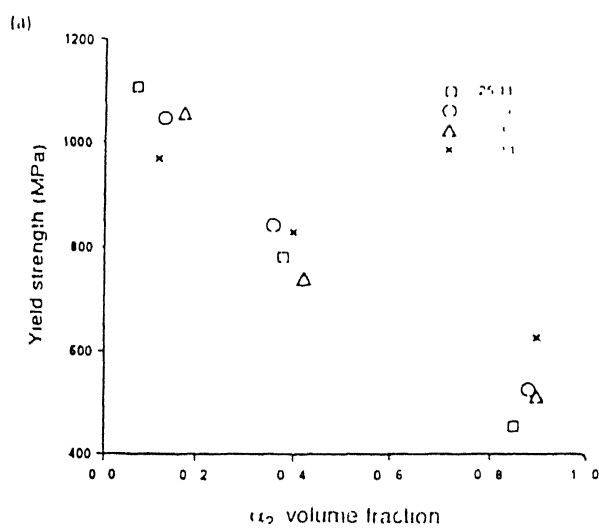


Figure 2.7

Effect of B2 volume fraction on the yield strength of various Ti_3Al-Nb alloys [76].

from this figure. It shows the variation of yield strength as well as percentage elongation as a function of α_2 volume fraction. It can be observed that the ductility at low B2 fractions is relatively high in comparison to single phase α_2 . This was due to the presence of B2 which delays the crack nucleation in α_2 to larger strains by accommodating plastic strains in itself. However, in case of high β (B2) containing alloys (18-20%), a step increase in the ductility of the alloys is observed. In these alloys the β phase is distributed in such a way as to avoid the α_2/α_2 grain boundary contact. The cleavage cracks present inside α_2 therefore propagate into the more ductile phase B2 during their growth. These higher Nb containing two-phase TiAl_3 base alloys are known to exhibit better creep properties as compared to many conventional superalloys used for high temperature applications [76].

2.5.2. TiAl Based Intermetallics:

Similar to Ti_3Al , TiAl also exists over wide a range of composition from 49-66 at.% Al depending on the temperature. Binary TiAl phase remains ordered upto its melting point of $\sim 1450^\circ\text{C}$ [23]. Crystal structure, microstructural control and mechanical behaviour of aluminides based on the TiAl phase are reviewed in the following subsections.

TiAl has the fcc derived ordered $\text{L}1_0$ structure and is represented in the TiAl phase diagram as γ . The crystal structure of TiAl is shown in Figure-2.4b. The alternate (200) planes of the

structure are occupied by Ti and Al atoms. Though the $L1_0$ structure is fcc derived, the TiAl structure was found to be tetragonal. For the stoichiometric composition, the $\frac{c}{a}$ ratio is equal to 1.02, while this ratio is observed to increase with increase in Al concentration upto 1.03 [79-81].

Deformation of TiAl (γ) occurs by slip of ordinary dislocations of the type $b = \frac{1}{2}\langle 110 \rangle$ and superdislocations of $b = \langle 011 \rangle$ and $\frac{1}{2}\langle 112 \rangle$ on $\{111\}$ planes (Figure-2.6b). The dissociation of superdislocations leads to the separation of a shockley partial $\frac{1}{6}\langle 112 \rangle$, creating a $\{111\}$ superlattice stacking fault [82]. However, it was shown that $\frac{1}{6}\langle 112 \rangle$ shockley partial does not get continuously get dissociated over the whole length of the superdislocation [83]. Instead, it was observed that sessile faulted dipoles form by local dissociation of superdislocations due to pinning of the $\frac{1}{6}\langle 112 \rangle$ partials [83]. In addition, it was observed that twinning on $\{111\}$ planes also contributes to the deformation of TiAl with the shockley partial $\frac{1}{6}\langle 112 \rangle$ as the twin dislocation [82, 83].

2.6. REACTION SYNTHESIS TECHNIQUE-APPLICATION TO ALUMINIDE SYSTEMS:

As discussed in the previous section, the main disadvantage associated with the use of the advanced materials belonging to the Ti-Al as well as the other aluminide based intermetallic materials is their lack of ductility and machinability at room temperature. This gives rise to problems in

the fabrication of Ti-Al parts for various applications. Though attempts have been made to improve the ductility of these aluminides by ternary alloying additions, the results have not been found to be satisfactory. Alternatively, researchers have focussed their attention on the development of near net shape (NNS) technologies [84] for the processing of parts made of these intermetallic materials. One of such NNS technologies is the processing of Ti-Al intermetallic materials from the elemental Ti and Al powders.

Most of the powder processing methods applied to intermetallics are mainly focussed on the development of materials by consolidation of prealloyed powders or ribbons. In such cases the consolidation techniques include compaction and sintering, hot pressing, hot isostatic pressing, hot extrusion, hot rolling etc., [85-88]. Although successfully employed, these methods have been found to involve several processing steps which make the process(s) expensive. Though high costs are justified in some cases, due to the improvements in the performance, the utility of these aluminides can be improved further only through development of low cost processing methods.

As compared to the other powder processing methods, reactive powder processing techniques are preferred in many cases, particularly when the constituents have a tendency to react chemically at a certain temperature. These techniques have been used since long time for ceramic powders.

2.6.1. RESEARCH ACTIVITIES IN THE REACTION SYNTHESIS SYSTEMS:

Much of the research in the area of reaction/combustion synthesis/Self propagating high temperature synthesis (SHS) of materials has been done by Russians. Originally started in the Soviet Union in the late 1960s, more than 500 materials using this technique have been produced. Materials processed using the SHS technique include a wide range materials such as electronic materials, metallic and ceramic super conductors, composites, intermetallics, abrasives and refractories. Research activities on reaction synthesis in the United States of America started in the early 1980's with the work of Crider [89]. Consequently several research activities have been started all over the world on the reaction synthesis owing to its several attractive features for processing of a wide range of materials. Various reviews have been presented on several aspects of the reaction synthesis system by Merzhanov [90], Holt [91], Munir [92], Munir and Anselmi Tamburini [93], Yi and Moore [94], Subrahmanyam and Vijayakumar [95]. Principles of reactive synthesis were first applied to synthesize intermetallics in 1970's [96-97].

2.6.2. REACTION SYNTHESIS PROCESSES IN GENERAL:

In reactive processing of intermetallics, two intimately mixed metallic reactants, for example powders of A and B exothermally react in a self-sustaining manner to form an intermetallic product A_xB_y . The formation of the compound occurs as a result of large difference in the free energy and enthalpy of the reactants and product(s) [Figure-2.8].

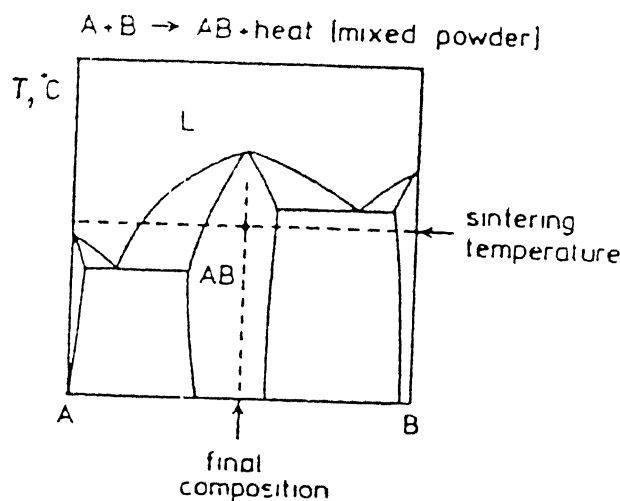


Figure 2.8

A schematic diagram showing the reaction synthesis system.

In most of the cases of reaction synthesis, partial or complete melting of some of the species involved in the reaction takes place. Formation of a liquid phase is advantageous since densification of the product material is accelerated due to capillary forces exerted by the liquid formed. Also, the mass transport processes take place much faster in the liquid state. However, liquid formation may turn out to be disadvantageous if it causes swelling and loss of shape of the compact may be observed as it has been shown in several systems undergoing a reaction during the synthesis process [98]. Furthermore, the enthalpy of fusion of the melted species is absorbed without increase in the overall temperature, resulting in a reduction in the maximum temperature of the product thus leading to incomplete reaction in certain cases [98].

The maximum temperature obtained during adiabatic reactive synthesis is mostly controlled by the amount of liquid reactants at the beginning of the reaction, since the enthalpy of fusion of the reactants is usually high compared to the total enthalpy needed to bring the reactants from their initial temperature to the final temperature of reaction.

According to the physical state of the reactants at the onset of the reaction, the reactive synthesis processes can be categorized into three classes as described below:

CLASS-I: WHEN ALL THE REACTANTS ARE IN THE SOLID STATE:**(a) Self Propagating High Temperature Synthesis (SHS):**

In this method, a mixture of reactant materials is compacted into a porous self supporting preform. The preform is subjected to a localized temperature increase (e.g. by heating with an electric arc, plasma torch etc.,) initiating the reaction locally. The reaction propagates in the preform in the form of a wave front.

(b) Reactive Sintering (RS)

Here, a porous preform (either a uniaxially pressed or a cold isostatically pressed powder compact) of the reactant mixture is heated uniformly until a self-sustaining reaction takes place simultaneously within the whole volume of the preform.

(c) Reactive Annealing (RA)

The process of reactive annealing is very much similar to that of reactive sintering except that the difference is, in case of reactive annealing the mixture of reactants is a pore free body (produced either by lamination of foils, extrusion of powders or infiltration of preforms).

(d) Reactive Hot Pressing / Hot Isostatic Pressing (RHP / RHIP)

Reactive hot pressing or reactive hot isostatic pressing are reactive synthesis processes involving in-situ compaction of the product during its synthesis. In the later case, hydrostatic

pressure is imposed on the reacting preform, thus compacting the product. On the otherhand, in the case of reactive hot pressing, a uniaxial compressive stress is applied mechanically on the preform which is usually contained in a die.

(e) Reactive Shock Synthesis (RSS)

In this method, a porous preform of the reactant powder mixture is subjected to rapid increase in temperature and pressure using a shock wave thus initiating a self-sustaining reaction leading to the product formation.

CLASS-II: SOME REACTANTS ARE IN THE LIQUID STATE:

Reactive Infiltration (RI)

In the process of reactive infiltration, a preform of solid reactant is infiltrated with a liquid reactant, and the two reactants form the product.

CLASS-III: ALL THE REACTANTS ARE IN THE LIQUID STATE:

(a) Reactive Spray Deposition (RSD)

In this technique, reactant powders are injected into, and melted within, a stream of inert hot gase or plasma, and deposited upon a substrate where they react to form the product.

(b) Reactive Casting (RC):

Reactive casting involves mixing two streams of reactant liquids so that they are reacted in the liquid state to form the product.

All the above processes have their advantages as compared to the other NNS synthesis/manufacturing processes like casting and powder metallurgy of prealloyed powders. The main advantages of reactive synthesis processes can be enumerated as follows:

- (i) Since the enthalpy released by the reaction internally heats the product, the need for external source of energy gets reduced.
- (ii) Heat released from the volume of the reactant preform (unlike most other external heating methods where heat is conducted from its surface) and the high density of stored chemical energy being liberated in a self-sustaining manner results in rapid heating. On the otherhand, if the reaction is initiated at a low temperature and the product is kept in contact with cold surroundings, rapid cooling can be achieved. These rapid heating and cooling rates result in short production cycles, fine grained microstructure and reduced contamination from the surroundings.
- (iii) Due to high temperature of reaction, the volatile impurities get evaparated giving rise to a high purity product.
- (iv) Near net shape processing is possible which allows the processing of difficult to shape materials like intermetallics and their composites.

However, there are certain associated disadvantages of reactive synthesis processes. These include

- (i) difficulty in controlling the reaction kinetics, once synthesis has been initiated,
- (ii) the use of powders, which may increase contamination as a result of their large surface area, and are more expensive than melts,
- (iii) final porosity in the product, which can however, be minimized by the application of pressure either during or after the reaction,
- (iv) loss of shape in case of self standing preforms as a result of slumping upon melting and swelling upon gas evolution,
- (v) loss of volatile reactants or products.

An understanding of the reactive synthesis processes is essential in order to exploit the prominent features of this system for processing a sound material according to the requirement. Both fundamental and applied investigations were carried out on reactive synthesis/SHS over the past few decades. However, the basic mechanisms associated with the SHS processes are not very clear, due to their complex nature. Complexity of these processes lie in the fact that the reactions occurring in such systems deviate highly from the equilibrium conditions, take place at relatively high temperatures and are associated with extremely large temperature gradients [99]. The nature of the reaction/combustion synthesis process, the modes of reaction synthesis process, effect of process parameters on the nature of the reaction product etc., have been reviewed in this subsection. Special attention towards the end of the section is given to the

processing of several intermetallics using the concept of reaction synthesis, specially with reference to processing several aluminide base intermetallics.

2.6.3. THERMODYNAMICS OF COMBUSTION/REACTON SYNTHESIS:

The thermodynamic principles governing the mechanisms of reactive synthesis processes are important in order to estimate various parameters such as the adiabatic temperature of reaction, amount of liquid phase formed during the synthesis etc. [15, 94, 95].

Once the synthesis reaction is initiated at few local areas of the reaction mixture, extremely high temperatures are achieved in very short times. at the reaction interface due to the exothermic energy release associated with compound formation. It is, therefore, reasonable to assume that a thermally isolated system exists because of the negligible amount of time available for any heat losses to the surroundings. Therefore, the maximum temperature to which the product is raised can be assumed to be the adiabatic temperature A_{ad} as suggested by Gaskell [100]. Similar assumptions were made by Holt and Munir during adiabatic temperature calculations in the combustion synthesis of titanium carbide [13].

As the enthalpy of the system is a stat function, the heat liberated during the reaction, ΔH^0 is given by

$$\Delta H^0 = \Delta H_{298}^0 + \int_{298}^{T_{ad}} (\Delta C_p)_{prod.} dT$$

... 2.1

where

ΔH_{298}^0 = Standard enthalpy of formation of the product at 298K,

ΔC_p = Change in the heat capacity due to the formation of the products.

For a thermally isolated (adiabatic) system, $\Delta H^0 = 0$. Hence,

$$-\Delta H_{298}^0 = \int_{298}^{T_{ad}} (\Delta C_p)_{prod.} dT$$

... 2.2

This can be explained as shown in Figure-2.9, for the case where T_{ad} is less than the melting point T_{MP} of the product.

In the case where $T_{ad} = T_{MP}$,

$$-\Delta H_{298}^0 = \int_{298}^{T_{ad}} (\Delta C_p)_{prod.} dT + f_p \Delta H_m$$

... 2.3

where,

f_p = Fraction of the product in the liquid state

and ΔH_m = Heat of fusion of the product

For the case when $T_{ad} > T_{MP}$, the corresponding relationship will be given by

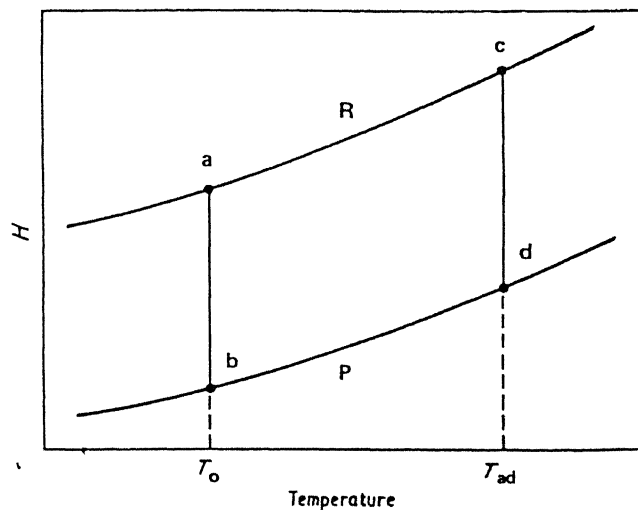


Figure 2.9

A schematic diagram explaining the calculation of T_{ad} .

$$-\Delta H_{298}^{\circ} = \int_{298}^{T_{MP}} (\Delta C_p)_{\text{prod. (s)}} dT + \Delta H_m$$

$$+ \int_{MP}^{T_{ad}} (\Delta C_p)_{\text{prod. (l)}} dT \quad \dots 2.4$$

In many systems undergoing reaction synthesis, the synthesis reactions generally occur only when the reactants are at an elevated temperature T_{ig} , which is known as the ignition temperature. In such cases the adiabatic temperature ' T_{ad} ' will be dependant on the ignition temperature T_{ig} [16], and can be calculated for various cases according to the following equations:

$$-\Delta H_{T_{ig}}^{\circ} = \int_{T_{ig}}^{T_{ad}} (\Delta C_p)_{\text{prod.}} dT \quad \text{for } T_{ad} > T_{MP} \quad \dots 2.5$$

$$-\Delta H_{T_{ig}}^{\circ} = \int_{T_{ig}}^{T_{MP}} (\Delta C_p)_{\text{prod.}} dT + f_p \Delta H_m \quad \text{for } T_{ad} = T_{MP} \quad \dots 2.6$$

$$-\Delta H_{T_{ig}}^{\circ} = \int_{T_{ig}}^{T_{MP}} (\Delta C_p)_{\text{prod.}} dT + \Delta H_m + \int_{T_{MP}}^{T_{ad}} (\Delta C_p)_{\text{prod. (l)}} dT$$

for $T_{ad} > T_{MP}$ \dots 2.7

It is possible using the above equations to calculate the adiabatic temperature T_{ad} . The required thermodynamic parameters are obtained from the literature. However, it was

CENTRAL LIBRARY
IIT KANPUR

Cat. No. A 123583

reported that there is a lack of agreement between the experimentally observed combustion temperature, T_c , and the calculated adiabatic temperature, T_{ad} . The discrepancy in these values has been attributed to the assumptions incorporated in developing the theoretical model [94]. Hence it can be supposed that the values of T_{ad} that can be obtained from equations 2.5-2.7 are the upper limits for T_{ad} . From the knowledge of T_{ad} , certain systems can either be eliminated for experimentation or combined with other more exothermic reactions to make them amenable for reactive synthesis. Merzhanov [14] has suggested an empirical criteria that if $T_{ad} < 1500K$, combustion does not occur, and if $T_{ad} > 2500K$, self propagating combustion occurs. In the range $1500K < T_{ad} < 2500K$, combustion wave cannot propagate, but can be made to do so by special techniques such as initial heating of the reactants.

2.6.4. MODES OF COMBUSTION SYNTHESIS:

Different modes of combustion were reported in systems undergoing reaction synthesis as described in the reviews of Yi and Moore [94] and Munir [99]. Different modes of combustion were reported in systems undergoing reactive synthesis. The concept of SHS diagrams has been proposed with the objective of providing the criteria for the existence of different modes of combustion. These diagrams are represented in graphical form. A schematic SHS diagram as given by Munir [99] is shown in figure-2.10. As shown in the figure, SHS diagrams reveal the expected mode of combustion at various degrees of dilution and initial temperature.

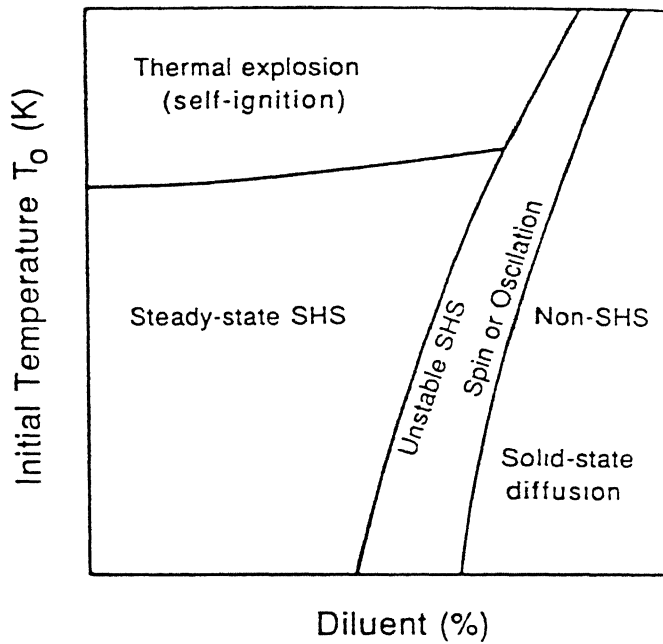


Figure 2.10 A schematic SHS diagram.

Since the propagation of reaction wave front is closely related to the activation energy of the combustion reaction, it is expected that changes in activation energy will be influencing the mode of wave propagation. As the activation energy (E^*) increases, the mode changes from a steady state propagation to a non steady state propagation (oscillatory mode of wave motion) and with further increase in E^* , the combustion process gets extinguished. Or in other words, the boundary between SHS/non-SHS regimes can be determined.

Of the several possibilities, the reaction modes can be classified into various techniques and these are described in the following:

(i) Stable or Steady State Combustion:

Stable or steady state combustion phenomenon has been observed in several cases. These are identified by synthesis occurring between solid-solid reactions. Or in otherwords, the combustion temperature existing in the corresponding binary system. In this mode, it was observed that the combustion front advances at a constant rate with time [94].

(ii) Unstable Combustion:

Unstable mode of combustion is obtained by conversion from stable mode by altering the conditions of combustion. These changes can be brought about by the addition of an inert component or diluent. Here the propagation of the combustion wave changes with time. Depending on the combustion wave front propagation, two

variations in the reaction product are possible. In certain cases, combustion occurs only over a narrow surface layer and the bulk of the sample remains unaltered [94]. In some cases, the final product is found to have a layered structure.

(iii) Thermal Explosion:

Thermal explosion mode of reaction is observed in the combustion of intermetallic compounds. The thermal explosion mode of reaction is the case in which the combustion reaction occurs simultaneously throughout the powder compact. Intermetallics are in general processed using this technique because they exhibit low exothermic heats of formation and also they are processed at low ignition temperatures in general. Systems belonging to this mode of combustion show exothermic peaks associated with combustion reaction correspond to compound formation. In general, the combustion temperatures does not exceed 2000°C.

2.6.5. COMBUSTION SYNTHESIS OF ALUMINIDE INTERMETALLICS:

The principle of reaction synthesis has been applied for the processing of various intermetallic compounds. Out of a number of published research works available on reactive synthesis of intermetallic materials, major work has been focussed on studies on different aluminides. The reactive synthesis of aluminides has the following characteristics that make them distinguished from the reactive synthesis processes applied to ceramics and other intermetallic materials.

- (i) Forms eutectics with almost all aluminide forming metals.
- (ii) Aluminides exhibit lower melting points.
- (iii) Heats of formation of aluminides are in general are lower than those of ceramics.
- (iv) The phase diagrams of all binary aluminium- transition metal systems exhibit a number of intermetallic phases, which often possess similar enthalpy and free energy of formation.

Of the aluminides produced by reactive synthesis, the aluminides of Ni, Ti, and Fe have received considerable attention [12,19,20,101-106]. In addition, a few studies have also been done on the processing of Cu, Zr and Nb based aluminides also [107-108].

For the preparation of aluminides, both combustion and thermal explosion modes are utilized. In the following few subsections, reactive synthesis of some of these aluminides has been discussed.

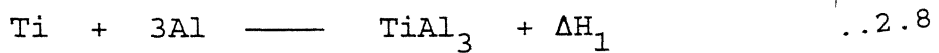
2.6.5.1. Reaction Synthesis of Titanium Aluminides:

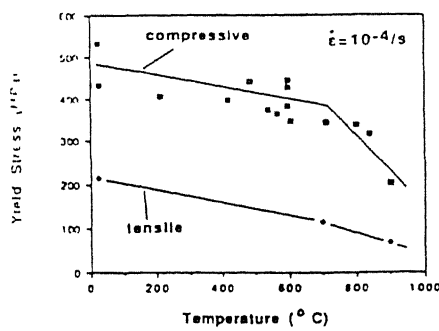
A number of studies have been carried out on the reaction synthesis of titanium aluminides [106,109-116]. Of these, major amount of work has been focussed on the synthesis of compounds based on TiAl. In general, TiAl has been produced by the combustion mode of reactive synthesis [109-116]. The reaction in

such cases was in general, initiated by rapid heating of one end of the sample, so that the combustion wave propagated from one end to throughout the sample. However, the products produced by this mode of synthesis were in general, porous and hot isostatic pressing was employed in order to fully densify the material. The mechanism of TiAl formation has been studied extensively by Wang and Dahms [110,114,116] and by Rawers and Wrzesinski [109,112,113]. Results obtained by Wang and Dahms on reactive powder processing of TiAl alloys are shown in Figure-2.11 [114].

Rawers et al. [109,112,113] studied the formation of TiAl as well as composites based on TiAl. In their experiments of the self-propagating high temperature synthesis technique, reaction was initiated by the ignition of cold pressed powder compact using a fine tip oxyacetylene torch. In a parallel route, synthesis was done using the reactive hot pressing technique. In the former case, the product had high porosity, negligible strength and the phases formed were identified to be Ti_3Al and $TiAl_3$ in addition to TiAl. However, in the case of reactive hot pressed samples, only traces of Ti_3Al were found to be present along with TiAl.

Based on their Differential Scanning Calorimetric (DSC) results, Rawers et al. [109] have proposed the following reaction sequence for the formation of Ti-Al intermetallics:





The 0.2% yield stress for alloy Ti-48 at % Al in condition A as a function of testing temperature for both tensile and compressive loading

Figure 2.11

Results obtained on reactive powder processing of TiAl alloys [114].

The exothermic energy released by the above reaction was observed to be sufficient to melt $TiAl_3$. The molten $TiAl_3$ thus formed reacts with the surrounding Ti to form TiAl according to the reaction



The driving force for SHS reaction was attributed to the combination of the two exotherms associated with the formation of $TiAl_3$ and TiAl. The process map for the formation of $TiAl_3$ and TiAl intermetallics has been shown in Figure-2.12 [117].

The mechanism of aluminide formation as identified by several of these studies [106,109-116] agree with the fact that the reaction between Ti and Al gives rise to formation of $TiAl_3$ at the reaction interface. Further reaction between Ti and $TiAl_3$ leads to the formation of the other intermetallic compounds of Ti-Al system, namely, Ti_3Al , TiAl and some times $TiAl_2$ also. However, $TiAl_2$ formed has been found to react with Ti_3Al to form TiAl. An extensive review on the reactive synthesis of Ti-Al aluminides has been done by Wang and Dahms [110,114].

The influence of various factors like heating rate, reactant particle size and stoichiometry in reactive synthesis of Ti-Al intermetallic compounds has been studied by Yi et al. [106]. In their studies, the combustion temperature was found to be of the order of 1573 K. However, the combustion temperature was found

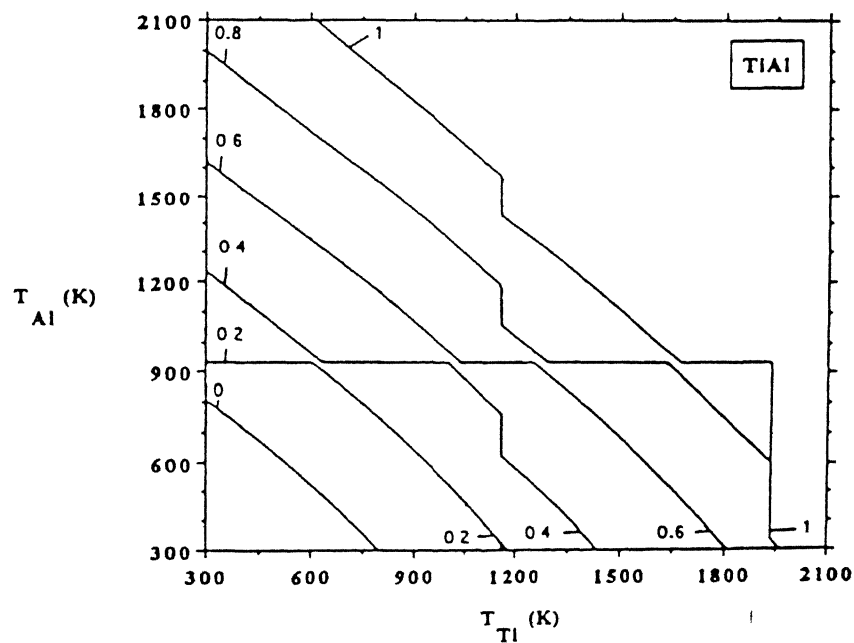
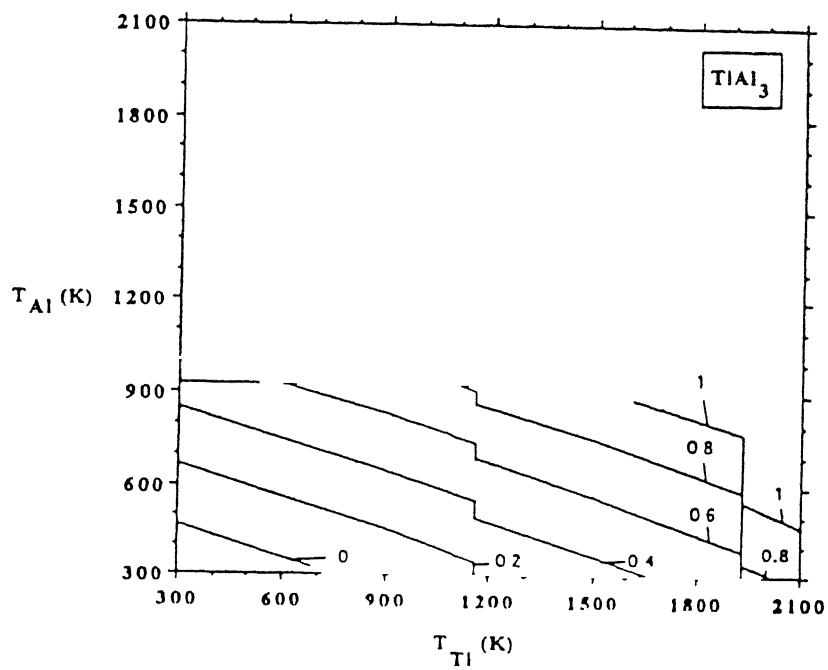


Figure 2.12 Process maps for the formation of TiAl_3 and TiAl intermetallics [117].

to vary with the ignition temperature of the compact. The product was found to be mainly TiAl with traces of TiAl_3 and Ti_3Al . Heating rate had a substantial influence on the density of the product. It was observed that the increase in heating rate from 10 K/min to 50 K/min had improved the density of the product from 48% to 58%.

Heating rate was found to influence the reaction mechanism also. Under lower heating rates (≤ 10 K/min), liquid Al and solid Ti react to form TiAl_3 , till the entire Al in the reactant mixture gets consumed. Further reaction gives rise to TiAl and Ti_3Al . Thus the product formed in the case of samples reacted at lower heating rates show a mixture of all the three phases. On the other hand, at higher heating rates, the reaction mechanism is solid - solid reaction due to the exothermic energy released corresponding to the reaction of moisture with Al, Ti triggering the reaction at a lower temperature (< melting point of Al). This supports the formation of single phase TiAl_3 product, as observed in samples reacted at a heating rate of 50 K/min [106].

2.6.5.2. Reaction Synthesis of Ni-Al Intermetallics:

The reactive synthesis approach for the processing of nickel aluminides has been extensively applied by several researchers [20, 101, 103, 104]. Many of these studies have been carried out using the technique of reactive sintering. The reactive sintering treatment has been found most appropriate near the lowest eutectic temperature, which is $\sim 640^\circ\text{C}$. Under controlled

reaction conditions through appropriate selection of particle sizes, composition, heating rate, sintering temperature and atmosphere, a product with density as high as 95% theoretical was synthesized [103]. Highest densities could be achieved with low sintering temperatures and short sintering times. In order to achieve near full density material, techniques like reactive hot pressing and reactive hot isostatic pressing have been successfully tried [104]. Other reactive synthesis processes like reactive infiltration were also applied to synthesize Ni_3Al based intermetallics.

The formation of nickel aluminides by self-propagating high temperature synthesis via thermal explosion mode was done by Philpot et al. [101]. It was observed in these studies that the combustion temperatures as high as ~2100K can be achieved at a preheating temperature of 773K. Also, it was observed that the combustion temperature can be increased enormously by using higher heating rates, thus obtaining denser products. To realize the potential of combustion synthesis of nickel aluminides, extensive amount of studies were carried out by Bose et al. [20]. The results of their studies show that combustion synthesis offers considerable flexibility in terms of controlling the alloying and microstructure. For example, it was possible to add boron or other additions directly to the reactant powder mixture.

Initial assessment of the mechanical properties of the combustion synthesized nickel aluminides were found quite

promising. For example, a sample of combustion synthesized Ni_3Al containing about 0.06 % boron (hipped to assist further densification) has shown a room temperature tensile strength of 722 MPa and a ductility of 10% [117] as compared to the mechanical properties of ingot metallurgical processed $\text{Ni}_3\text{Al-B}$.

2.6.5.3. Reaction Synthesis of Fe-Al based intermetallics:

The technique of reaction synthesis was employed by Rabin and Wright [21,31] to produce Fe_3Al and FeAl based alloys from elemental Fe and Al powders by reactive sintering. It was observed that synthesis of the Fe_3Al compound takes place within several minutes (2sec.) during rapid heating of the compact [21]. The observed effects of green density, heating rate and Al powder particle size on the sinterability of Fe_3Al has were attributed to the net result of swelling and shrinkage processes that occur during compact heating. Highest sintered density of approximately 75 % theoretical for Fe_3Al was achieved by using fine aluminum of size 3 μm . Near theoretical density alloys of Fe_3Al and $\text{Fe}_3\text{Al-Cr}$ have been fabricated from elemental powders by simultaneous reaction synthesis and hot isostatic pressing.

2.6.5.4. Reactive Synthesis of NbAl_3 :

Reactive synthesis of NbAl_3 aluminides has been studied by Murray and German [118] using the techniques of reactive sintering and reactive hot isostatic pressing with the objective of finding the effect of process variables on the microstructure and density of synthesized NbAl_3 . Reactive sintering was found to

be an effective and efficient technique in synthesizing NbAl_3 with a uniform microstructure and a maximum density of 95 % theoretical was obtained. It was pointed out that higher heating rate is needed for rapid melting of Al and hence achieve reactive synthesis in Nb-Al compact faster. Also this was found essential for densification of the structure by capillary action as well as for the quick release of exothermic heat to promote interparticle bonding. At the same time, it was suggested that higher heating rates are not advised in order to let the evolved gases escape freely from the compact during the reaction. Hence optimization of heating rate is essential by balancing the needs for liquid phase densification, interparticle bonding and sufficient degassing.

2.6.5.5. Reaction Synthesis of Cu-Al Intermetallics:

Reactive synthesis of copper aluminides has been studied by Itin et al. [107,108]. Reactive synthesis experiments have been carried out on compacts of Cu-Al powder mixes by ignition in a furnace [108]. Ignition of the compact was done on a Ti-B (of composition corresponding to TiB_2) placed above above the Cu-Al compact. It was pointed out in these studies that initial heating of the compacts was essential to initiate the synthesis process. For the stoichiometric composition Cu_2Al and Cu_3Al , minimum temperatures at which combustion was observed are 350 and 400°C .

2.7 TiAl_3 FORMATION DURING INTERACTION OF Ti WITH LIQUID Al:

Numerous studies have been carried out on the aluminide formation during the interaction between solid Ti and liquid Al over the last few decades. Major works done in this area are

- (i) kinetic studies on the interaction of Ti with Al melt by Mackowiak and Shrier [119-121] and
- (ii) studies on hot dip aluminide coatings on Ti as well as those dealing with crystallization of $TiAl_3$ crystals from Al-Ti melts [122,123].

In addition to these, some contributions to this area has been made through studies on laser surface alloying [124,125], welding and brazing of Ti with Al/Al alloy filler material [126]. Majority of attention in all these studies was in general, aimed at understanding the mechanism of $TiAl_3$ formation during the interaction between solid Ti and liquid Al.

In addition, effect of alloying elements present in Ti or Al on the growth kinetics of $TiAl_3$ phase have also been attempted in most of these studies. The results obtained in these studies [119-126] on different aspects of $TiAl_3$ formation have been reviewed in the following subsections.

2.7.1. Nature of samples used for studies on $TiAl_3$ formation:

Preliminary studies on $TiAl_3$ formation have been carried out by Mackowiak and Shreir [119,120]. Samples of two different geometries were used for this purpose. Initially studies were carried out on cuboidal shaped Ti specimens (Figure-2.13). These specimens were immersed in molten Al contained in an Al_2O_3 crucible and were heated at different temperatures and times in a vacuum furnace. Studies were also carried out on cylindrical Ti specimens by holding in Al melt [121].

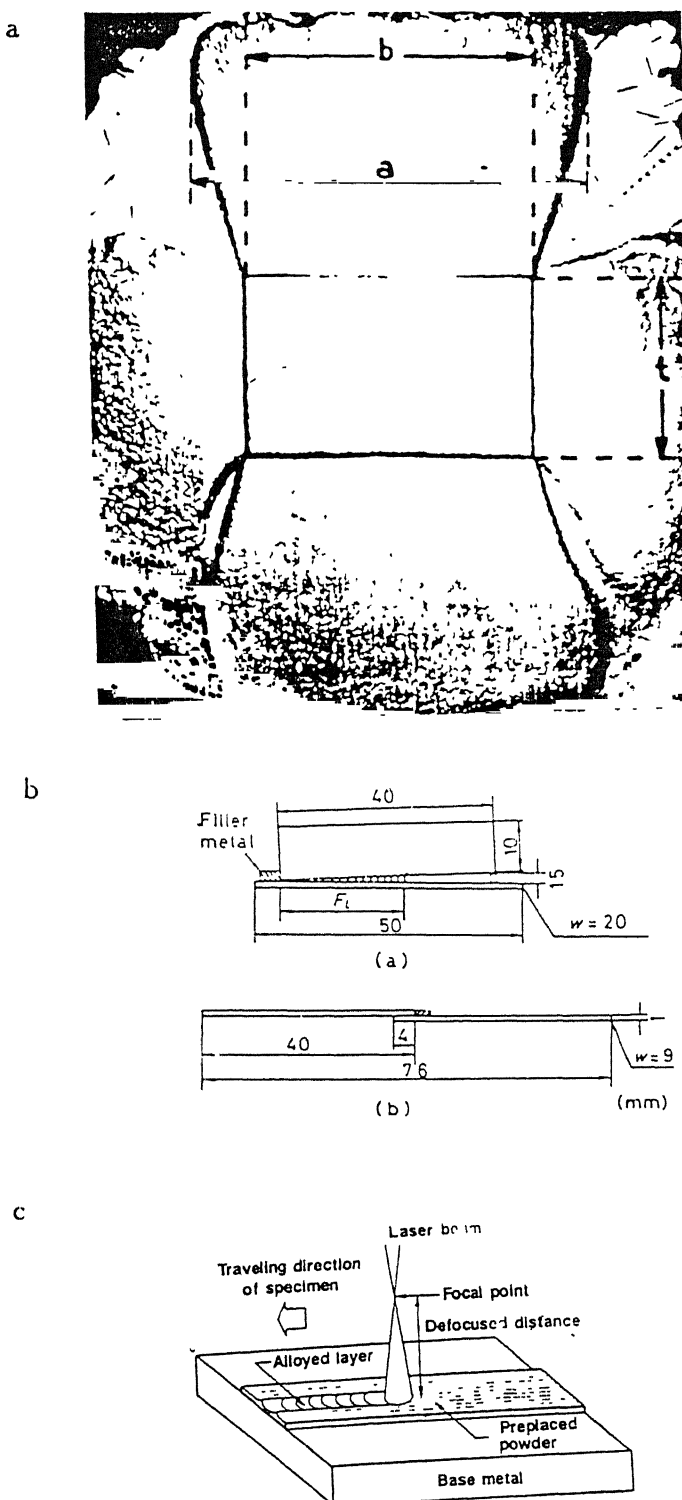


Figure 2.13 Nature of specimens used for studies on $TiAl_3$ formation [119]: (a) cuboidal shape samples used by Mackowiak and Shreir, (b) Ti/Ti weld samples [126] and (c) samples used for laser surface alloying

Studies on formation aluminide based intermetallics were reported by Takemoto and Okamoto [126] during brazing of Ti with Al filler metals at a temperature of 680°C . The samples used for this purpose were pure Ti plates of 1mm thick on which brazing experiments were done using either a pure Al filler metal or Al alloyed with one or more of the alloying elements Cu, Sn, Ag and Si (Figure-2.13b).

Most recent studies on TiAl_3 formation by interaction between Ti and liquid Al were reported by Abdel-Hamid [122,123]. These studies consisted of crystallization of aluminide compounds from either ternary Al-T-M or quaternary Al-Ti-M-M' (M/M' = Ta, Zr, V and Mo). TiAl_3 base compounds were crystallized from 1000°C to room temperature [122,123]. In addition to [122], Abdel-Hamid carried out work TiAl_3 formation using hot dipped coatings on Ti in a molten Al bath [127]. Eremenko et al. [128] carried out kinetics of aluminide formation by holding cylindrical Ti specimens in a molten Ti-Al alloy in the temperature range of 700°C - 900°C . In a similar study, coupons of titanium were hot dipped at $\geq 1200^{\circ}\text{C}$ and the aluminide coatings formed were subjected to microstructural examination and microhardness measurements.

2.7.2. Chemical composition and microstructures of the aluminides formed:

Mackowiak and Shreir [119-121] carried out X-ray diffraction studies and metallographic examination of the interaction layers formed. X-ray diffraction results revealed the

presence of $TiAl_3$ phase. Microstructures of the interaction layers showed the presence of a thin layer of $TiAl_3$ adjacent to the Ti surface. Ahead of this $TiAl_3$ layer, a two phase microstructure of $TiAl_3$ in Al were reported to be present [121]. It was also reported that no diffusion of Al in Ti was observed. Similar observations were made by Slama and Vignes as far as the microstructure of the interaction layer formed is concerned [129]. However, they report that diffusion of Al inside Ti has also been observed. During studies on brazing of Ti with Al filler metals, microstructures of the interaction layers formed consisted of thin layer ($\sim 13.3\mu m$ thick) of $TiAl_3$ layer at the Ti/Al interface.

Similar microstructures were reported in the case of hot dip aluminide coatings formed on Ti [127]. Even in the case of Ti solid solutions containing one or more of the elements of Ti, Ta, Cu, Si, Mg, Fe, Zn, Sn, Zr V and Mo, the microstructures the aluminide formed by hot dipping showed a thin layer of $TiAl_3$ at the Ti/Al interface with a two phase region of $(Al+TiAl_3)$ ahead of this thin $TiAl_3$ layer.

Aluminide formation reported during various other processes have shown similar microstructures for the interaction layer. For example, studies were conducted on CO_2 laser alloying on Al surfaces (Figure-2.13c) [124]. The aluminide layers thus formed contained dendrites of $TiAl_3$ in a matrix of Al. In the central region of the coating, the microstructure showed approximately 100% $TiAl_3$ phase. At farther distances from the

surface, granular $TiAl_3$ precipitates dispersed in a matrix of Al were observed [124]. However, by controlling the processing conditions, produced coatings consisting of homogeneous microstructure of $TiAl_3$ grains. This could be achieved by laser alloying a powder mixture of Ti-75 at.% Al at a high travelling speed of 5mm/sec. In this case, melting of base metal Al was avoided by high travelling speed of the laser and microstructures consisting of $TiAl_3$ grains free of elemental Al.

2.7.3. Growth kinetics of $TiAl_3$ formation:

Growth kinetics of $TiAl_3$ layer formed during the interaction of Ti with liquid Al has been studied in detail by several workers [119-128]. The results obtained in these studies are reviewed in this subsection. As mentioned in section-2.7, preliminary studies on aluminide formation were carried out by Mackowiak and Shreir [119-121]. One aspect of their studies dealt with kinetics of interaction of Ti with liquid Al. Kinetics were evaluated from measurements made on decrease in thickness of Ti due to dissolution in liquid Al while forming $TiAl_3$. Results obtained on two different Ti samples (containing 99.75 wt% Ti and 99.00 wt.%) are shown in Figure-2.14(a) to 2.14(b). The growth rate constants 'k' were evaluated from the slopes of the plots shown in figures-2.14. From this data, the activation energy for dissolution of Ti was calculated from the Arrhenius plots of $\log(k)$ versus $\frac{1}{T}$ (Figure-2.15).

These results showed an activation energy of 22 ± 2 kCal/mole. In addition, [121] presented results obtained on

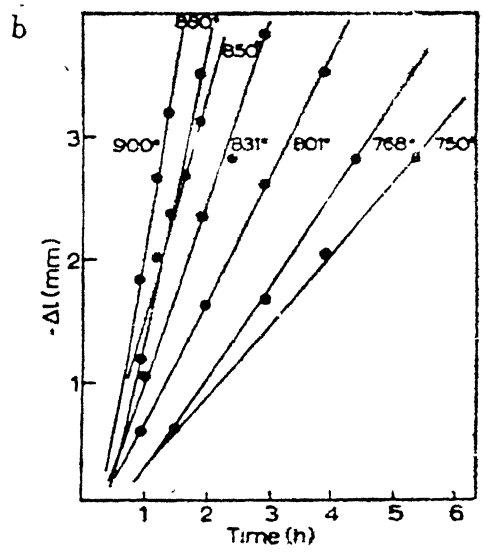
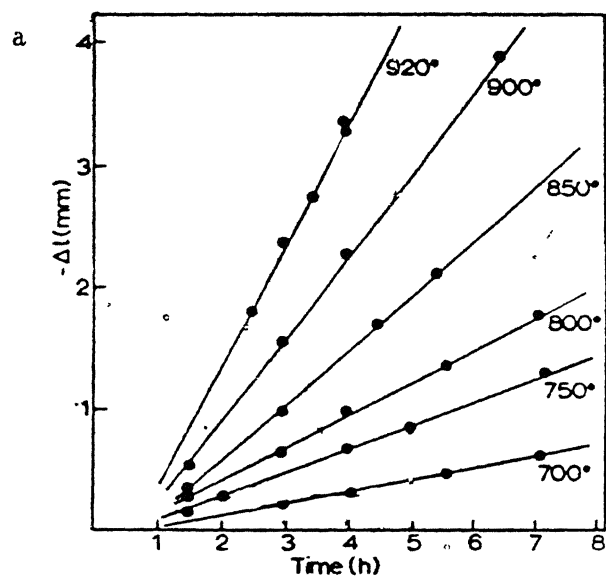


Figure 2.14 Decrease in thickness of Ti specimens due to dissolution in liquid Al; (a) 99.75 wt.% Ti and (b) 99.00 wt.% Ti.

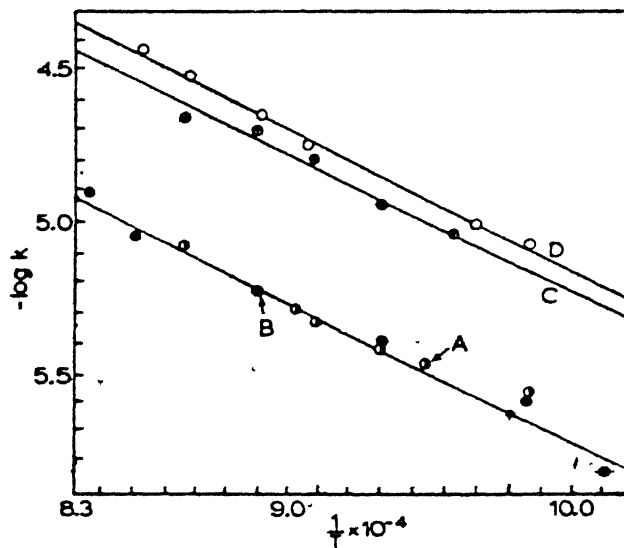


Figure 2.15 Arrehenius plots of $\log (k)$ versus $\frac{1}{T}$ for the dissolution of Ti in liquid Al; A: 99.00 wt.% Ti and B: 99.75 wt.% Ti.

variation of interaction layer thickness with time for the same specimens of Ti (of composition 99.75 wt.% Ti) used for the previously mentioned study (Figures-2.16(a) and 2.16(b)). Activation energy for the growth of interaction layer was found to be 23 ± 2 kCal/mole.

From the results obtained from these two data it was observed that the activation energy for dissolution of Ti as well as for the growth of the interaction layers in the case of commercial pure titanium were found to be in good agreement. Hence it was proposed that the mechanism of aluminide formation is chemical interaction between Ti (s) and Al (l) and not by diffusion.

In a later study, Eremenko et al [128] reported that the product layer thickness formed on Ti varied linearly with time in the range of 700°C - 900°C . The increase in the length of the titanium specimen due to formation of a layer of reaction products was found to vary linearly with time (Table-2.7). From these results it was observed that within the limits of experimental error, the activation energy for growth of Ti during interaction with solid as well as liquid Al matched with the heat of fomation of TiAl_3 [128]. Based on these observations as well as the linear dependency of the growth rate with time, it was concluded that chemical kinetics is the mechanism of TiAl_3 formation.

Growth kinetics of TiAl_3 layer has been studied by

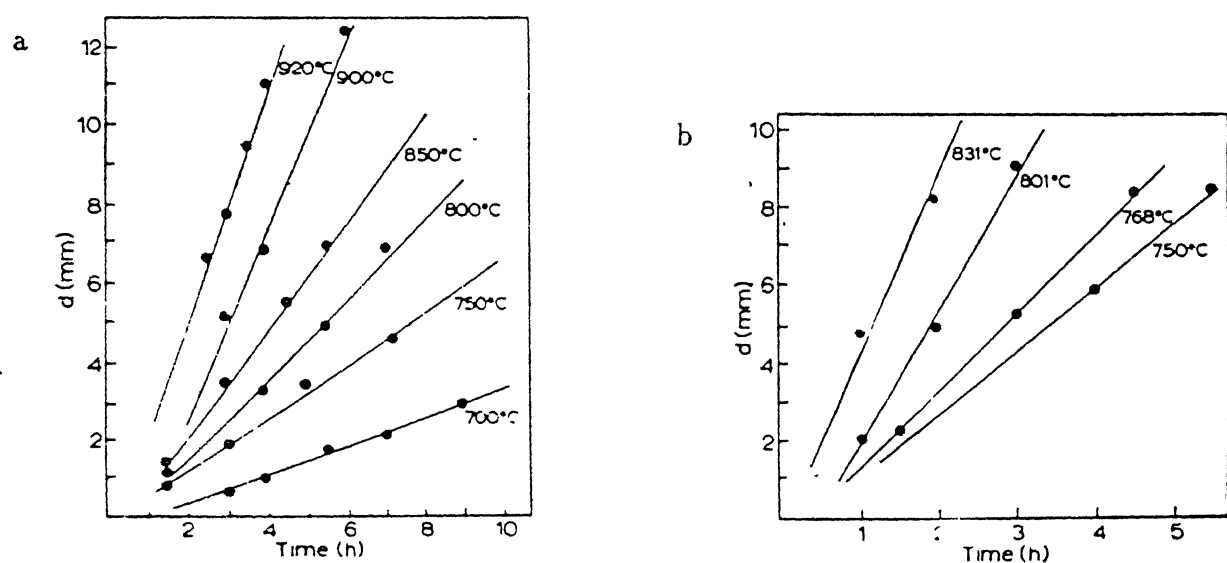


Figure 2.16 Variation of interaction layer thickness with time;
(a) 99.75 wt.% Ti and (b) 99.00 wt.% Ti.

Table 2.7 : Constants of growth rate of TiAl_3 + Al layer (K_C) and formation of TiAl_3 phase (K) [128]

T, $^{\circ}\text{C}$	$K_C \cdot 10^7 \cdot \text{m}/\text{sec}$	Mean $K_C \cdot 10^7, \text{m/sec}$	Time 5. $10^{-3}, \text{sec}$	Decrease in Ti specimen length $\Delta l, 10^4, \text{m}$	$K \cdot 10^3 \text{ moles}/\text{m}^2, \text{sec}$
700	0.62	0.5 ± 0.2	2.88	0.6	2.03 ± 0.10
	0.30		7.62	1.7	
800	2.13	2.3 ± 0.2	1.08	1.2	10.8 ± 1.2
	2.58		1.20	1.6	
	2.25		1.38	1.5	
	2.10		1.62	1.7	
900	4.67	6.7 ± 1.7	0.45	1.3	29 ± 9
	7.68		0.69	2.85	
	7.62		1.26	2.8	

Takemoto and Okamoto [126] during brazing of Ti/Ti joints by (i) pure Al and (ii) Al-0.8 at.% Si alloy. It was reported that the $TiAl_3$ compound grows linearly with time in the temperature range of 670^0C - 700^0C following the relation

$$d = kt + a \quad \dots 2.10$$

where

d = thickness of the intermetallic compound layer (μm)

k = growth rate constant ($\mu m/min$)

t = holding time at the brazing temperature (min)

and a = constant (μm)

The Arrhenius plots of k against $\frac{1}{T}$ obtained are shown in Figure-2.17(a). Activation energies calculated from the slopes of these plots were found to be equal to 166 kJ/mole (39.7 kCal/mole) in the case of pure Al and 359 kJ/mole (85.9 kCal/mole) for Al-0.8 Si. Comparing this value of 179 ± 5.9 kJ/mole for $TiAl_3$ formation by solid state diffusion of Ti/Al couples, it was suggested that diffusion might be the rate-controlling process for $TiAl_3$ formation. However, the reason for increased activation energy for $TiAl_3$ formation while using Al-0.8 Si filler metals has not been explained.

Growth kinetics of $TiAl_3$ on hot dip aluminide coatings on Ti has been studied by Abdel-Hamid. In this study, the the coating layer formed as a result of hot dipping consisted of $TiAl_3$ particles in a mixture of $TiAl_3$ and Al. The coating layer thicknesses were measured in order to assess the growth kinetics of the layer at 700^0C , 750^0C and 800^0C . The results obtained show

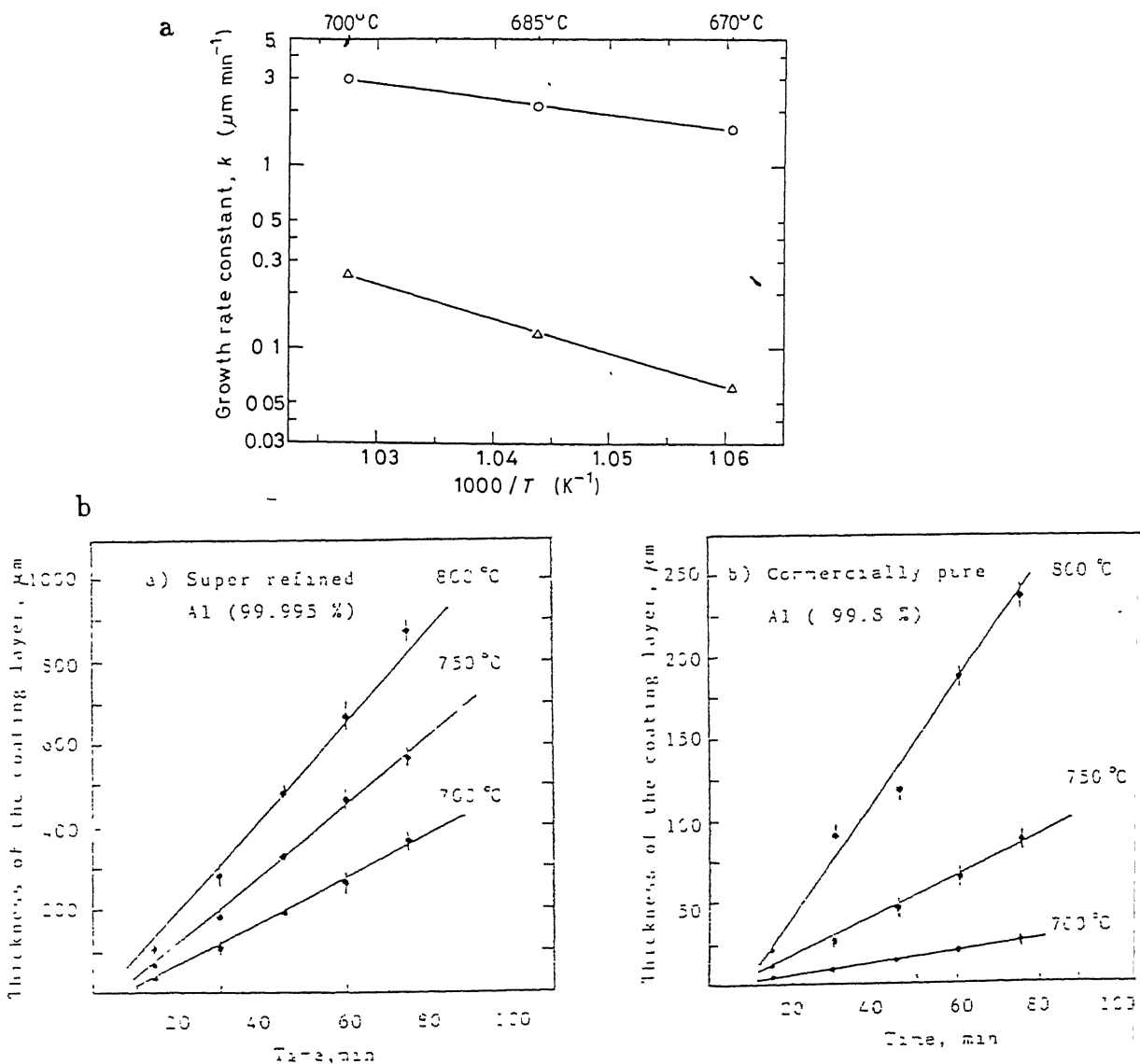


Figure 2.17 (a) Arrhenius plots of growth rate constant (k) as a function of $1/T$ obtained on the thickness of TiAl_3 [126], and (b) coating layer thickness obtained at different dipping times.

that the coating layer thickness varied with dipping time as shown in Figure-2.17(b) with a constant growth rate. The growth rate was found to increase with increase in temperature of the molten Al bath (hot dipping temperature). An activation energy of 82.34 kJ/mole (19.7 kCal/mole) was obtained from this data. Since the activation energy data obtained matched closely with that of diffusion of Ti in liquid Al (81.22 kJ/mole) as well as that for solution of Ti in molten Al (104.9 kJ/mole) through a viscous boundary layer, it was proposed that the coating layer thickness is controlled by diffusion of Ti in Al. However, it is worth mentioning here that their value of activation energy obtained for growth kinetics (82.34 kJ/mole) is quite close to that obtained by Mackowiak and Shreir [121] (92±8 kJ/mole) where chemical reaction was proposed to be the mechanism of $TiAl_3$ formation.

2.7.4. Effect of alloying elements on the growth kinetics of $TiAl_3$:

The effect of various alloying elements on the growth kinetics of $TiAl_3$ compounds formed has been studied by several workers [121,126,127]. Mackowiak and Shreir [121] studied the effect of the alloying elements in Ti on the aluminide formation. Ti alloys corresponding to the compositions Ti-2Mo-2Fe-2Cr and Ti-2.68Cr-1.32Fe-0.02Mo-0.20 (in wt.%) were used to obtain the interaction layers containing the $TiAl_3$ phase. Presence of these elements in Ti were found to influence the growth of the interaction layer. However, these did not affect the mechanism of aluminide formation. The effect of alloying elements in Ti/Ti alloys on the activation energy values was explained in terms of

- (a) selective dissolution of the alloying elements in Al and/or
- (b) increased rate of nucleation of $TiAl_3$ in the presence of certain alloying elements.

Effect of the alloying elements Ti, Ta, Zr, Mo, V, Fe, Mg, Cu, Zn and Sn (present in the Al bath) on the growth kinetics of the $TiAl_3$ formation has been studied by Abdel-Hamid [127] during their studies on hot dip aluminide coatings. It was observed in their studies that the coating layer thickness increased due to the presence of Ti, Ta and Mg with noticeable effect in the case of Ti and Ta. However, the alloying elements Zn, Sn, Cu and Si decreased the thickness of the coating layer with a prominent effect of reduction in the case of Al bath containing Si. On the otherhand, the elements Zr, V and Mo when present in the Al bath, are found to increase the coating thickness even when present in amounts as low as 0.3 wt.% (in Al). Among these three elements, Mo was found to be more effective in increasing the coating layer thickness as compared to Zr and V as shown in Table-2.8 when Ti was held in the Al bath at 800^0C for a period of 600min. Also, it was observed that increase in the amount of Mo increases the coating layer thickness further.

Table 2.8 : Effect of some alloying elements on the thickness of the coating layer formed on Ti dipped in an Al bath of super or commercial purity held at 800°C [127]

Alloying element	Super refined Al			Commercially pure Al	
	Element wt. %	Layer thickness μm		Element wt. %	Layer thickness μm
		30 min	60 min		60 min
-	0.0	280 \pm 20	680 \pm 30	-	190 \pm 10
Ti	2.0	400 \pm 50	-	2.0	375 \pm 25
Ta	1.2	385 \pm 15	-	0.8	235 \pm 15
Fe	2.1	300 \pm 35	-	-	-
Fe	2.7	-	750 \pm 50	2.7	280 \pm 30
Mg	2.0	325 \pm 50	900 \pm 80	2.0	225 \pm 25
Zn	3.1	240 \pm 10	625 \pm 25	3.0	165 \pm 15
Sn	2.5	200 \pm 30	380 \pm 40	-	-
Sn	1.5	-	400 \pm 50	1.5	125 \pm 25
Cu	1.2	200 \pm 35	-	1.1	200 \pm 50
Si	1.5	10 \pm 5	-	-	-
Si	1.2	-	65 \pm 15	1.2	90 \pm 15
Zr	-	-	-	0.3	250 \pm 30
V	-	-	-	0.3	225 \pm 25
Mo	-	-	-	0.3	300 \pm 50
Mo	-	-	-	0.5	350 \pm 50

Chapter 3

Aims of the Present Study

It has already been discussed in Chapter - 2 that $TiAl_3$ and $TiAl_3$ base aluminides can be formed using the technique of reaction synthesis involving reaction of solid titanium and liquid aluminium (Section - 2.7). However, the studies made so far have been confined to the temperature range of $700^{\circ}C$ - $900^{\circ}C$ [119-121]. In principle, it is possible to carry out reaction synthesis of $TiAl_3$ above $900^{\circ}C$. No systematic microstructural characterization of the reaction product has been undertaken till now. The present work was undertaken to study the formation of $TiAl_3$ and $TiAl_3$ base aluminides by the reaction synthesis between solid titanium and liquid aluminium in the temperature range of 973 K-1373 K ($700^{\circ}C$ - $1100^{\circ}C$). Early experiments of the present work showed that the aluminide formed by reaction synthesis was in the form of a powder aggregate in which individual aluminide particles were well sintered with each other. However, microstructural features have been found to vary with the reaction conditions. In view of these observation, the present study was undertaken with the following aims:

- (i) to study the mechanism of $TiAl_3$ formation by reaction synthesis in pure Ti/Al, Ti-Al-V alloy/Al and Ti-Al-Mo-Zr-Si alloy/Al couples in the range of 973 K - 1373 K ($700^{\circ}C$ - $1100^{\circ}C$),

- (ii) to find out the effect of reaction conditions such as temperature and time of reaction and alloying elements on the formation of various phases including $TiAl_3$,
- (iii) to understand the microstructural evolution in the reaction products and its consequence to the particle size and morphology of aluminide(s) formed, and
- (iv) to study the effect of reaction temperature as well as alloying elements on the kinetics of aluminide formation.

Chapter 4

Experimental Procedures

It has already been stated that the reaction synthesis between solid Ti/Ti alloy and liquid aluminium was studied by using reaction couples. Details of starting materials, method of preparation of reaction couples, reaction conditions followed for various reaction synthesis experiments and different experimental procedures used for characterizing the reaction product are described in this chapter.

4.1. PREPARATION OF PURE Ti/Al AND Ti ALLOY/Al REACTION COUPLES:

Reaction synthesis between solid titanium/titanium alloy and liquid aluminium was studied by reacting couples made from pure Ti/Al, Ti-Al-V alloy/Al and Ti-Al-Mo-Zr-Si alloy/Al. A schematic diagram of reaction couples used in the present study is shown in Figure-4.1. Pure titanium, Ti-Al-V and Ti-Al-Mo-Zr-Si alloys used in this study were obtained from Midhani, Ltd., India and they were in the form of round hot rolled bars of 20.00mm diameter. Chemical compositions of these alloys are shown in Table-4.1. Aluminium of >99.9% purity was used for the preparation of reaction couples. Aluminium was in the form of ingots and was obtained from Semi Metals Incorporation, Saxonburg, U.S.A.

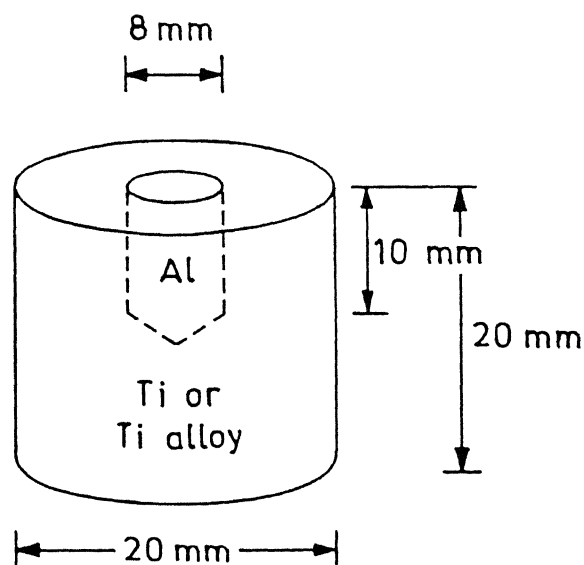


Figure 4.1

Schematic diagram of reaction couples used in the present study.

Table- 4.1 Chemical Compositions of Titanium Alloys Used for Preparing Reaction Couples

Alloy	Composition (wt%)									
	Al	V	Mo	Zr	Si	Fe	O	H	N	Ti
Pure Ti	-	-	-	<.2	-	.2	.15	.01	.05	bal
Ti-Al-V	6.1	4.2	-	-	-	.25	.15	.01	.05	bal
Ti-Al-Mo-Zr-Si	6.5	-	3.5	1.6	.25	.25	.15	.01	.05	bal

In order to prepare pure Ti/Al and Ti alloy/Al reaction couples, pure titanium/titanium alloy bars were cut into 20.0mm long cylindrical specimens and a blind hole of 8.0mm diameter and 10.0mm depth was drilled in each of them along their axes. 10.0mm long machined cylindrical pieces of 8.0mm diameter Al were then inserted into these blind holes.

Wetting of solid Ti by liquid Al is an important factor for the initiation of reaction between them. While no data regarding the surface energy between liquid Al and solid Ti γ_{Al-Ti} is readily available, the transient liquid phase sintering of Ti-Al system has been reported [130-131] indicating that sufficient wetting of solid titanium with liquid Al indeed occurs. However, proper wetting between the two is ensured only when a clean reaction interface between titanium and liquid aluminium is maintained. The importance of clean reaction interface was realized during early experiments of the present work. For instance, while performing initial synthesis experiments, it was noticed that even small traces of lubricant material, left on the surfaces of Ti and/or Al during their machining, were sufficient enough to cause non-wetting and inhibit the reaction between them. Thus in order to maintain a clean reaction interface so that proper wetting of Ti by liquid Al could be ensured, the titanium and aluminium samples were thoroughly cleaned first with acetone and then with dilute HF-HNO₃ solution prior to insertion of aluminium pieces in blind holes. Thus any carbonaceous material or oxide layer, if present, on surfaces could be effectively eliminated.

The two Ti alloys used in the present study were of $(\alpha+\beta)$ type and had the nominal composition corresponding to Ti-6Al-4V and T-6.8Al-3.2Mo-1.8Zr-0.3Si (in wt %). They were found to contain about 10-15% of β phase at room temperature. Microstructures of as-received Ti and Ti alloys are shown in Figure-4.2. It can be clearly seen from the figure, that while pure Ti had the single phase polycrystalline structure corresponding to the α phase, the two Ti alloys had two-phase $(\alpha+\beta)$ structure containing 10-15% β . Grain size of pure Ti used for the present study was found to be equal to $\sim 24\mu\text{m}$. It may also be noted that in Ti-6Al-4V alloy, the β phase was present along the α grain boundaries whereas in the case of Ti-6.8Al-3.2Mo-1.8Zr-0.3Si alloy, the β phase was present as thin lamellae in the α - β mixture.

4.2. EXPERIMENTAL SET-UP AND CONDITIONS OF REACTION SYNTHESIS:

The Ti/Al and Ti alloy/Al couples were reacted in a specially designed furnace under an inert atmosphere of high purity flowing argon. The schematic diagram of the set-up used for reaction synthesis experiments has been shown in Figure-4.3.

The reaction chamber consisted of an alumina tube of ID = 46 mm and OD = 52 mm which was closed at one end. The other end of the tube was fitted with a flange through which the provisions for sample insertion and gas inlet were made. This alumina tube was placed inside another Kanthal wound alumina tube of ID = 58 mm. The temperature calibration of the reaction chamber showed that it had a constant temperature zone of approximately 10

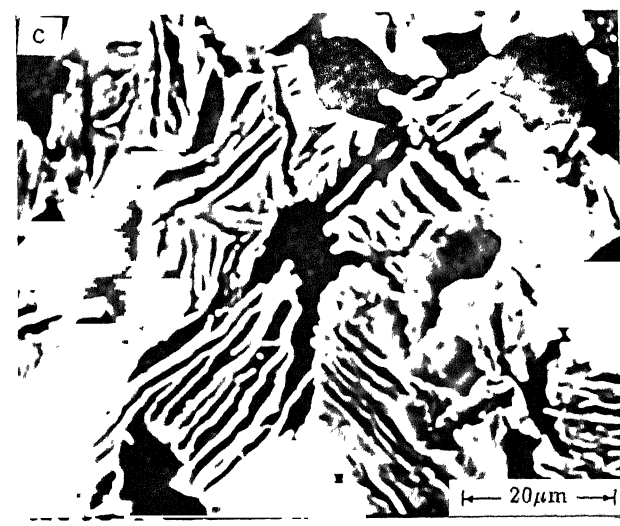
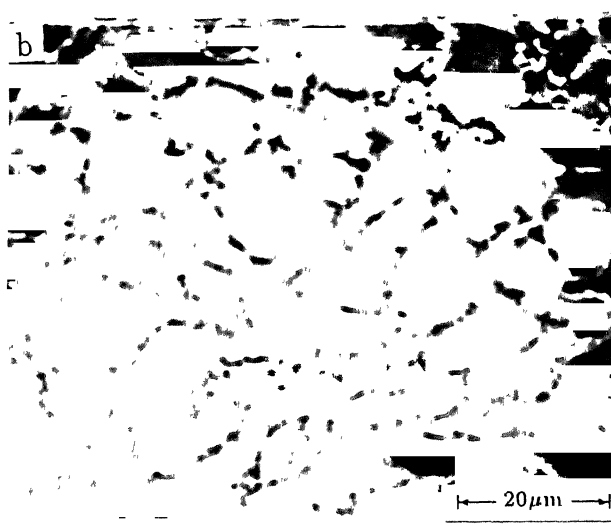
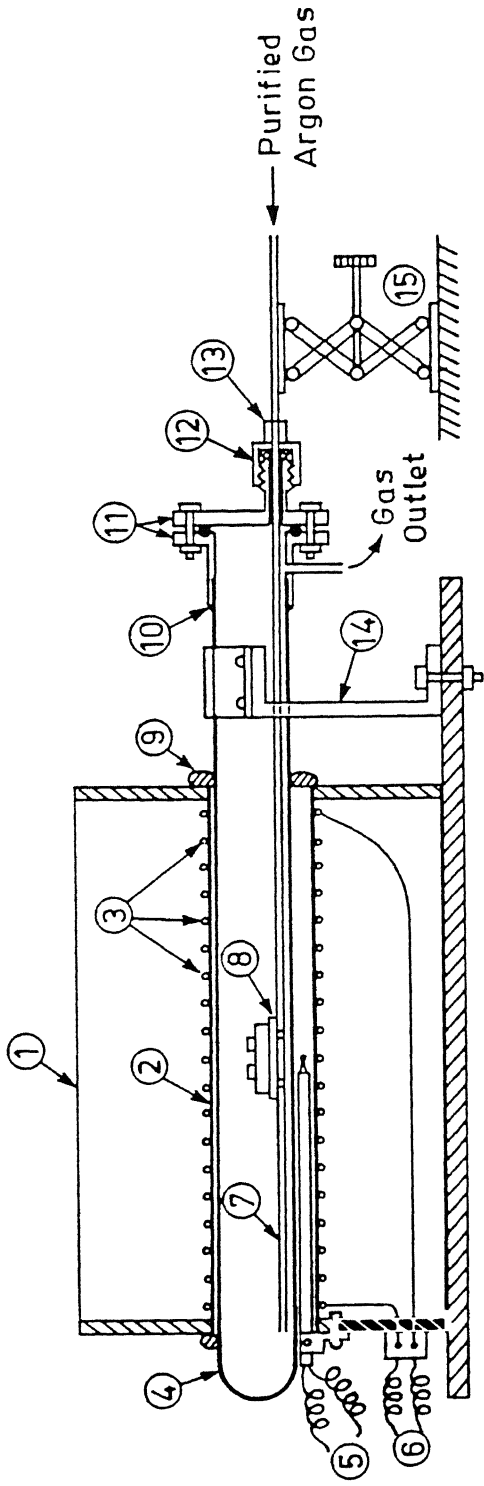


Figure 4.2 Microstructures of the as-received Ti and Ti alloys.
(a) Pure Ti, (b) Ti-6Al-4V and (c) Ti-6.5Al-3.2Mo-1.8Zr-0.3



1. Furnace Body
2. Alumina Tube
3. Kanthal Wire
4. One End Closed Alumina Tube
5. Thermocouple
6. Power Connection
7. S.S. Tube
8. S.S. Trolley & Ceramic
- Sample Holder
9. Asbestos Rope
10. Silicone Rubber Seal
11. S.S. Coupling and
- S.S. Flange
12. O-Ring Seal
13. Sample Alignment / Adjustment Jig
14. Support
- & Clamp
15. Jack

Figure 4.3 Schematic diagram of the set-up used for reaction synthesis experiments.

cm. The gas inlet tube was guided to pass through an O-ring arrangement. For reaction synthesis experiments, reaction couples were introduced into the reaction chamber through a stainless steel trolley fitted with a refractory sample holder as shown in Figure-4.4. Before inserting the couples, reaction chamber was flushed with argon. In order to remove any traces of oxygen and water vapour present, the gas was passed through a purification unit. The gas purification unit consisted of glass tubes containing heated copper turnings and calcium chloride. Passage of argon gas through heated copper turnings removed oxygen traces while that through the calcium chloride absorbed moisture, if present.

Isothermal reaction synthesis experiments were carried out on Ti/Al couples at temperatures ranging from 973K (700°C) to 1373K (1100°C) for times varying between 900s (0.25hr) to 14400s (4hr). Reaction synthesis experiments on Ti alloy/Al couples were carried out in the temperature range of 973K (700°C) to 1173K (900°C) for 3600s (1hr) and 7200s (2hr).

Details of the reaction procedure adopted for various reaction synthesis experiments are as given below;

- (1) Reaction couples were inserted into the cold zone of the reaction chamber after which the flange arrangement was closed.
- (2) Prior to heating the furnace to the set reaction temperature, the reaction chamber was thoroughly flushed

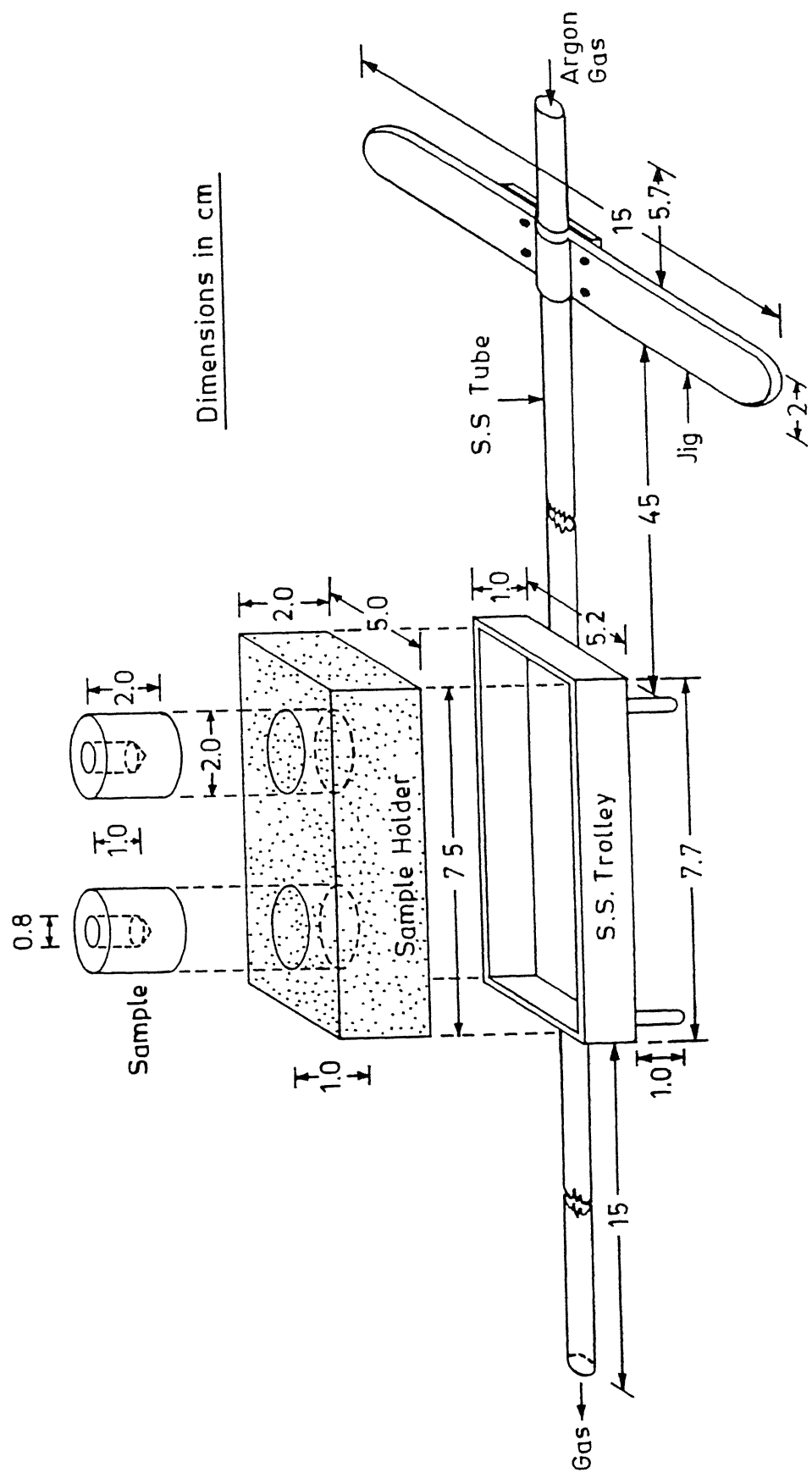


Figure 4.4 Stainless steel trolley and sample holder assembly used for reaction synthesis experiments.

with purified argon for about 900s (0.25hr).

- (3) The temperature of the reaction chamber was raised slowly till it reached the set reaction temperature. During this period the reaction couples were maintained in the cold zone of the reaction chamber under the flowing argon atmosphere.
- (4) Once the reaction chamber attained the set reaction temperature within its constant temperature zone, reaction couples were pushed into the reaction zone by pushing in the stainless steel trolley.
- (5) Reactions were carried out at the set reaction temperature for specific times.
- (6) After the synthesis reaction, reaction couples were pulled out into the cold zone where they were cooled under argon atmosphere to room temperature.

4.3. CHARACTERIZATION OF THE REACTION PRODUCT:

For the characterization of the reaction product, couples, after performing the reaction for the set reaction conditions, were longitudinally cut into two halves using a spark erosion unit (Model MK-2, Materials Science Ltd., North West, USA) for the characterization of the reaction product. Longitudinal cut-sections of reaction couples were coarse polished on 1/0, 2/0, 3/0 and 4/0 emery papers respectively. These coarse-polished samples were subsequently polished on a polishing wheel lapped with coarse alumina ($\sim 1\mu\text{m}$) suspension. Final polishing of samples was carried out on polishing wheel using first a fine alumina

suspension of $0.3\mu\text{m}$ and then that of $0.05\mu\text{m}$.

As shown in Figure-4.5(a), longitudinal sections of partially reacted couples were found to contain unreacted titanium/titanium alloy and unreacted aluminium which were separated by a thin layer of the reaction zone (RZ). A schematic view of a typical reaction zone showing general features of its structure is shown in Figure-4.5(b). For the purpose of the present study the following terminology for specific microstructural features of the reaction zone was adopted:

- (a) The continuous thin layer of aluminide adjacent to the unreacted titanium was termed as the *reaction layer* (RL)
- (b) The interface between the unreacted titanium and the reaction layer was termed as the *reaction interface* (RI)
- (c) The domain ahead of the reaction layer in which aluminide particles remain dispersed in the matrix of aluminium was termed as the *dispersed reaction domain* (DRD),
- (d) The total amount of reaction product in the reaction zone, continuous thin aluminide layer as well as particulate aluminide dispersed in the dispersed reaction domain, was termed as the *reaction product* (RP).

Polished surfaces of the longitudinal sections were subjected to a number of characterization techniques as described in the following.

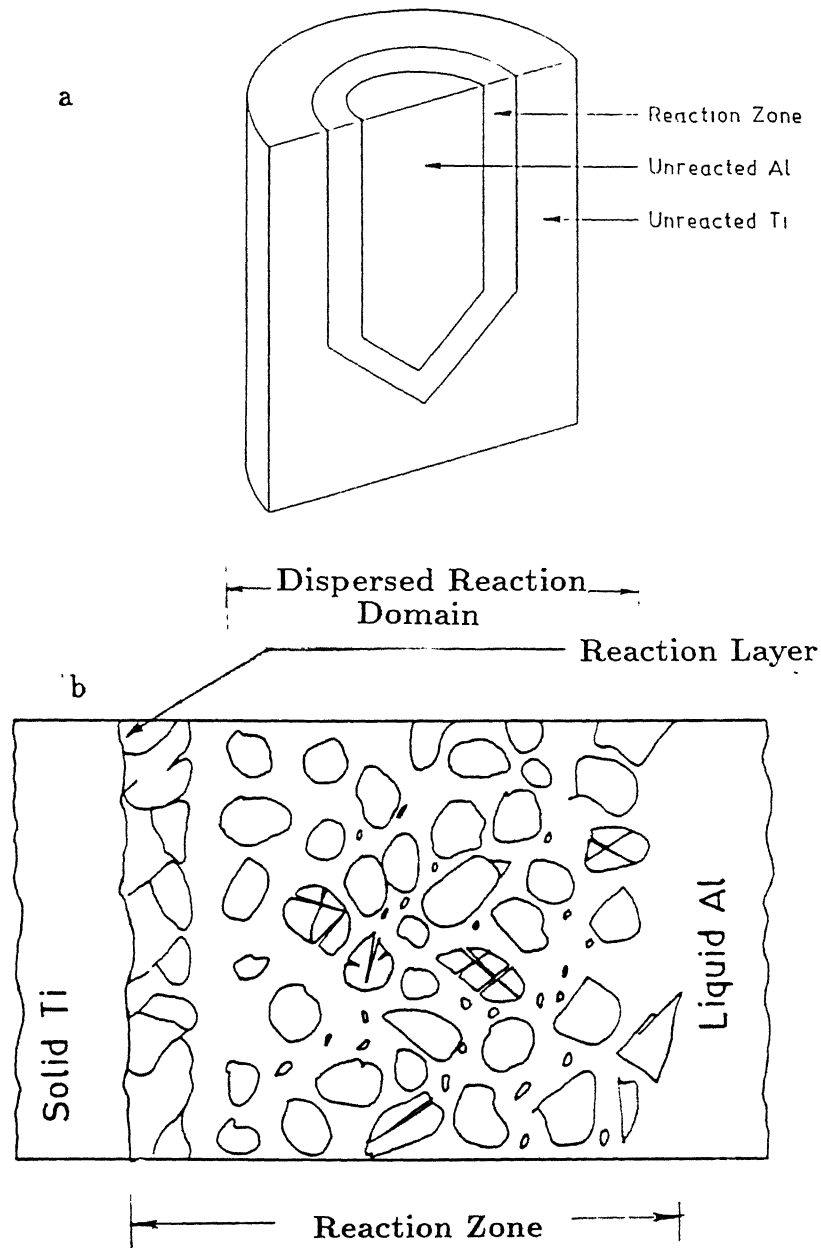


Figure 4.5 (a) Longitudinally sectioned partially reacted couple showing the unreacted Ti/Ti alloy, unreacted Al and the reaction zone and (b) Schematic view of a typical reaction zone.

4.3.1. X-ray Diffraction Analysis:

In order to identify the phases present in the reaction product, X-ray diffraction (XRD) studies were carried out on Seifert, ISODEBYEFLEX 2002 diffractometer using copper K_{α} radiation. The unit was operated at 30kV and 10mA and the scanning speed was kept at $1.2^{\circ}/\text{min}$ in 2θ . The intensity was recorded at 10 counts per minute. The X-ray diffraction patterns obtained were indexed and identification of phases was done by matching 'd' values corresponding to each of the peak positions of the diffraction pattern with 'd' values of all possible phases from the standard data given in Joint Committee for Powder Diffraction (JCPD) files. As described in Chapter-5, TiAl_3 and $\text{Ti}_9\text{Al}_{23}$ were the only two aluminides formed by reaction synthesis in the temperature range of 973K-1373K. Both these aluminides possess the ordered tetragonal crystal structures (Section-2.1). After indexing the XRD peaks of the reaction product(s), the lattice parameters of the compounds formed were calculated.

The lattice parameters 'a' and 'c' for the two tetragonal phases TiAl_3 and $\text{Ti}_9\text{Al}_{23}$ can be calculated using the equation

$$\frac{1}{d^2} = \frac{h^2+k^2}{a^2} + \frac{l^2}{c^2} \quad \dots 4.1$$

where d is the interlamellar spacing for the plane (hkl) . Since the above equation contains two unknowns, the 'a' and 'c' lattice parameters were calculated using Eq-4.1 and

$$\frac{c^2}{a^2} = \frac{l_2^2 - (d_1/d_2)^2 l_1^2}{(d_1/d_2)^2 (h_1^2 + k_1^2) - (h_2^2 + k_2^2)} \dots 4.2$$

by considering two consecutive diffraction peaks $(h_1 k_1 l_1)$ and $(h_2 k_2 l_2)$.

4.3.2. Microstructural Examination:

In order to examine the morphology and its evolution in the reaction products, their microrstructural features were observed. Microstructural studies were carried out under (i) Optical Microscope (OM), (ii) Scanning Electron Microscope (SEM) equipped with an energy dispersive spectrometer, (iii) Electron Probe Micro Analyzer (EPMA) and (iv) Transmission Electron Microscope (TEM).

4.3.2.1. Optical Microscopy:

Samples polished by the procedure described in section-4.3 were etched with 2% HF + 5% HNO_3 solution in water. An etching time of 5-10 seconds provided optimum results. Etched samples were then examined under Leitz Metallux 3 optical microscope at suitable magnifications.

4.3.2.2. Scanning Electron Microscopy:

In order to examine further details of their microstructural features, several polished and etched samples were also examined under a JEOL-JSM 840A scanning electron microscope (SEM). Microstructural observations were made in both secondary

electron (SE) as well as backscattered electron (BE) modes. Samples were generally observed under an accelerating voltage of 15 kV. Occasionally, unpolished samples were also observed under SEM. In addition to the microstructural observation, compositional analysis and X-ray dot mapping were performed in various phases using the energy dispersive spectrometer (EDS) at 24 kV, 6×10^{-10} mA. These parameters were obtained by standardization using a Ti-Al sample of known chemical composition (Ti-75 at % Al). These operating parameters were counter-checked with a sample of Ti-25 at % Al.

4.3.2.3. Electron Probe Microanalysis (EPMA):

A few sections of the reaction synthesized couples were examined under a JEOL JSM Super Probe 840A EPMA under an operating voltage of 20 kV. Chemical composition at few locations of some of the reaction couples was obtained using the wavelength dispersive spectrometer (WDS).

4.3.2.4. Transmission Electron Microscopy (TEM):

In order to characterize the phases present in the reaction product, thin foils of the reaction zones obtained from couples reacted under different conditions were observed under a JEOL 2000-FXII Transmission Electron Microscope (TEM). Foils for observation under TEM were prepared as described below.

0.3mm-0.5mm thick slices were cut from the reaction zones using either a diamond wafer cutter or a spark erosion unit.

These slices were mechanically thinned down to about 60-70 μm thickness by polishing on SiC emery papers. 3.0 mm diameter discs were punched out from these slices by spark erosion. The discs thus obtained were further thinned down to obtain transparent areas using two different methods. The details of the parameters used in these two methods are given in the following.

Twin Jet Polishing:

3.0mm discs were subjected to twin jet polishing at a temperature of 243 K (-30°C) at 12 mA and V. A solution of nitric acid and methanol in the ratio of 1 : 3 was used as the electrolyte. The temperature of the system was maintained at -30°C by holding the bath inside a flask containing a mixture of liquid nitrogen and methanol.

Ion Beam Milling:

Due to the differential polishing response of the two phases present in the reaction zone (aluminide particles and aluminium matrix), twin jet polishing technique could not be employed successfully in producing sufficient transparent area containing both the phases. In view of this problem, few discs of the reaction zones were thinned by ion beam milling. Argon gas was used as the ion source. Milling was performed for 20 hrs each at a bombarding angle of 15° and 10° respectively. Final milling was done at an angle of 7° till performance was obtained.

The phase identification was also done using selected area diffraction patterns (SADP). SAD patterns obtained from various regions of the reaction zone were indexed according to the

procedure given below:

Distances R_1 and R_2 between the central spot and the two diffraction spots corresponding to the planes $(h_1 k_1 l_1)$ and $(h_2 k_2 l_2)$ were measured. The interplanar spacing 'd' corresponding to $(h_1 k_1 l_1)$ and $(h_2 k_2 l_2)$ was obtained using the equation

$$\lambda L = Rd \quad \dots 4.3$$

where

λL is the camera constant

R is the distance between the central spot and the respective dffraction spot.

The 'd' values thus obtained were matched with the 'd' values of the expected phases from the powder diffraction files and the phase corresponding to these values was identified.

In order to confirm the phase identification, the angles between the planes $(h_1 k_1 l_1)$ and $(h_2 k_2 l_2)$ were measured from the diffraction patterns and compared with the angles between the respective planes of the phase.

4.4. QUANTITATIVE METALLOGRAPHY:

As discussed in Section-4.3, and discussed in detail in section-5.1.3, the reaction zone in all reacted couples was found to contain a thin aluminide layer and a two phase mixture consisting of titanium aluminide particles dispersed in a matrix of Al. The schematic diagram showing the general features of the

structure in the reaction zone of partially reacted couples is shown in Figure-4.5(b) and terminologies for specific microstructural features such as reaction interface (RI), reaction layer (RL), dispersed reaction domain (DRD) and reaction product (RP) have already been defined in Section-4.3. Quantitative metallographic studies were undertaken to measure and analyze

- (i) the thickness of the reaction zone,
- (ii) average volume fraction of the reaction product and its variation as a function of distance from the Ti/Al reaction interface,
- (iii) size distribution and shape of the aluminide particles.

The methods used for these measurements and analysis are described in the following subsections.

4.4.1. Measurement of Reaction Zone Thickness:

As shown in Figure-4.5(b), the reaction zone (RZ) thickness was found to be microscopically non-uniform. Thickness of the reaction zone in a given sample was measured at atleast five different places under SEM (Figure-4.6) and the mean value obtained from these measurements was taken as the average thickness of the reaction zone, x .

4.4.2. Measurement of Volume Fraction of the Reaction Product as a Function of Distance from the Reaction Interface:

Volume fraction of the reaction product in the dispersed reaction domain (DRD) i.e. aluminide particles in the matrix of Al

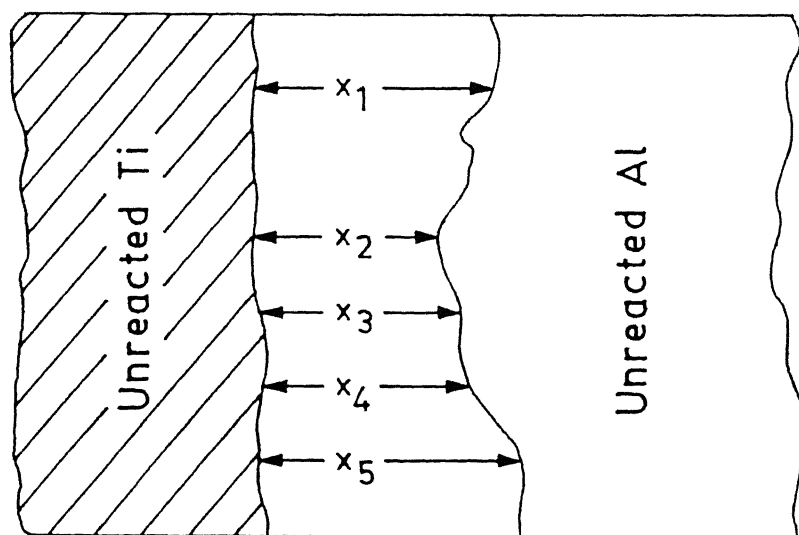


Figure 4.6 Schematic diagram showing the non-uniform nature of reaction zone thickness.

was measured as a function of distance from the reaction interface. Measurements were done using the areal analysis. Volume fraction measurements were done at different distances from the reaction interface (shaded portions in Figure - 4.7). Areal fraction measurements were carried out at 3-6 distances from the reaction interface depending on the reaction zone thickness obtained at a specific reaction condition. At each distance, micrographs were taken from four different locations as shown in the schematic diagram (Figure-4.7).

The volume fraction was calculated as follows:

If A_p is the total area occupied by the aluminide particles and A_T is the total field area in which measurements were done, then the volume fraction of the reaction product $V_V(x_i)$ at a particular distance x_i is calculated using the formula

$$V_V(x_i) = \frac{A_p}{A_T} \quad \dots 4.4$$

4.4.3. Determination of Average Volume Fraction of the Reaction Product in the Reaction Zone:

Volume fraction of the reaction product varied with the distance from the reaction interface. As will be shown in section-5.3.3.5, the volume fraction of the reaction product was found to vary with x . Best fit curve for the variation of volume fraction ($V_V(x_i)$) as a function of distance from the reaction interface (x_i) was obtained by performing a least-square fit. It was observed that in most of the cases, volume fraction varied as

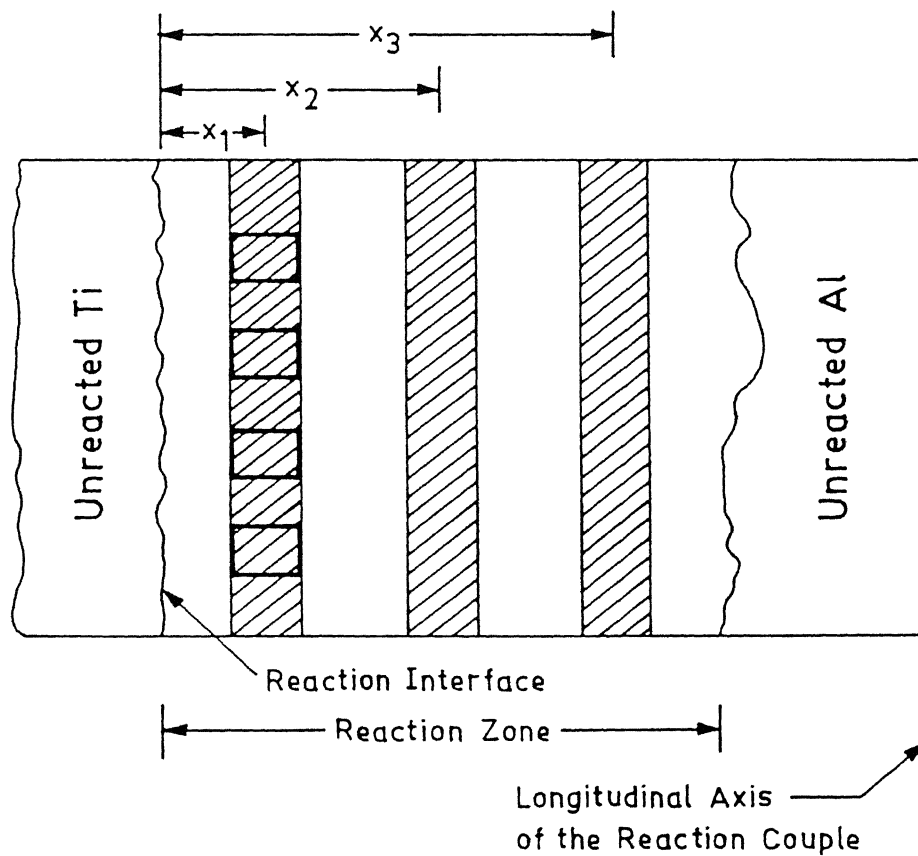


Figure 4.7 Schematic diagram showing the regions at which volume fraction measurements were made.

a 3rd order polynomial function in distance from the reaction interface.

The average volume fraction of the reaction product in the reaction zone was obtained by integrating the area under $v_v(x_i)$ vs. x curve using the Simpson's one third rule as follows:

$$\int_{x_0}^{x_n} v_v dx = \frac{h}{3} \left[v_0 + 4(v_1 + v_3 + \dots + v_{n-1}) + 2(v_2 + v_4 + \dots + v_{n-2}) + v_n \right] \dots 4.5$$

where

h is the interval (distance) between two successive values of v_v (volume fraction).

$v_0, v_1, v_2 \dots$ represent the volume fractions at the distances $x_0, x_1, x_2 \dots$

4.4.4. Estimation of Reaction Product Formed Per Unit Area of the Reaction Interface:

Volume of the aluminide formed in each reaction couple was calculated from the total volume of the reaction zone and the average volume fraction of the reaction product as follows:

The schematic diagram of a partially reacted couple (in which the entire aluminium provided for reaction is not consumed) is shown in Figure-4.8. From the figure,

$$\text{Volume of the cylindrical shell } \} = \pi Hx(D-x) \dots 4.6$$

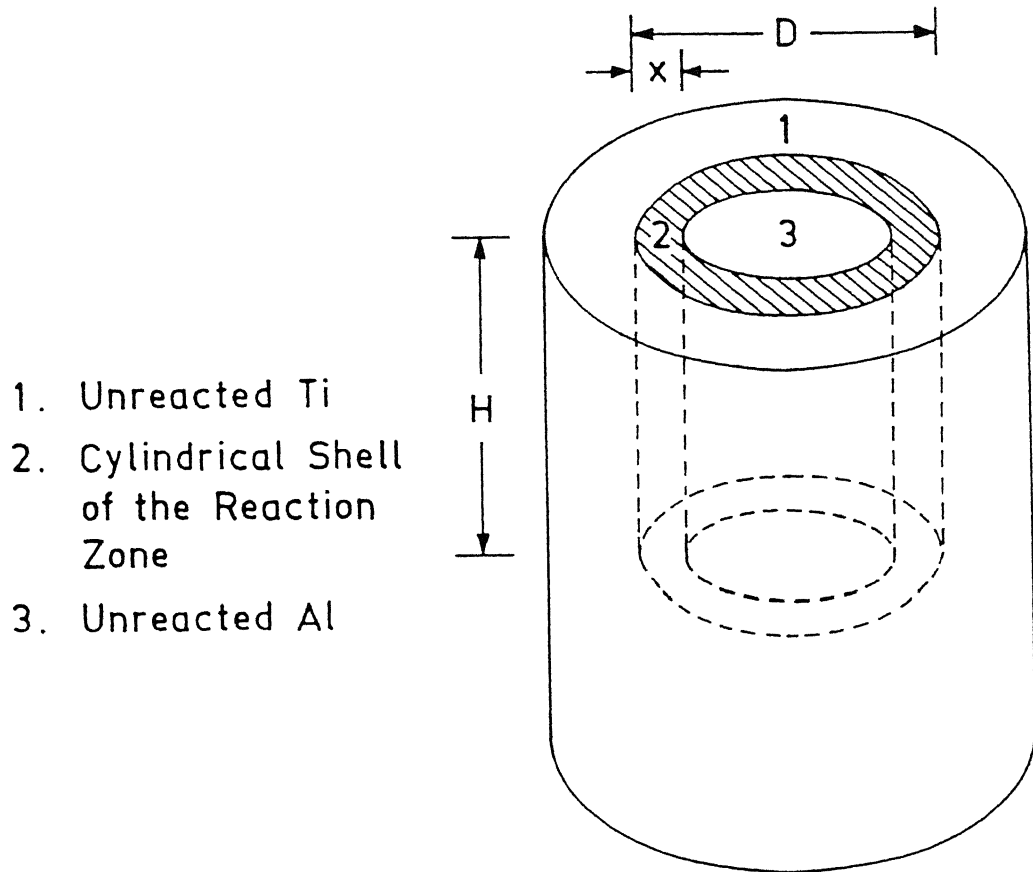


Figure 4.8 Schematic diagram of a partially reacted couple.

where H (10 mm) and D (8 mm) represent the height and diameter of the cylindrical Al pieces used for the reaction couple preparation and 'x' is the thickness of the reaction zone.

Volume of the reaction product in the

Reaction zone, $v_p = \frac{\text{Volume fraction of the reaction product}}{v} \times \text{Volume of the reaction zone}$

$$v_p = v_v \pi H x (D-x)$$

where v_v = Average volume fraction of the reaction product

From the volume of the reaction product, total mass of the reaction product (m_p) is calculated using the following equation:

$$m_p = \frac{v_v \rho_p [\pi H x (D-x)]}{100} \dots 4.7$$

where

ρ_p = Density of the reaction product.

Therefore, mass of the reaction product formed per unit area of the reaction interface $m_{p(i)}$ is calculated using the equation

$$m_{p(i)} = \frac{v_v \rho_p [\pi H x (D-x)]}{100 \pi D H} \dots 4.8$$

where $\pi D H$ represents the area of the reaction interface for the geometry of the reaction couple used in the present study.

4.4.5. Measurement of Aluminide Particle Size and Its Distribution in the Reaction Zone:

Particle size of the reaction product (aluminide) in the reaction zone was measured using the Spektor's method from the distribution of the chord lengths as described below. Since the

aluminide particles had equiaxed shape, their shapes were assumed to be spherical.

A secant is traversed on the micrograph of the specimen and the lengths of the chords intercepted by each individual particle of the reaction product is measured. These chord lengths are then classified into suitable class intervals.

Specktor's method relates the distribution of chord intercept lengths and the distribution of particles in 3-dimensions.

The number of chords per unit length of the secant [$N_L(i)$] was calculated for the i^{th} class by dividing the number of chords in the i^{th} class by the total length of the secant traversed.

From the $N_L(i)$ data, the number of particles per unit volume in the i^{th} class was calculated using the equation [132]

$$N_V(i) = \frac{4}{\pi \Delta^2} \left[\frac{N_L(i)}{2i - 1} - \frac{N_L(i+1)}{2i + 1} \right] \quad \dots 4.9$$

where $N_V(i)$ is the number of particles per unit volume in the i^{th} class,

$N_L(i)$ represents the number of chords per unit length of the secant belonging to the i^{th} class,

$N_V(i+1)$ represents the number of chords per unit length of the secant belonging to the $(i+1)^{th}$ class, and 'Δ' is the width of the class interval.

The assumptions involved in and the derivation of the equation-4.7 are described in Appendix-A.

4.4.6. Analysis of Morphology of the Reaction Product:

Aluminide particles formed in the reaction couples made from titanium alloys and aluminium were found to vary in their shape. Their shapes were, in general, found to be non-equiaxed. Aspect ratio of aluminide particles was used as an index to characterize their shapes.

Aspect ratio is defined as the ratio of the longest dimension of the particle to its perpendicular dimension.

4.4.7. Microhardness Measurements:

Microhardness measurements were made on different phases of the reaction zone, as well as in the unreacted constituents. Measurements were done using a Leitz Miniload Microhardness Tester under a load of 25 g. Atleast 5 indentations were made in each phase and the average value of the microhardness was calculated.

Chapter 5

Results

It has already been said in Chapter-4 that the reaction synthesis of titanium aluminide(s) was studied in the temperature range of 973K-1373 K (700°C to 1100°C) for times varying from 900s (0.25hr) to 14400s (4.00hr). For this purpose reaction couples of pure Ti/Al Ti-Al-V alloy/Al Ti-Al-Mo-Zr-Si alloy/Al were employed. The details of the experimental procedures adopted in carrying out the reaction and subsequent characterization of the reacted couples have already been described. Results obtained from the characterization of reacted couples are presented in the present chapter.

It is worth mentioning here that for the geometry and dimensions of reaction couples used in the present work and various reaction times employed, it was not possible to consume the entire Al in forming the aluminides under all reaction conditions. Thus two kinds of reacted samples were obtained after the reaction synthesis:

- (i) couples which contained some unreacted elemental Al and/or elemental Al in the reaction zone or
- (ii) couples that contained no elemental Al after reaction.

In order to distinguish between the above, these samples are termed as "partially reacted couples" and "fully reacted couples" respectively. Unless stated otherwise, the term "reacted

couple" employed in the present work implies a partially reacted couple. Time intervals for different reaction temperatures for which fully reacted couples were obtained are shown in Table-5.1.

(i) Thus at higher reaction temperatures of 1073K (800°C) and 1173K (900°C), reaction time intervals greater than 14400s (4hr) at 1073 K and 7200s (2hr) respectively resulted in fully reacted couples. However, since the objective of the present work was to study the microstructural evolution during the formation of titanium aluminide(s) by reaction synthesis, studies on couples reacted for time intervals larger than these were not studied.

(ii) Similarly, time intervals smaller than 3600s (1hr) were not considered because, these reaction conditions resulted in the formation of relatively too thin reaction zones (in the range of $50\mu\text{m}$ - $230\mu\text{m}$). The errors in the measurement of average reaction zone thickness for these cases were found to be relatively high and hence such reacted couples were not considered in the present work.

5.1 FORMATION OF TITANIUM ALUMINIDE(S) AS THE REACTION SYNTHESIS PRODUCT:

5.1.1 General Microstructural Features of the Reaction Couples:

A typical low magnification scanning electron micrograph of the longitudinal section of the partially reacted couple synthesized at 973K (700°C) for 3600s (1 hr) at 50X is shown in

Table-5.1 : The minimum reaction time (t_{\min}) at which complete consumption of Al occurs in Ti/Al couples.

Reaction temperature (K)	Minimum reaction time (t_{\min}) at which complete consumption of Al occurs
973	18000
1073	14400
1173	7200
1273	3600

Table-5.2 : Effect of reaction temperature and time on the thickness of the reaction zone in Ti/Al reaction couples

Reaction temperature (K)	Thickness of reaction zone (mm)					
	Reaction time (ks)					
	0.9	1.8	3.6	7.2	10.8	14.4
973	-	-	0.3	0.8	1.7	2.3
1073	-	-	1.1	1.8	2.2	-
1173	0.6	1.1	1.8	-	-	-

Figure-5.1(a). The micrograph clearly shows three distinct regions, namely, (i) the unreacted Ti, (ii) the reaction zone and (iii) the unreacted Al. As shown schematically in Figure-4.5(b), the reaction zone was found to consists of (i) reaction interface, (ii) reaction layer and (iii) dispersed reaction domain containing aluminide particles in an Al matrix.

When viewed at a higher magnification (1000X), the reaction interface, RI (the interface between the unreacted Ti and the reaction zone) revealed the thin continuous layer of the aluminide as shown in Figure-5.1(b). This thin layer of the aluminide is referred to as the reaction layer, RL. Ahead of the reaction layer, the two phase mixture of aluminide particles dispersed in a matrix of Al can be seen.

Microstructural features similar to those observed in a pure Ti/Al couple (Figure-5.1(a)), were also observed for other reaction conditions as well as in the case of Ti alloy/Al couples.

5.1.2 Variation of Reaction Zone Thickness as a Function of Reaction Conditions:

As depicted in the schematic diagram (Figure-4.5b), and shown in Figure-5.1b, the dispersed reactioin domain of the reaction zone consisted of aluminide particles dispersed randomly in a matrix of Al. Due to this reason, the reaction zone was found to be non-planar and its thickness varied microscopically. As illustrated in Figure-4.6, average thickness of the reaction zone for each reaction couple was obtained from measurements taken directly under the scanning electron microscope at more than 5

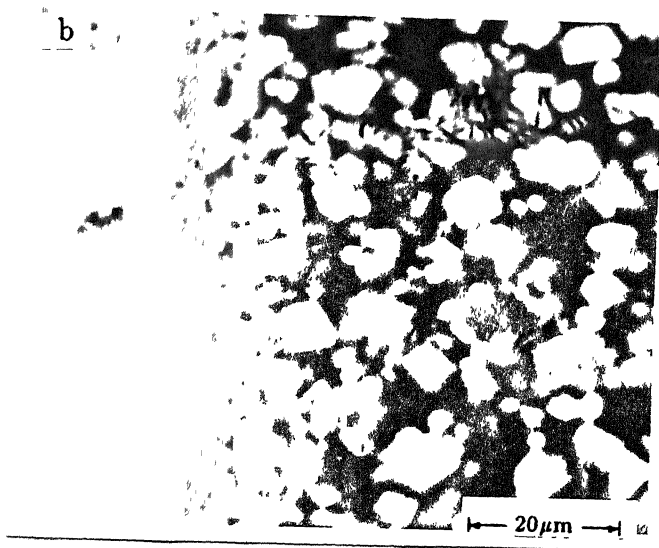
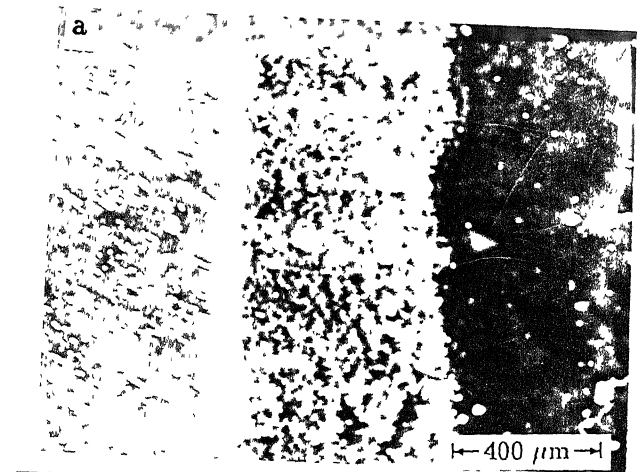


Figure 5.1 SEM micrograph of the longitudinal section of the reaction couple showing the reaction zone and the adjacent unreacted Ti and Al layers;
(a) Low magnification micrograph
(b) High magnification micrograph sample reacted at 973 K (700°C) for 7200 s (2 hr).

different locations and the scatter in the reaction zone thickness was calculated for 95% confidence level.

The average thickness of reaction zones formed in couples partially reacted for different temperatures and time intervals are shown in Table-5.2. The dashes in Table-5.2 indicate the conditions at which reaction synthesis experiments were not performed because of the reasons already discussed.

The variation of average reaction zone thickness with reaction time has been shown in Figure-5.2. The scatter in the reaction zone thickness has been calculated for 95% confidence level and the resultant confidence interval is also indicated in Figure-5.2. It can be seen from the figure that an increase in reaction time lead to an increase in the reaction zone thickness. The plots in Figure-5.2 show that the thickness of the reaction zone varied more or less linearly with reaction time in the temperature range investigated in the present work except in the case of samples reacted at 1073 K (800°C). The deviation observed in linearity of reaction zone thickness with time may be attributed to (i) non-uniformity in the reaction zone thickness and (ii) errors arising from measurements taken at higher magnifications carried out directly under the scanning electron microscope(SEM). The error arising from factor (ii) could have been minimized by carrying out measurements at very large number of locations.

Average thickness of the reaction zones formed in Ti alloy/Al couples reacted at different reaction temperatures for

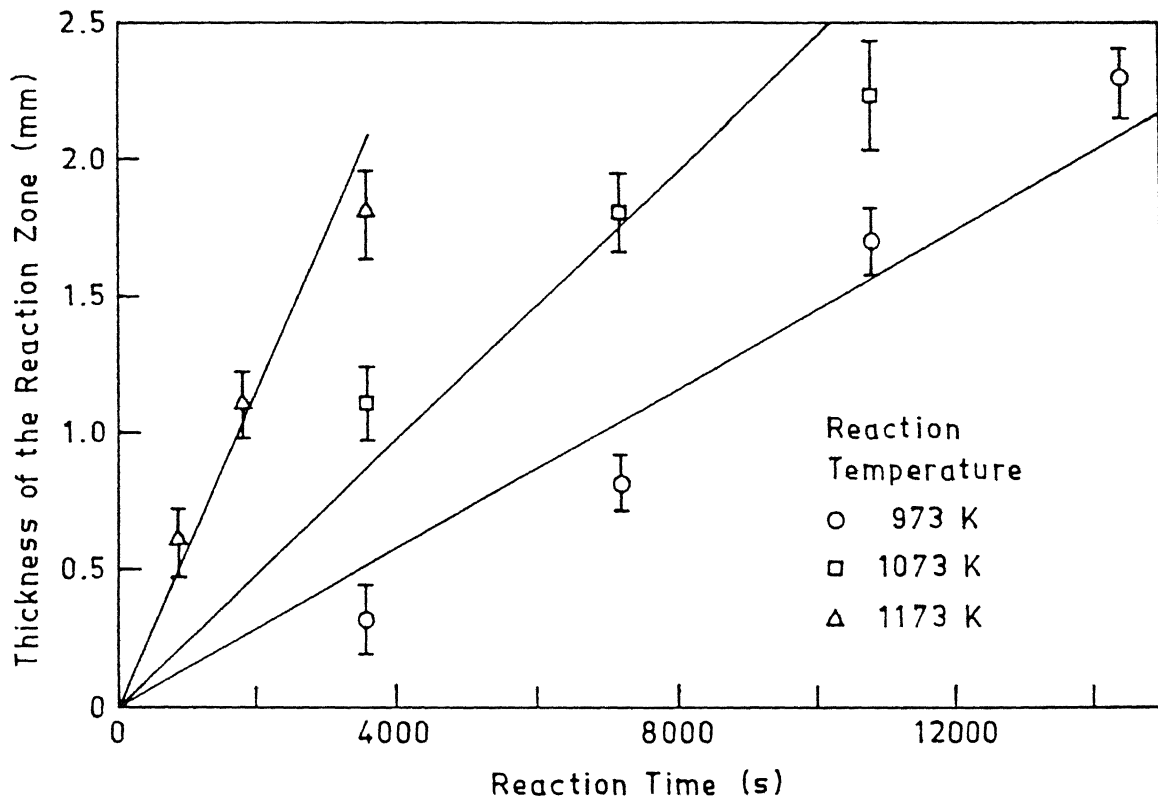


Figure 5.2 Variation of average thickness of the reaction zone with reaction time for different reaction temperatures in pure Ti/Al couples .

3600s (1hr) and 7200s (2hr) are listed in Table-5.3. These data are plotted in Figure-5.3 and for the sake of comparison the data obtained from pure Ti/Al couples reacted under similar conditions have also been included in the figure. The scatter in reaction zone thickness for 90% confidence level has also been indicated in the figure.

At reaction temperatures of $\leq 1073\text{K}$ (800°C) and for reaction times of 3600s (1hr), the reaction zone thicknesses for Ti alloy/ Al couples and pure Ti/Al couples were found to be almost the same. However, when the reaction was carried out at 1173K (900°C) for 3600s (1 hr), the reaction zone thickness in the case of Ti-Al-V alloy/Al couples (1.5 mm) was more or less same as that of Ti/Al couple (1.8 mm). However, the reaction zone thickness of Ti-Al-Mo-Zr-Si/Al couples under similar reaction conditions was found to be almost double (3.2 mm) when compared to that of pure Ti/Al couples.

Almost a 5-fold increase in reaction zone thickness could be observed in Ti-Al-Mo-Zr-Si/Al couple when the reaction temperature was increased from 973K (700°C) to 1173K (900°C), though the increase was only about 3-fold in Ti-Al-V/Al and pure Ti/Al couples. As shown in Figure-5.3(b), when the reaction times were increased from 3600s (1hr) to 7200s (2hr) at any given reaction temperature, significantly higher reaction zone thicknesses were obtained in Tialloy/Al couples as compared to pure Ti/Al couples. It can also be seen from the Figure-5.3(a) and (b) that doubling the reaction time from 3600s (1hr) to 7200s

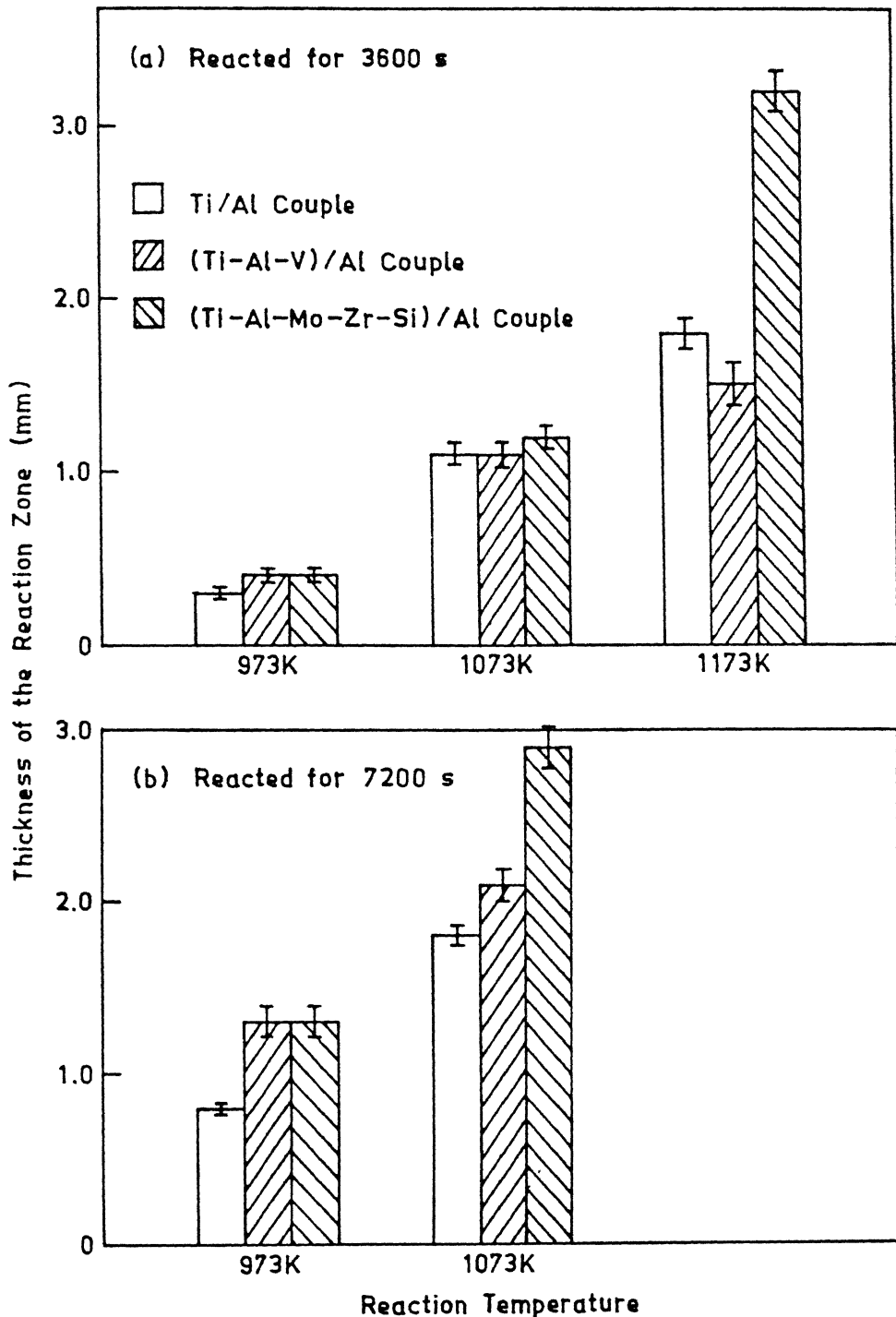


Figure 5.3 Comparison of reaction zone thickness obtained in Ti alloy/Al and pure Ti/Al couples reacted at different temperatures;
 (a) reacted for 3600 s (1 hr) and
 (b) reacted for 7200 s (2 hr).

Table-5.3 : Effect of reaction temperature and time on the thickness of the reaction zone in Ti alloy/Al couples

Reaction couple	Reaction temperature (K)	Thickness of reaction zone (mm)	
		Reaction time (ks)	
		3.6	7.2
(Ti-6Al-4V) /Al	973	0.4	1.3
	1073	1.1	2.1
	1173	1.5	
(Ti-6.5Al-3.2Mo-1.8Zr-0.35Si) / Al	973	0.4	1.3
	1073	1.2	2.9
	1173	3.2	

(2hr) resulted in a 3-fold increase in reaction zone thickness when the reaction was carried out at 973K (1hr) both the alloy couples (Table-5.2). However, at 1073K, (800⁰C) approximately a 2-fold increase in the reaction zone thickness was observed when the reaction time was increased from 3600s (1hr) to 7200s (2hr).

5.1.3 Compositional Analysis of Phases Presented in the Partially Reacted Couples:

Typical microstructure of the reaction zone adjacent to the reaction interface in a couple partially reacted at 1073K (3600 s) is shown in Figure-5.4(a). A continuous thin film of the reaction layer can be clearly seen. The details of the compositional analysis performed by the energy dispersive spectrometer (EDS) are shown in Tables-5.4(a) to 5.4(e). The X-ray dot maps for the elements Ti and Al respectively on the regions shown in Figure-5.4(a) are shown in Figures-5.4(b) and 5.4(c). It can be observed from these figures that the unreacted Ti region did not contain any significant amount of Al. In a similar way, no systematic trend could be observed for the distribution of Ti in the unreacted Al region. Concentration profiles of Ti and Al on the phases present adjacent to the reaction interface are shown in Figures- 5.5(a) and 5.5(b).

As stated in Section 5.1.1, a thin reaction layer of aluminide layer was present at the reaction interface in all the partially reacted pure Ti/Al, Ti-Al-V alloy/Al and Ti-Al-Mo-Zr-Si alloy/Al couples. Compositional analysis of RL showed that this phase corresponded to the $TiAl_3$ composition (Table-5.4c). The reaction zone ahead of the thin reaction layer was in the form of

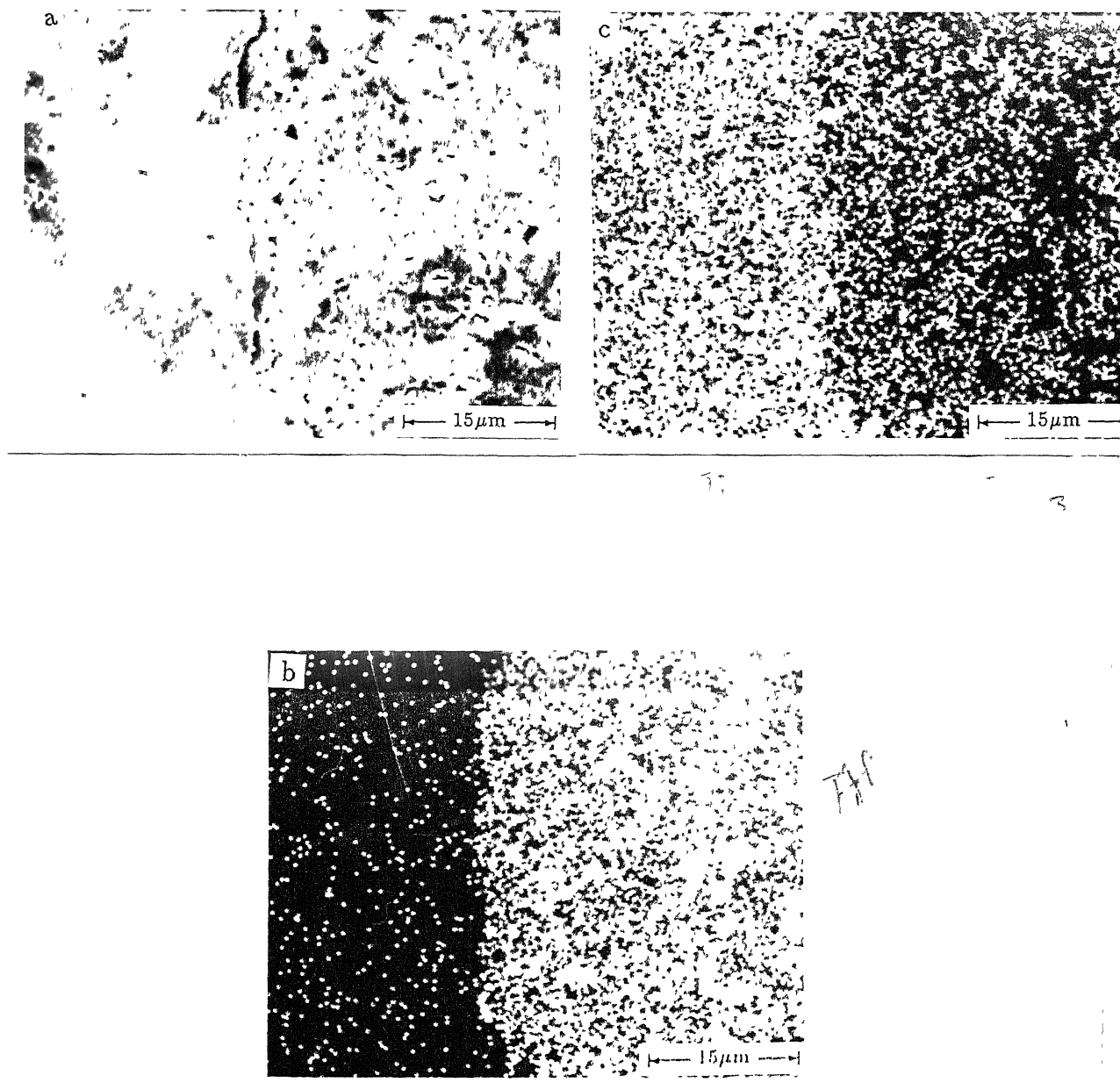


Figure 5.4 (a) SEM micrograph showing phases present adjacent to the reaction interface of Ti/Al couple reacted at 1073 K (800°C) for 3600 s (1 hr); (b), (c) X-ray dot mapping for the element, Ti (b) and Al (c) on the region shown in (a).

able-5.4a : Composition of the unreacted Ti in Ti/Al couples reacted at 1073 K for 7200 s

Average composition		Range of composition	
wt. % Ti	wt. % Al	wt. % Ti	wt. % Al
99.98	0.02	99.93-100.00	0.00-0.07

Table-5.4b : Composition of the unreacted Al in the Ti/Al couple reacted at 1073 K for 7200 s

Average composition		Range of composition	
wt. % Ti	wt. % Al	wt. % Ti	wt. % Al
0.03	99.97	0.00-0.06	99.94-100.00

able-5.4c : Composition of the $TiAl_3$ reaction layer in Ti/Al couples reacted at 1073 K for 7200 s

Analysis by EDS				Analysis by EPMA				
Average composition		Range of composition		Average composition		Range of composition		
at. % Ti	at. % Al	at. % Ti	at. % Al	at. % Ti	at. % Al	at. % Ti	at. % Al	at. % Ti
24.89	75.11	24.37 to 25.41	74.59 to 75.63	24.92	75.08	24.61 to 25.23	74.77 to 75.39	

Table-5.4d : Composition of the $TiAl_3$ particles present in the two phase mixture of the reactions zone of couples reacted at 1073 K for 7200 s

Average composition		Range of composition	
at. % Ti	at. % Al	at. % Ti	at. % Al
25.26	74.74	24.32-25.96	74.04-75.68

Table-5.4e : Composition of the Al-rich matrix of the reaction zone in Ti/Al couples reacted at 1073 K for 7200 s

Average composition		Range of composition	
wt. % Ti	wt. % Al	wt. % Ti	wt. % Al
1.29	98.71	0.02-1.97	98.03-99.98

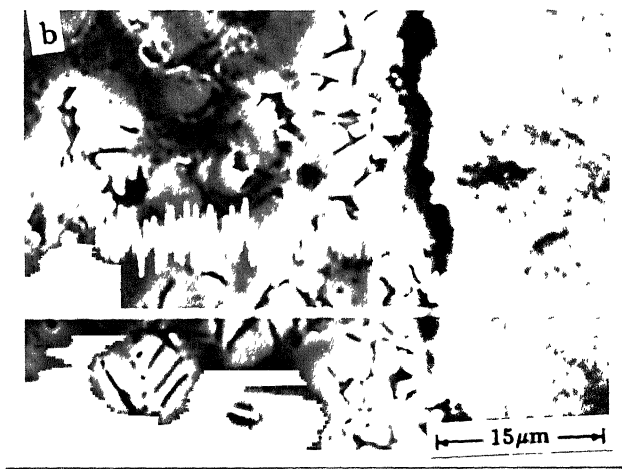
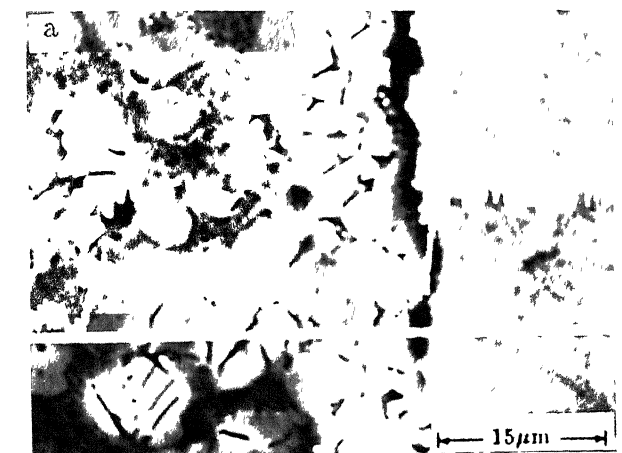


Figure 5.5

SEM micrograph of Ti/Al couple reacted at 1073 K (800°C) for 3600 s (1 hr) showing the presence of thin $TiAl_3$ reaction layer adjacent to the unreacted Ti and concentration profile of Ti (a) and concentration profile of Al (b) in the phases present adjacent to the reaction interface.

dispersed reaction domain and was found to contain a two phase microstructure. As shown in Table-5.4(d) the particles in this two phase mixture were found to have composition corresponding to that of $TiAl_3$. The matrix surrounding the $TiAl_3$ particles was found to contain <2at.% Ti (Table-5.4(e)) and was mainly that of Al. at any location (Table - 5.4e).

The distributions of elements Ti and Al in different phases of the reaction zone as obtained by X-ray dot mapping are shown in Figures-5.6 and 5.7 for pure Ti/Al couples reacted at 973K (700^0C) and 1173K (900^0C) for 3600s (1hr) respectively. These results also confirm that the aluminium matrix in the two phase mixture does not contain any appreciable amount of Ti, thus ruling out the possibility of diffusion of Al in Ti.

From the results shown in Figures 5.4, 5.5, 5.6, 5.7 and Tables- 5.4(a)-5.4(e), it is evident that diffusion of Ti in Al or Al in Ti does not occur during the formation of aluminide by reaction synthesis.

Microstructures of the region adjacent to the reaction interface in case of Ti-Al-V alloy/Al reaction couple synthesized at 1073K (800^0C) for 7200s (2hr) is shown in Figures-5.8(a). X-ray dot mapping for Al and Ti on this region is shown in Figures-5.8(b) - (c). From the distribution of Al in the unreacted Ti alloy and Ti in unreacted Al, it is evident that even in the case of Ti alloy/Al couples, diffusion of Al in Ti or Ti in Al does not lead to the aluminide formation. Similar results were observed even in the case of Ti-Al-Mo-Zr-Si alloy/Al couples.

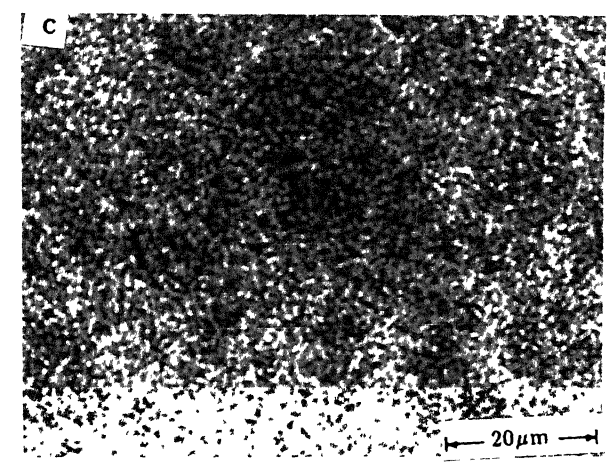
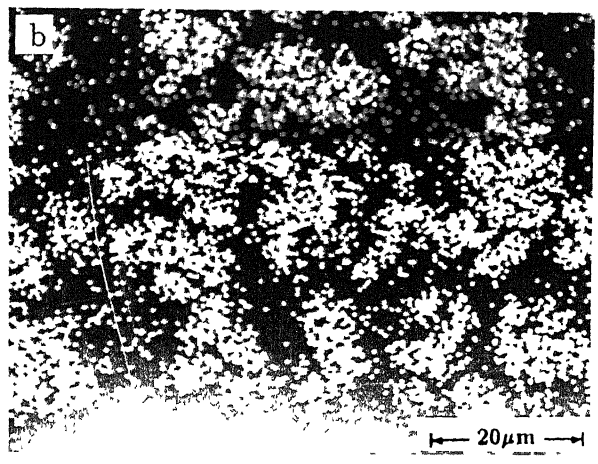
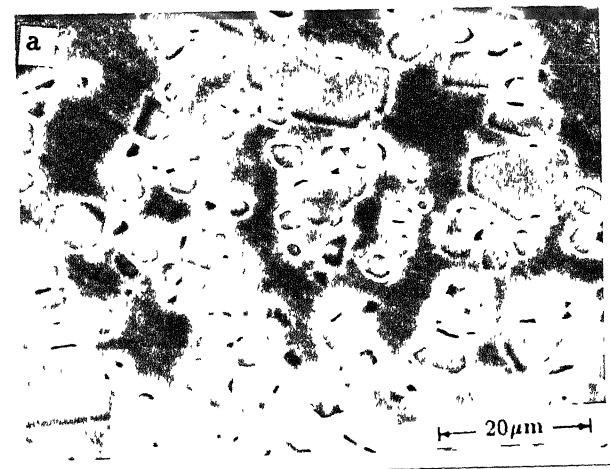


Figure 5.6 (a) SEM micrograph of the reaction zone formed in Ti/Al couple reacted at 973 K (700°C) for 3600s (1 hr);
(b), (c) X-ray dot mapping for element Ti (b) and Al (c) for the region shown in (a)

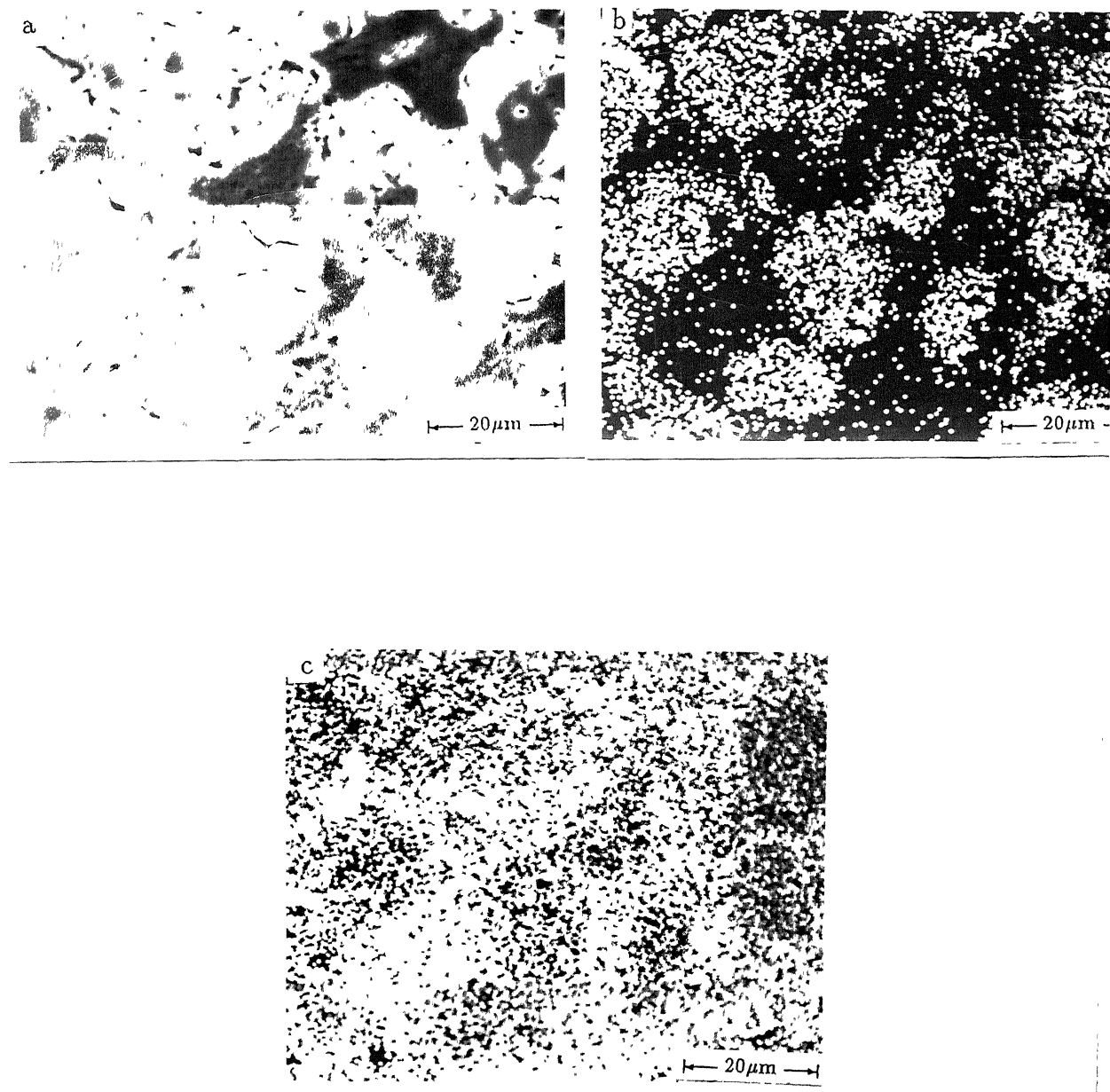


Figure 5.7 (a) SEM micrograph of the reaction zone formed in Ti/Al couple reacted at 1173 K (900°C) for 3600 s (1 hr); (b), (c) X-ray dot mapping for element Ti (b) and Al (c) for the region shown in (a).

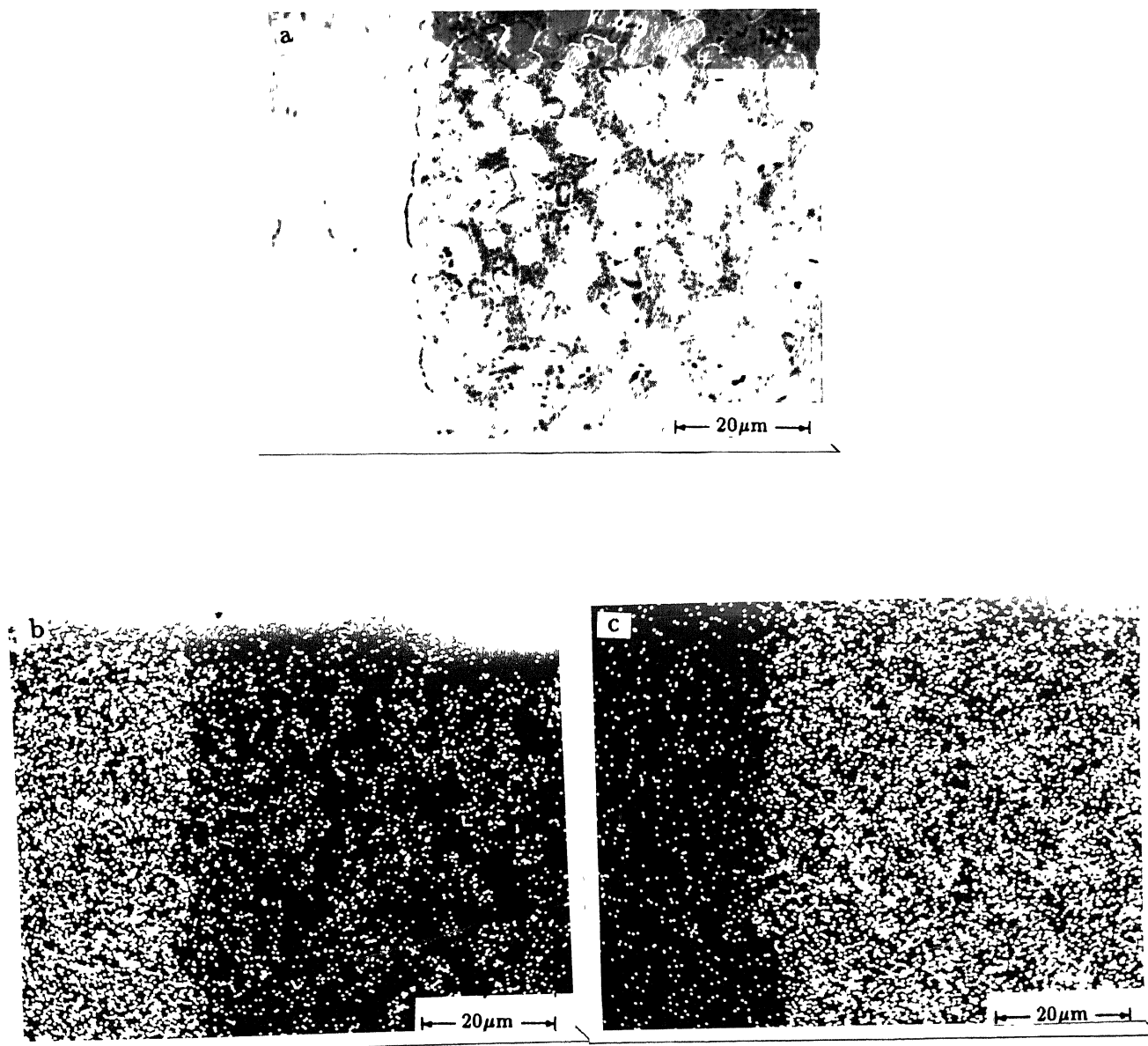


Figure 5.8 (a) SEM micrograph of the reacted zone formed in $(\text{Ti-Al-V})/\text{Al}$ couple reacted at 1073 K (800°C) for 3600 s (1 hr); (b), (c) X-ray dot mapping for the element Ti (b) and Al (c) for the region shown in (a).

5.2 STRUCTURAL ANALYSIS OF PHASES PRESENT IN THE REACTION PRODUCT:

Literature data on the formation of aluminide during interaction of Ti and Al showed that more than one aluminide can form during chemical reaction as well as interdiffusion of Ti and Al [119-128]. For example, studies of van Loo and Reick on Ti-Al diffusion couples in the temperature range of 516°C - 642°C have shown that TiAl_3 is the only aluminide formed as a result of interdiffusion of Ti and Al as long as the entire Al in the diffusion couple is consumed [136]. However, formation of other Ti-Al compounds, namely, Ti_3Al , TiAl , TiAl_2 etc., were observed when the Ti- TiAl_3 couples obtained by interdiffusion of Ti and Al were annealed for long time at 800°C .

Hence, possibility exists regarding their formation by reaction synthesis. However, it is difficult to predict theoretically which of these phases form during reaction synthesis since during the synthesis experiments, the system often deviates from equilibrium conditions. Formation of phases corresponding to compositions different from the stoichiometric composition of the powder compact was observed during the reaction synthesis of several aluminide base intermetallics [12, 19, 20, 101-106]. For example, Philpot et al. [101] reported that the formation of aluminium rich compounds such as NiAl_3 and Ni_2Al_3 occurred during the reaction synthesis of NiAl . Similar observations have been made in the synthesis of Fe_3Al base compounds also by reactive sintering [12]. Rabin and Wright have reported the formation of Fe_2Al_3 during reactive sintering of Fe_3Al compounds [12]. Even in

the case of reaction synthesis of TiAl intermetallics, presence of $TiAl_3$ and Ti_3Al phases in the synthesized product has been reported [106].

In view of the possibility of formation of the off-stoichiometric compounds in the reaction synthesized product, analysis of the phases in the reaction zone was performed. Since different intermetallics viz. Ti_3Al , $TiAl$, $TiAl_2$, Ti_2Al_5 , $TiAl_3$ and Ti_9Al_{23} are present in the Ti-Al system, identification of phases present in the reaction zone was carried out mainly using the X-ray diffraction technique. In addition to X-ray diffraction, reaction zones of few couples were also characterized by TEM. The results obtained on aluminide(s) formation as characterized by these techniques are presented in subsequent sections.

5.2.1 Aluminide Formation in Ti/Al Couples in the Temperature Range of 973 K - 1273 K ($700^{\circ}C$ - $1000^{\circ}C$):

XRD patterns obtained from pure Ti/Al couples reacted at temperatures of 973 K - 1273 K for a period of 3600 s (1 hr) are shown in Figures - 5.9(a) - (d) respectively. These XRD patterns revealed the presence of peaks corresponding to pure Ti, pure Al and those from the aluminide phase. The pure Ti and pure Al peaks were due to the presence of the unreacted regions of elemental Ti and elemental Al respectively.

A comparison of the 'd' values of the peaks corresponding to the aluminide phase with the standard ' d_{hkl} ' values of various Ti-Al aluminides from the powder diffraction

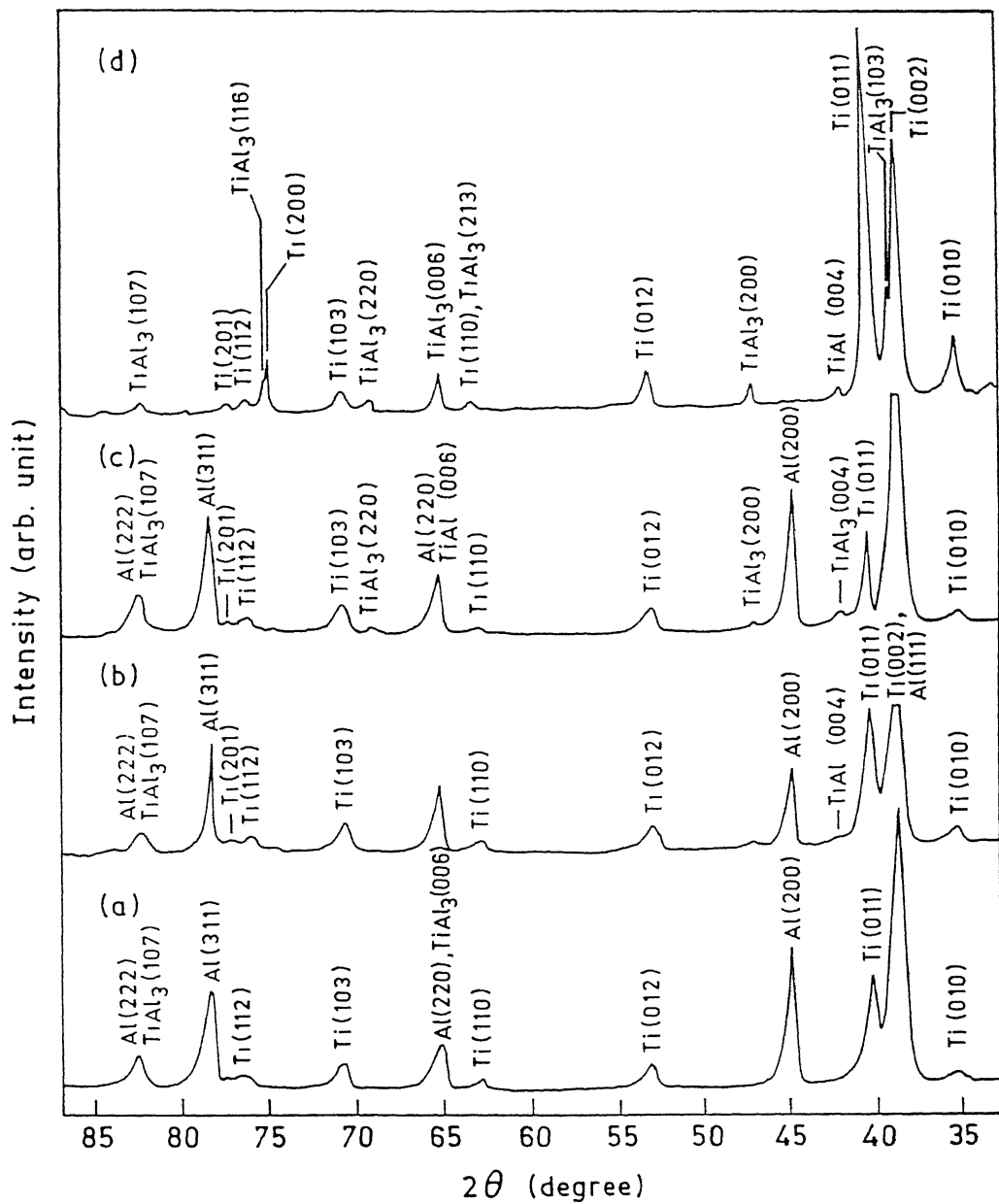


Figure 5.9 X-ray diffraction patterns obtained from the couples reacted for 3600 s (1 hr) at (a) 973 K (700°C), (b) 1073 K (800°C), (c) 1173 K (900°C) and (d) 1273 K (1000°C).

files showed that ' d_{hkl} ' values of the aluminide phase matched with those of the $TiAl_3$ phase. No peaks corresponding to the 'd' values of other aluminides belonging to the Ti-Al system, such as Ti_3Al , $TiAl$, Ti_2Al_5 , $TiAl_2$ and Ti_9Al_{23} were observed in XRD patterns. As shown in the figure, increase in reaction temperature from 973 K ($700^{\circ}C$) to 1273 K ($1000^{\circ}C$) resulted in an increase in the relative intensities of peaks from higher intensity planes of the $TiAl_3$ phase, such as (006) and (107).

Moreover, increase in reaction temperature led to appearance of low intensity peaks. For example, increase in reaction temperature from 973 K ($700^{\circ}C$) to 1173 K ($900^{\circ}C$) resulted in appearance of (220) peak ($I/I_0 = 40\%$) of the $TiAl_3$ phase (Figure - 5.9(a)-(c)). Further increase in reaction temperature to 1273 K ($1000^{\circ}C$) showed the presence of other low intensity peaks corresponding to (103), (220) and (116) planes of $TiAl_3$ (Figure - 5.9(d)). In addition, it can be observed from Figure - 5.9(d) that the reacted couples showed absence of Al at this reaction temperature indicating that complete consumption of Al occurred at a reaction temperature of 1273 K ($1000^{\circ}C$) when the reaction was carried out for 3600 s (1 hr).

The XRD patterns of Ti/Al couples reacted at 1073 K ($800^{\circ}C$) for time intervals of 3600 s (1 hr), 7200 s (2 hr) and 14400 (4 hr) respectively are shown in Figures - 5.10(a) to 5.10(c). Similar to the diffraction patterns shown in Figure - 5.9, Figure - 5.10 also showed the presence of the three phases, i.e., elemental Ti, elemental Al and the $TiAl_3$ compound. Also,

Intensity (arb. units)

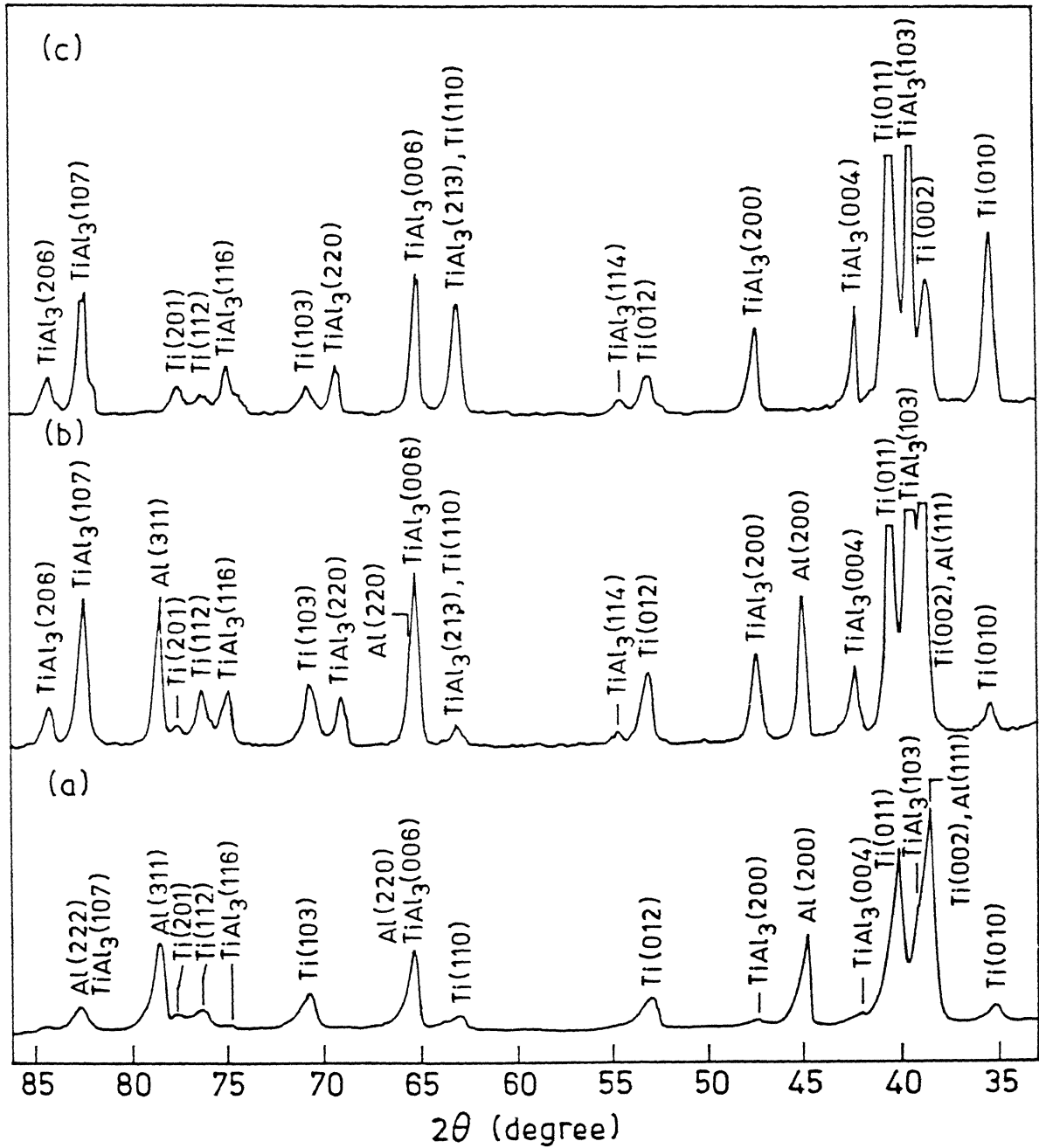


Figure 5.10

X-ray diffraction patterns from the Ti/Al couples reacted at 1073 K (800°C) for different time intervals; Reacted for (a) 3600 s (1 hr), (b) 7200 s (2 hr) and (c) 14400 s (4 hr).

Figure - 5.10 shows that increase in reaction time clearly resulted in enhancement of relative intensity of $TiAl_3$ peaks with respect to the unreacted Ti and Al. For example, marked increase in the intensities of the (004), (200), (213), (006) and (107) can be seen as a result of increase in reaction time from 3600 s (1 hr) to 14400 s (4 hr). Reaction time of 14400 s (4 hr) at 1073 K ($800^\circ C$) showed the absence of Al in the reacted couples indicating the complete consumption of Al under these reaction conditions (Figure - 5.11).

However, neither increase in reaction temperature nor reaction time gave rise to the appearance of any additional peaks corresponding to other Ti-Al intermetallics thus revealing that $TiAl_3$ was the only aluminide formed in the temperature range of 973 K - 1273 K ($700^\circ C$ - $1000^\circ C$). These results agree with the data reported in the literature on interaction between Ti and liquid Al [121-129]. As discussed in Chapter 2 (Section 2.7), studies on aluminide formation during several of these investigations (e.g. hot dip aluminide coatings, diffusion welding, brazing of Ti by Al filler metal etc.) reported that $TiAl_3$ was the only aluminide formed in the temperature range of 973 K - 1273 K ($700^\circ C$ - $1000^\circ C$).

Typical bright field TEM micrograph of the dispersed reaction domain of pure Ti/Al couple reacted at 1073 K ($800^\circ C$) for 7200 s (2 hr) is shown in Figure - 5.11. Microstructure shows parts of two aluminide particles (indicated as A and B) in the

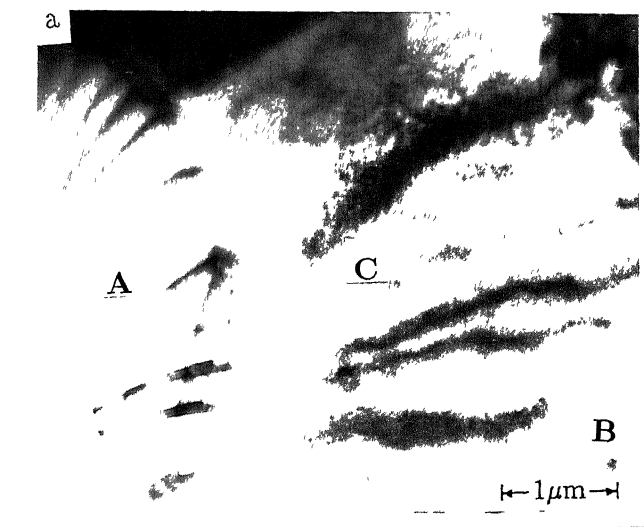


Figure 5.11 (a) Bright field electron micrograph of the dispersed reaction domain from Ti/Al couples reacted at 1073 K (800°C) for 7200 s (2 hr); selected area diffraction patterns corresponding to the regions A, (b) and region C, (c), (d) and (e) are indexed patterns corresponding to the regions A and C.

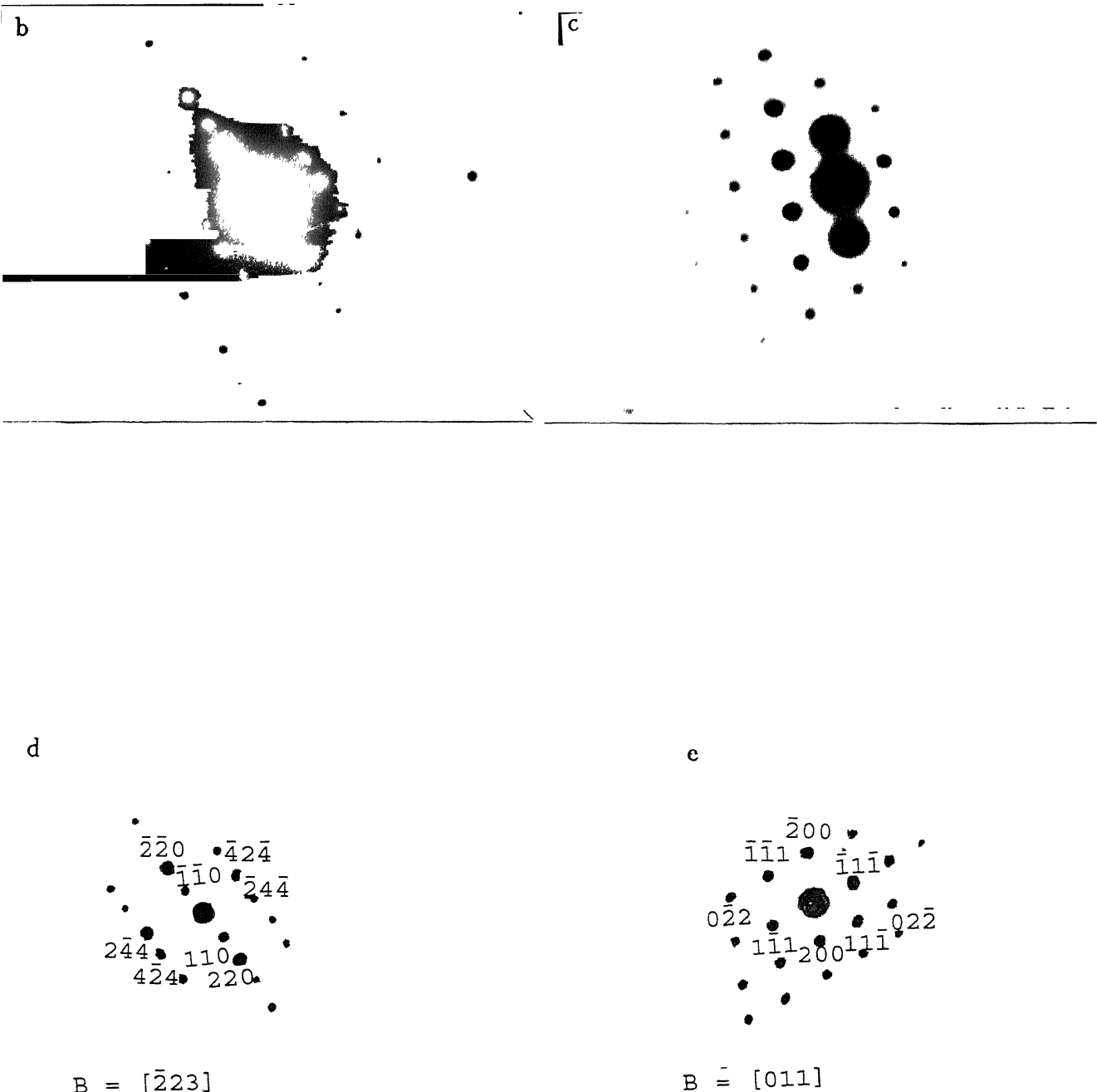


Figure 5.11 (a) Bright field electron micrograph of the dispersed reaction domain from Ti/Al couples reacted at 1073 K (800°C) for 7200 s (2 hr); selected area diffraction patterns corresponding to the regions A, (b) and region C, (c), (d) and (e) are indexed patterns corresponding to the regions A and C.

matrix (C). Selected area diffraction patterns obtained from regions A and C are shown in Figures - 5.11(b) and 5.11(c).

As indicated by XRD patterns shown in Figure - 5.10, the aluminide formed in the dispersed reaction domain of couples reacted in the temperature range of 973 K - 1273 K (700°C - 1000°C) corresponded to the DO_{22} lattice of TiAl_3 . Thus the diffraction pattern from the aluminide phase (region A) as shown in Figure 5.11(b) was indexed using the fcc notation followed generally for indexing the DO_{22} lattice of TiAl_3 [51]. The complete indexed pattern of Figure - 5.11(b) is given in Figure - 5.11(d) and it can be seen that the pattern represented the $(\bar{1}14)$ foil of TiAl_3 . The superlattice reflections of the spots corresponding to DO_{22} structure can also be seen. On the other hand, the diffraction pattern from the matrix, i.e. region C, was found to be corresponding to the (011) foil of fcc Al as identified from Figure - 5.11(a). Selected Area Diffraction patterns obtained from Ti/Al couples reacted at the temperatures of 973 K (700°C) and 1173 K (900°C) also showed similar results confirming the results obtained from X-ray diffraction that TiAl_3 is the only aluminide formed in the temperature range of 973 K - 1273 K (700°C - 1000°C).

5.2.2 Aluminide Formation in Ti/Al Couples at the Reaction

Temperature of 1373 K (1100°C):

Reaction behaviour of pure Ti/Al couples at the temperature of 1373 K (1100°C) was found to be somewhat different than that in the temperature range of 973 K - 1273 K

(700°C-1000°C). XRD pattern of pure Ti/Al couples reacted at 1373 K (1100°C) for 3600 s (1 hr) is shown in Figure - 5.12(c). Again, for the sake of comparison, the diffraction patterns obtained from couples reacted at temperatures lower than 1373 K are also shown in Figure - 5.12(a) and (b). Comparison of Figure - 5.12(c) with Figures - 5.12(a) and 5.12(b) shows that the sample reacted at 1373 K shows some additional peaks, other than those from the elemental Ti and Al and the $TiAl_3$ compound. The peak positions and the probable phases corresponding to different peaks of the phases present in couples reacted at 1373 K are given in Table - 5.5. The additional peaks other than Ti, Al and $TiAl_3$ are indicated by '*' in Table - 5.5. Comparison of the 'd' values of these additional peaks with the 'd' values of the intermetallics of the Ti-Al system (Annexure - B) indicates the possibility of these peaks coming from the compound Ti_8Al_{24} and/or Ti_9Al_{23} .

As discussed earlier, compounds $TiAl_3$, Ti_8Al_{24} and Ti_9Al_{23} poses ordered tetragonal crystal structure. In addition, Ti_8Al_{24} and Ti_9Al_{23} have their lattice parameters 'a' and 'c' very close to each other ($a_{Ti_8Al_{24}} = 3.875 \text{ \AA}$, $a_{Ti_9Al_{23}} = 3.84 \text{ \AA}$ and $c_{Ti_8Al_{24}} = 33.835 \text{ \AA}$, $c_{Ti_9Al_{23}} = 33.46 \text{ \AA}$). Hence, a close matching of some of their d_{hkl} values are also very close to each other.

For the sake of indexing the X-ray diffraction patterns, the '2θ' values of the (hkl) reflections for CuK_α radiation of the three aluminides $TiAl_3$, Ti_8Al_{24} and Ti_9Al_{23} , in the range of 36° -

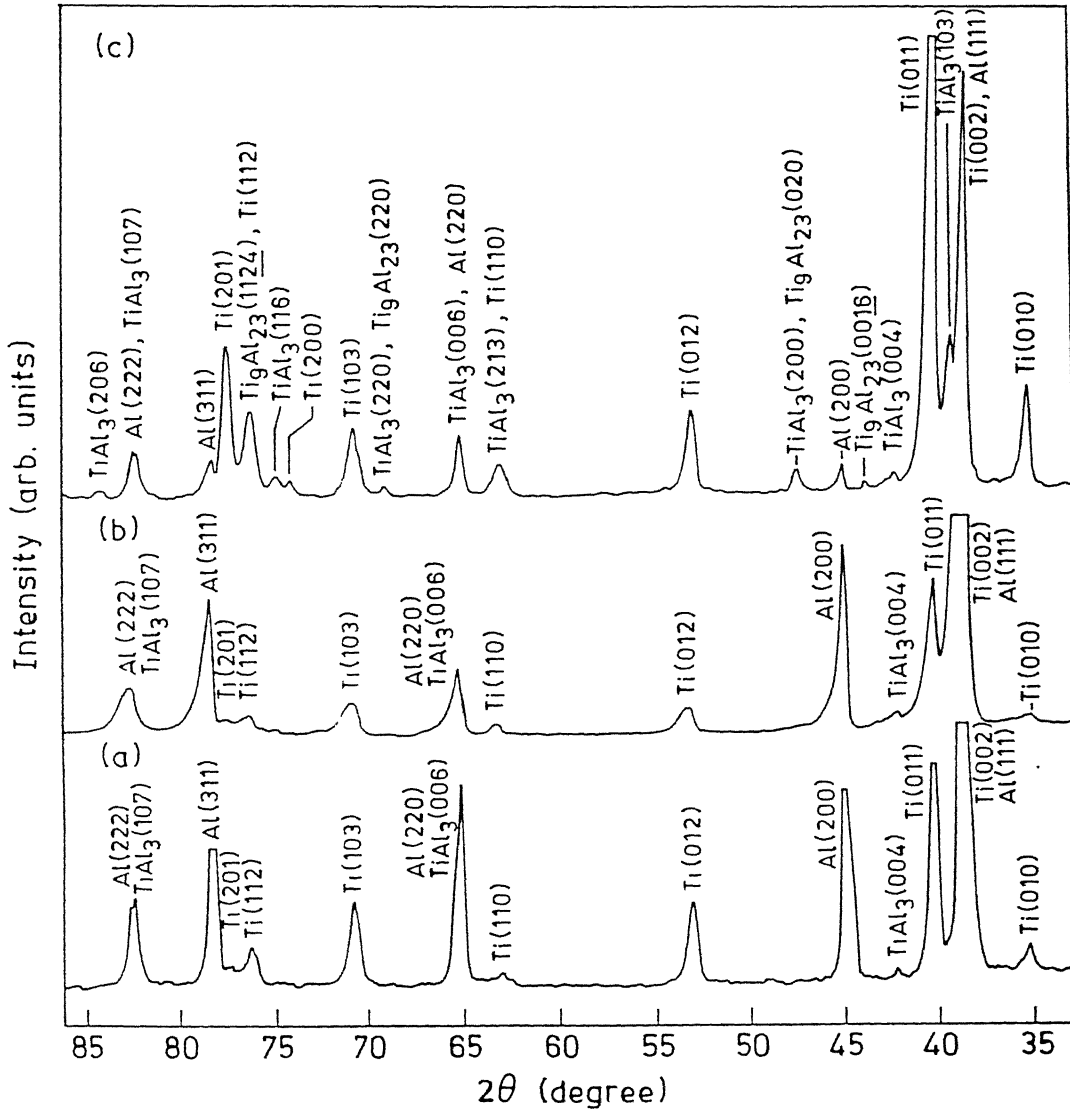


Figure 5.12

X-ray diffraction patterns from the Ti/Al couples reacted for 3600 s (1 hr) at (a) 973 K (700°C), (b) 1173 K (700°C) and (c) 1373 K (1100°C).

Table-5.5 : Peak positions (2θ), interplanar spacings and probable phases observed in pure Ti/Al couples reacted at 1373 K (1100°C) for 3600 s (1 hr)

2 θ degree)	d (\AA)	Probable phases (hkl)
35.2	2.552	Ti (010)
38.3	2.348	Ti (002), Al (111)
39.2	2.297	TiAl_3 (103)
39.6	2.278	$\text{Ti}_9\text{Al}_{23}$ (118)*
40.1	2.251	Ti (011)
42.1	2.147	TiAl_3 (004)
43.3	2.088	$\text{Ti}_9\text{Al}_{23}$ (0016)
44.7	2.028	Al (200)
47.3	1.922	TiAl_3 (200), $\text{Ti}_9\text{Al}_{23}$ (020)
53.2	1.723	Ti (012)
63.1	1.473	TiAl_3 (213), Ti (110)
65.2	1.430	TiAl_3 (006), Al (220)
66.24	1.411	$\text{Ti}_9\text{Al}_{23}$ (0216)*
69.10	1.359	TiAl_3 (220), $\text{Ti}_9\text{Al}_{23}$ (220)
70.6	1.334	Ti (103)
73.9	1.282	Ti (200)
75.6	1.258	TiAl_3 (116)
76.3	1.248	$\text{Ti}_9\text{Al}_{23}$ (1124), Ti (112)
76.9	1.240	Ti (201)
77.8	1.227	Al (311)
82.45	1.170	TiAl_3 (107), $\text{Ti}_9\text{Al}_{23}$ (138)
82.5	1.170	Al (220)
83.9	1.153	TiAl_3 (206)

85° , are listed in Table - 5.6. As shown in the table, most prominent peaks of $\text{Ti}_8\text{Al}_{24}$ and $\text{Ti}_9\text{Al}_{23}$ corresponding to the (118) reflection ($I/I_0 \sim 100\%$) exist in the '2 θ ' range of $39.1^\circ - 39.6^\circ$. Similarly other prominent peaks of $I/I_0 = 80\%$ of these two compounds lie very close. For example, the (0016) peaks of both these phases lie in the range of $2\theta = 42.7^\circ - 43.3^\circ$. Similarly peaks belonging to (200) of $\text{Ti}_8\text{Al}_{24}$ and TiAl_3 and (020) peak of $\text{Ti}_9\text{Al}_{23}$ exist in the 2θ range of $46.8^\circ - 47.3^\circ$. The existence of two or more peaks of these aluminides in a 2θ -range of less than 0.5° can be seen for several other (hkl) planes also (Table - 5.6). Inspite of the fact that both $\text{Ti}_8\text{Al}_{24}$ and $\text{Ti}_9\text{Al}_{23}$ posses the same crystal structure with matching ' d_{hkl} ' values for some of the (hkl) reflections, these additional peaks were indexed based on the following observations;

(i) the peaks corresponding to the angular positions of $2\theta = 47.3^\circ, 69.10^\circ$ and 82.45° with their respective ' d ' = $1.922 \text{ \AA}, 1.359 \text{ \AA}, 1.170 \text{ \AA}$, can exist from either the phase $\text{Ti}_8\text{Al}_{24}$ and/or $\text{Ti}_9\text{Al}_{23}$ (Table - 5.5, Annecture-B).

But,

(ii) the peaks corresponding to the positions $2\theta = 39.56^\circ, 43.3^\circ, 66.24^\circ$ and 76.3° ($d = 2.278 \text{ \AA}, 2.089 \text{ \AA}, 1.411 \text{ \AA}$ and 1.248 \AA) are from the (118), (0116), (0216) and (1124) planes of the $\text{Ti}_9\text{Al}_{23}$ phase.

Based on (i) and (ii) it was concluded that the additional peaks observed in Figure - 5.12(c) were from the $\text{Ti}_9\text{Al}_{23}$ phase. Therefore, in addition to the formation of TiAl_3 , $\text{Ti}_9\text{Al}_{23}$ also

Table-5.6 : Interplanar spacing ' d_{hkl} ', 2θ for CuK_α radiation and relative intensities of (hkl) of the phases TiAl_3 , $\text{Ti}_8\text{Al}_{24}$ and $\text{Ti}_9\text{Al}_{23}$

d hkl (\AA)	2θ (degree)	Phase (hkl)	I/I_0 (%)
1.409	37.33	$\text{Ti}_8\text{Al}_{24}$	10
1.384	37.73	$\text{Ti}_9\text{Al}_{23}$ (0111)	5
1.303	39.11	TiAl_3 (103)	100
1.301	39.15	$\text{Ti}_8\text{Al}_{24}$ (118)	100
1.279	39.54	$\text{Ti}_9\text{Al}_{23}$ (118)	100
1.153	41.96	TiAl_3 (004)	80
2.116	42.73	$\text{Ti}_8\text{Al}_{24}$ (0016)	80
2.092	43.25	$\text{Ti}_9\text{Al}_{23}$ (0016)	80
1.939	46.85	$\text{Ti}_8\text{Al}_{24}$ (200)	80
1.926	47.20	TiAl_3 (200)	80
1.921	47.32	$\text{Ti}_9\text{Al}_{23}$ (020)	80
1.763	51.86	$\text{Ti}_8\text{Al}_{24}$ (208)	10
1.713	53.49	$\text{Ti}_8\text{Al}_{24}$ (213)	10
1.689	54.31	TiAl_3 (114)	20
1.676	54.77	$\text{Ti}_8\text{Al}_{24}$ (1116)	10
1.618	56.91	$\text{Ti}_8\text{Al}_{24}$ (1019)	10
1.573	58.69	TiAl_3 (105)	10
1.511	61.36	$\text{Ti}_8\text{Al}_{24}$ (2014)	10

Contd...

Table-5.6 (continued)

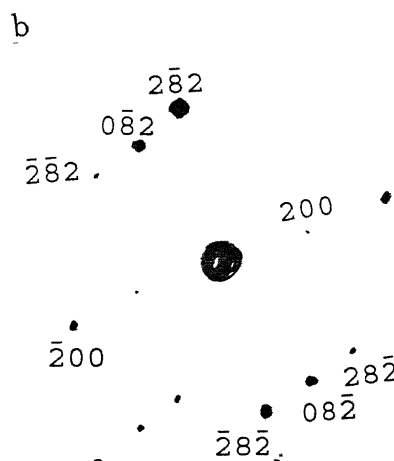
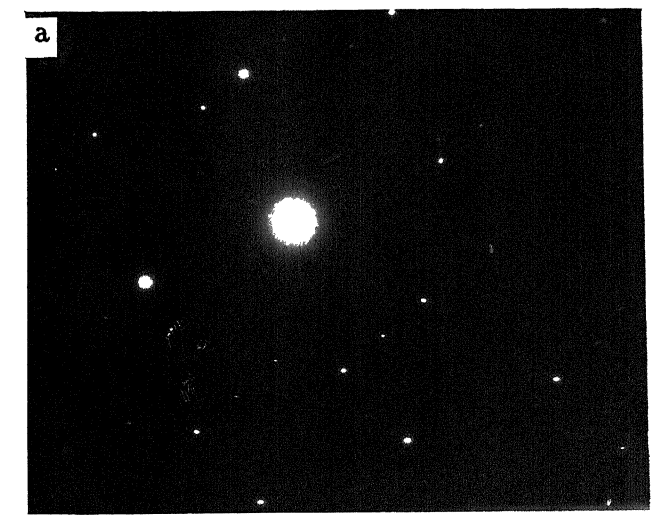
d hkl (\AA)	2 θ (degree)	Phase (hkl)	I/I ₀ (%)
.477	62.93	TiAl ₃ (213)	10
.436	64.94	TiAl ₃ (006)	60
.430	65.25	Ti ₈ Al ₂₄ (20 <u>16</u>)	60
.414	66.08	Ti ₉ Al ₂₃ (02 <u>16</u>)	80
.372	68.37	Ti ₈ Al ₂₄ (220)	60
.362	68.95	TiAl ₃ (220)	40
1.358	69.18	Ti ₉ Al ₂₃ (220)	70
1.270	74.75	TiAl ₃ (116)	60
1.255	75.80	Ti ₈ Al ₂₄ (11 <u>24</u>)	60
1.240	76.88	Ti ₉ Al ₂₃ (11 <u>24</u>)	70
1.218	78.53	TiAl ₃ (215)	10
1.178	81.75	Ti ₈ Al ₂₄ (318)	60
1.172	82.26	TiAl ₃ (107)	60
1.165	82.86	Ti ₉ Al ₂₃ (138)	70
1.151	84.10	Ti ₈ Al ₂₄ (31 <u>10</u>)	60
1.151	84.10	TiAl ₃ (206)	40
1.138	85.29	Ti ₉ Al ₂₃ (22 <u>16</u>)	70

formed at the reaction temperature of 1373 K (1100°C).

The selected area diffraction (SAD) pattern of the aluminide phase of the dispersed reaction domain of Ti/Al couple reacted at 1373 K (1100°C) for 3600 s (1 hr) is shown in Figure 5.13(a). The pattern indexed according to fcc notation is shown in Figure - 5.13(b). This pattern represents the (014) foil of $TiAl_3$. However, no SAD pattern from Ti_9Al_{23} phase could be obtained possibly due to its absence in the regions of the foil prepared for TEM examination. Moreover, due to the shortage of material, large number of foils could not be prepared from the dispersed reaction domain of couples reacted at 1373 K.

5.2.3 Aluminide Formation in the Ti-Al-V alloy/Al and Ti-Al-Mo-Zr-Si alloy/Al Couples:

The X-ray diffraction patterns obtained from Ti-Al-V/Al and Ti-Al-Mo-Zr-Si/Al couples reacted at 1073 K (800°C) for 7200 s (2 hr) have been shown in Figures - 5.14(b) and 5.14(c) respectively. For the sake of comparison, the XRD patterns from Ti/Al couple reacted under same conditions is also presented in Figure - 5.14. Similar to the observations made in the case of Ti/Al couples, peaks corresponding to other Ti-Al compounds were absent in the Ti-Al-V alloy/Al and Ti-Al-Mo-Zr-Si alloy/Al couples. These XRD patterns given in Figures - 5.14(b) and 5.14(c) indicate the formation of $TiAl_3$ base compound as the only reaction product. Further, a shift in peak positions of $TiAl_3$ base compounds (Figures - 5.14(b) and 5.14(c)), with respect to the peak positions of unalloyed $TiAl_3$ compound formed in pure



$B = [014]$

Figure 5.13 (a) Selected area diffraction pattern of aluminide formed in Ti/Al couple reacted at 1373 K (1100°C) for 3600 s (1 hr)
(b) Indexed pattern of Figure - 5.13(a).

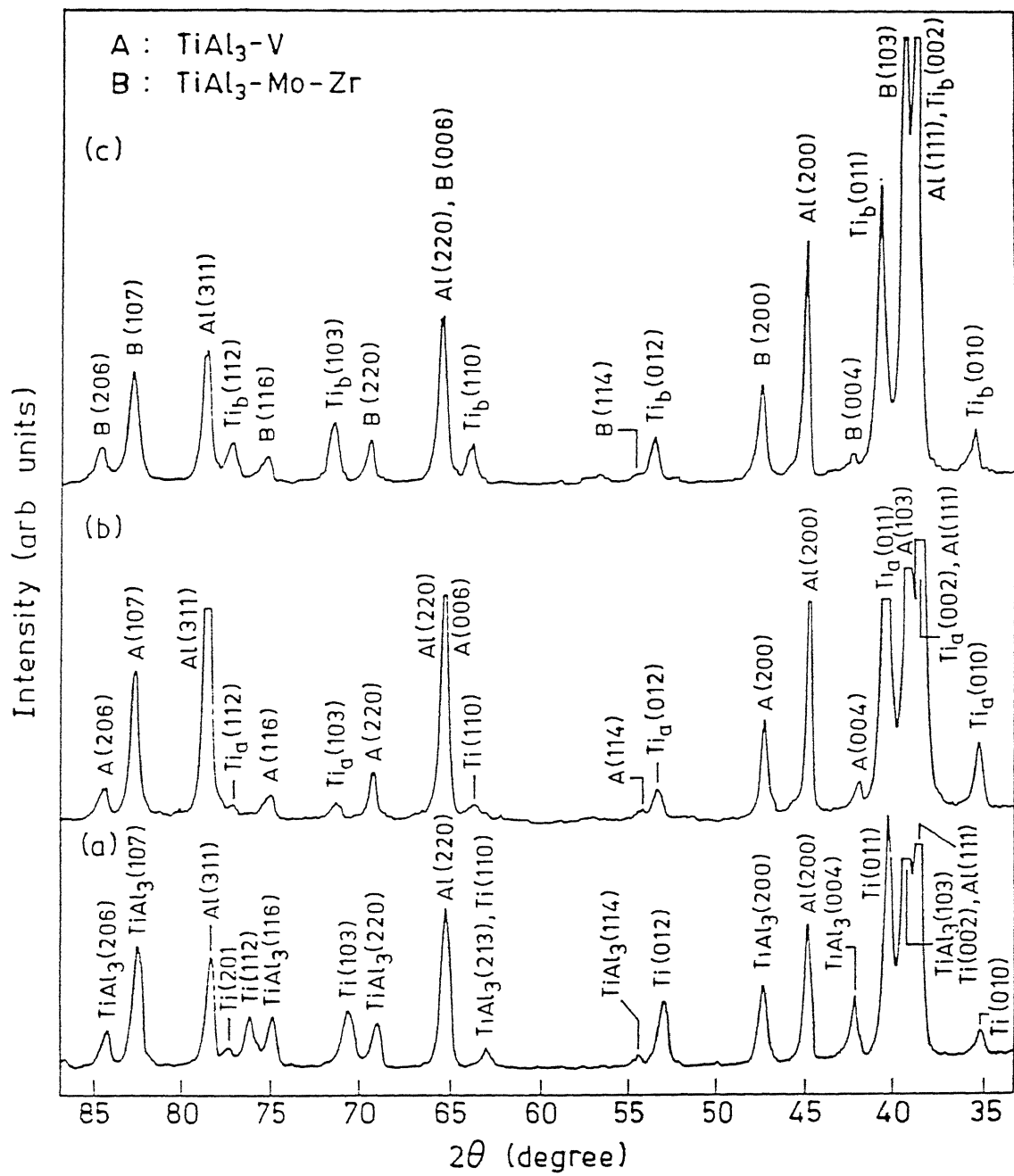


Figure 5.14 X-ray diffraction patterns from couples reacted at 1073 K (800°C) for 7200 s (2 hr); (a) Ti/Al couple, (b) Ti-Al-V alloy/Al and (c) Ti-Al-Mo-Zr-Si alloy/Al.

(Ti_a and Ti_b represent the peaks corresponding to the Ti-Al-V and Ti-Al-Mo-Zr-Si alloys used respectively.)

Ti/Al couple (Figure - 5.15(a)) can be noted. This observation indicates that change in the lattice parameter of the $TiAl_3$ base compounds occurred as a result of alloying with element V present in Ti-Al-V alloy and that with Mo, Zr, Si present in Ti-Al-Mo-Zr-Si alloy reaction couples. Lattice parameters of the $TiAl_3$ base compounds were calculated by the general procedure followed for lattice parameter determination in tetragonal systems as described in Section 4.3.1.

The 'a' and 'c' parameters obtained for the $TiAl_3$ base compounds formed in both the alloy couples, as well as the binary $TiAl_3$ compound formed in pure Ti/Al couples, are shown in Table - 5.7. A decrease in both 'a' as well as 'c' parameters of $TiAl_3$ is evident due to the alloying effect occurring in the case of Ti-Al-V alloy/Al and Ti-Al-Mo-Zr-Si alloy/Al couples. However, the combined effect of (Mo + Zr + Si) was found to be more prominent in decreasing the lattice parameters as compared to that from alloying with V.

Similarly bright field micrographs of $TiAl_3$ particles of Ti-Al-V alloy/Al and Ti-Al-Mo-Zr-Si alloy/Al are shown in Figures - 5.15(a) and 5.15(b). The selected area diffraction patterns corresponding to these two particles are shown in Figures - 5.16(a) and 5.16(b) respectively. The indexed patterns of 5.16(a) and 5.16(b) are given in Figures - 5.16(c) and 5.16(d) respectively. It can be noted that Figure - 5.16(c) and 5.16(d) correspond to (012) and (223) foils respectively of DO_{22} $TiAl_3$ phase.

Table-5.7 : Lattice parameters of TiAl_3 base compounds formed in pure Ti/Al and Ti alloy/Al couples by reaction synthesis at 1073 K for 7.2 ks

Parameter	Lattice parameter value (\AA)		
	TiAl_3	$\text{TiAl}_3\text{-V}$	$\text{TiAl}_3\text{-Mo-Zr-Si}$
a	3.852	3.834	3.824
c	8.612	8.556	8.528

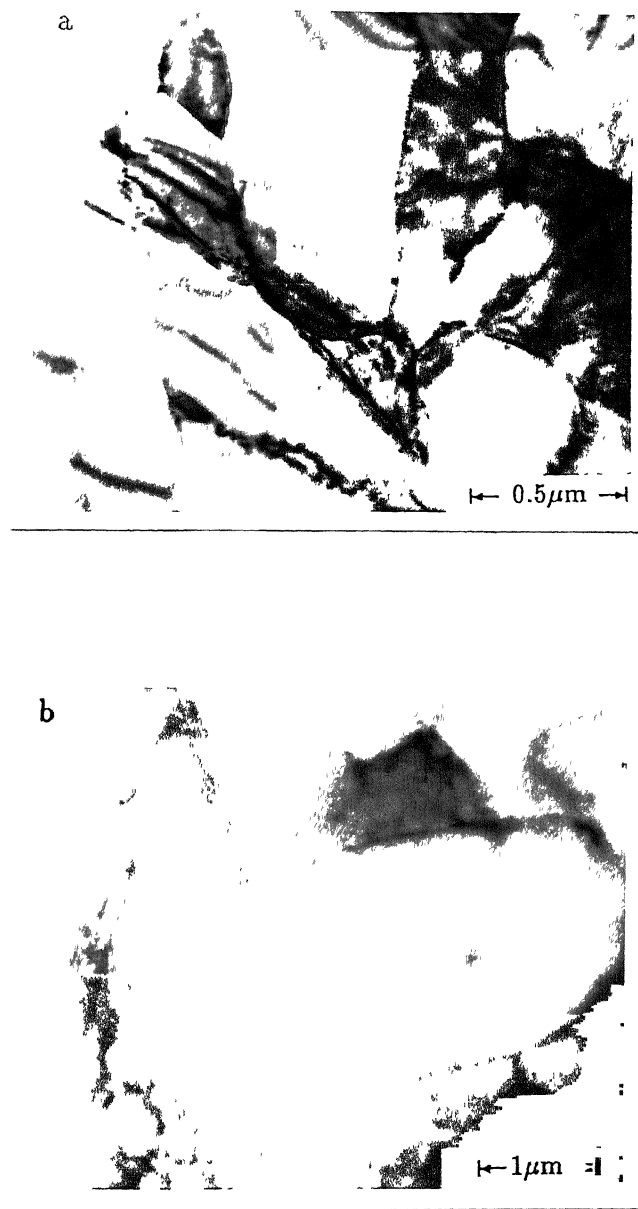


Figure 5.15 Bright field transmission electron micrograph of TiAl_3 base particles in (a) Ti-Al-V alloy/ Al reaction couple and (b) Ti-Al-Mo-Zr-Si alloy/Al reaction couple; Couples reacted at 1073 K (800°C) for 7200 s (2 hr).

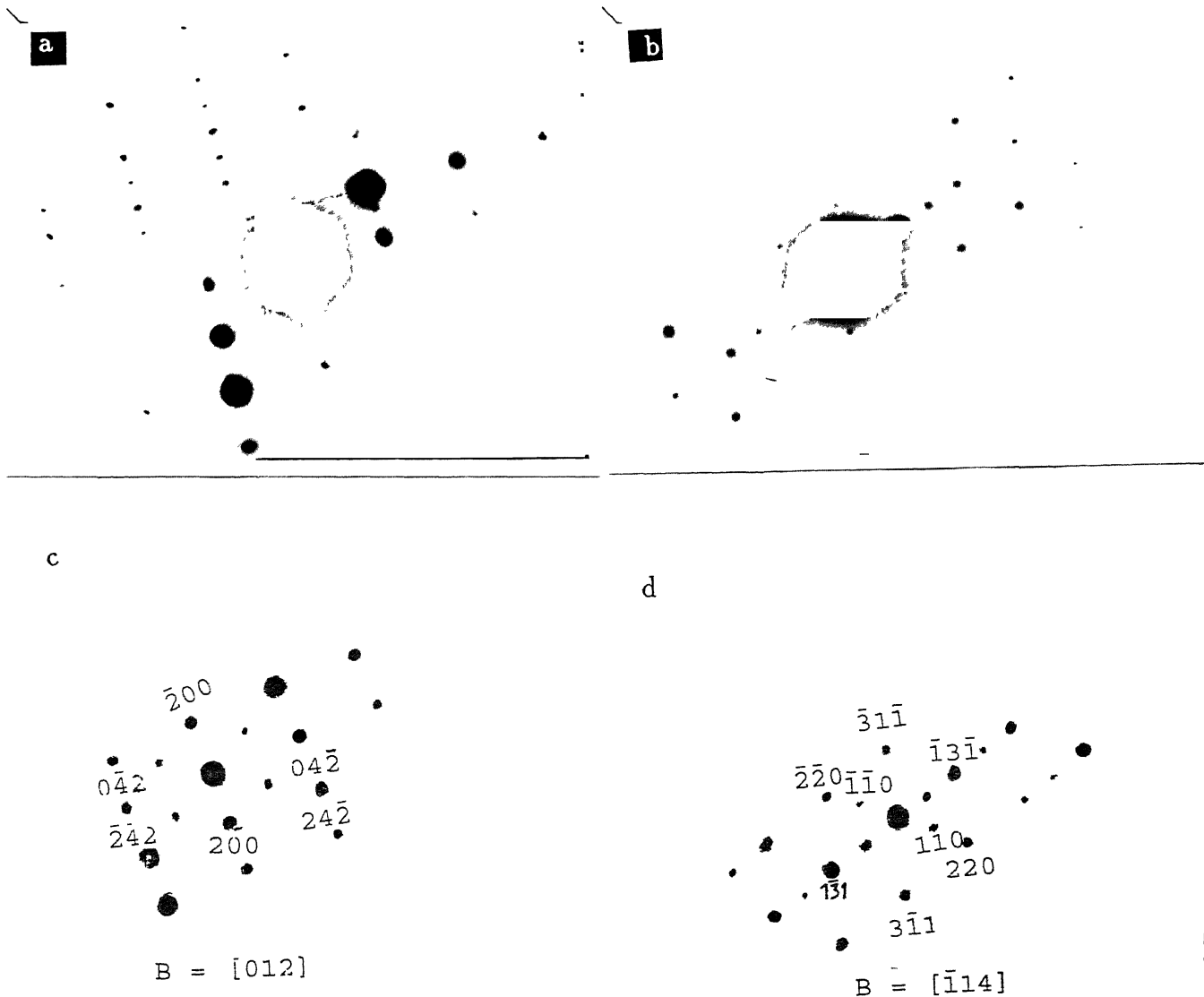


Figure 5.16 Selected area diffraction patterns from TiAl_3 base particles shown in (a) Figure - 5.16(a) and (b) Figure - 5.16(b); Indexed diffraction patterns of (c): Figure - 5.16(a) and (d): Figure - 5.16(b).

5.3 VARIATION OF REACTION ZONE MICROSTRUCTURAL FEATURES IN PARTIALLY REACTED COUPLES:

It has already been shown that the microstructural features of reaction zones in partially reacted pure Ti/Al, Ti-Al-V alloy/Al and Ti-Al-Mo-Zr-Si alloy/Al couples, reacted under different temperature-time conditions consisted of a reaction interface, continuous thin reaction layer and a dispersed reaction domain. In the reaction temperature range of 973 K (700°C) to 1273 K (1000°C) the reaction product was found to be only TiAl_3 in pure Ti/Al, Ti-Al-V alloy/Al and Ti-Al-Mo-Zr-Si alloy/Al couples. On the other hand, TiAl_3 as well as $\text{Ti}_9\text{Al}_{23}$ were found to form at the reaction temperature of 1373 K.

A closer examination of microstructural features of reaction interface, reaction layer and dispersed reaction domain revealed that they varied with reaction conditions, i.e. reaction time and temperature. Also, these features were influenced considerably by the alloy chemistry of the TiAl_3 base intermetallics formed. Further, within the dispersed reaction domain (DRD) of a partially reacted couple, volume fractions of aluminide particles, particle size distribution, mean particle size, particle shape and morphology varied with distance from the reaction interface (RI). These changes in various microstructural features are due to different physical phenomena occurring during reaction synthesis. These phenomena such as (i) exothermic heat evolution at the reaction interface, (ii) build up of thermal gradients in the phases adjacent to the reaction interface, (iii)

development of thermal currents inside liquid Al, (iv) morphological instability of the $TiAl_3$ layer, (v) dissolution and reprecipitation of aluminide particles inside liquid Al and (vi) neck formation by solid state sintering are discussed in the next chapter. Experimental results obtained by quantitative metallography on their variation are given in the following subsections.

5.3.1 Morphological Features of the Reaction Interface:

SEM micrograph of the reaction interface with the adjacent unreacted Ti and the dispersed reaction domain from Ti/Al couple reacted at 973 K ($700^{\circ}C$) for 7200 s (2 hr) is shown in Figure - 5.17. It can be seen from the figure that the reaction interface possesses microscopically non-planar morphology. Occasionally, in Ti/Al couples reacted at 1073 K ($800^{\circ}C$) and above, presence of islands of phases other than those belonging to the dispersed reaction domain were observed ahead of the reaction interface [Figure - 5.18(a)]. As indicated by EDS analysis and shown by X-ray dot mapping in Figures - 5.18(b) and 5.18(c), these islands were identified to be that of Ti.

The non-planar nature of the reaction interface was observed even in the case of Ti-Al-V alloy/Al and Ti-Al-Mo-Zr-Si alloy/Al reaction couples. The microstructures of the reaction interface of these couples are shown in Figures - 5.17(b) and 5.17(c). As compared to that of pure Ti/Al couple, the non-planarity of the reaction interface in the case of Ti-Al-V

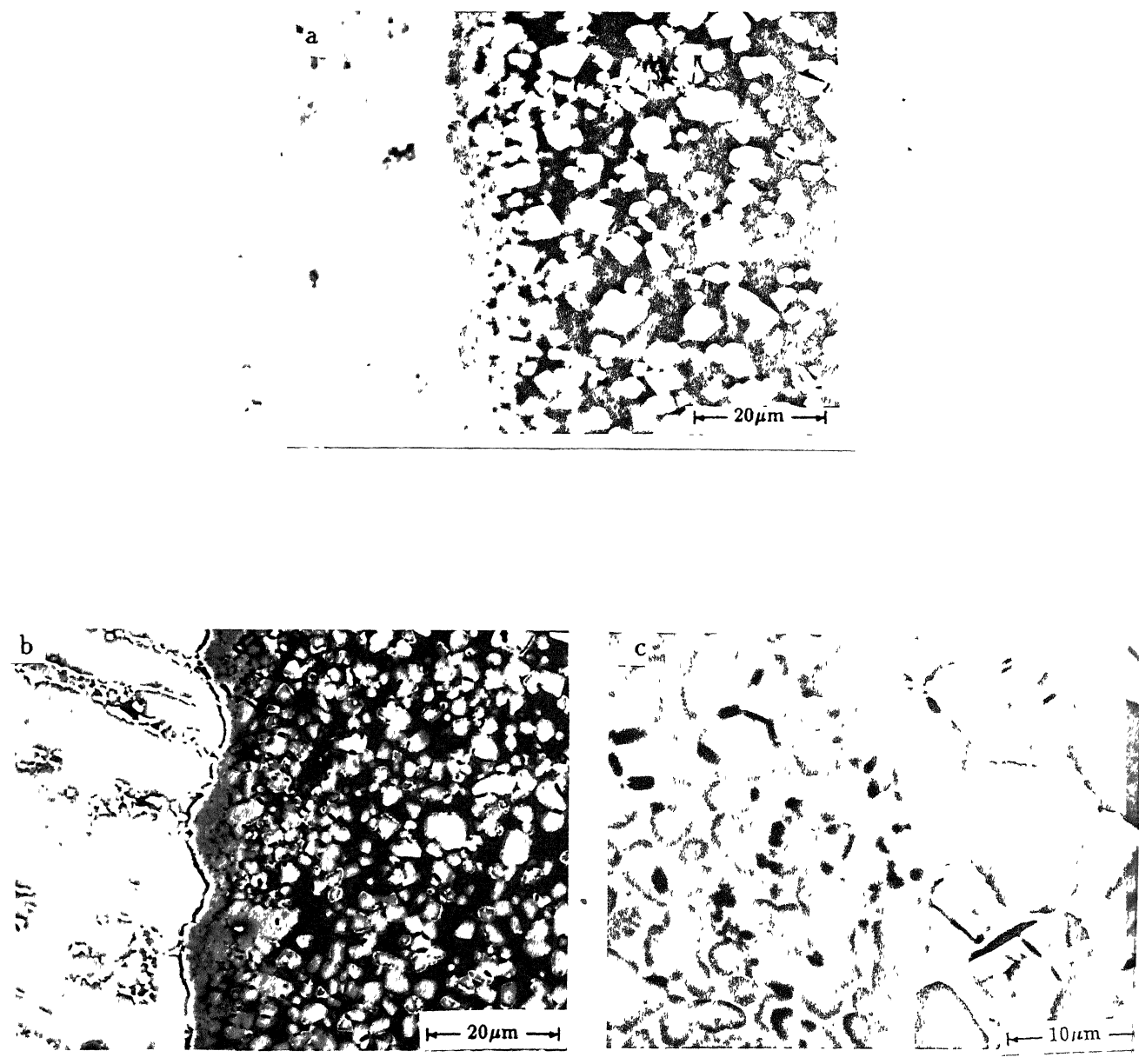


Figure 5.17 SEM micrographs showing the nature of reaction interface and reaction layer in TiAl_3 base compound with increase in distance from the reaction interface;

- (a) Ti/Al couple reacted at 973 K (700°C) for 7200 s (2 hr)
- (b) Ti-Al-V alloy/Al couple reacted at 973 K (700°C) for 7200 s (2 hr)
- (c) Ti-Al-Mo-Zr-Si alloy/Al couple reacted at 1073K (800°C for 3600s (1hr).

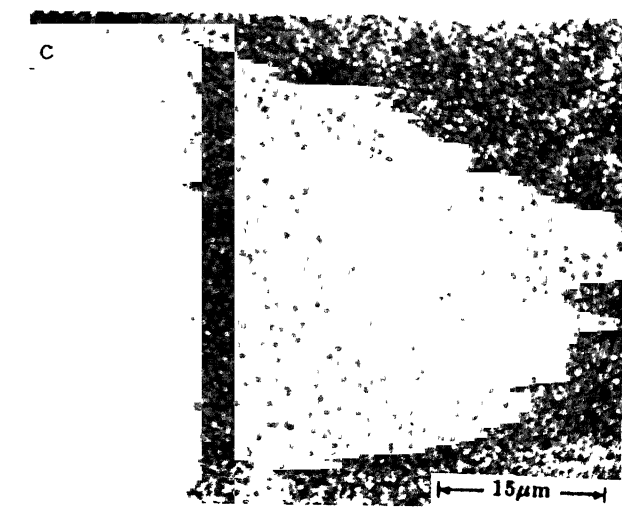
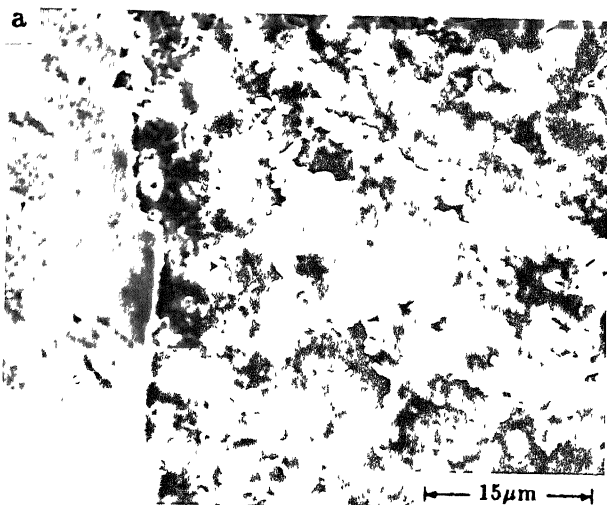


Figure 5.18 (a) Phases present adjacent to the reaction interface in Ti/Al couple reacted at 1073 K (800°C) for 3600 s (1 hr) showing the presence of Ti islands inside the reaction zone ahead of the reaction interface.

(b) X-ray dot mapping of the element Ti on the region shown in Figure - 5.18(a)

(c) X-ray dot mapping of the element Al on the region shown in Figure - 5.18(a).

alloy/Al and Ti-Al-Mo-Zr-Si alloy/Al couples appeared to be more prominent [Figures - 5.17(a) to 5.17(c)].

It appears from Figures-5.17(a)-5.17(c) that differential concentration of the alloying elements in α and β phases of two phase Ti-Al-V and Ti-Al-Mo-Zr-Si alloys leads to different times of reaction initiation in the two phases. As shown in higher magnification micrograph from Ti-Al-Mo-Zr-Si alloy/Al couple [Figure - 5.18(c)] reaction appears to start later in the α phase.

5.3.2 Morphological Features and Microstructural Details

of the Reaction Layer:

As presented in Section 5.1.3, presence of a continuous reaction layer was observed in the reaction zone as shown in Figures - 5.17(a) to 5.17(c). Compositional analysis of the reaction layer by EDS showed that it consisted of the $TiAl_3$ phase. It can be noticed that similar to the nature of the reaction interface, the nature of the reaction layer remained non-planar. In general, the Ti-side of the reaction layer was found to be intact [Figure - 5.17(a) to (c)], whereas, cracks and fissures were observed on its dispersed reaction domain side.

Inspite of being non-planar, the thickness of the reaction layer was found to be more or less constant across the entire length of reaction interface. As the reaction temperature increased, the thickness of reaction layer in pure Ti/Al couples

varied between $\sim 7 \mu\text{m} - 12 \mu\text{m}$. In contrast, in the case of Ti-Al-V alloy/Al and Ti-Al-Mo-Zr-Si alloy/Al couples, the thickness of the reaction layer varied from $\sim 3 \mu\text{m} - 8 \mu\text{m}$. Also, it was observed that at a given reaction temperature, the thickness of the reaction layer did not depend on the reaction time.

The nature of reaction layers of larger thickness ($\sim 12 \mu\text{m}$) is shown in Figures - 5.19(a) and 5.19(b) which were obtained from Ti/Al couples reacted at 973 K (700°C) for 14400 s (4 hr) and 1073 K (800°C) for 7200 s (2 hr) respectively. At higher reaction temperatures the reaction layer sometimes underwent its decohesion as shown in Figure - 5.19(b).

As shown in Figure-5.20, examination of the reaction layer under TEM revealed the substructural details of the TiAl_3 phase indicative of heavily dislocated region at many places. Several TiAl_3 grains were found to have planar defects such as stacking faults as well as some super dislocations.

5.3.3 Morphological Features and Microstructural

Details of the Dispersed Reaction Domain:

5.3.3.1 Sub-structural features of titanium aluminide particles:

As explained earlier, the dispersed reaction domain revealed presence of TiAl_3 particles in an Al matrix (Section 5.1.3, Figure - 5.11(a)). These aluminide particles were formed by the fragmentation of the reaction layer which consisted of heavily deformed regions consisting of planar defects such as stacking faults and super- dislocations. A magnified view of the

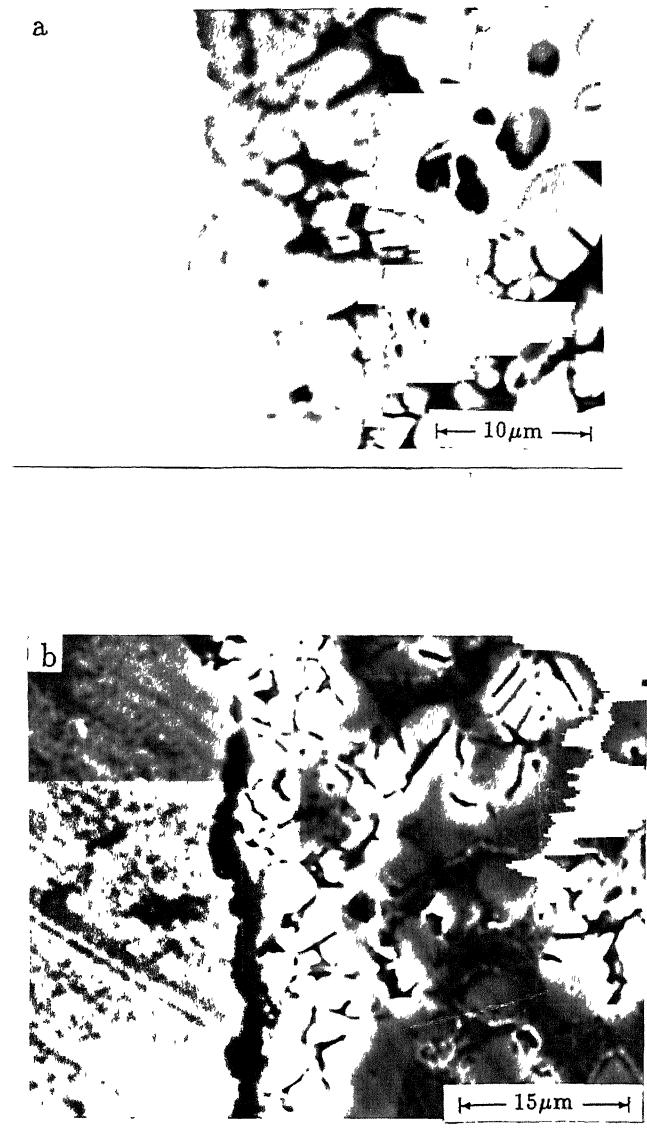


Figure 5.19 SEM micrographs showing the reaction layers of couples reacted at (a) 973 K (700°C) for 14400 s (4 hr) and (b) 1073 K (800°C) for 7200 s (2 hr); Figures (a) and (b) show the nature of cracking inside the reaction layer leading to its decohesion from Ti.

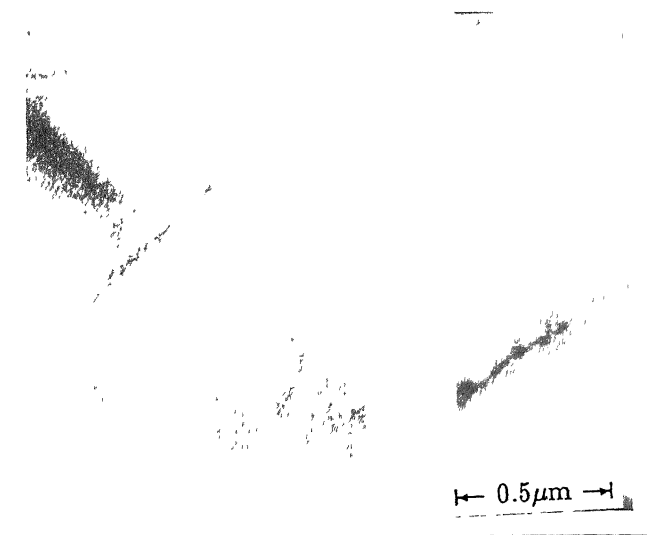


Figure 5.20

Bright field transmission electron micrograph of a region of the reaction layer formed in Ti/Al couples reacted at 1073 K (800°C) for 7200 s (2 hr).

TiAl_3 region in Al matrix shown in Figure - 5.10(a) is given in Figure 5.21(a). In the case of the reaction layers, the substructure of TiAl_3 particles also showed heavily dislocated regions. Other substructural features observed in TiAl_3 particles are shown in Figures - 5.21(b) and 5.21(c). Figure - 5.21(b) shows the presence of stacking faults inside a TiAl_3 particle of a pure Ti/Al couple reacted at 1073 K (800°C) for 3600 s (1 hr). TiAl_3 base particles belonging to reaction zones of Ti-Al-V alloy/Al and Ti-Al-Mo-Zr-Si alloy/Al couples also revealed similar stacking faults. Some regions of the TiAl_3 particles showed presence of moving dislocations originating from a grain boundary which in turn may result in the formation of slip traces. The dislocation arrays originating at a grain boundary 'GB' of the TiAl_3 particle can be observed from Figure - 5.21(c). This typical type of dislocation configuration is generally observed in materials undergoing continuous deformation where the partials become further and further separated [133].

5.3.3.2 Cracking and Fissuring in Titanium Aluminide Particles:

As shown in the scanning electron micrographs (Figures - 5.17, 5.19) a large number of the TiAl_3 particles present in the dispersed reaction domain showed numerous cracks and fissures inside them. This occurrence of cracks was found to be a common feature observed in TiAl_3 base particles synthesized in pure Ti/Al, Ti-Al-V alloy/Al and Ti-Al-Mo-Zr-Si alloy/Al couples reacted under almost all the reaction conditions though the extent of cracking in particles was found to be substantially lower in

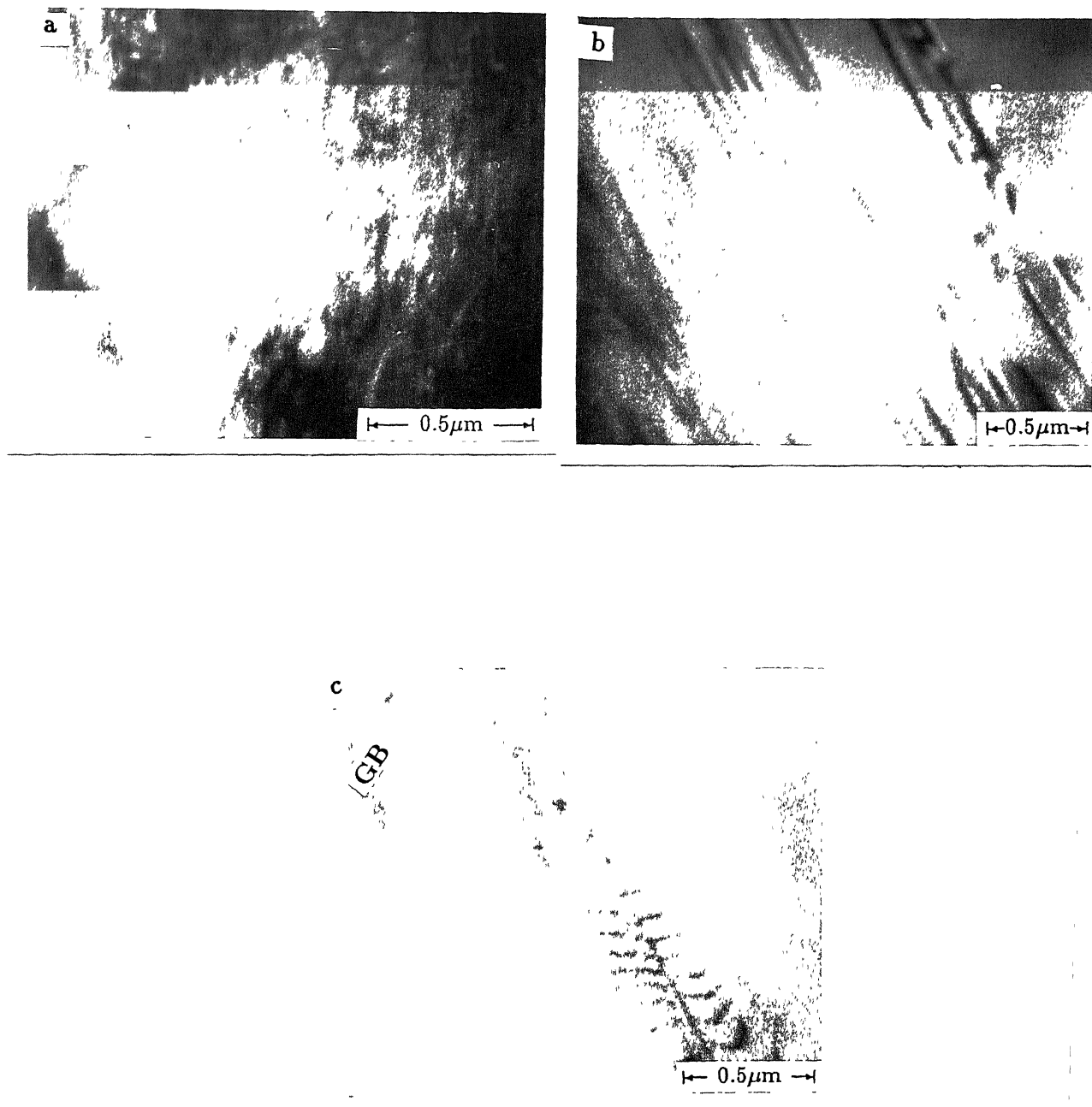


Figure 5.21 Bright field TEM micrographs of TiAl_3 particles of the dispersed reaction domain showing (a) heavily dislocated regions, (b) stacking faults and (c) dislocations originating at a grain boundary.

pure Ti/Al couples reacted at 1373 K (1100°C).

The cracks in general, were found to grow parallel to each other in different orientations (Figure - 5.22). These observations suggest that they perhaps propagated in specific crystallographic directions. The phenomena of cracking shown in Figure - 5.22 was found to be more prominent in the case of TiAl_3 alloy/Al couples [Figures - 5.22(a) to 5.22(c)].

The nature of cracking and the finer details of substructural features around the cracked regions of the TiAl_3 particles were further examined under TEM. The microstructural features around the cracked regions, as observed under TEM are shown in Figure - 5.23(a) to 5.23(c). Figure - 5.23(a) shows long straight edge dislocations (Regions A and B) terminating at a crack inside a TiAl_3 particle. Similarly, some dislocations of mixed nature (Region C) were also observed [Figure - 5.23(a)]. Occasionally, dislocation arrays and network configuration were also observed in regions surrounding the cracks [Figures - 5.23(b) and 5.23(c)]. The nature of such dislocation networks near a TiAl_3 /Al interface can be seen in Figure - 5.23(b). Similarly, the crack configuration in the vicinity of heavily deformed regions of a TiAl_3 particle is seen in Figure - 5.23(c). Quite often, cracks changed crystallographic directions of their propagation as evident from the segments AB, BC and CD in Figure - 5.23(c).

5.3.3.3 Particle shape changes in pure Ti/Al couples:

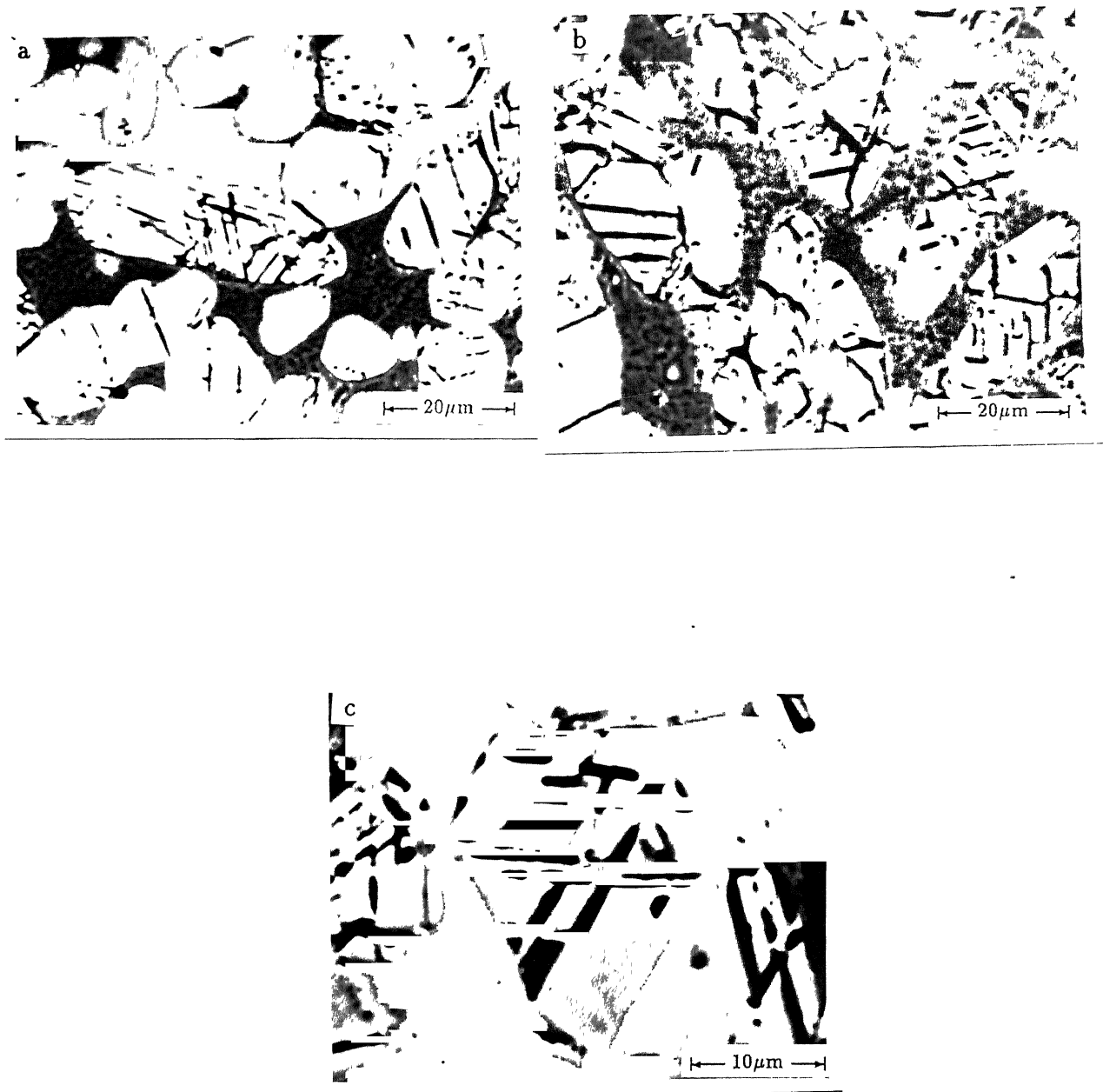


Figure 5.22 SEM micrographs showing the nature of cracking inside the TiAl_3 base particles in the reaction zones of (a) Ti/Al , (b) Ti-Al-V alloy/ Al and (c) Ti-Al-Mo-Zr-Si alloy/ Al couples reacted at 1073 K (800°C) for 7200 s (2 hr).

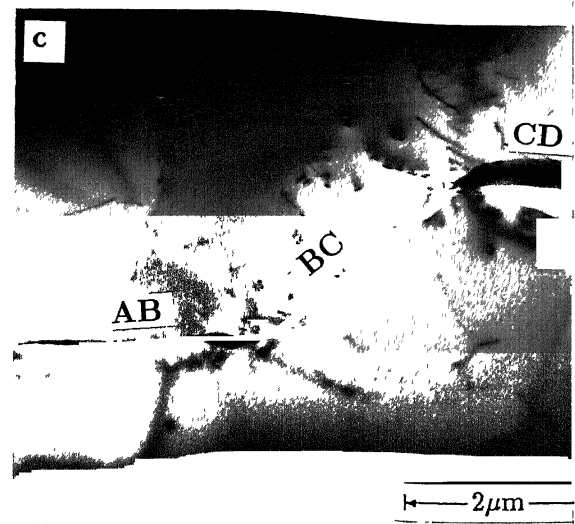
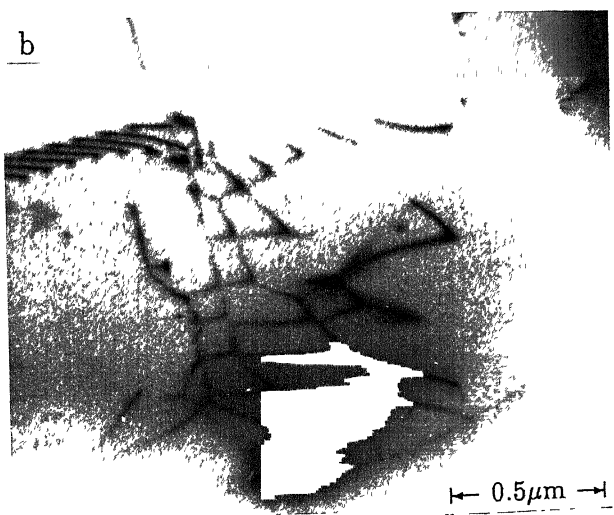
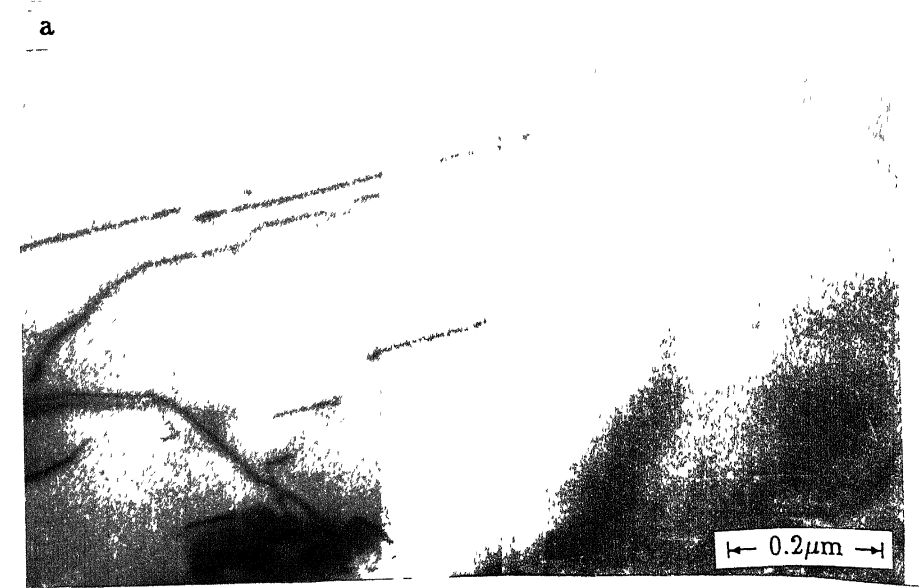


Figure 5.23 Bright field TEM micrographs of $TiAl_3$ particles inside the reaction zones showing the substructural features adjacent to cracked regions in Ti/Al couples reacted at 1073 K ($800^\circ C$) for 7200 s (2 hr)

(a) long straight edge dislocations regions A and B

(b) and (c) dislocation arrays and network configurations inside $TiAl_3$

(c) crack configuration.

Aluminide particles in the dispersed reaction domain were found to have either round smooth surfaces or flat surfaces having sharp angular turns. However, the population of particles possessing these two contrasting morphological features varied with distance from the reaction interface. The changes associated with the shapes of $TiAl_3$ particles of Ti/Al couples are presented in this section.

Typical SEM view of $TiAl_3$ particles in couples reacted at 1073 K ($800^{\circ}C$) for 3600 s (1 hr) at different distances from the reaction interface are shown in Figures - 5.24(a) to 5.24(c).

In general, it was observed that about 75-80% of the particles near the reaction interface had smooth and round surfaces while the percentage of particles having these characteristics decreased to about 50% in the mid region of the dispersed reaction domain and to about 20-25% at the end of the reaction zone. Similarly, aspect ratio of particles having flat angular surface varied between 1.1 to 1.8 with the number of particles of higher aspect ratio increasing with distance from the reaction interface.

SEM micrographs of the mid regions of Ti/Al couples reacted at 973 K, 1073 K, 1173 K and 1273 K are shown in Figures - 5.25(a) to 5.25(d). It can be observed from these figures that the reaction temperature did not significantly influence specific morphological features of $TiAl_3$ particles at a specific normalized distance, i.e. distance/reaction zone thickness.

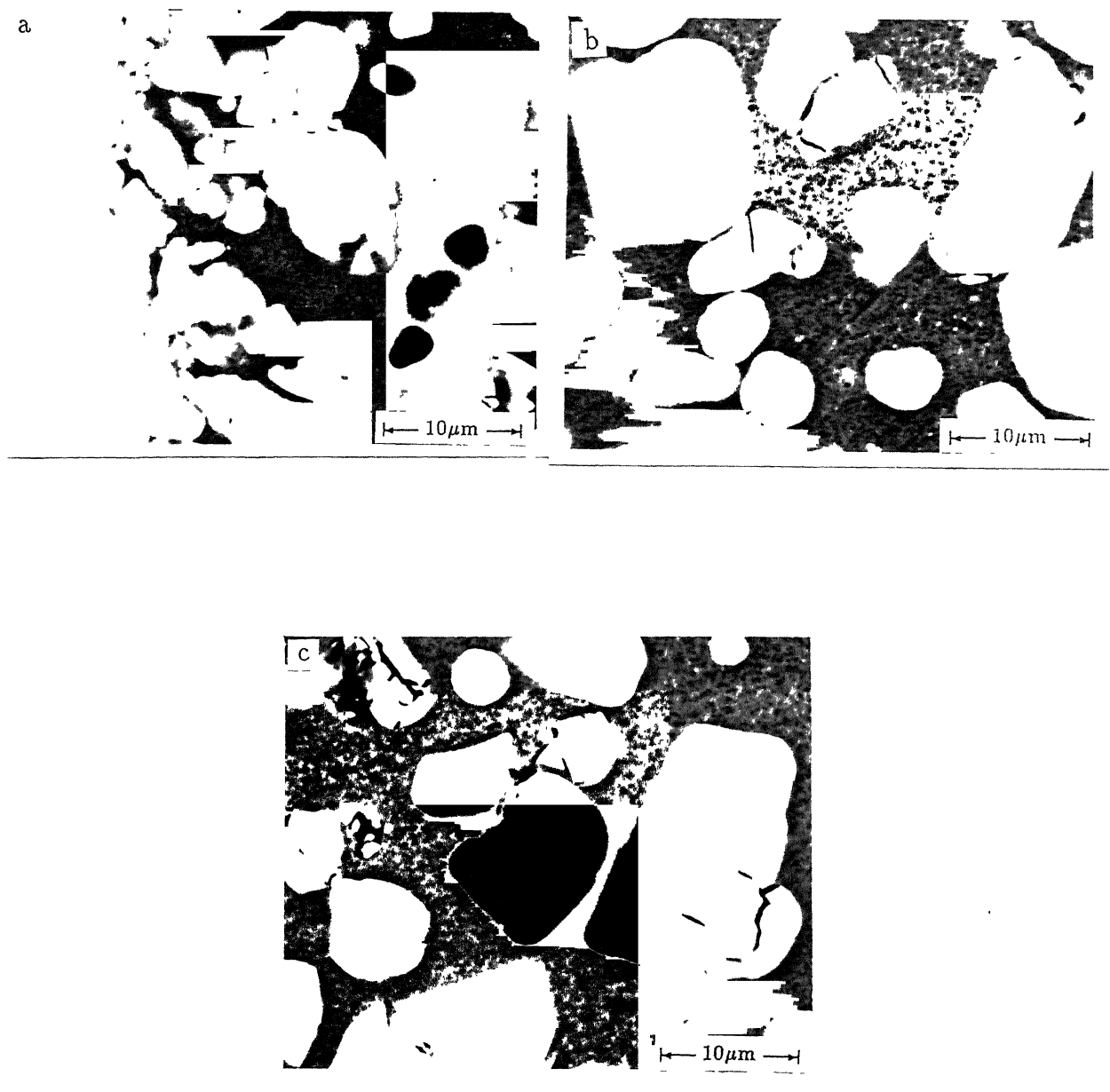


Figure 5.24 SEM microstructures showing changes in the particle size and morphology of TiAl_3 base particles at varying distances from the reaction interface in Ti/Al couples reacted at 1073 K (800°C) for 3600 s (1 hr).

(a) adjacent to the interface, (b) 0.4 mm and (c) 1.0 mm from the reaction interface.

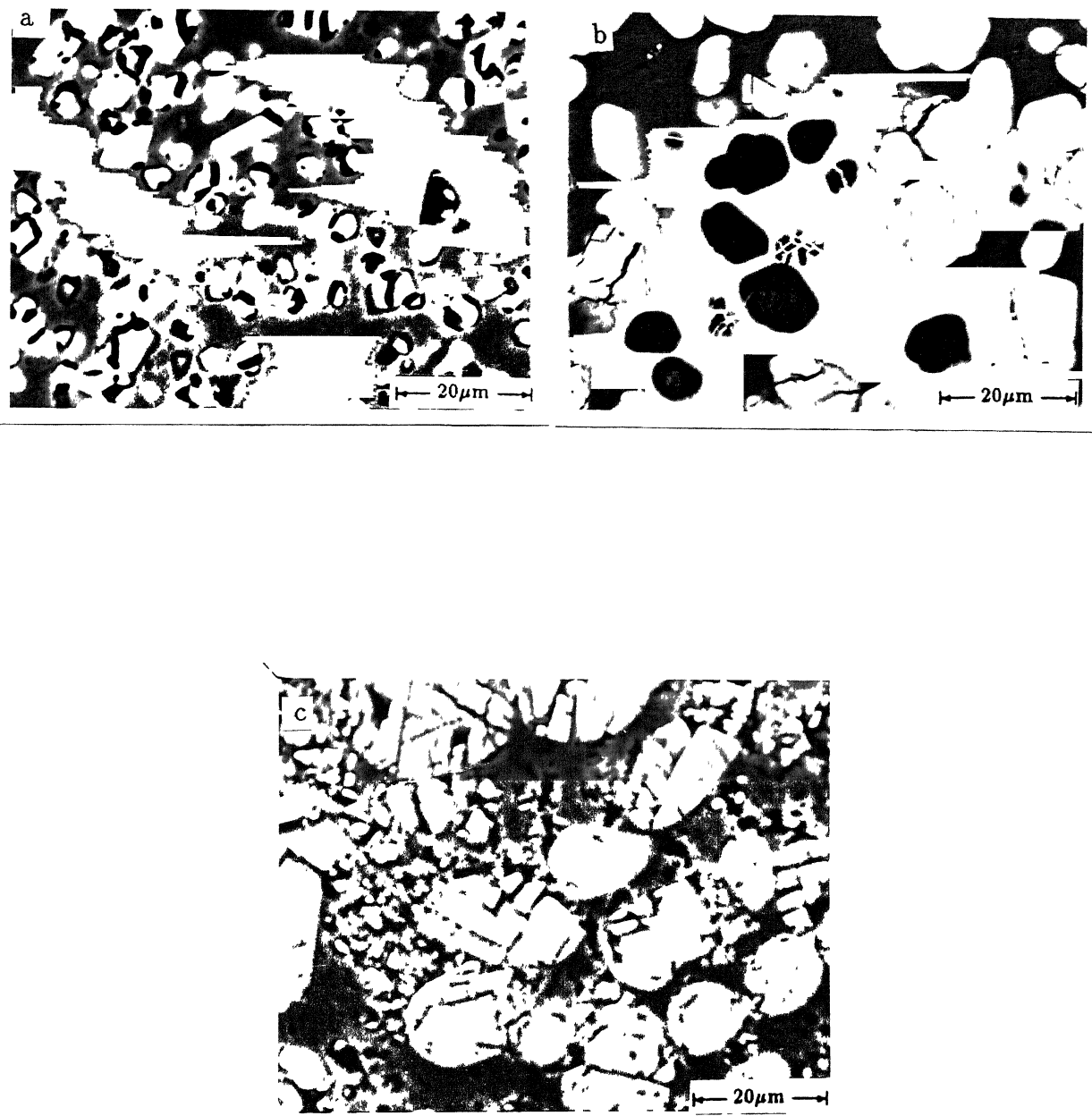


Figure 5.25 SEM micrographs showing the effect of reaction temperature on the particle size and morphology of TiAl_3 formed in Ti/Al couples reacted for 3600 s (1 hr) at (a) 973 K (700°C), (b) 1073 K (800°C), (c) 1173 K (900°C), (d) 1273 K (1000°C) and (e) 1373 K (1100°C).

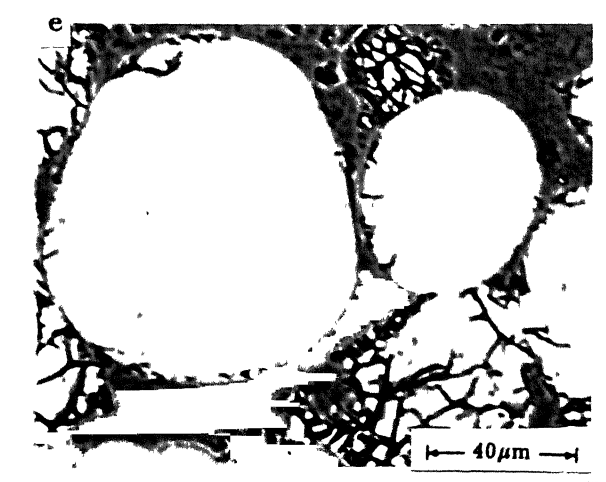
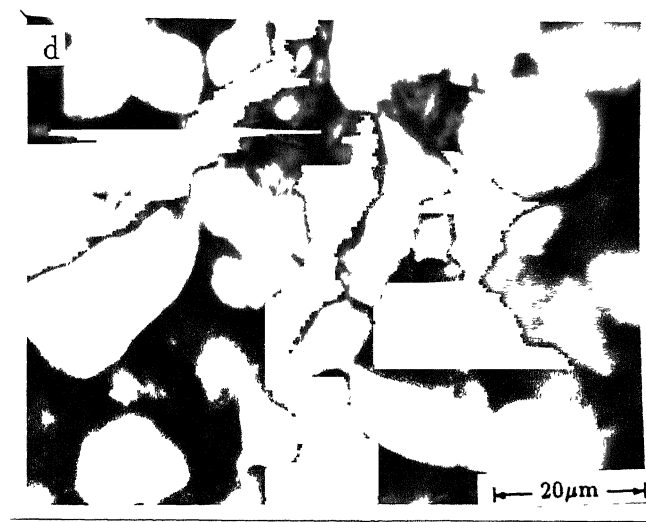


Figure 5.25 SEM micrographs showing the effect of reaction temperature on the particle size and morphology of TiAl₃ formed in Ti/Al couples reacted for 3600 s (1 hr) at (a) 973 K (700°C), (b) 1073 K (800°C), (c) 1173 K (900°C), (d) 1273 K (1000°C) and (e) 1373 K (1100°C).

At the reaction temperature of 1373 K (1100°C), distinctly large sized aluminide particles were observed [Figure - 5.25(e)] in the reaction domain. However, the population of particles having angular surfaces at any distance from the reaction interface was found to be less than 10%.

5.3.3.4 Particle shape in Ti-Al-V alloy/Al and Ti-Al-Mo-Zr-Si alloy/Al reaction couples:

The particle shape variation as a function of distance from the reaction interface has been shown in Figures - 5.26(a) to 5.26(c) and 5.27(a) to 5.27(c) for Ti-Al-V alloy/Al and Ti-Al-Mo-Zr-Si alloy/Al couples respectively which were reacted at 1073 K (800°C) for 7200 s (2 hr). In contrast to the morphology of unalloyed TiAl_3 formed in the case of pure Ti/Al couples, morphology of TiAl_3 base compounds formed in Ti alloy/Al couples containing V or (Mo + Zr + Si) was found to be significantly different. Optical micrographs of dispersed reaction domain in Ti-Al-V alloy/Al and Ti-Al-Mo-Zr-Si alloy/Al couples reacted at 1073 K for 7200 s are shown in Figure - 5.28(a). In contrast to the morphology of particles in pure Ti/Al couples, the particles in both the alloy couples had aspect ratios ranging from 1.1-2.3 in Ti-Al-V alloy/Al couple and from 1.1-4.6 in Ti-Al-Mo-Zr-Si alloy/Al couple. Also, the percentage of particles having angular surfaces and sharp edges was significantly different than those found in Ti/Al couples.

As discussed in the previous section, the particles

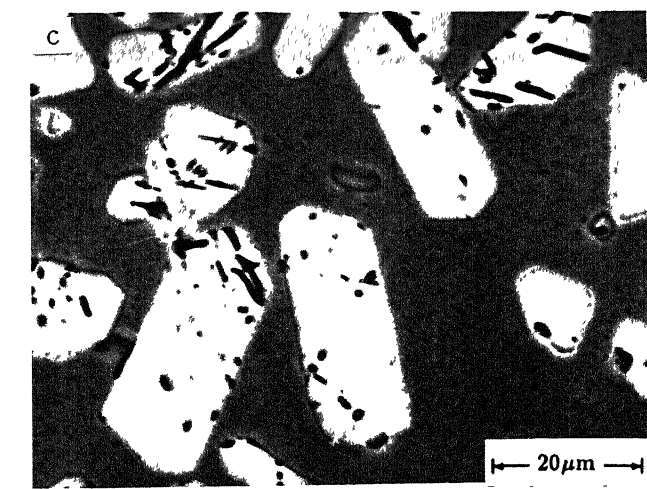
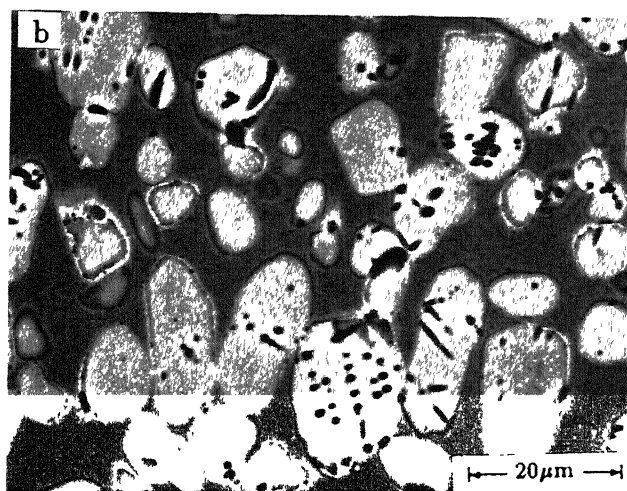
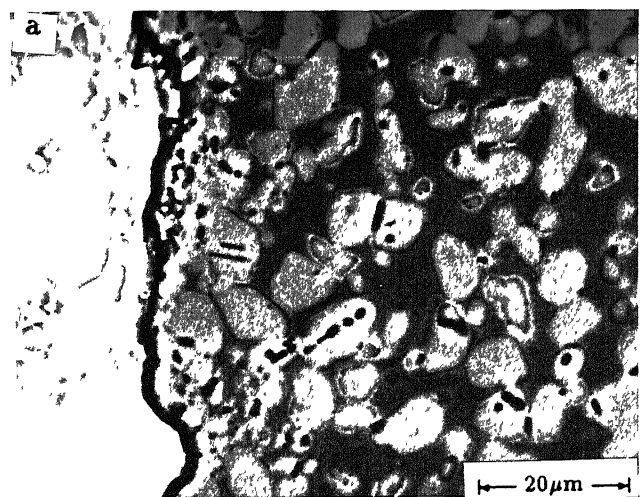


Figure 5.26 SEM micrograph showing the variation in particle size and morphology of vanadium containing $TiAl_3$ based compound formed in Ti-Al-V alloy/Al couple as a function of distance from the interface in couples reacted at 1073 K (800°C) for 7200 s (2 hr) (a) adjacent to the interface, (b) 0.4 mm and (c) 1.6 mm from the reaction interface.

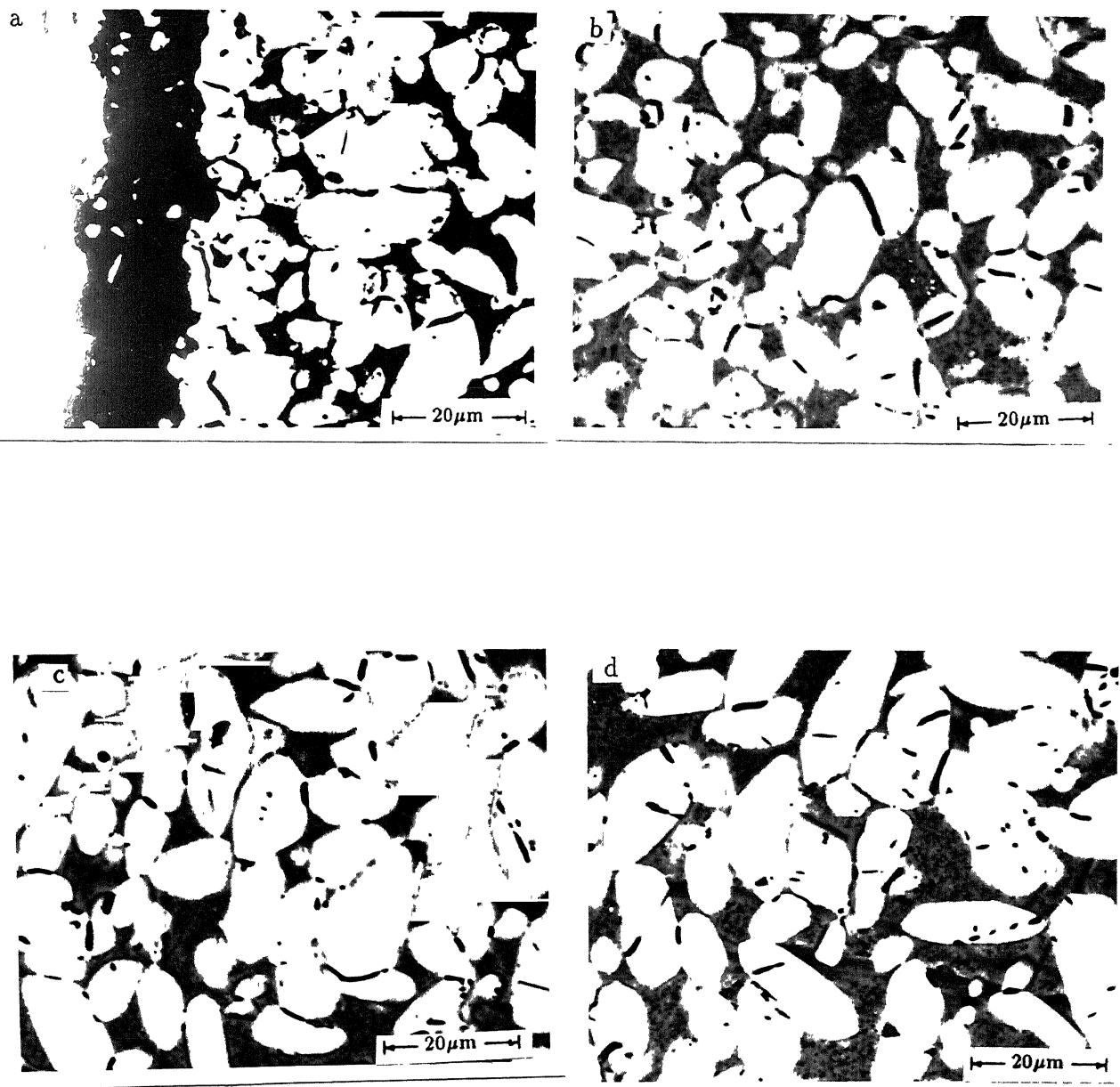


Figure 5.27 SEM micrograph showing the variation in particle size and morphology of molybdenum, zirconium and silicon containing TiAl_3 based compound formed in Ti-Al-Mo-Zr-Si alloy/Al couple as a function of distance from the reaction interface in couples reacted at 1073 K (800°C) for 7200 s (2 hr):
(a) adjacent to the interface, (b) 0.2 mm,
(c) 0.4 mm, (d) 0.8 mm, (e) 1.6 mm, (f) 2.4 mm
and (g) 2.8 mm.

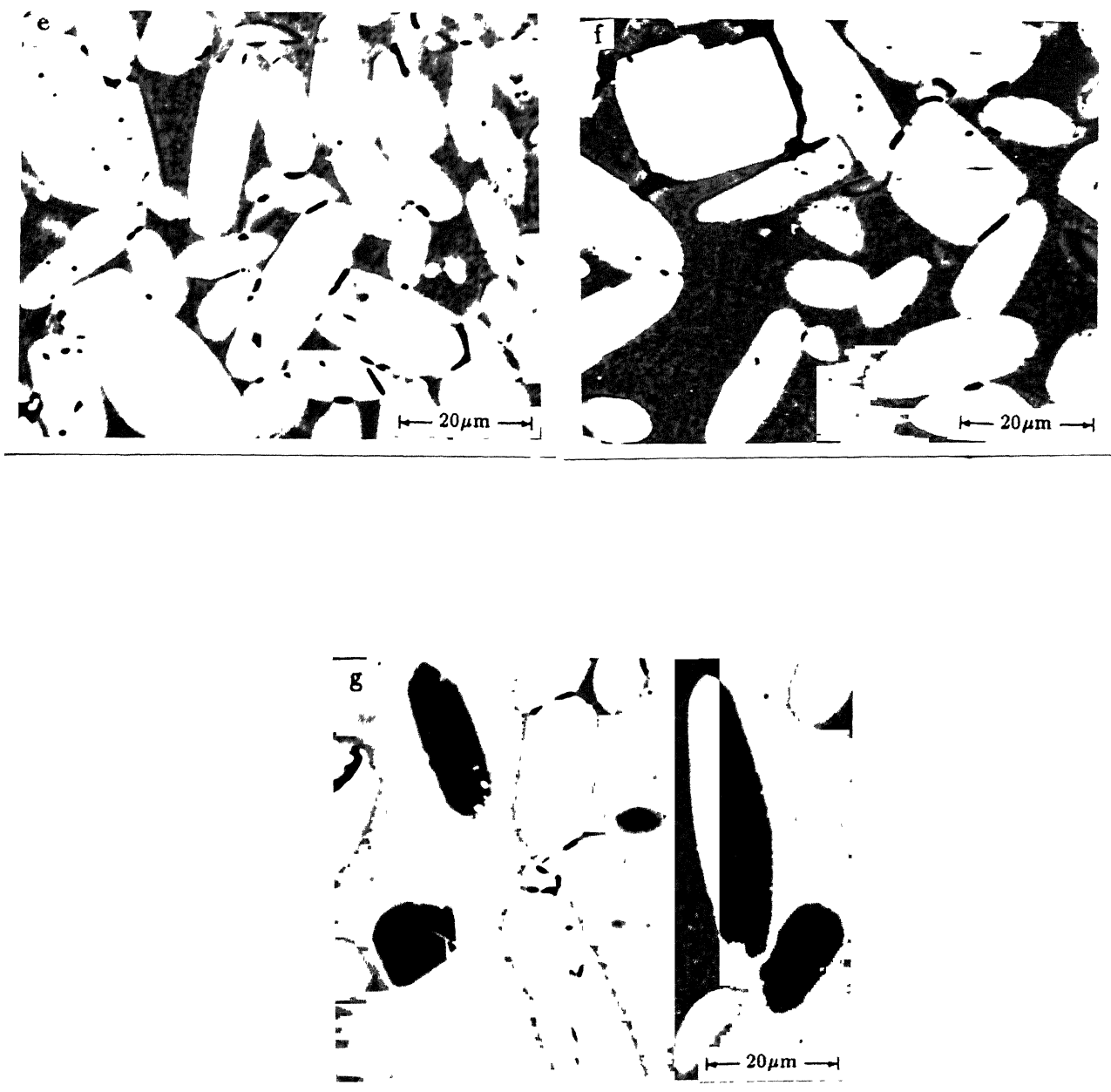


Figure 5.27 SEM micrograph showing the variation in particle size and morphology of molybdenum, zirconium and silicon containing TiAl_3 based compound formed in Ti-Al-Mo-Zr-Si alloy/Al couple as a function of distance from the reaction interface in couples reacted at 1073 K (800°C) for 7200 s (2 hr):
(a) adjacent to the interface, (b) 0.2 mm,
(c) 0.4 mm, (d) 0.8 mm, (e) 1.6 mm, (f) 2.4 mm
and (g) 2.8 mm.

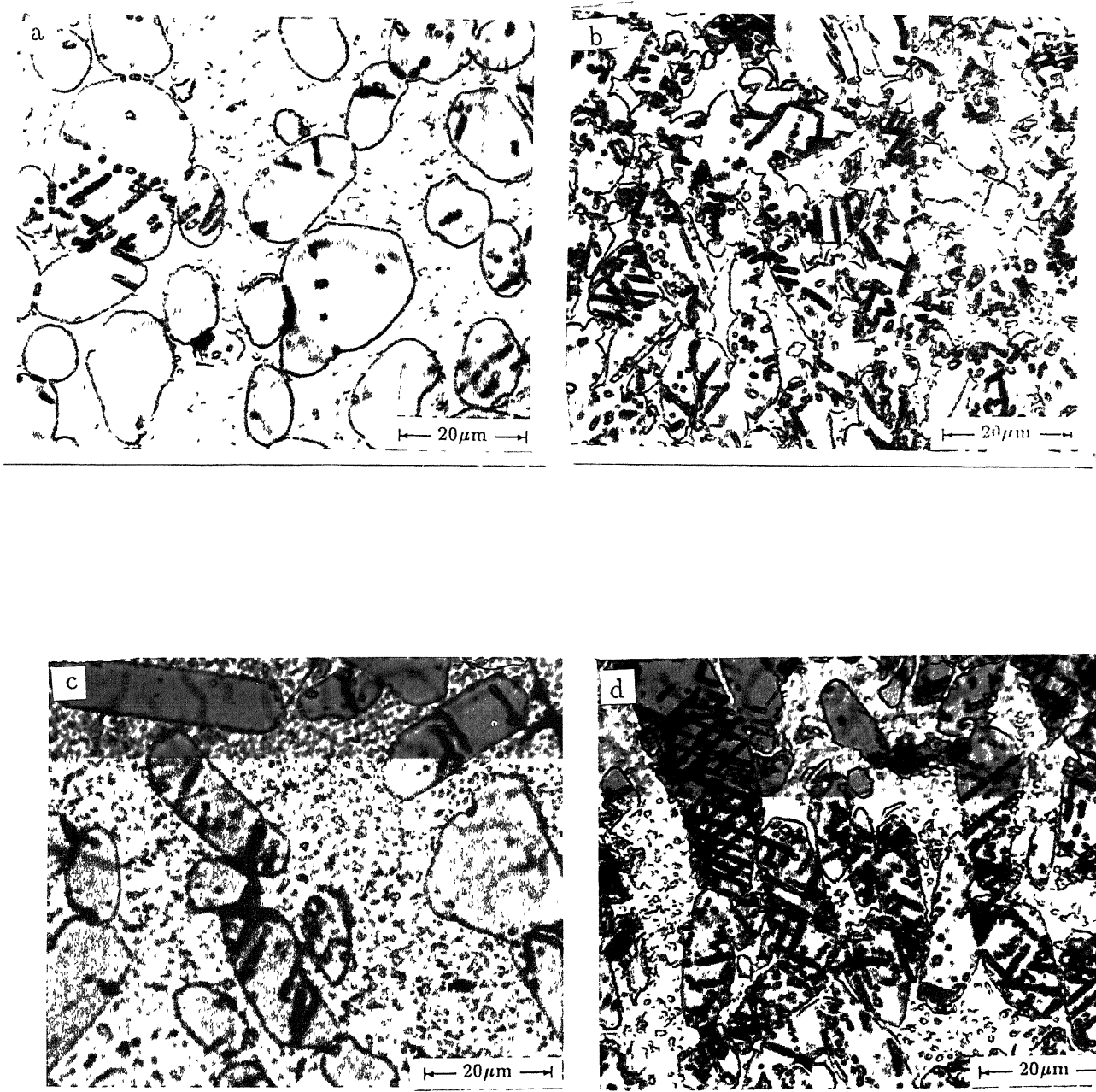


Figure 5.28

Optical micrographs of the dispersed reaction domain reaction zones formed in Ti alloy/Al couples reacted at 1073 K (800°C) for 7200 s (2 hr); Near the reaction interface: (a) and (b) Ti-Al-V alloy/Al couple and (b) Ti-Al-Mo-Zr-Si alloy/Al; Away from the reaction interface: (c) Ti-Al-V alloy/Al couple and (d) Ti-Al-Mo-Zr-Si alloy/Al couple.

having smooth and round surfaces were found to be about 75%, 50% and 20-25% near the reaction layer, mid region and the end of the dispersed reaction domain respectively in Ti/Al couples. However, these values were found to be between 20-25% upto the mid region and <1% at the end in Ti-Al-V alloy/Al couples. Similarly, about 10-15% particles had round and smooth surfaces upto mid region in Ti-Al-Mo-Zr-Si alloy/Al couples and <1% towards the end of the dispersed reaction domain.

To describe these changes quantitatively, the variation of aspect ratio of $TiAl_3$ base particles with distance from the reaction interface was measured. These results are presented in Figure - 5.29. As shown in the figure, the mean aspect ratio of particles varied from 1.1 to 2.3 in Ti-Al-V alloy/Al couples. More pronounced changes occurred in the case of Ti-Al-Mo-Zr-Si alloy/Al couples which showed the aspect ratio variation from 1.1 to 4.6 as the distance from the reaction interface increased to the end of the reaction zone.

As observed in the optical micrographs shown in Figures - 5.28(a) to 5.28(d), the $TiAl_3$ base particles had round corners and smoother surfaces near to the reaction interface. In contrast to the V containing $TiAl_3$, the extent of such changes in (Mo + Zr + Si) containing $TiAl_3$ particles was found to be more significant.

The variation of $TiAl_3$ base particle shape and morphology with reaction temperature has been shown in Figure - 5.30(a) and 5.30(b) for Ti-Al-Mo-Zr-Si alloy/Al couples . The figure reveals that reaction temperature does not result in any

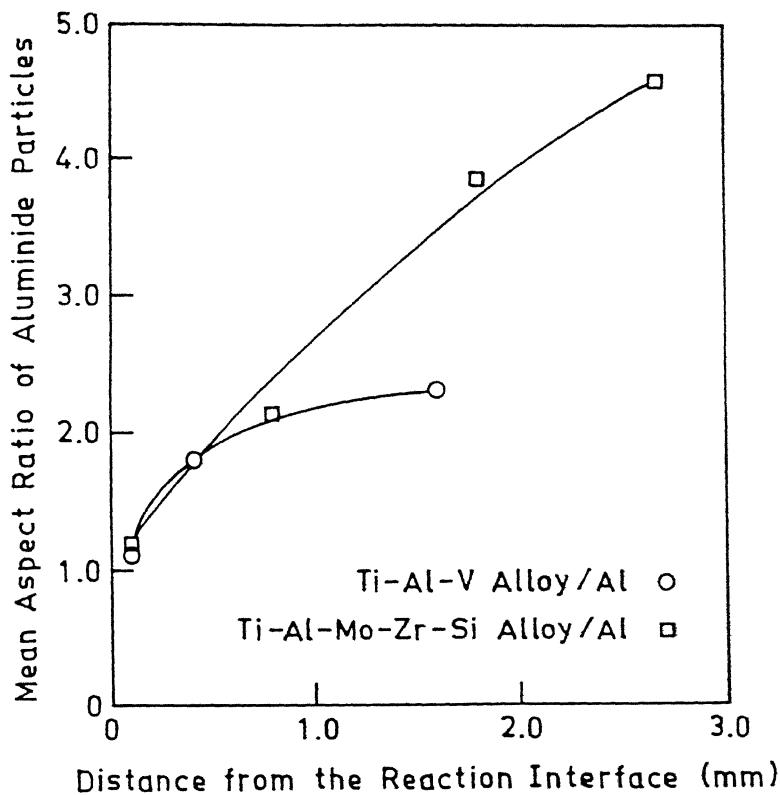


Figure 5.29 Variation of aspect ratio of TiAl_3 base particles formed in Ti-Al-V alloy/Al and Ti-Al-Mo-Zr-Si alloy/Al couples with distance from the reaction interface of couples reacted at 1073 K (800°C) for 7200 s (2 hr).

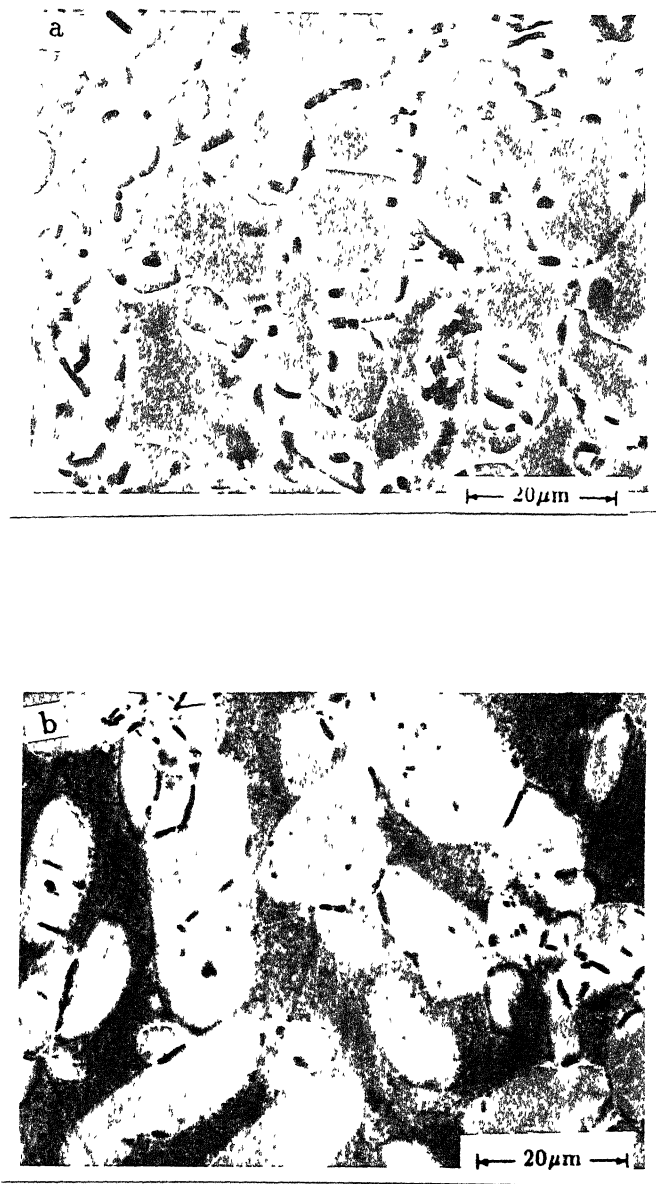


Figure 5.30 SEM micrographs showing the effect of reaction temperature on the particle size of TiAl_3 base compound formed in Ti-Al-Mo-Zr-Si alloy/Al couples; (a) reacted at 973 K (700°C) for 7200 s (2 hr) and (b) reacted at 1073 K (800°C) for 7200 s (2 hr).

shape changes in the $TiAl_3$ base particles similar to the changes observed in case of pure Ti/Al couples. Even in the case of $TiAl_3$ base particles formed in both the alloy couples, increase in reaction temperature resulted only in increase in particle size.

5.3.3.5 Volume fraction of aluminide particles in the dispersed reaction domain as a function of distance from the reaction interface:

Quantitative metallographic measurements done on pure Ti/Al as well as Ti-Al-V alloy/Al and Ti-Al-Mo-Zr-Si alloy/Al reaction couples revealed that volume fraction of titanium aluminide particles systematically varied with distance from the reaction interface.

The variation of volume fraction of $TiAl_3$ particles, V_v as a function of distance, x , from the reaction interface in pure Ti/Al couples reacted for 3600 s (1 hr) at reaction temperatures of 973 K ($700^{\circ}C$), 1073 K ($800^{\circ}C$) and 1173 K ($900^{\circ}C$) respectively is shown in Figures - 5.31(a) to 5.31(c). Similarly, plots showing the variation of volume fraction, V_v of $TiAl_3$ base compound particles in Ti-Al-V alloy/Al and Ti-Al-Mo-Zr-Si alloy/Al couples reacted at 1073 K ($800^{\circ}C$) for 7200 s (2 hr) as a function of distance, x , have been shown in Figure - 5.32(b) and 5.32(c). For the purpose of comparison the plot obtained in the case of pure Ti/Al couple reacted under identical reaction conditions has also been included in Figure - 5.32(a). Similar data was obtained for couples prepared at other reaction conditions. From the Figures - 5.31 and 5.32 as well as from the data obtained from

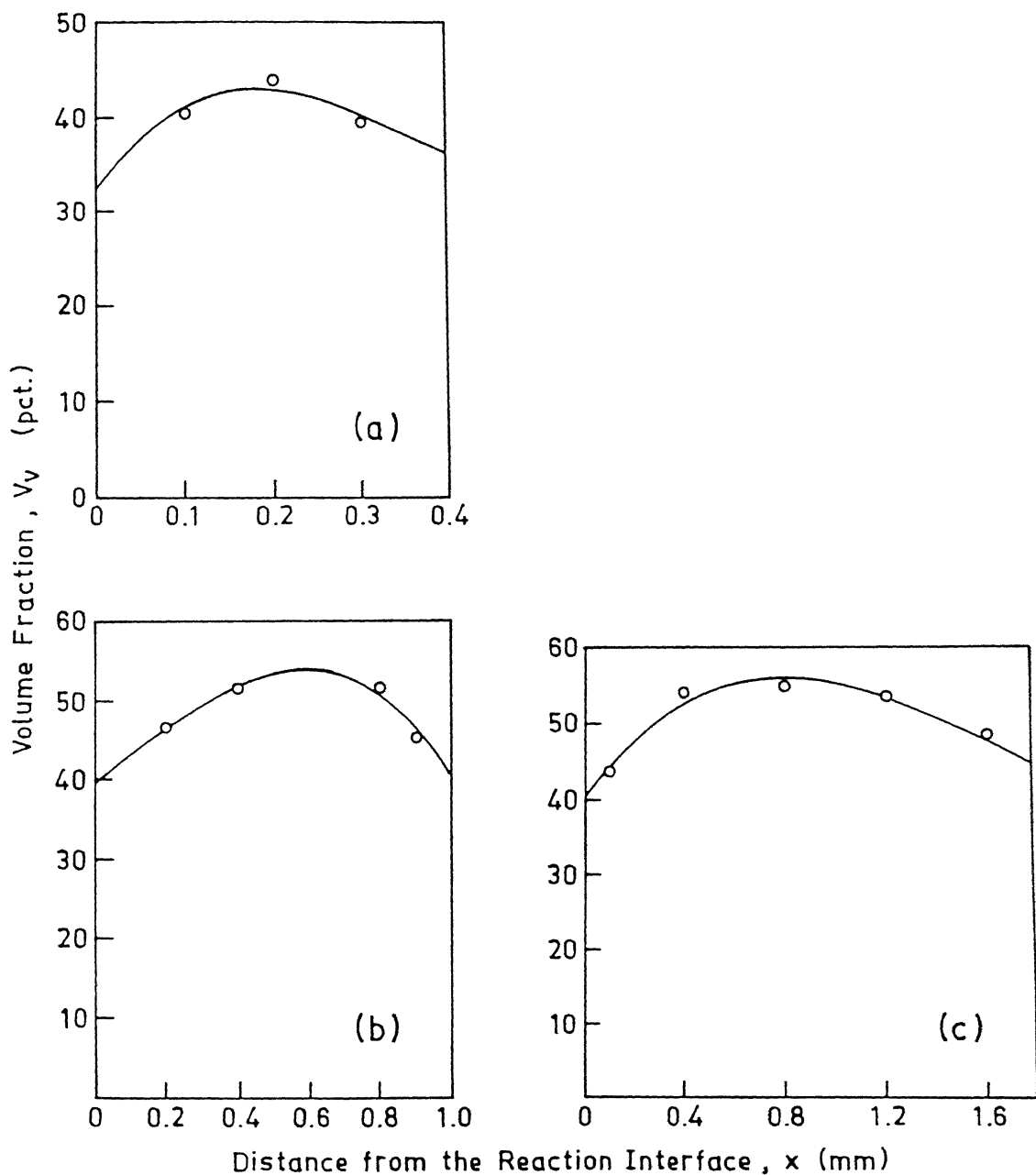


Figure 5.31 Variation of volume fraction of TiAl_3 in the reaction zone as a function of distance from the reaction interface in Ti/Al couples reacted for 3600 s at (a) 973 K (700°C), (b) 1073 K (800°C) and (c) 1173 K (900°C).

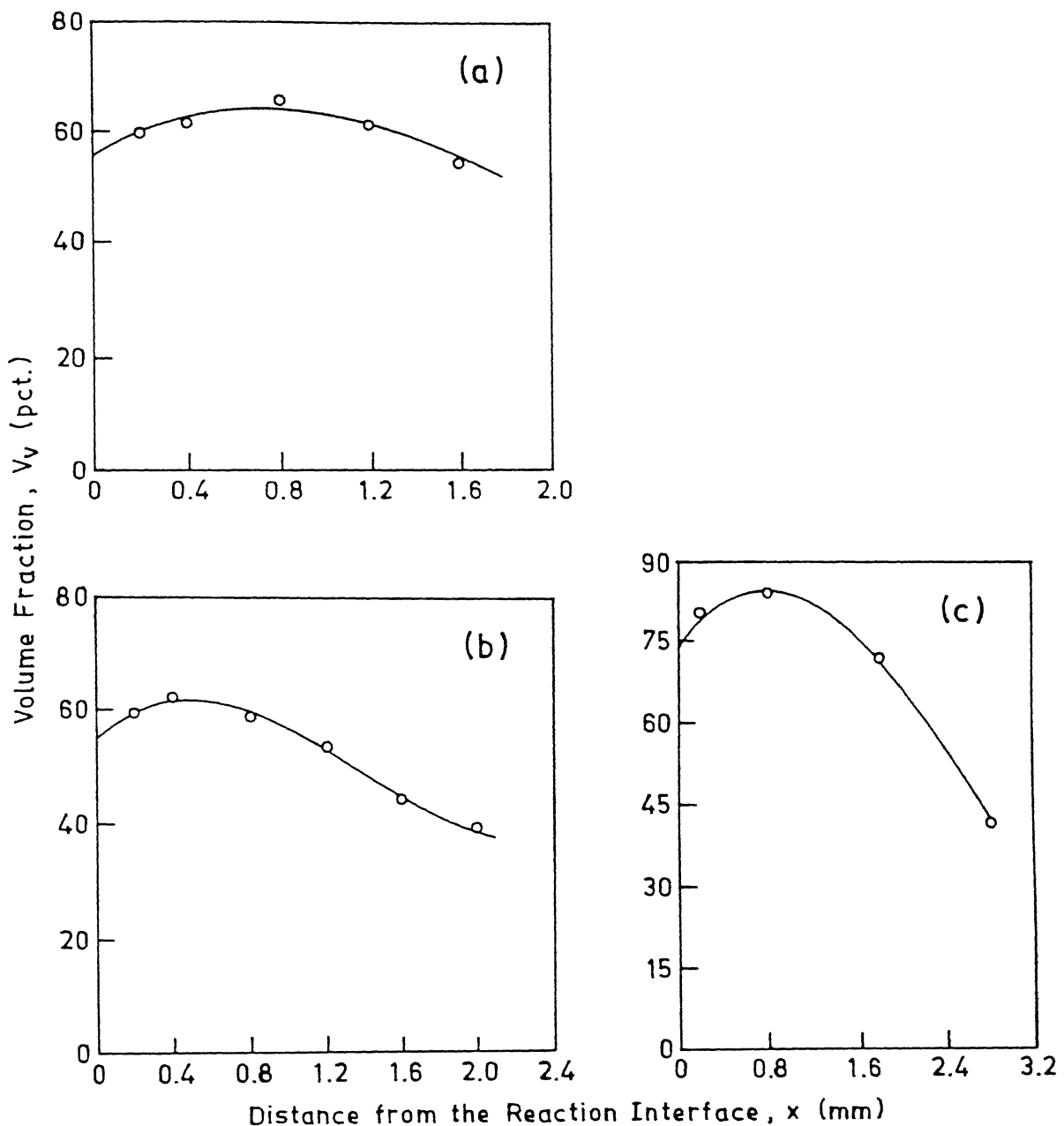


Figure 5.32 Variation of volume fraction of TiAl_3 base compounds in the reaction zone as a function of distance from the reaction interface in couples reacted at 1073 K (800°C) for 7200 s (2 hr) in (a) Ti/Al , (b) $\text{Ti-Al-V alloy}/\text{Al}$ and (c) $\text{Ti-Al-Mo-Zr-Si alloy}/\text{Al}$.

other reacted couples, it was noted that the volume fraction of $TiAl_3$ particles in the dispersed reaction domain systematically varied with the distance from the reaction interface going through a maximum in each case. In addition, the distance at which the maximum in the volume fraction of $TiAl_3$ particles occurred was found to be characteristic of specific reaction temperature, time and the reaction couple used.

The distance at which maximum volume fraction occurred, the reaction zone thickness, the maximum and the minimum values of particle volume fractions in the dispersed reaction domain are shown in Table - 5.8 for both Ti/Al couples as well as Ti alloy/Al couples.

Using the method of least squares fit, the variation of volume fractions of $TiAl_3$ particles, v_v with distance x from the reaction interface for different reaction conditions was approximated as a polynomial function of 3rd order. The coefficients obtained for these polynomial functions for different reacted couples are given in Table 5.9 (a),(b). The variation of maximum and minimum volume fractions of aluminide particles in pure Ti/Al couples function of reaction time are plotted in Figure - 5.33. It can be observed from this figure that both maximum and minimum volume fractions increased with reaction time at the reaction temperatures of 973 K ($700^{\circ}C$), 1073 K ($800^{\circ}C$) and 1173 K ($900^{\circ}C$). Similarly, the distance at which peak in volume fraction

Table-5.8 : The reaction zone thickness, distance at peak volume fraction of $TiAl_3$ and the maximum and minimum volume fractions of $TiAl_3$ in the dispersed reaction domain of pure Ti/Al, Ti-Al-V/Al and Ti-Al-Mo-Zr-Si/Al couples reacted under various conditions

Couple	Reaction conditions		Reaction zone	Distance at peak	Volume fraction of $TiAl_3$ (%)	
	(Temperature, Time)		thickness (mm)	volume fraction	Maximum (mm)	Minimum (mm)
ure Ti/Al	973 K,	3600 s	0.4	0.177	43.00	36.3
	973 K,	7200 s	0.8	0.314	53.19	40.02
	973 K,	10800 s	1.7	0.933	57.08	46.55
	973 K,	14400 s	2.3	1.138	63.19	42.43
	1073 K,	3600 s	1.1	0.585	54.08	32.04
	1073 K,	7200 s	1.80	0.7	64.32	51.90
	1073 K,	10800 s	2.19	0.966	67.99	54.80
	1173 K,	900 s	0.62	0.388	40.00	35.20
	1173 K,	1800 s	1.12	0.574	52.96	47.14
	1173 K,	3600 s	1.74	0.8	56.34	45.67
Ti-Al-V/Al	973 K,	3600 s	0.4	0.163	49.97	44.65
	973 K,	7200 s	1.3	0.315	43.57	34.41
	1073 K,	3600 s	1.2	0.4	56.28	51.05
	1073 K,	7200 s	2.1	0.581	67.12	52.06
	1173 K,	3600 s	1.48	0.63	70.83	69.9
Ti-Al-Mo-Zr-Si/Al	973 K,	3600 s	0.42	0.237	51.54	42.09
	973 K,	7200 s	1.3	0.315	43.57	34.41
	1073 K,	3600 s	1.2	0.4	56.28	51.05
	1073 K,	7200 s	2.1	0.581	64.12	52.06
	1173 K,	3600 s	3.20	0.55	74.58	66.32

able-5.9(a): Polynomial expressions representing the variation in volume fraction (V_v) of $TiAl_3$ in the reaction zone with distance from the reaction interface (x) in pure Ti/Al couples reacted at different conditions

Reaction conditions Temperature, Time)	Polynomial expression for V_v
973 K, 3600 s	$483.3 x^3 - 505.3 x^2 + 134.8 x + 32.3$
973 K, 7200 s	$39.6 x^3 - 104.6 x^2 + 50.2 x^2 + 46.5$
973 K, 10800 s	$0.3 x^3 - 17.6 x^2 + 30.9 x - 43.$
973 K, 14400 s	$-0.5 x^3 - 12.8 x^2 + 30.9 x - 45.4$
1073 K, 3600 s	$-39.2 x^3 + 4.5 x^2 + 35.6 x + 39.5$
1073 K, 7200 s	$3.3 x^3 - 21.4 x^2 + 25.9 x + 55.0$
1073 K, 10800 s	$5.6 x^3 - 24.6 x^2 + 32.4 x + 54.6$
1173 K, 10800 s	$-5.3 x^3 - 7.4 x^2 + 13.8 x + 48.5$
1173 K, 3600 s	$7.4 x^3 - 36.8 x^2 - 144.8 x + 40.2$

ble-5.9(b): Polynomial expressions representing the variation in volume fraction (V_v) of $TiAl_3$ base particles from the reaction interface in Ti-Al-V alloy/Al and Ti-Al-Mo-Zr-Si alloy/Al couples

Couple	Reaction condition (Temperature, Time)	Polynomial expression for V_v
i-Al-V/Al	973 K, 3600 s	$693.3x^3 - 633x^2 + 159.4x + 37.8$
	973 K, 7200 s	$20.5x^3 - 50.2x^2 + 26.7x + 39.5$
	1073 K, 3600 s	$16.1x^3 - 42.8x^2 + 28.0x + 50.9$
	1073 K, 7200 s	$9.3x^3 - 33.6x^2 + 27.2x + 57.5$
	1173 K, 3600 s	$16.9x^3 - 61.5x^2 + 58.6x + 63.1$
Ti-Al-Mo-Zr-Si/Al	973 K, 3600 s	$-224.0x^3 - 97.8x^2 + 87x + 39.4$
	973 K, 7200 s	$16.4x^3 - 43.2x^2 + 26.1x + 39.9$
	1073 K, 3600 s	$-21.2x^3 + 1.3x^2 + 38.8x + 68.9$
	1073 K, 7200 s	$2.80x^3 - 22.5x^2 + 29.9x + 73.9$
	1173 K, 3600 s	$2.5x^3 - 11.7x^2 + 10x + 72.2$

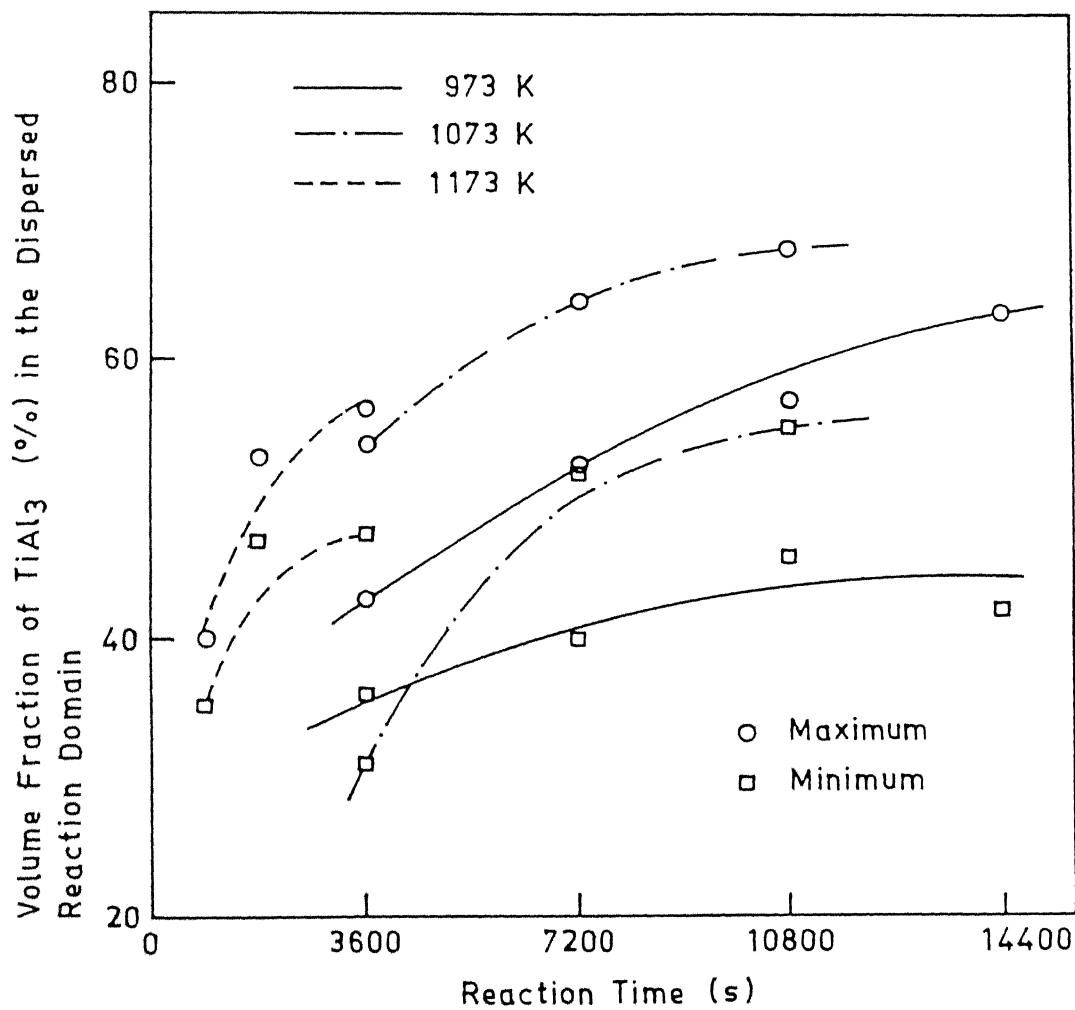


Figure 5.33 Variation of maximum and minimum volume fractions of aluminide particles as a function of reaction temperature and reaction time in pure Ti/Al couples.

occurred also increased with reaction time at a given reaction temperature (Figure - 5.34).

5.3.3.6 Variation of average volume fraction of aluminide particles as a function of reaction conditions:

As shown in Figures - 5.31 and 5.32 (Section 5.3.3.5) the volume fraction of $TiAl_3$ varied with distance from the reaction interface. The kinetic studies of aluminide ($TiAl_3$) formation by reaction synthesis, as reported in the literature (Section 2.7.3), have, in general, utilized the total thickness of the reaction zone as the basis of calculating the amount of reaction product. However, as mentioned in the present study (i) the reaction zone consisted of an Al rich matrix in addition to $TiAl_3$ and (ii) the volume fraction of aluminide particles within the reaction zones varied with distance from the reaction interface. Therefore, the evaluation of kinetics of $TiAl_3$ formation, as well as the estimation of activation energies involved, on the basis of reaction zone thickness is expected to give errors. In order to reduce these errors, the average volume fraction of $TiAl_3$ in the reaction zone was estimated.

The average volume fraction of $TiAl_3$ present in the reaction zone was calculated for each reaction condition by numerically integrating the curves ($\int v_v dx$) for the variation of volume fraction with distance, over the entire reaction zone thickness as represented by polynomial equations of Table 5.9 (see Section 4.4.3).

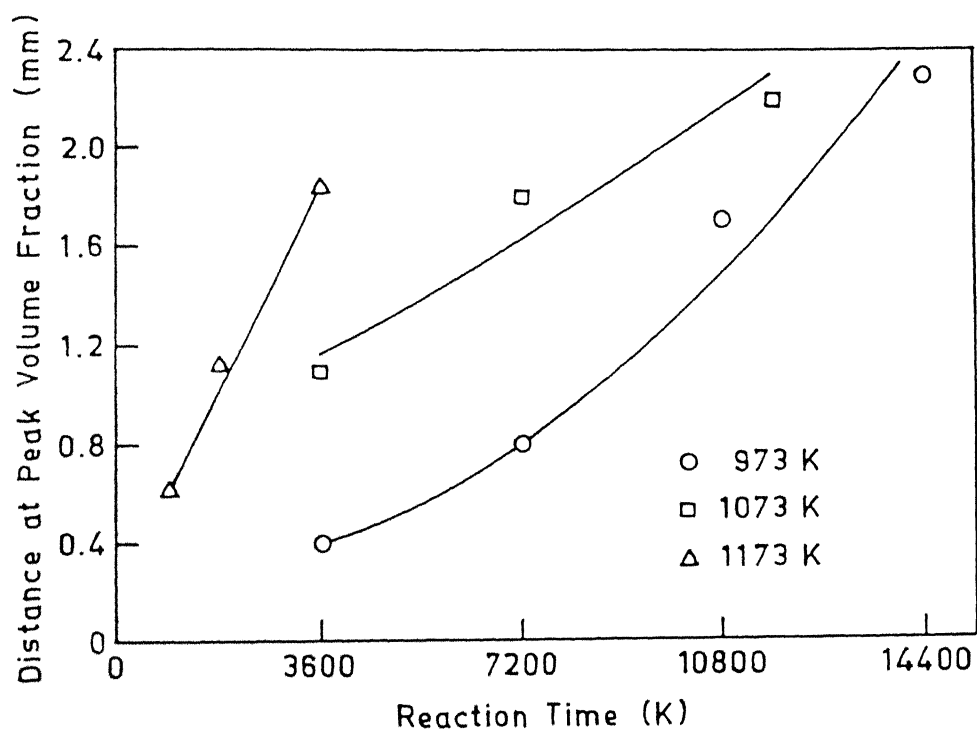


Figure 5.34 Effect of reaction temperature and time on the distance at the peak volume fraction of aluminide particles.

(a). Average volume fraction of $TiAl_3$ in pure Ti/Al reaction couples:

Effect of reaction temperature and time on the average volume fraction of $TiAl_3$ in the reaction zone of Ti/Al couple is given in Table - 5.10 and has been shown in Figure 5.35. The data clearly shows that the increase in reaction temperature as well as reaction time leads to increase in the average volume fraction of $TiAl_3$ in the reaction zone.

(b). Average volume fraction of $TiAl_3$ in Ti alloy/Al reaction couples:

Average volume fractions of $TiAl_3$ base intermetallic compounds formed in Ti-Al-V alloy/Al and Ti-Al-Mo-Zr-Si alloy/Al couples reacted for different temperature and time conditions are given in Table - 5.11. It is evident from the table that at the reaction temperature of 973 K ($700^{\circ}C$) , an increase in reaction time from 3600 s (1 hr) to 7200 s (2 hr) resulted in a decrease in the average volume fraction of $TiAl_3$ in the reaction zone of both the alloy couples. However, when the reaction temperature increased to 1073 K longer reaction times lead to an increase in the average volume fraction of $TiAl_3$. At higher reaction temperature (1173 K), the results obtained are similar to those seen in the case of Ti/Al couples.

5.3.3.7 Particle size distribution in the dispersed reaction domain:

Analysis by quantitative metallography revealed that in all the partially reacted couples, particles of $TiAl_3$ or $TiAl_3$

ble-5.10 : Effect of reaction temperature and time on the average volume fraction of $TiAl_3$ in the two phase (Al + $TiAl_3$) dispersed reaction domain of Ti/Al couples

Reaction temperature (K)	Average volume fraction of $TiAl_3$ (%)					
	Reaction time (ks)					
	0.9	1.8	3.6	7.2	10.8	14.4
973	-	-	40.06	49.35	53.00	56.76
1073	-	-	49.10	60.51	62.68	-
1173	38.30	51.20	51.83	-	-	-

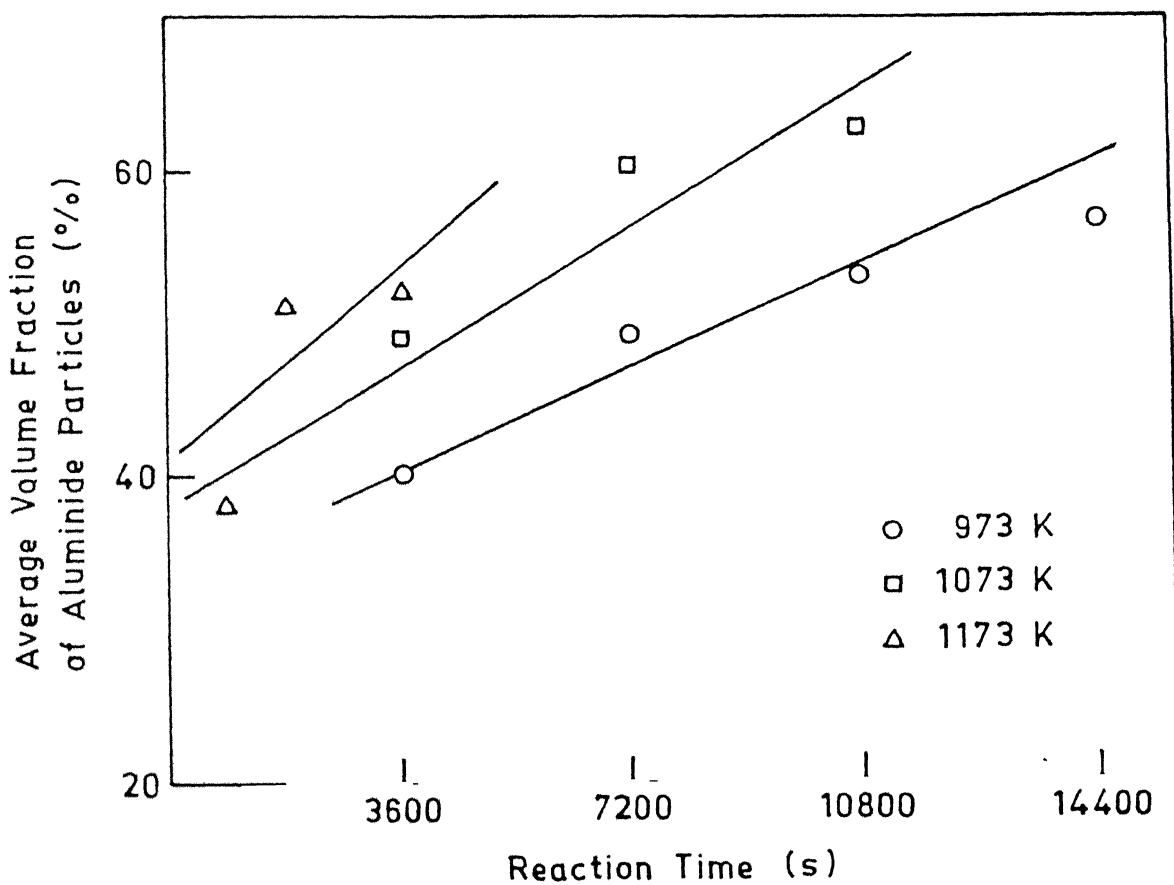


Figure 5.35 Variation of average volume fraction of aluminide particles in the dispersed reaction domain with reaction temperature and time in pure Ti/Al couples.

ble-5.11 : Effect of reaction temperature and time on the average volume fraction of $TiAl_3$ in the two phase (Al + $TiAl_3$) dispersed reaction domain of Ti alloy/Al couples

Reaction couple	Reaction temperature (K)	Thickness of reaction zone (mm)	
		Reaction time (ks)	3.6
			7.2
Ti-6Al-4V)/Al	973	65.59	39.82
	1073	54.26	58.25
	1173	75.19	-
Ti-6.5Al-3.2Mo- .2Zr-0.3Si)/Al	973	47.77	41.39
	1073	69.65	71.49
	1173	68.43	-

base intermetallic compounds had a size distribution which varied with reaction temperature and time. A careful examination of microstructures showed that at different distances from the reaction interface, local particle size distributions also existed in the dispersed reaction domain.

In view of the above mentioned observations, a *mean particle size* was defined to indicate the variation of particle size with distance from the reaction interface. This mean particle size at a given distance was obtained from the data about the local particle size distribution. In addition, an *average particle size* was defined to describe the overall particle size change as influenced by reaction temperature as well as reaction time.

Typical SEM micrographs of $TiAl_3$ particles in the dispersed reaction domain of pure Ti/Al couples reacted at 973 K ($700^{\circ}C$) for 7200 s (2 hr) at various distances from the reaction interface are shown in Figures - 5.36(a) to 5.36(c). Optical micrographs of mid regions of the reaction zone in couples reacted for 3600 s (1 hr) at 973 K ($700^{\circ}C$), 1073 K ($800^{\circ}C$), 1173 K ($900^{\circ}C$) and 1373 K ($1100^{\circ}C$) are shown in Figures - 5.37(a) to 5.37(d). Similarly, SEM micrographs of the mid regions of the reaction zones of Ti/Al couples reacted at 1073 K ($800^{\circ}C$) for different reaction times are shown in Figures - 5.38(a) - 5.38(c). Similar microstructural features were observed for pure Ti/Al couples reacted under other reaction conditions.

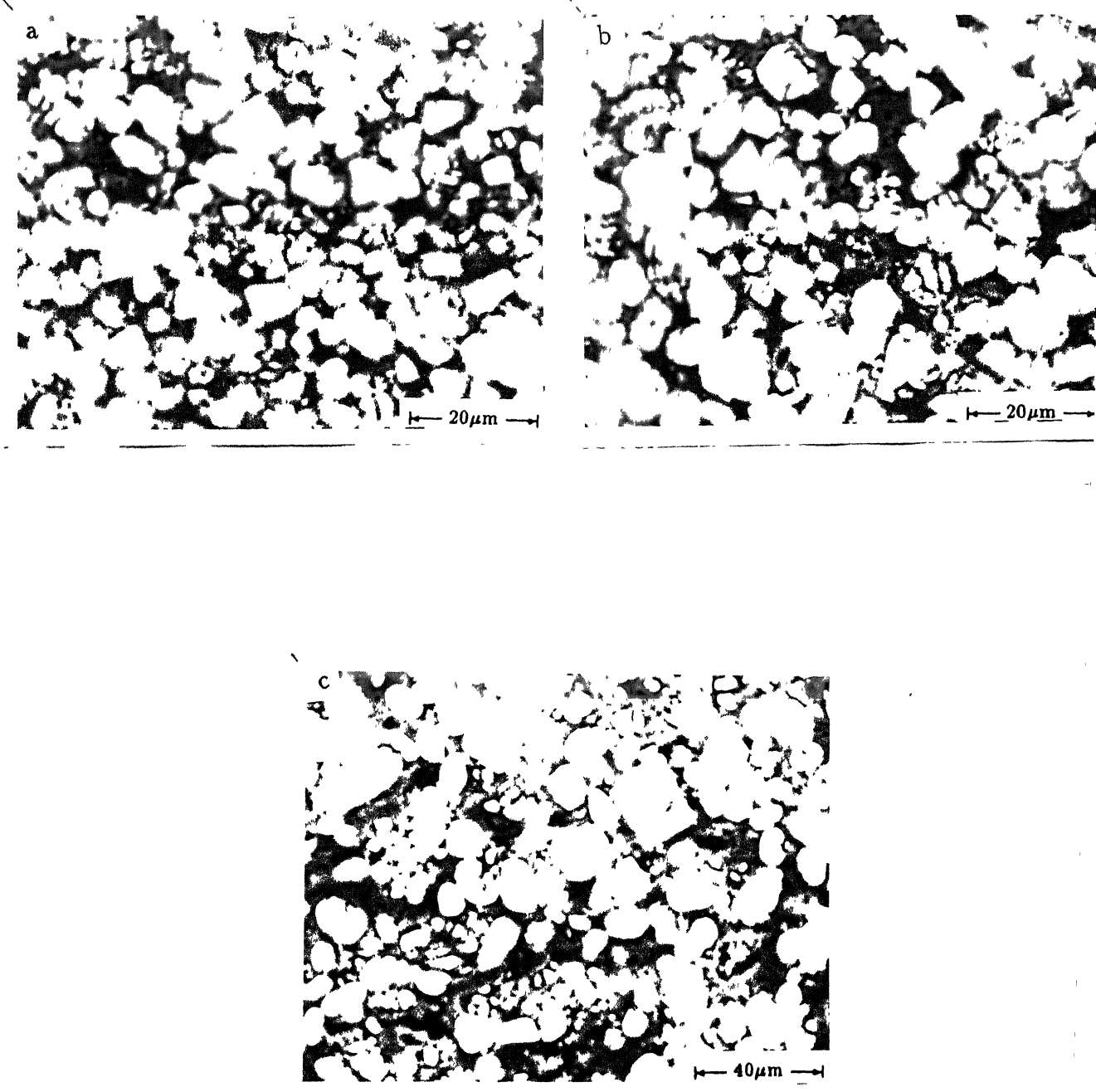


Figure 5.36 SEM microstructures showing the changes in the particle size and morphology of TiAl_3 base particles at increasing distance from the reaction interface in Ti/Al couples reacted at 973 K (700°C) for 7200 s (2 hr):
(a) 0.4 mm, (b) 1.2 mm and (c) 2.0 mm.

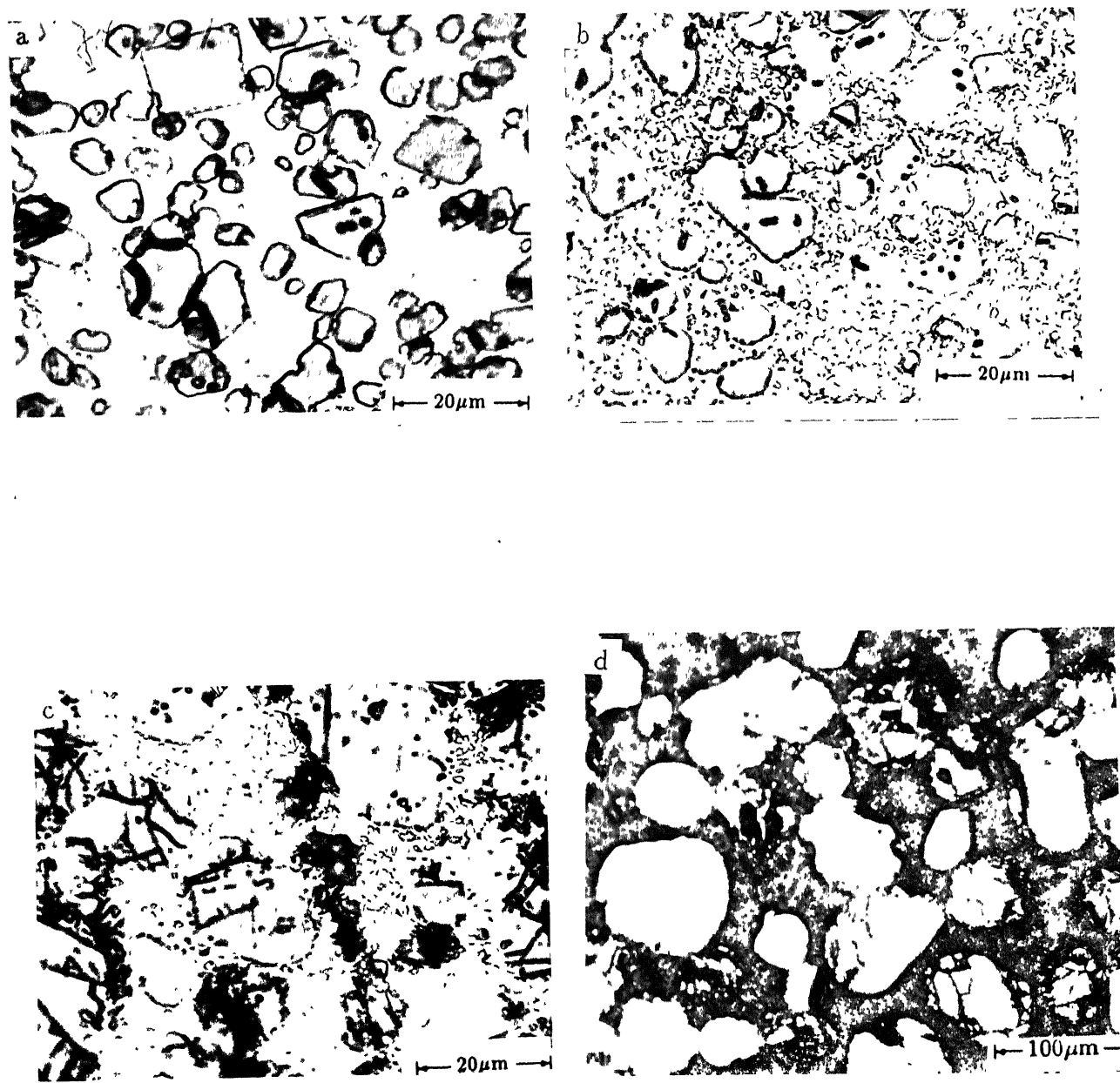


Figure 5.37

Optical microstructures of the reaction zones formed in Ti/Al couples reacted for 3600 s (1 hr) at (a) 973 K (700°C), (b) 1073 K (800°C), (c) 1173 K (900°C) and (d) 1373 K (1100°C).

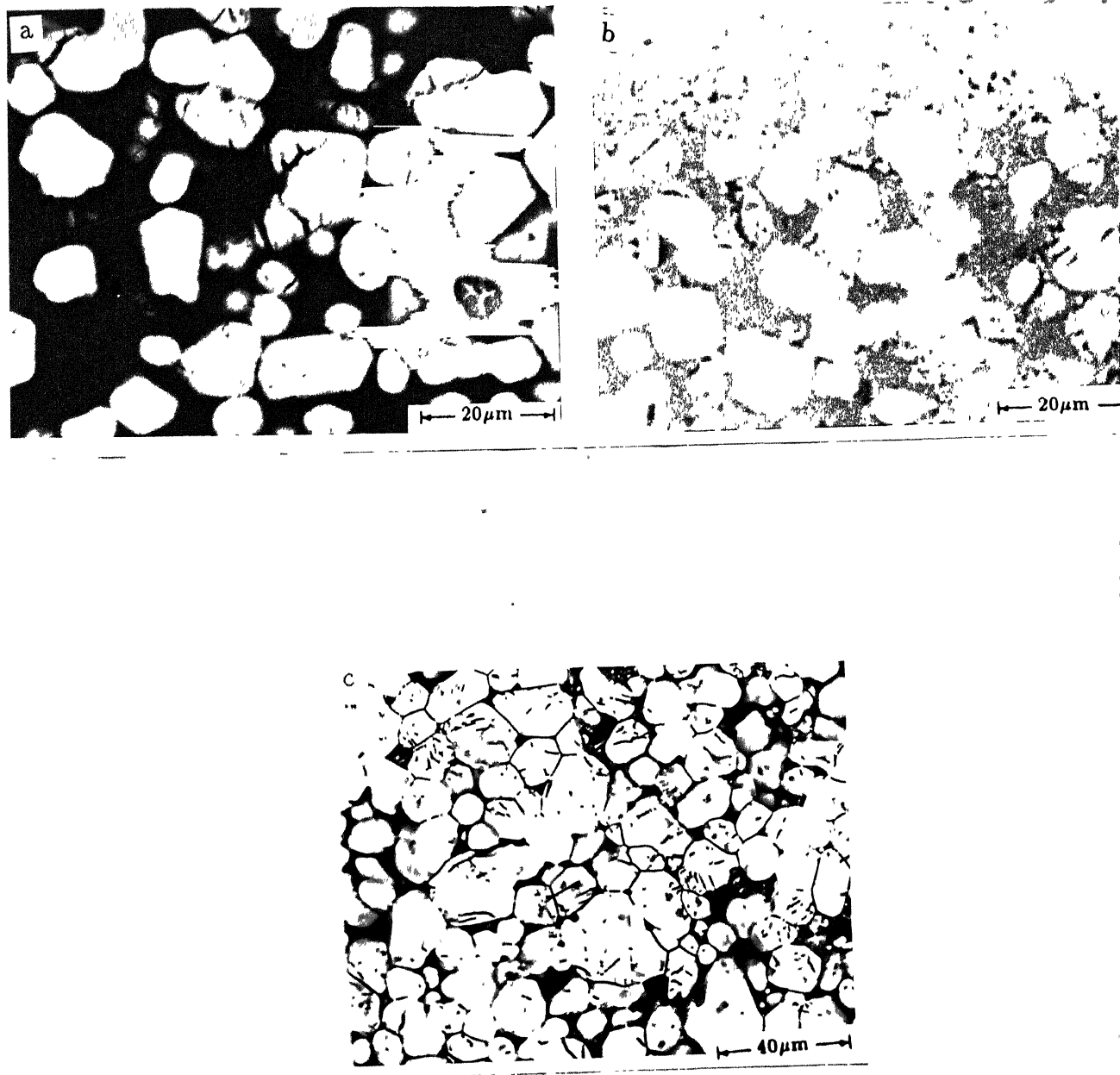


Figure 5.38

SEM micrographs showing the effect of reaction time on the morphology and particle size of TiAl₃ in Ti/Al couples reacted at 1073 K (800°C) for (a) 3600 s (1 hr), (b) 7200 s (2 hr) and (c) 14400 s (4 hr).

Effect of reaction temperature on the particle size distribution existing in the mid region of the reaction zone in Ti-Al-Mo-Zr-Si alloy/Al couples reacted for 7200 s (2 hr) at 973 K (700°C) and 1073 K (800°C) is shown in Figures - 5.30(a) and 5.30(b). The contrast in the particle size distribution in the mid region of the reaction zone of Ti/Al, Ti-Al-V alloy/Al and Ti-Al-Mo-Zr-Si alloy/Al couples reacted under identical conditions, i.e. at 973 K (700°C) for 7200 s (2 hr) is shown in Figure - 5.39(a) to 5.39(c). The quantitative metallographic results obtained from such samples are discussed below. It is to be noted that the particle size distribution has been plotted in terms of number of particles per unit volume.

Particle size distribution in the dispersed reaction domain of pure Ti/Al couples reacted for 3600 s (1 hr) at 973 K (700°C), 1073 K (800°C) and 1173 K (900°C) are shown in Figures - 5.40(a) to 5.40(c) respectively. This figure clearly shows the effect of reaction temperature on the development of bimodal distribution with increase in reaction temperature. While at the reaction temperature of 973 K (700°C), most of the particles were less than 8 μm in size, the number of particles finer than 8 μm decreased as the reaction temperature is increased to 1073 K. In contrast, the percentage of particles $>12 \mu\text{m}$ size was negligible upto the reaction temperature of 1073 K (800°C) while it increased considerably at 1173 K (900°C).

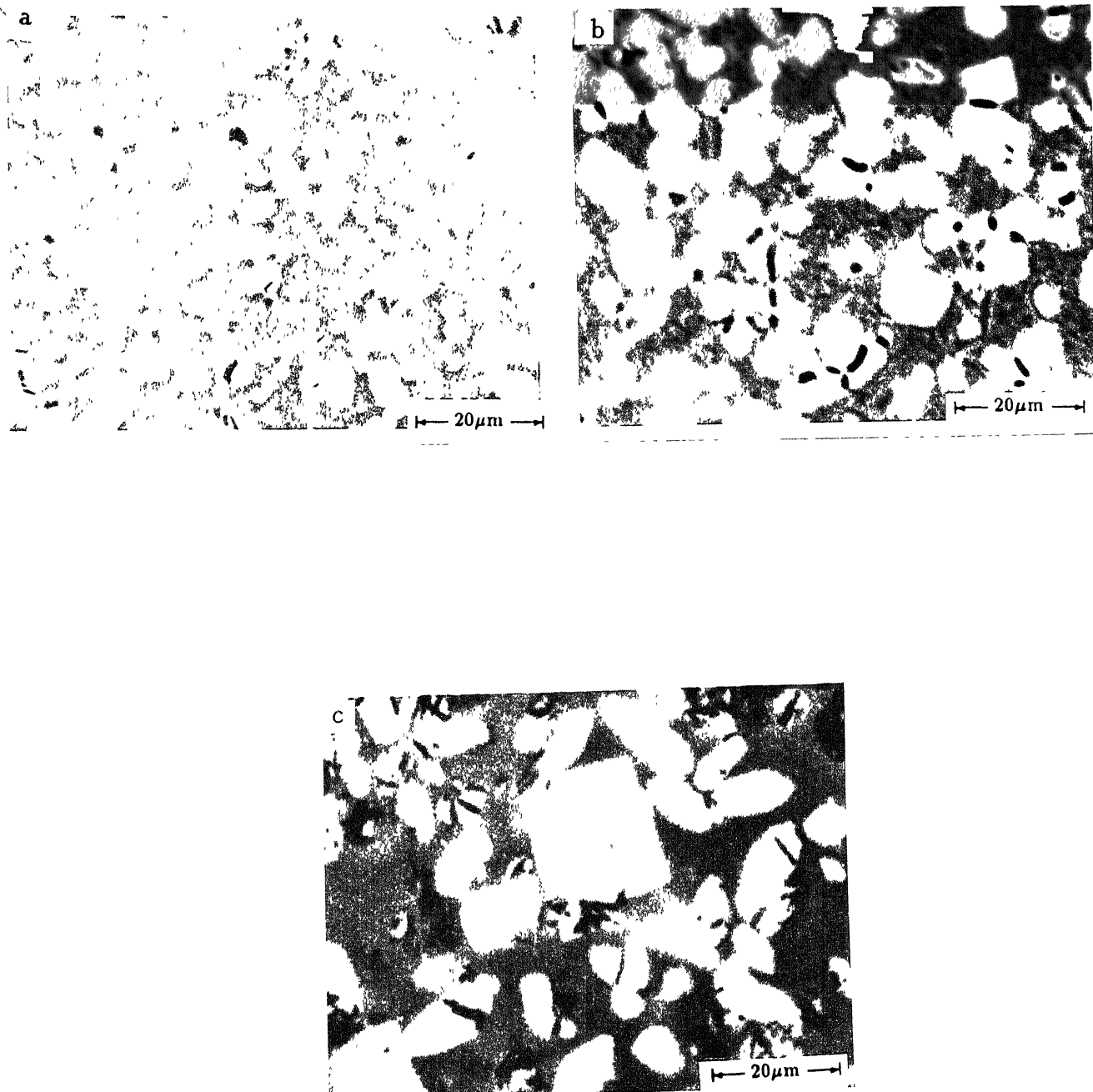


Figure 5.39 SEM micrographs showing the effect of alloying elements on the particle size and morphology of Ti-Al₃ based compounds formed in couples reacted at 973 K (700°C) for 7200 s (2 hr); (a) Ti/Al, (b) Ti-Al-V alloy/Al and (c) Ti-Al-Mn-Zr-Si alloy/Al.

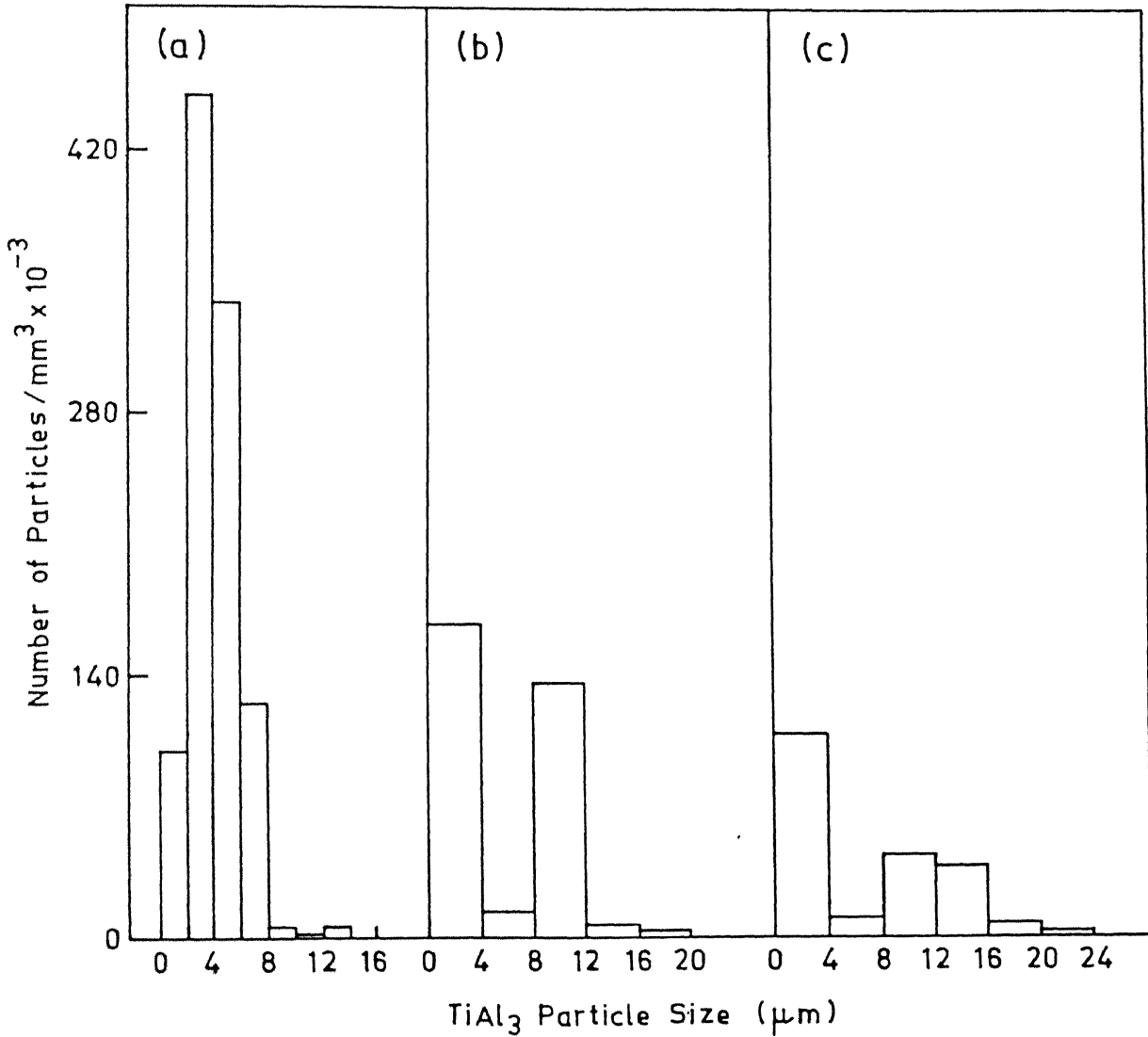


Figure 5.40 Variation of particle size distribution of TiAl₃ in the dispersed reaction domain of pure Ti/Al couples reacted for 3600 s (1 hr) at (a) 973 K (700°C), (b) 1073 K (800°C) and (c) 1173 K (900°C).

Similarly, the variation in particle size distribution as a function of reaction time in pure Ti/Al couples reacted at 1073 K (800°C) for 3600 s (1 hr), 7200 s (2 hr) and 14400 s (4 hr) are shown in Figures - 5.41(a) to 5.41(c). It can be seen that when the reaction was carried out for 3600 s, most of particles were <12 μm in size and roughly a bimodal size distribution existed. However, as the reaction time increased to 7200 s, the number of particles finer than 12 μm decreased considerably and the number of particles in the size range of 12-24 μm increased. As the reaction time is further increased to 14400 s, the number of particles finer than 8 μm remain more or less same and the number of particles in the size range of 20-24 μm increased considerably.

Local particle size distributions in pure Ti/Al couples reacted at 1073 K (800°C) for 7200 s (2 hr) at distances of 0.2 mm, 0.4 mm, 0.8 mm and 1.6 mm from the reaction interface are shown in Figures - 5.42(a) to 5.42(d). It is evident from the figure that near to the reaction interface i.e. at 0.2 mm distance, most of the particles lied in the size range of 0-8 μm . With increase in distance from the reaction interface to 0.4 mm, number of particles in this size range decreased [Figure 5.42(b)]. With further increase in distance to the mid region of the reaction zone, a substantial decrease in the population of particles lying in the 0-8 μm range occurred, while the population of particles in the range of 8-24 μm size increased showing roughly a bimodal size distribution. At farther distances from

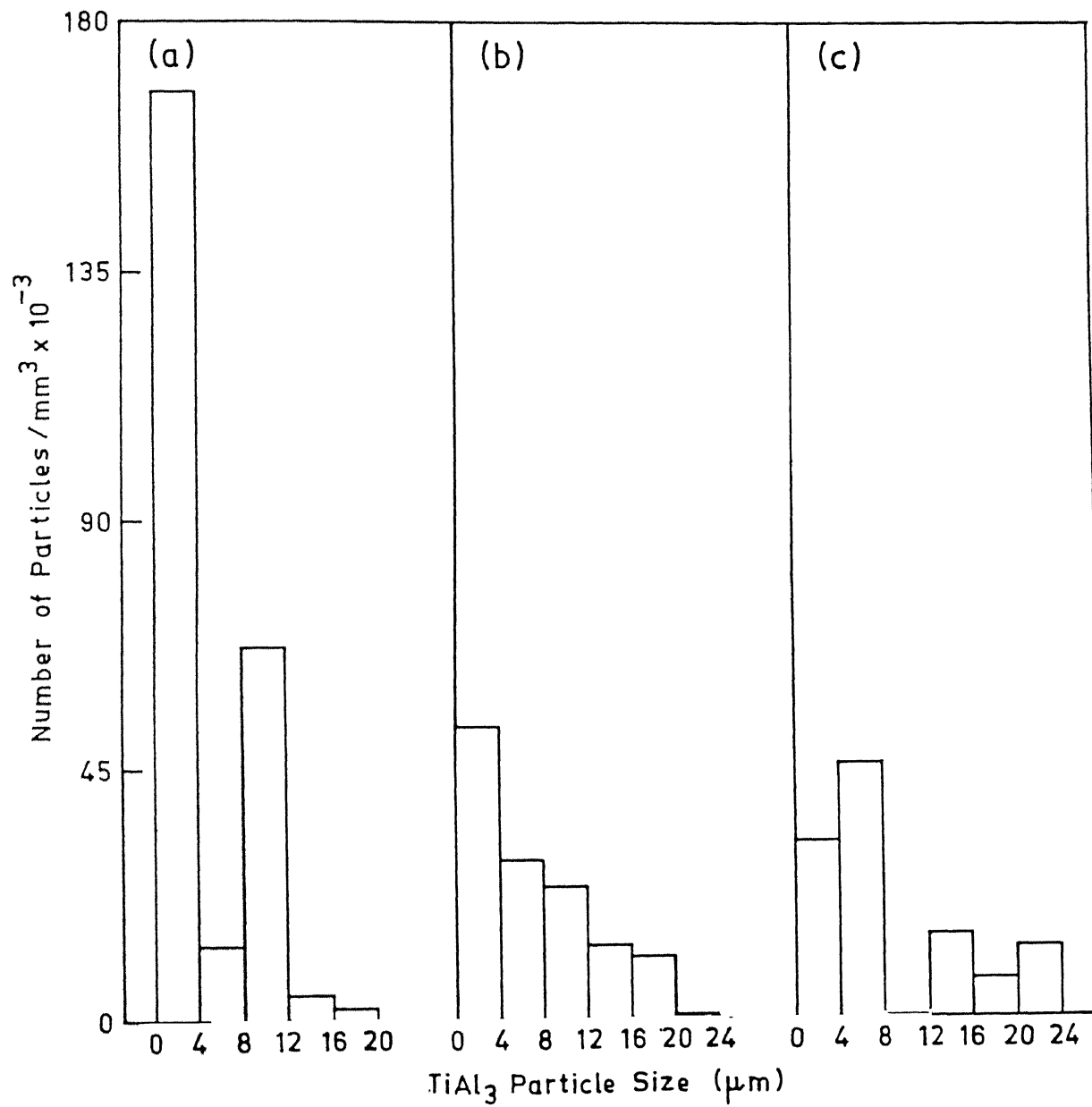


Figure 5.41 Variation of particle size distribution as a function of reaction time in pure Ti/Al couples reacted at 1073 K (800°C) for (a) 3600 s (1 hr), (b) 7200 s (2 hr) and (c) 14400 s (4 hr).

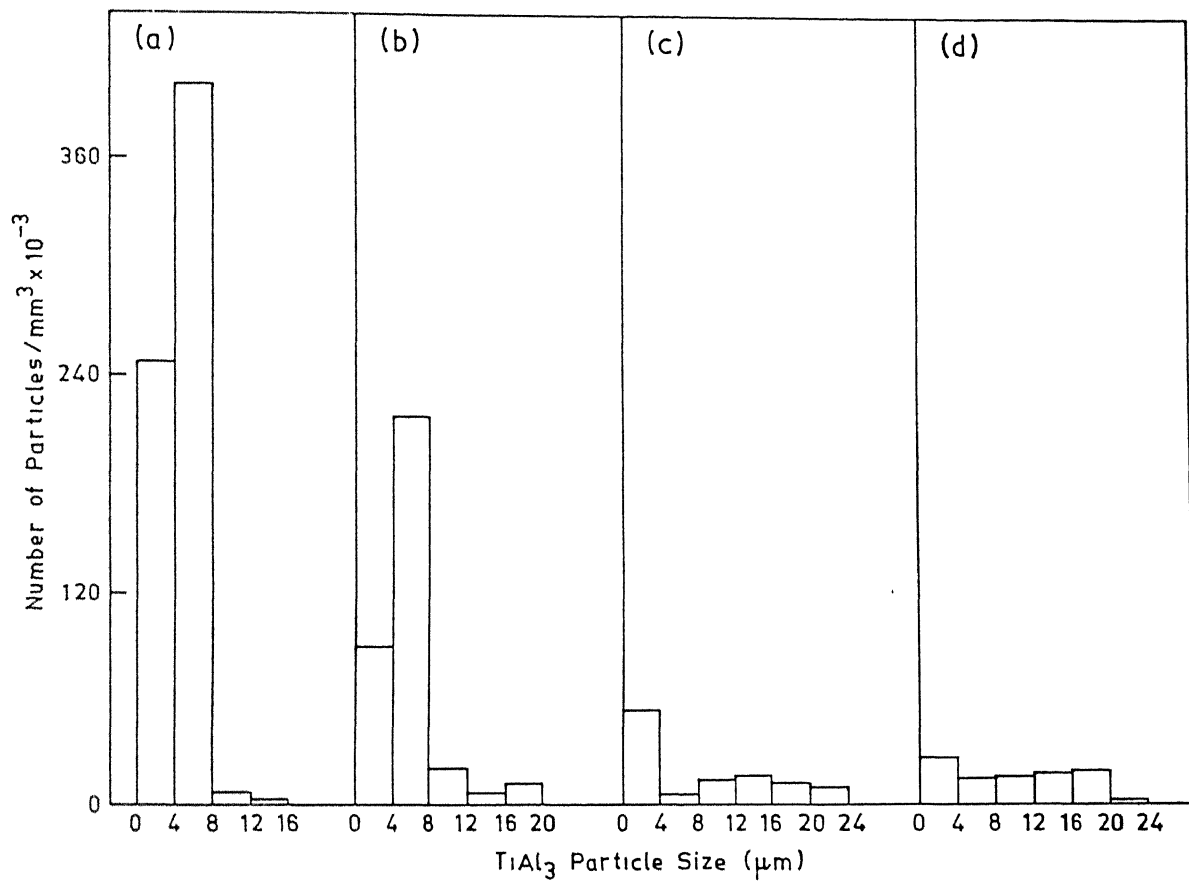


Figure 5.42 Particle size distribution of TiAl_3 at different distances from the reaction interface in pure Ti/Al couples reacted at 1073 K (800°C) for 7200 s (2 hr); (a) 0.2 mm, (b) 0.4 mm, (c) 0.8 mm and (d) 1.6 mm.

the reaction interface, i.e. at 1.6 mm, the number of particles in the size range of 0-4 μm further decreased and the population of particles of different sizes in the range of 0-20 μm became even.

The analysis of the above results showed that the average particle size increased with reaction time as well as reaction temperature.

The variation of the average particle size with reaction time in pure Ti/Al couples reacted at 1073 K (800°C) has been shown in Figure - 5.43 by curve A. It can be observed that with increase in reaction time, the average particle size increased. As discussed earlier, due to existence of roughly a bimodal distribution, the average particle size in the range of (4-24) μm was also calculated and is shown by curve B. It can be noted from the figure that while the mean particle size for (0-24) μm increased with time, the mean particle size of (4-24) μm range remained more or less same.

Similarly the variation of average particle size with reaction temperature in pure Ti/Al couples reacted for 3600 s (1 hr) has been shown in Figure - 5.44 by curve A. Curve B shows the average particle size for the range of (4-24) μm . It can be noted from the figure that with increase in reaction temperature from 973 K to 1273 K resulted in a gradual increase in average particle size of both the size ranges. However, further increase in reaction temperature to 1373 K resulted in a steep increase in the

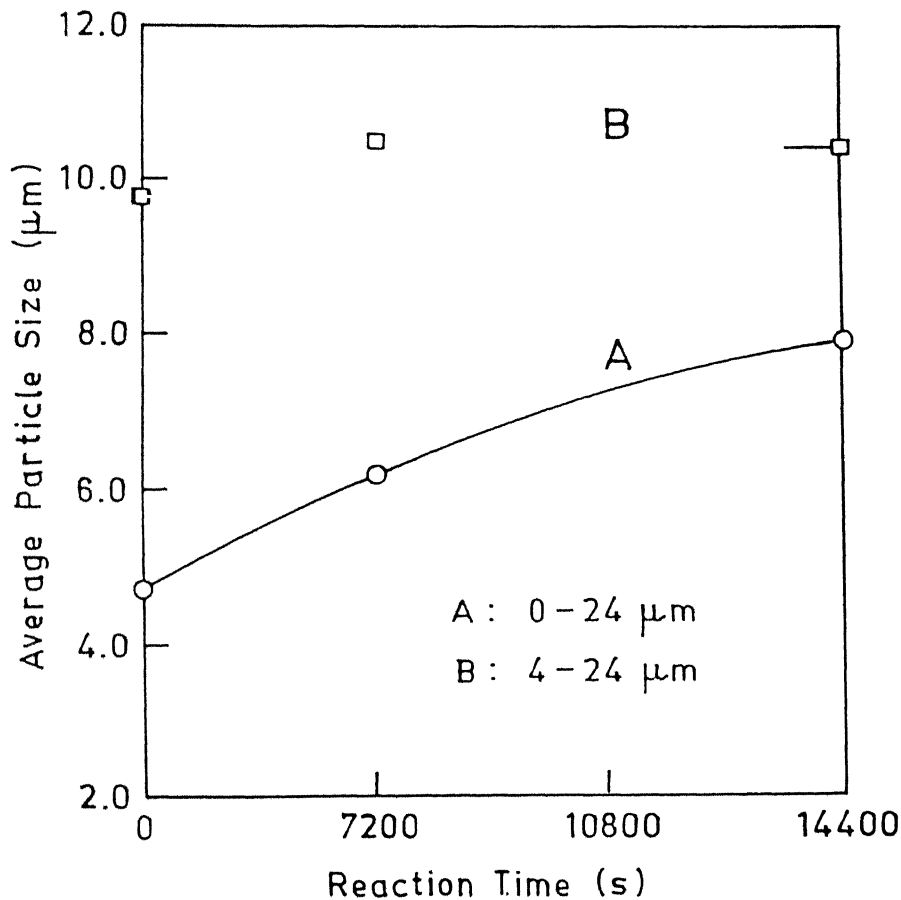


Figure 5.43 Variation of average particle size of TiAl_3 with reaction time in Ti/Al couples reacted at 1073 K (800°C);

A: for the size range of 0-24 μm
B: for the size range of 4-24 μm .

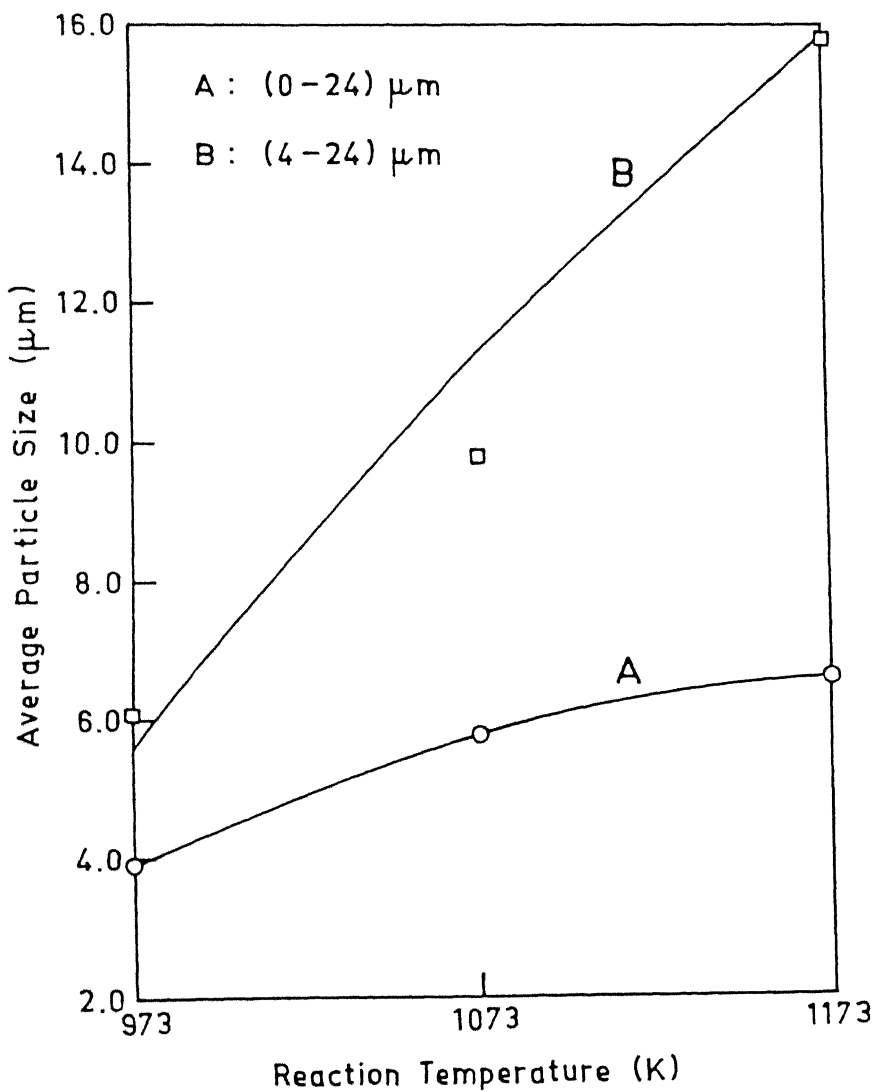


Figure 5.44 Variation of average particle size of TiAl_3 with reaction temperature in Ti/Al couples reacted for 3600 s (1 hr);
A: for the size range of $0-24 \mu\text{m}$
B: for the size range of $4-24 \mu\text{m}$.

average particle size of aluminide (Figure - 5.45).

The mean particle size of $TiAl_3$ with distance from the reaction interface in Ti/Al couples reacted at 1073 K ($800^{\circ}C$) for 7200 s (2 hr) has been shown in Figure - 5.46. Curve A represents the mean particle size for the entire range ($0-24 \mu m$), while curve B represents the mean particle size of $4-24 \mu m$ range particles. It can be noted from the figure that variation in mean particle size occurred till the mid region of the reaction zone (0.8 mm). The mean particle size of both the size ranges increased with distance from the reaction interface to 0.8 mm . Beyond 0.8 mm , the increase is gradual and reaches more or less a constant value at about 1.2 mm .

5.3.4 Hardness Variation in Ti/Al Couples:

Microhardness measurements in the unreacted Ti and Al regions of the Ti/Al couples showed no increase in the hardness of either the Ti or Al phases. Similar observations were made even in the case of unreacted regions of Ti alloys and Al in Ti-Al-V alloy/Al, Ti-Al-Mo-Zr-Si alloy/Al couples.

Microhardness values of $TiAl_3$ based particles formed at various reaction temperatures have been shown in Table - 5.12. In case of samples reacted at 973 K and 1073 K, particles of $TiAl_3$ were too small for microhardness measurements and therefore, the microhardness data for these samples represents the hardness of the two phase mixture of ($TiAl_3 + Al$). However, it was possible

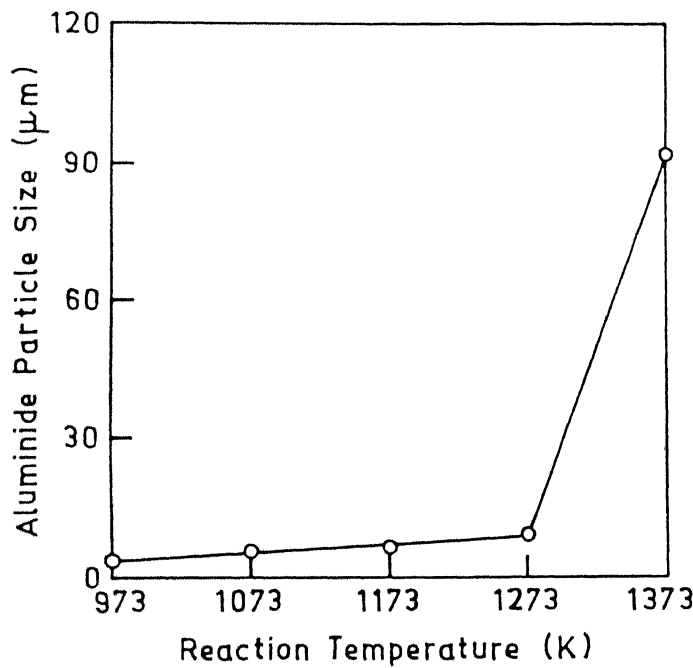


Figure 5.45 Variation of average particle size of aluminide with reaction temperature in pure Ti/Al couples reacted for 3600 s (1 hr).

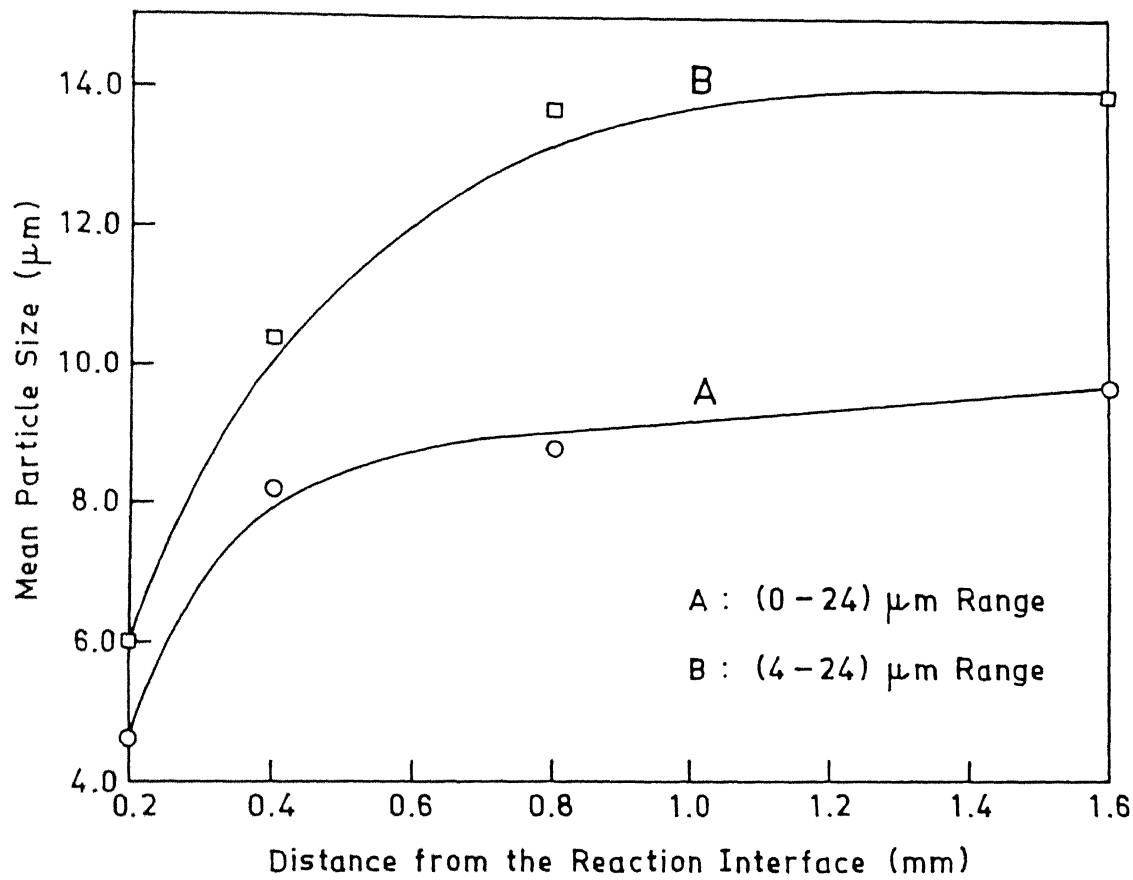


Figure 5.46 Variation of mean particle size of TiAl_3 with distance from the reaction interface in pure Ti/Al couples reacted at 1073 K (800°C) for 7200 s (2 hr)

Table-5.12: Mean values of microhardness of different phases in the reaction zone alongwith those of unreacted Ti and Al (confidence interval for 95% confidence level are shown)

Reaction temperature (K)	Microhardness (VHN)			
	Reaction zone		Unreacted	
	Aluminide	Al	Ti	Al
973	86.4 ± 3.0	Bulk	260.9 ± 8.4	34.1 ± 0.8
1073	319.5 ± 6.8	Bulk	283.7 ± 12.7	34.2 ± 0.8
1173	446.0 ± 46.3	48.5 ± 2.9	292.2 ± 11.1	39.6 ± 2.7
1273	671.9 ± 46.0	49.7 ± 3.4	295 ± 25.5	49.4 ± 8.3

to make indentations within the large sized $TiAl_3$ particles (which are formed at higher reaction temperatures). While the hardness values on samples reacted at 1173 K and 1273 K are found to be comparable with that of arc melted $TiAl_3$ reported in the literature [133], the values obtained in the case of samples reacted at 1373 K were significantly higher than that of melt spun $TiAl_3$ ribbons [134].

Chapter 6

Discussion

Results obtained on the formation of $TiAl_3$ or $TiAl_3$ base alloys and Ti_9Al_{23} by reaction synthesis between solid titanium / Ti-Al-V alloy / Ti-Al-Mo-Zr-Si alloy and liquid aluminium under different reaction conditions have already been given in Chapter-5. It has also been shown that a systematic variation of various microstructural features of the dispersed reaction domain such as volume fraction, size and shape distribution, the mean and the average size of aluminide particles varied systematically with reaction conditions. The difference in the evolution of these microstructural features arose due to the occurrence of several physical phenomena in the reaction zone during the course of reaction synthesis. These microstructural variations and different physical phenomena responsible for their evolution are discussed in the present chapter.

6.1 $TiAl_3$ FORMATION IN THE TEMPERATURE RANGE OF 973 K - 1273 K ($700^{\circ}C$ - $1000^{\circ}C$):

Results of the present study have shown that $TiAl_3$ was the only reaction synthesis product formed in couples reacted between 973K-1273K ($700^{\circ}C$ - $1000^{\circ}C$). Formation of $TiAl_3$ was confirmed by the results of

- (i) X-ray diffraction (Section-5.2.2),
- (ii) Energy dispersive spectrometry, EDS (Section-5.1.3),
- (iii) Electron probe microanalysis, EPMA (Section-5.1.3),

- (iv) Transmission electron microscopy, TEM (Section-5.2.2)
- (v) Microhardness measurements (Section-5.3.4).

It is worth mentioning here that similar results have also been reported by studies on (i) interaction between Ti and liquid Al [119-121], (ii) hot dip aluminide coatings formed on Ti [127], (iii) brazing of Ti using Al filler metals [126] and (iv) aluminide coatings formed by CO_2 laser alloying [124,125]. However, no attempt has been made by any of these workers to explain the formation of only TiAl_3 by reaction synthesis from solid Ti and liquid Al. Formation of TiAl_3 has also been reported during interaction between solid Ti and solid Al [136,137]. Similar observations were made during studies on Ti-Al diffusion couples by van Loo and Reick [135]. Reasons based on thermodynamic considerations for the formation of TiAl_3 will be discussed in this section.

The binary Ti-Al phase diagram (Figure-2.1) shows that several intermetallic compounds, namely, Ti_3Al , TiAl , TiAl_2 , Ti_2Al_5 , $\text{Ti}_5\text{Al}_{11}$, $\text{Ti}_9\text{Al}_{23}$ and TiAl_3 are present in the Ti-Al system. Among these compounds while Ti_3Al , TiAl and TiAl_3 can form by reactions involving solid Ti and liquid Al, the formation of Ti_2Al_5 , TiAl_2 , $\text{Ti}_5\text{Al}_{11}$ and $\text{Ti}_9\text{Al}_{23}$ occur through a series of solid-liquid and/or solid state reactions necessarily involving TiAl as one of the starting phase [23]. For the purpose of the present study, these Ti-Al aluminides have therefore been classified into two categories. Type - I aluminides are designated as those aluminides which can form by reactions between solid Ti and liquid Al; i.e. Ti_3Al , TiAl and TiAl_3 . In contrast,

aluminides which necessarily require TiAl as an intermediate product for their formation are designated as Type - II aluminides. Thus Ti_2Al_5 , $TiAl_2$, Ti_5Al_{11} and Ti_9Al_{23} are aluminides of Type - II.

Kattner et al. [49] have recently made the thermodynamic assessment of binary Ti-Al system and have calculated Gibb's free energy of formation of different Ti-Al intermetallic compounds. In view of the differences between Ti-Al aluminides of Type - I and Type - II, Kattner et al. used two different equations for describing the concentration and temperature dependence of free energies of formation of these compounds. However, they calculated free energy of formation of only $TiAl_2$ and Ti_2Al_5 compounds among the compounds belonging to Type - II Ti-Al aluminides.

The sublattice model (Wagner-Schottky model) was used to calculate free energies of formation of the ordered compounds Ti_3Al , $TiAl$ and $TiAl_3$. Calculations were made taking into consideration that these compounds exist over a range of composition. Thus, it was assumed that (i) for the formation of perfectly ordered compounds, two sublattices, one each occupied by Ti and Al atoms, existed and (ii) the deviation from the stoichiometry or perfect ordering could be explained by the presence of the substitutional atoms in each of the sublattices. Under the second situation, each of the sublattices was assumed to be a random mixture of Ti and Al atoms. Application of this model for the $TiAl_3$ compound assumes that the compound $TiAl_3$ also exists

over a range of composition. However, it is to be noted here that the phase equilibria studies reported the existence of $TiAl_3$ as a line compound [22,23] though Kattner et al. [49] considered $TiAl_3$ to exist over a range of composition.

According to the sublattice model, the expression for the free energy, G , for this case, is given by [138,139]

$$\begin{aligned}
 G = & x_{Ti} G_{Ti}^O + x_{Al} G_{Al}^O + RT \{ [n_{Ti}^1 \ln(n_{Ti}^1) + n_{Al}^1 \ln(n_{Al}^1)] \\
 & + [n_{Ti}^2 \ln(n_{Ti}^2) + n_{Al}^2 \ln(n_{Al}^2)] - N^1 \ln(N^1) \\
 & - N^2 \ln(N^2) \} - + \Delta G^f + n_{Ti}^2 G_{Ti}^2 + n_1^1 G_1^1 + n_i^1 n_i^1 [G^1 \\
 & + (n_i^1 - n_1^1) G^1] + n_{Ti}^2 n_A^2 [G_0^2 + (n_{Al}^2 - n_{Ti}^2) G_1^2] \\
 & + n_{Ti}^2 n_1^1 G^{12} \quad \dots 6.1
 \end{aligned}$$

where

n_{Ti}^1 , n_{Al}^1 , n_{Ti}^2 and n_{Al}^2 are mole fractions of Ti and Al atoms on sublattices 1 and 2.

N^1 and N^2 are the site fractions of sublattices 1 and 2.

G_{Ti}^2 and G_{Al}^1 are the Gibb's energy of formation of one mole of substitutional Ti or Al atoms on sublattice 2 and 1 respectively.

On the other hand, for the stoichiometric compounds $TiAl_2$ and Ti_2Al_5 , the Gibb's energy 'G' is given by

$$G = x_{Ti}^O G_{Ti}^O + x_{Al}^O G_{Al}^O + \Delta G^f \quad \dots 6.2$$

where

x_{Ti}^{O} and x_{Al}^{O} are the respective reference states of Ti and Al,

G_{Ti}^{O} and G_{Al}^{O} are the respective reference states of Ti and Al and ΔG^{f} is the Gibbs energy of formation of the compound.

The final expressions obtained for free energies of formation for the compounds TiAl_2 , Ti_2Al_5 , Ti_3Al , TiAl and TiAl_3 using equations 6.1 and 6.2 are shown in Table - 6.1. From these expressions [49], values of free energy of formation were calculated in the temperature range of 273 K - 1473 K and the results obtained are shown in Figure - 6.1.

It can be seen from the figure that in the temperature range of the present work, i.e. from 973 K to 1373 K, TiAl_3 has the minimum free energy of formation among ordered compounds Ti_3Al , Ti and TiAl_3 of Type - I aluminides. It is also seen that the compounds TiAl_2 and Ti_2Al_5 have slightly lower free energies of formation as compared to that of TiAl_3 . However, formation of TiAl_3 as the only reaction product in the temperature range of 973K-1273 K (700°C - 1000°C) can be understood from the steps involved in Ti_2Al_5 and TiAl_2 formation. Formation of Ti_2Al_5 and TiAl_2 can occur through a series of solid-liquid and/or solid state reactions involving TiAl as one of the starting phase. In addition, since in the present situation an excess amount of liquid Al was always present during the reaction synthesis, it can be expected that the Ti-rich compounds Ti_3Al and TiAl do not form during the reaction between Ti and liquid Al. Based on the above, the formation of TiAl_2 and Ti_2Al_5 therefore is ruled out from thermodynamic considerations. Assumption of Wagner-Schottky model

Table 6.1 : Temperature dependence of free energy of formation of various Ti-Al compounds as reported by Kattner et al [49]

Compound	Free energy of formation, ΔG^f
Ti_3Al	- 29633.6 + 6.70801 T
$TiAl$	- 37445.1 + 16.79376 T
$TiAl_3$	- 40349.6 + 10.36525 T
$TiAl_2$	- 43858.4 + 11.02077 T
Ti_2Al_5	- 40495.4 + 9.52964 T

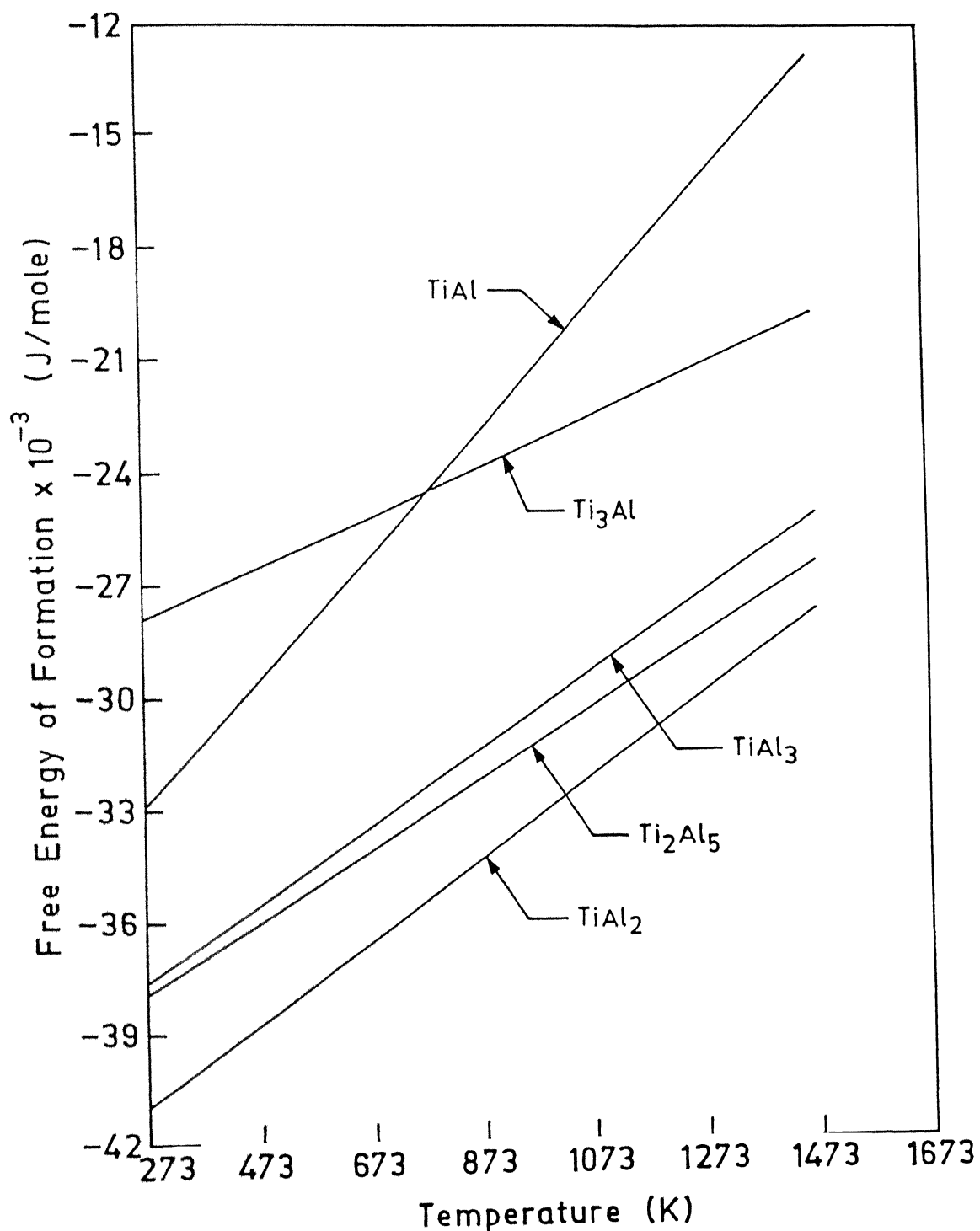


Figure 6.1

Free energies of formation of various Ti-Al compounds as a function of temperature obtained from [49].

for $TiAl_3$ might also be responsible for the higher free energy of $TiAl_3$ in comparison of Ti_2Al_5 and $TiAl_2$.

It is therefore, not surprising that the XRD (Figures -5.9, 5.10 and 5.14) and EDAX results [Tables - 5.4(c) and 5.4(d)] obtained in this study indicated the presence of $TiAl_3$ phase as the only aluminide formed during the reaction synthesis in the range of 973K-1273K ($700^{\circ}C$ - $1000^{\circ}C$). The results obtained by TEM also are in agreement with this. Formation of $TiAl_3$ is also confirmed by microhardness measurements done on the reaction layer. Hardness values of $TiAl_3$ layer formed at 1173 K and 1273 K were found to be comparable with that of arc melted $TiAl_3$ reported in the literature (Table - 5.12) [134].

6.2 MECHANISM OF $TiAl_3$ FORMATION:

6.2.1 Formation of $TiAl_3$ by Chemical Reaction:

As shown in Chapter - 5, the following observations were made regarding the aluminide formation at the Ti/Al interface:

- (i) presence of a thin layer of $TiAl_3$ at the Ti/Al reaction interface as confirmed by EDS and EPMA (Section - 5.1.3)
- (ii) no traces of Al on moving towards Ti side from the reaction interface (Section - 5.1.3) and
- (iii) no variation in the microhardness of Ti as a function of distance from the Ti/Al reaction interface (Section - 5.3.4).

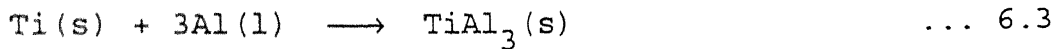
Similar results were obtained even in the case of Ti alloy/Al couples as shown in the previous chapter.

From the observation (ii) it can be noted that insignificant diffusion of Al in Ti/Ti alloy occurs during the reaction synthesis. Aluminium when dissolved in titanium up to ~26at.% forms solid solution and stabilizes the α (hcp) phase of titanium. It causes solid solution strengthening and thus increases the hardness of Ti. Thus, results obtained from the microhardness measurements (Table - 5.12) also showed the absence of solid solution strengthening of titanium by aluminium in the region adjacent to the reaction interface. Therefore observation (iii) also indicate that diffusion of Al in Ti does not occur during the reaction synthesis.

The observation (i) showing the presence of a thin reaction layer of $TiAl_3$ at the reaction interface suggests that formation of $TiAl_3$ occurs by chemical reaction. From the absence of diffusion of Al in Ti and Ti in Al, as well as the presence of thin $TiAl_3$ at the reaction interface, it can be concluded that chemical reaction between Ti and liquid Al is the mechanism of $TiAl_3$ formation in the temperature range of 973 K-1273K ($700^{\circ}C$ - $1000^{\circ}C$).

Similarly, results obtained from the Ti-Al-V alloy/Al and Ti-Al-Mo-Zr-Si alloy/Al couples also suggest that the formation of $TiAl_3$ base compounds also occurs by chemical reaction between Ti alloy and Al and diffusion does not play any important role in the formation of $TiAl_3$ base alloys.

Therefore, the following chemical reaction is thought to occur at the Ti/Al reaction interface;



$$\Delta H = -8.75 \text{ K Cal/mole}$$

and the formation of TiAl_3 by the above reaction occurs as a thin layer at the reaction interface. As mentioned in Section-5.3.1, islands of Ti were occasionally observed at few locations of the reaction zone adjacent to the reaction interface. These were observed in couples reacted at 1073 K and above. This observation of finding some islands of pure Ti ahead of the reaction interface (Figure-5.18) can also be explained in terms of the discussion given above. Separation of Ti islands in these couples can be explained in terms of the faster reactivity of liquid Al with solid Ti at the high energy sites such as grain boundaries.

For example, the surface energy of a grain boundary is influenced by (i) foreign atoms (impurities/alloying additions), (ii) the defect concentration and (iii) the dihedral angle ϕ .

The dihedral angle is the angle between two adjacent grains in the presence of a liquid. The dihedral angle formed between two intersecting grains is shown in Figure-6.2(a) [140]

$$\phi = 2\cos^{-1}\left(\frac{\gamma_{ss}}{2\gamma_{sl}}\right) \quad \dots 6.4$$

where γ_{ss} and γ_{sl} are the solid-solid and solid-liquid interfacial energies respectively.

Depending on the energy ratio $\frac{\gamma_{ss}}{\gamma_{sl}}$, the dihedral angle

varies. The dihedral angle ϕ influences the liquid and the grain shape of the solid. The nature of the liquid shape at different angles has been reported [140] to be different at different values of ϕ [Figure-6.2(b)]. For example, when the energy ratio $\frac{\gamma_{ss}}{\gamma_{sl}}$ equals to 2, the dihedral angle is 0° and the liquid penetrates grain boundaries of the solid phase (Figure-6.2(b)) without facing any resistance.

Presence of islands ahead of the reaction interface can be understood in terms of these factors influencing surface energy. Thus, as soon as melting of Al in the reaction couple takes place, wetting of Ti surface by liquid Al occurs and grain boundary penetration by liquid Al may occur at some grain boundaries depending on the factors (i), (ii) and (iii), when the conditions become favourable [Figure-6.2(c)]. With increase in reaction time, reaction of Ti and liquid Al occurs at the Ti/Al interface. If conditions become favourable for liquid Al penetration along some Ti grain boundaries, $TiAl_3$ formation occurs along them as shown in figure. In view of the lower density of $TiAl_3$ as compared to that of Ti reaction of Al with Ti at these boundaries is expected to cause volumetric expansion due to $TiAl_3$ formation. This results in cracking inside $TiAl_3$ leading to detachment of unreacted Ti grain making it to enter into liquid Al in the form of small islands [Figure-6.3(a)]. Under such circumstances the surface of the separated Ti island acts as the reaction interface for further reaction.

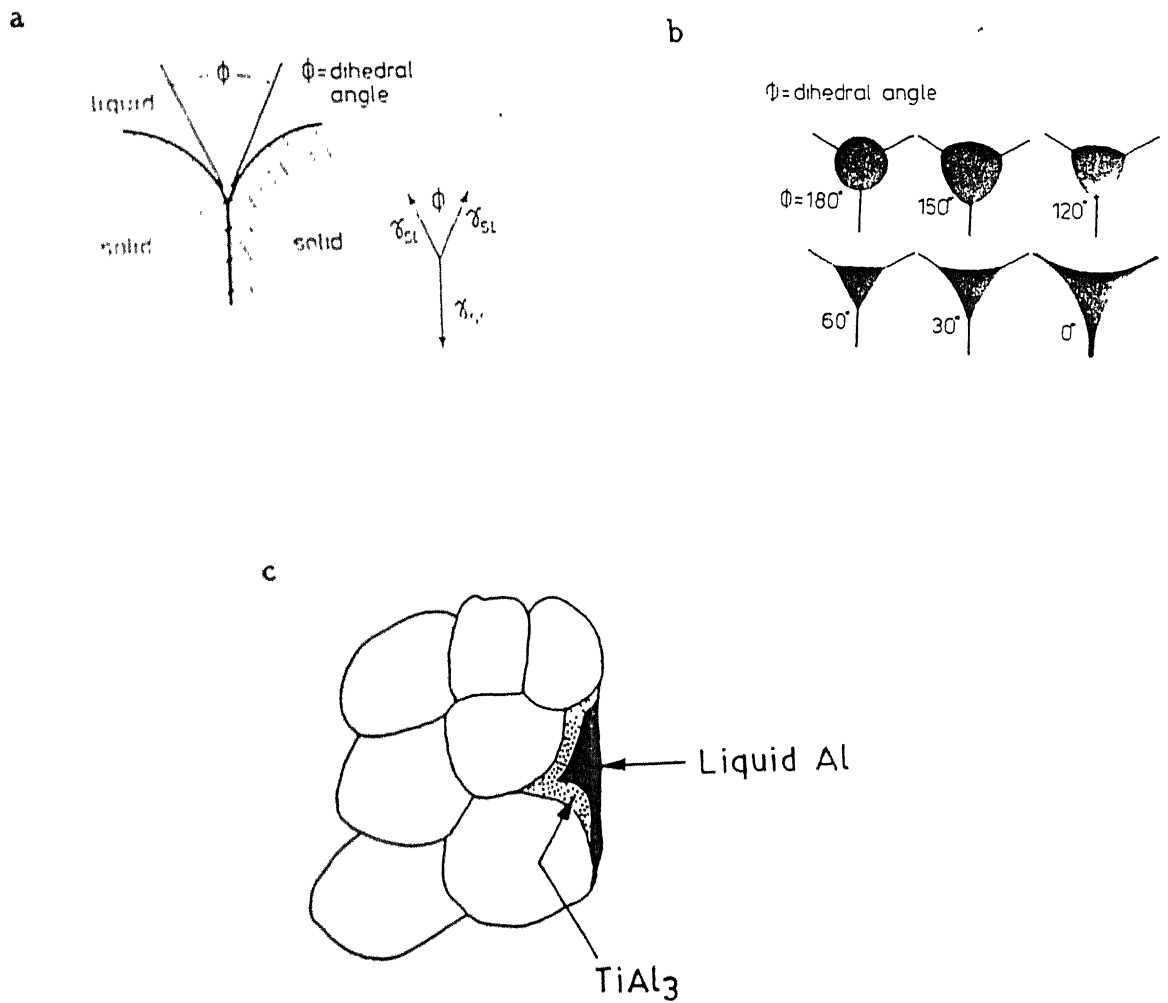


Figure 6.2

(a) The dihedral angle between intersecting grains, (b) nature of liquid shape at different dihedral angles and (c) liquid Al penetration through grain boundaries leading to TiAl_3 formation.

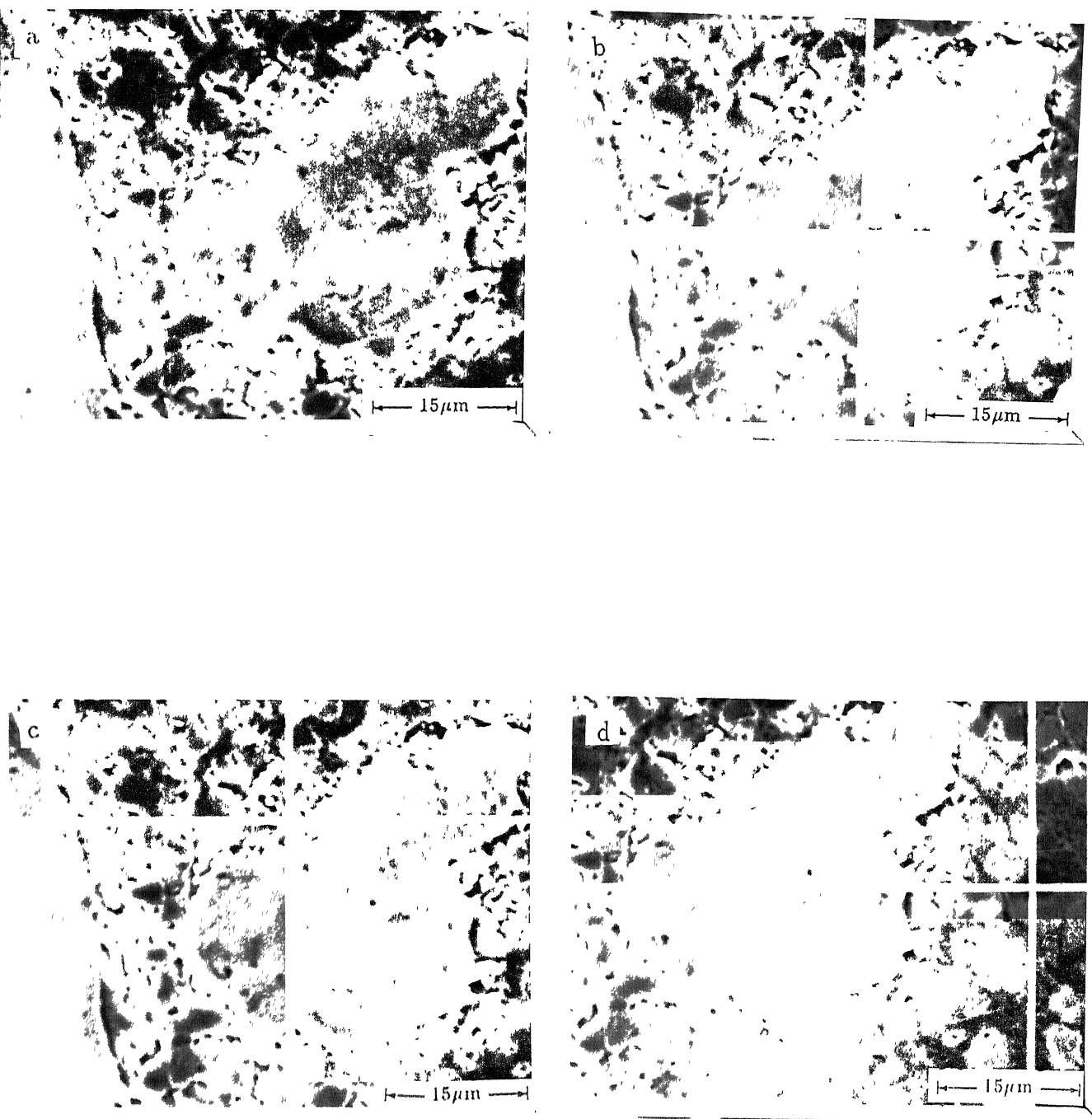


Figure-6.3 SEM micrographs of the separated Ti islands showing an envelope of $TiAl_3$ around them (a); Compositions of the regions marked (b) 100.0 at.% Ti, (c) Ti-74.68at.% Al and (d) Ti-99.46 at.% Al.

The phenomenon of separation of Ti grain was confirmed as shown in Figure-6.3 (a) to (d). This figure reveals the thin $TiAl_3$ envelope on a Ti island present in Al. Presence of $TiAl_3$ envelope was confirmed by chemical analysis using EDS [Figure - 6.3(c)]. It is to be noted here that the size of the Ti island ($\sim 32\mu m$) matches fairly well with that of the average grain size of pure Ti ($\sim 24\mu m$) used for the preparation of reaction couples.

6.2.2 Growth of the Reaction Layer:

Once the thin layer of $TiAl_3$ forms by the chemical reaction at the reaction interface, the direct contact between Ti and Al is stopped. Under these conditions further growth of thin $TiAl_3$ layer requires diffusion of either Ti towards Al or that of Al towards Ti through DO_{22} lattice of $TiAl_3$ thin layer. Intrinsic diffusivities of Al and Ti respectively in the lattice of $TiAl_3$ has been recently obtained by Tardy and Tu [137] and can be given by the expressions

$$D_{Al} = 0.14 \text{ (cm}^2/\text{s}) \exp\left(-\frac{41.63}{RT}\right) \quad \dots 6.5$$

and

$$D_{Ti} = 2.0 \times 10^{-3} \text{ (cm}^2/\text{s}) \exp\left(-\frac{38.64}{RT}\right) \quad \dots 6.6$$

Therefore, it can be seen that intrinsic diffusivity of Al in $TiAl_3$ is higher than that of Ti in $TiAl_3$ by about 2 orders of magnitude. Results of Loo and Rieck [135] can thus be readily understood who from marker experiments concluded that Al was the only diffusing component during the growth of $TiAl_3$ layer formed

by the solid-state reaction between Ti and Al. Similar observations were made by Takemoto and Okamoto [126] and Thuillard et al. [136].

In view of the above data, it can be assumed that the growth of the $TiAl_3$ reaction layer occurred predominantly by the diffusion of Al towards Ti rather than that of Ti towards Al. Further, the reaction layer growth being diffusion controlled, its thickness after a given reaction time increased with increasing the reaction temperature.

It is worth noting that the density of $TiAl_3$ (3.354 gm/cm^3) is considerably lower than that of Ti (4.54 gm/cm^3). Due to the difference in densities of $TiAl_3$ and Ti, the $TiAl_3$ layer formed and grown over solid titanium tries to expand. Density differences of approximately 26.1% can be noted between Ti and $TiAl_3$. In view of this, it is expected that the reaction product formed will undergo an expansion. Also, due to the difference in the thermal expansion coefficients of Ti and $TiAl_3$, an imbalance in their expansion occurs. However, due to lack of data on the thermal expansion coefficient of $TiAl_3$, no quantitative calculations were done to find out the magnitude of the resultant volumetric expansion of $TiAl_3$. In essence, the imbalances in the volume expansion of Ti and $TiAl_3$ are expected to result in the development of a complex state of internal stresses in the reaction product $TiAl_3$. Since the incompatibility between the reaction product and the titanium substrate increases with the thickness of the reaction layer, the degree of such internal

stresses is expected to increase as the thickness of this layer increases. The stresses associated with such high expansion are presumably high to cause deformation of the $TiAl_3$ reaction layer. However, as reviewed in Section 2.3, due to the limited number of slip systems at temperatures below $620^{\circ}C$, $TiAl_3$ is highly brittle. Even at temperatures above $620^{\circ}C$, it was reported by Yamaguchi et al. [51,55] that irrespective of the augmented slip systems of [100], [010]_d and [110], $TiAl_3$ shows compression ductility of only ~ 1 % and almost negligible tensile ductility. The high volume expansion thus cannot be accommodated in $TiAl_3$ due to its poor plastic deformation. Due to the brittle nature of $TiAl_3$ and its alloys, the $TiAl_3$ at the reaction interface develops internal cracks. The amount of cracking inside the $TiAl_3$ layer is dependant on its accommodation capacity to withstand the strain associated with its volume expansion.

The resistance of $TiAl_3$ for cracking is dependant on 3 factors. These are

- (i) the temperature of the $TiAl_3$ layer, which determines its yield behaviour depending on the operative slip and twin systems at that temperature,
- (ii) the thickness of the $TiAl_3$ layer which decides the magnitude of the total strain inside the layer and
- (iii) the alloying elements present inside the $TiAl_3$ layer.

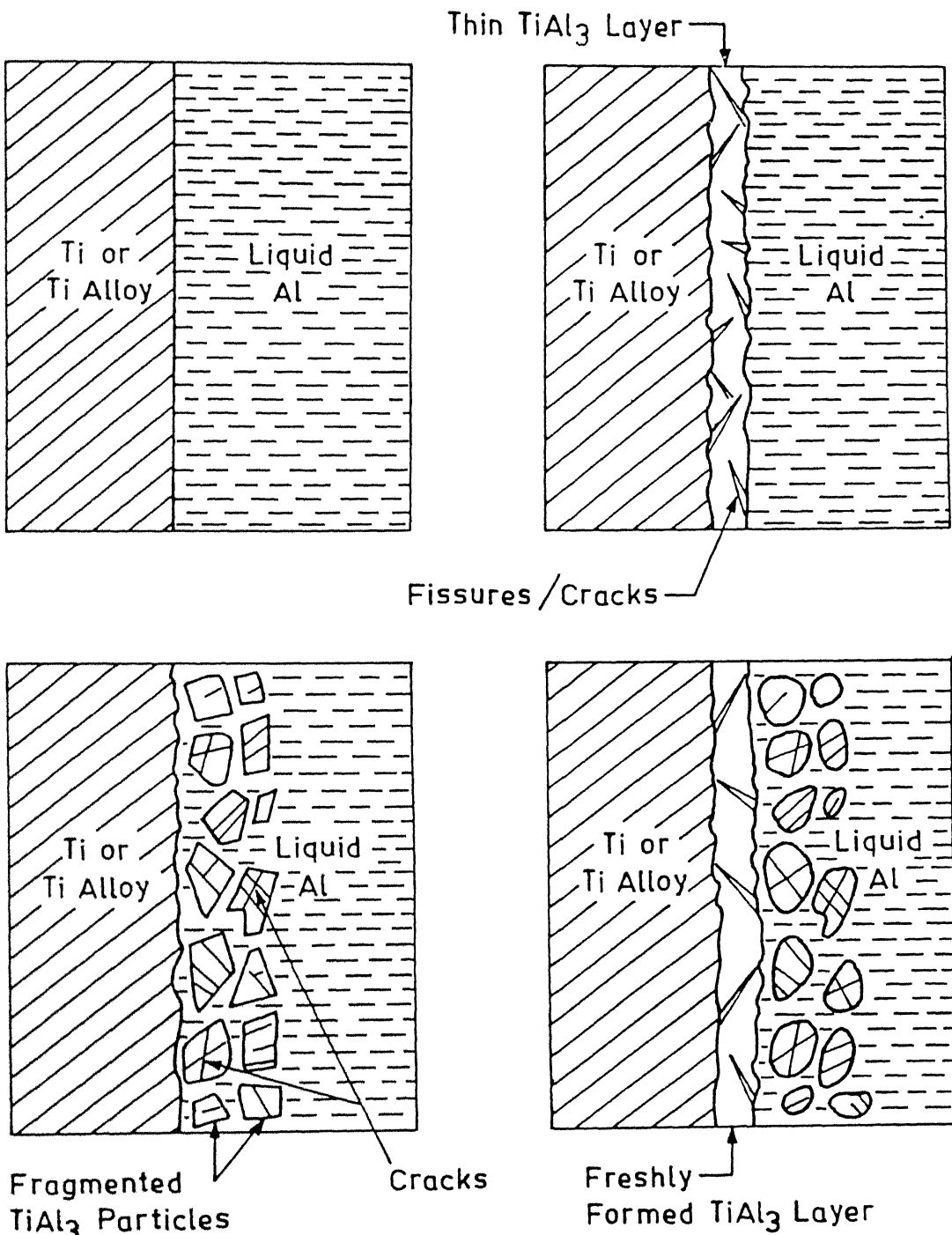
While increase in temperature of $TiAl_3$ reaction layer does not influence its cracking tendency, increase in its thickness induces more severe cracking (Figure - 5.17 and 5.19).

Depending on the modifications in the crystal structure and the associated modifications in the deformation modes, alloying elements present in $TiAl_3$ either increase or decrease its tendency towards cracking. For example, it is known that alloying elements such as Fe, Ni, Cr, Mn, Cr etc., which bring about the DO_{22} -to- $L1_2$ transformation in $TiAl_3$ result in less severe cracking in view of the more amount of slip systems in the $L1_2$ structure (Section-2.24) [66-69].

In the present case, presence of the alloying element V is expected to cause less severe cracking due to the improved deformation modes found in VAl_3 base compound [142]. After growing to a finite thickness, the reaction product which initially remains adherent to the solid titanium substrate [Figure-5.19(a)] undergoes its decohesion as shown in Figure-5.19(b). The cracking of reaction layer on the Al side can be seen from the figure (Figure-5.19). Under such conditions, the reaction layer fragments gets detached from the solid titanium and, in turn, exposes fresh solid surface over which the chemical reaction between solid titanium and liquid aluminium can start again. The process of reaction layer formation, its fragmentation and formation of fresh reaction layer are schematically in Figure-6.4.

6.3 PHYSICAL PHENOMENA OCCURRING IN THE REACTION ZONE:

In view of the discussion given in Section-6.2 of the present chapter, the following events occurring in the reaction zone of couples during reaction synthesis can be visualized:



Mechanism of Aluminide Formation by Reactive Synthesis Between Solid Ti and Liquid Al.

Figure-6.4 Schematic diagram showing the reaction layer formation, its fragmentation and formation of the fresh reaction layer.

- (1) Formation of $TiAl_3$ by chemical reaction at the reaction interface,
- (2) Growth of the reaction layer by diffusion of Al through DO_{22} lattice of $TiAl_3$,
- (3) Fragmentation and detachment of the reaction layer as a consequence of its cracking after reaching a critical thickness,
- (4) Rise in temperature of the reaction interface due to the exothermic nature of the chemical reaction,
- (5) Development of thermal currents due to build up of thermal gradients in liquid Al ahead of the reaction layer,
- (6) Further fragmentation of the detached reaction layer and flow of aluminide particles in thermal currents,
- (7) Smoothening of aluminide particles by their dissolution in liquid Al,
- (8) Reprecipitation of aluminide particles from supersaturated liquid Al,
- (9) Neck formation between aluminide particles by solid state sintering at the end of the reaction.

Among above mentioned events while events (1), (4) and (5) respectively occur in parallel, remaining of them occur sequentially. These events are governed by various physical phenomena and bear considerable influence on the microstructural evolution of the reaction product. Events (1), (2) and (3) have already been developed in Section - 6.2, the remaining ones are

being discussed in the present section.

6.3.1 Exothermic Heat Evolution and Rise in the Reaction Interface Temperature:

The formation of aluminides by the reaction between liquid Al and other elements such as Ti, Ni, Fe, Nb and Zr has been studied by several researchers by reactive sintering experiments [20, 106-118]. It has generally been observed that the sintering of compacts is accompanied with an intense heat evolution which is generated as a consequence of intermetallic compound formation. Swelling of compacts as a result of intermetallic compound formation is also a commonly observed feature of reactive sintering experiments. For example, intense amount of swelling has been reported during reactive sintering of nickel aluminides [103]. Swelling during sintering of 53 wt. % Nb - 47 wt. % Al compacts has also been reported [118]. Similar accounts have been given for sintering of Ti-Al and Fe-Al powder compacts [110, 112, 21]. Rise in temperature of compacts has also been measured. Experimentally measured values of powder compact temperature, T_I , at different reaction temperatures during reactive sintering experiments for various systems are given in Table-6.2. In all the cases, a rise in temperature of the order of about 300 K above the reaction temperature can be noted.

In principle, the rise in temperature of the product/reaction interface formed can be estimated from thermodynamic calculations.

Table-6.2 Adiabatic temperatures recorded at reaction temperatures during reaction synthesis studies of different aluminide intermetallics and ceramic materials.

Compound synthesized	Reaction temperature (T_R) K	Adiabatic temperature (T_I) K	Reference
TiAl	823	1270	Petric, Yi and Moore [106]
TiC	1873	3075	Munir [141]
Fe - 28 at. % Al	925	1253	Rabin and Wright [12]
Fe - 50 at. % Al	925	1493	Rabin and Wright [12]
TiAl	942	1573	Rawers and Wresinkschi [113]
Ti - 30 at. Al	912	1112	Hahn and Lee [111]
Ti - 50 at. % Al	935	1751	Hahn and Lee [111]
Ti - 60 at. % Al	933	1383	Hahn and Lee [111]

Thus the temperature of the reaction interface, T_I , at the given reaction temperature T_R can be obtained using the equation

$$[\Delta H(T_R)]_{\text{TiAl}_3} = \int_{T_R}^{T_I} (C_p)_{\text{TiAl}_3} \, dT \quad \dots 6.7$$

where

$[\Delta H(T_R)]_{\text{TiAl}_3}$ = Heat of formation of TiAl_3 at T_R

$(C_p)_{\text{TiAl}_3}$ = Heat capacity of TiAl_3 at the temperature T_R .

However, since heat of formation of TiAl_3 is available only at the temperature of 298 K, the reaction interface temperature at 298 K is evaluated first in order to estimate T_I . The reaction interface temperature at 298 K (T_{298}) can be estimated as follows:

$$[\Delta H(298)]_{\text{TiAl}_3} = \int_{298}^{T_{298}} (C_p)_{\text{TiAl}_3} \, dT \quad \dots 6.8$$

where

$[\Delta H(298)]_{\text{TiAl}_3}$ = Heat of formation of TiAl_3 at 298 K

$(C_p)_{\text{TiAl}_3}$ = Heat capacity of TiAl_3 in the temperature range of 298 K - T_{298}

The reaction interface temperature T_I corresponding to the set reaction temperature T_R is then given by

$$\int_{298}^{T_I} (C_p)_{\text{TiAl}_3} \, dT = \int_{298}^{T_R} (C_p)_{\text{TiAl}_3} \, dT \quad \dots 6.9$$

where $(C_p)_{\text{TiAl}_3}$ refers to the heat capacity of TiAl_3 in the respective temperature ranges of the integral.

The value of $\Delta H(298)$ for the $TiAl_3$ forming reaction (eqn.-6.3) is reported to be -35.0 K Cal/g atom by Kubascheuski and Dench [143] and to be 34 K Cal/g atom by Eremenko et al. [128]. However, the first value is generally accepted [Petric and Moore] and hence has been used in the present calculation also. Value of heat capacity, C_p for $TiAl_3$ is not available. For the purpose of calculation of reaction interface temperature using eqn.-6.3 it was estimated from the heat capacities of the elements Ti and Al assuming that $TiAl_3$ obeys the Newmann-Kopp's [141]. The reaction interface temperature thus calculated for different reaction temperatures are shown in Table-6.3.

It can be noted from the above results show that the temperature raises above 1240K at the reaction temperature of 973K. Similarly, at the reaction temperature of 1373K, the rise in temperature of the reaction interface is 1609K.

In the above calculations regarding the estimation of the adiabatic temperature during reaction synthesis, it is generally assumed that the entire exothermic energy is absorbed by the reaction product itself [141]. However, in reality, some of the exothermic heat may be consumed in increasing the temperature of (i) the reaction product itself, i.e. $TiAl_3$, (ii) conductive dissipation through solid titanium and (iii) conductive and convective dissipation through liquid aluminium. Thus, when the reaction begins, and covers the entire Ti/liquid Al interface with a thin layer of $TiAl_3$, the contact between Ti and Al atoms is

e-6.3 : Variations of the reaction interface temperature (T_{ad}) with reaction temperature (T_R)

T_R (K)	T_I (K)
973	1240.7
1073	1332.0
1173	1423.9
1273	1516.3
1373	1609.2
1473	1702.2

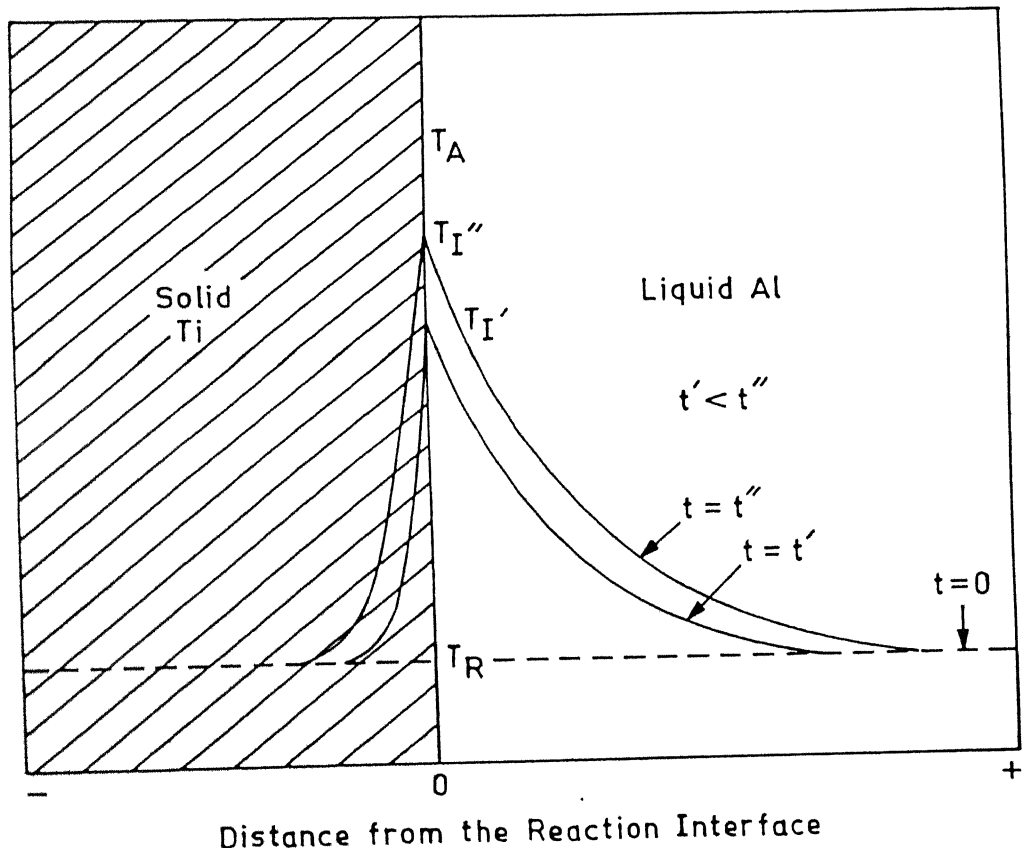
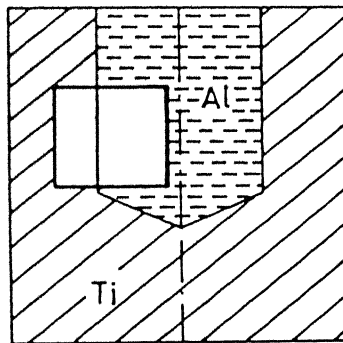
stopped and the further formation of $TiAl_3$ occurs by diffusion of Al through the lattice of $TiAl_3$ to the reaction interface. This second stage of chemical reaction after the arrival of Al atoms at the reaction interface occurs at a higher reaction temperature T_I such that $T_R < T_I < T_{ad}$. However, T_I is not constant and increases with growth of the reaction layer.

The schematic temperature profiles at the reaction interface, the adjacent solid Ti and liquid Al as a function of reaction time are shown in Figure-6.5. As the reaction layer of $TiAl_3$ grows with time the dissipation of heat generated at the reaction interface also incorporates the conductive heat transfer term through $TiAl_3$. Due to the complexity of the heat transfer problem as shown in Figure-6.5 and non-availability of the data regarding conductive and convective heat transfer, no estimation of reaction interface temperature was undertaken.

6.3.2 Build-up of Thermal Gradients and Convective Currents in Liquid Al:

It has been discussed in the previous section that exothermic energy evolution at the reaction interface raises its temperature to T_I which is much above the reaction temperature T_R . This sets up temperature gradients in liquid Al. Such a temperature gradient in liquid has been shown schematically in Figure-6.5.

Existence of thermal currents is a common phenomena in fluids having thermal gradients. Natural convection occurs in



T_R : Set Reaction Temperature

T_A : Adiabatic Temperature of the Reaction Interface

T_I' : Reaction Interface Temperature at $t = t'$

T_I'' : Reaction Interface Temperature at $t = t''$

Figure-6.5

Schematic diagram showing the temperature profiles of the reaction interface and the adjacent Ti and liquid Al.

such cases, due to the movement of fluid in response to local variations in density which arise from thermal gradient. In addition, the varying viscosity of the fluid also plays a role in thermal currents.

Under such circumstances, the flow inside the liquid Al can be described in terms of the equations of motion and continuity applicable to natural convection systems. Assuming steady state conditions, the continuity equation and the equation of motion are respectively [144]

$$\frac{\partial u_x}{\partial x} + \frac{\partial u_y}{\partial y} = 0 \quad \dots 6.10$$

and

$$u_x \frac{\partial u_x}{\partial x} + u_y \frac{\partial u_y}{\partial y} = \frac{\mu}{\rho} \left(\frac{\partial^2 u_x}{\partial y^2} \right) - \frac{1}{\rho} \frac{\partial p}{\partial x} + g_x \quad \dots 6.11$$

where ' u_x ' and ' u_y ' are the velocities of liquid Al in the x and y directions respectively (Figure-6.6).

' μ ' is the viscosity of liquid Al.

' ρ ' is the density of liquid Al.

The pressure gradient term, $\frac{\partial p}{\partial x}$, arises due to the variation in the density of liquid Al across the distance from the reaction interface. By involving the volumetric coefficient of thermal expansion $\beta = \frac{1}{\rho} \left(\frac{\partial \rho}{\partial x} \right)_p$ the equation of motion can be further simplified into the form

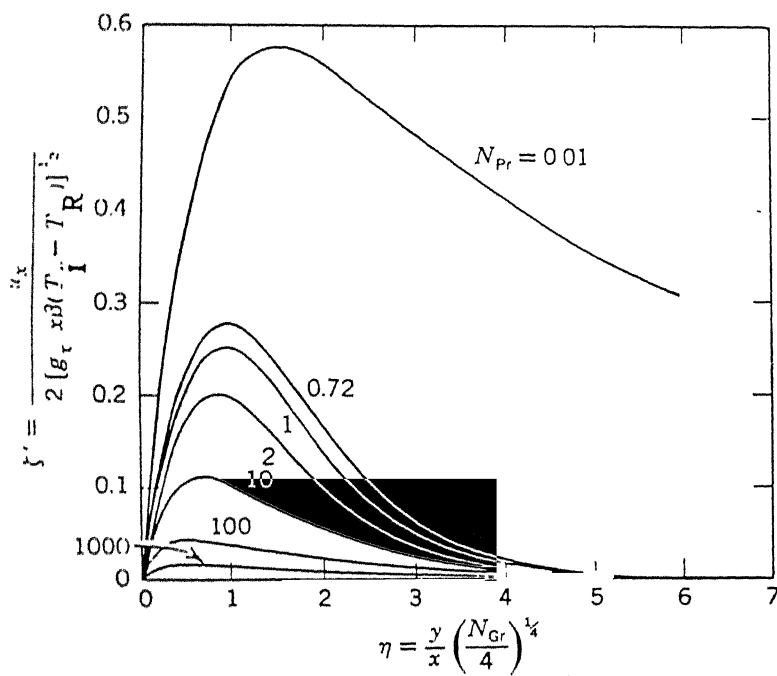


Figure-6.6

Schematic diagram showing the nature of the velocity profiles ahead of a hot solid surface (which is at a temperature of T_I) inside the fluid (initial fluid temperature is T_R).

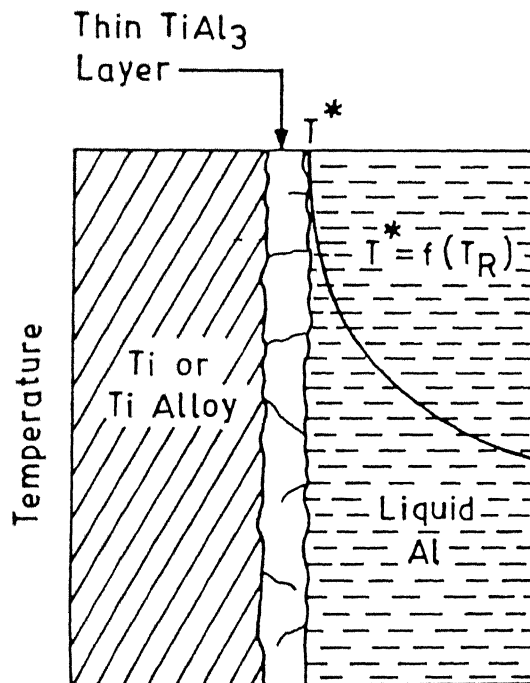
$$u_x \frac{\partial u_x}{\partial x} + u_y \frac{\partial u_x}{\partial y} = \nu \frac{\partial^2 u_x}{\partial y^2} + g_x \beta (T_I - T_R) \quad \dots 6.12$$

where ' T_I ' is the temperature at the reaction interface and ' T_R ' is the reaction temperature.

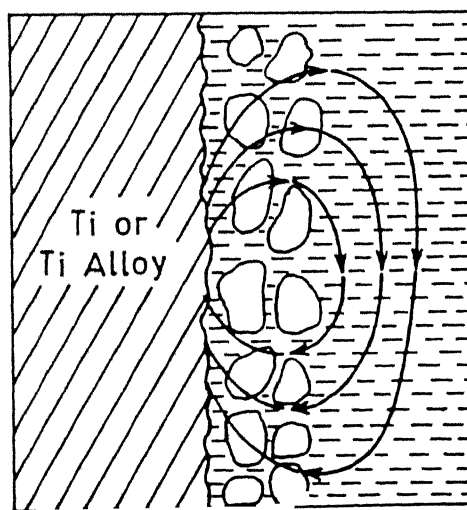
In order to solve for the temperature and velocity profiles inside the liquid Al, the above equation of motion must be coupled with the corresponding thermal energy balance equation and must be solved simultaneously.

Solutions for such equations have been obtained in the literature [144] for systems undergoing natural convection. The coupled equation of motion and thermal energy balance have been solved to get dimensionless temperature and velocity profiles by making use of dimensionless numbers. The nature of velocity profiles obtained are shown in Figure-6.6 for the case of flow when a vertical plate at a temperature T_I is immersed into a fluid having a temperature, T_I . As shown in the figure, the velocity profiles go through a maximum at some distance away from the hot surface. Similarly, the nature of the circulating loops in the present case are shown in Figure-6.7.

It has already been discussed in Section-6.2.2, that the thin reaction layer of $TiAl_3$ develops internal cracks leading to its fragmentation and decohesion. The fragmented $TiAl_3$ particles thus enter liquid Al. Under the influence of thermal gradient driven convective currents these separated $TiAl_3$ particles in liquid Al get carried away from the reaction interface towards Al



$T^* : 1523 - 1623 \text{ K}$
 [Rawers et.al]



$d_{\text{Al}} = d(T^*)$; $\mu_{\text{Al}} = \mu(T^*)$

Figure-6.7

Schematic diagram showing the nature of the circulating loops thermal currents inside the dispersed reactor domain.

side of the reaction zone. The formation of the dispersed reaction domain can thus be understood.

6.3.3 Smoothening of $TiAl_3$ Particles Surfaces by Selective Dissolution:

Figure-6.8 shows the Al-rich portion of the Ti-Al phase diagram. As shown in the figure, though the solubility of Ti in Al is negligible at lower temperatures limited solubility exists in liquid Al and it increases with increase in temperature. It has already been said that the reaction layer gets fragmented and aluminide particles enter liquid Al and are subsequently carried away under thermal currents. Enrichment of liquid Al with Ti, as dictated by the phase diagram, can occur by selective dissolution of $TiAl_3$ in liquid Al. Dissolution of $TiAl_3$ occurs as a result of higher chemical potential $\Delta\mu$ which can arise at several regions from different factors such as (i) difference in curvatures of regions of aluminide particles, (ii) higher defect concentrated at grain boundaries and other regions and (iii) cracks.

The selective dissolution of $TiAl_3$ particles along pre-existing cracks, grain boundaries and regions of higher defect densities may lead to their disintegration as shown in Figure-6.9. Thus, the selective dissolution of $TiAl_3$ particles occurs along cracks/grain boundaries by liquid Al which penetrates along the cracks due to capillary forces and along grain boundaries due to their higher local concentration of defects. Thus, $TiAl_3$ particles, which initially are coarse after their fragmentation from the reaction layer, transform into particles of smaller size.

The selective dissolution of $TiAl_3$ particles of irregular shape and sharp edged surfaces having sharp edges and corners arises from the local differences in their curvatures which, in turn, leads to differences in their chemical potential. These differences can be predicted by the well-known Laplace equation. Thus

$$\Delta\mu = \Delta p \Omega \quad \dots 6.13$$

where

Ω is the atomic volume of the solid material, and Δp is the pressure excess due to the curved nature of the solid liquid interface and is given by

$$\Delta p = \gamma \left[\frac{1}{R_1} + \frac{1}{R_2} \right] \quad \dots 6.14$$

where ' γ ' is the solid/liquid surface energy, and R_1 and R_2 are the two principal radii of curvature.

From the Laplace equation it can be easily seen that the surface areas having sharp edges and corners will preferentially dissolve and give rise to the smoothening of particle surfaces which to start with after their separation from the reaction layer are expected to be irregular in shape.

6.3.4 Reprecipitation of $TiAl_3$ particles from the Al melt:

As shown in the Al-rich portion of the Ti-Al phase diagram (Figure-6.8), the solubility of Ti is very limited even at higher temperatures (maximum of 1 at. % Ti at a temperature of

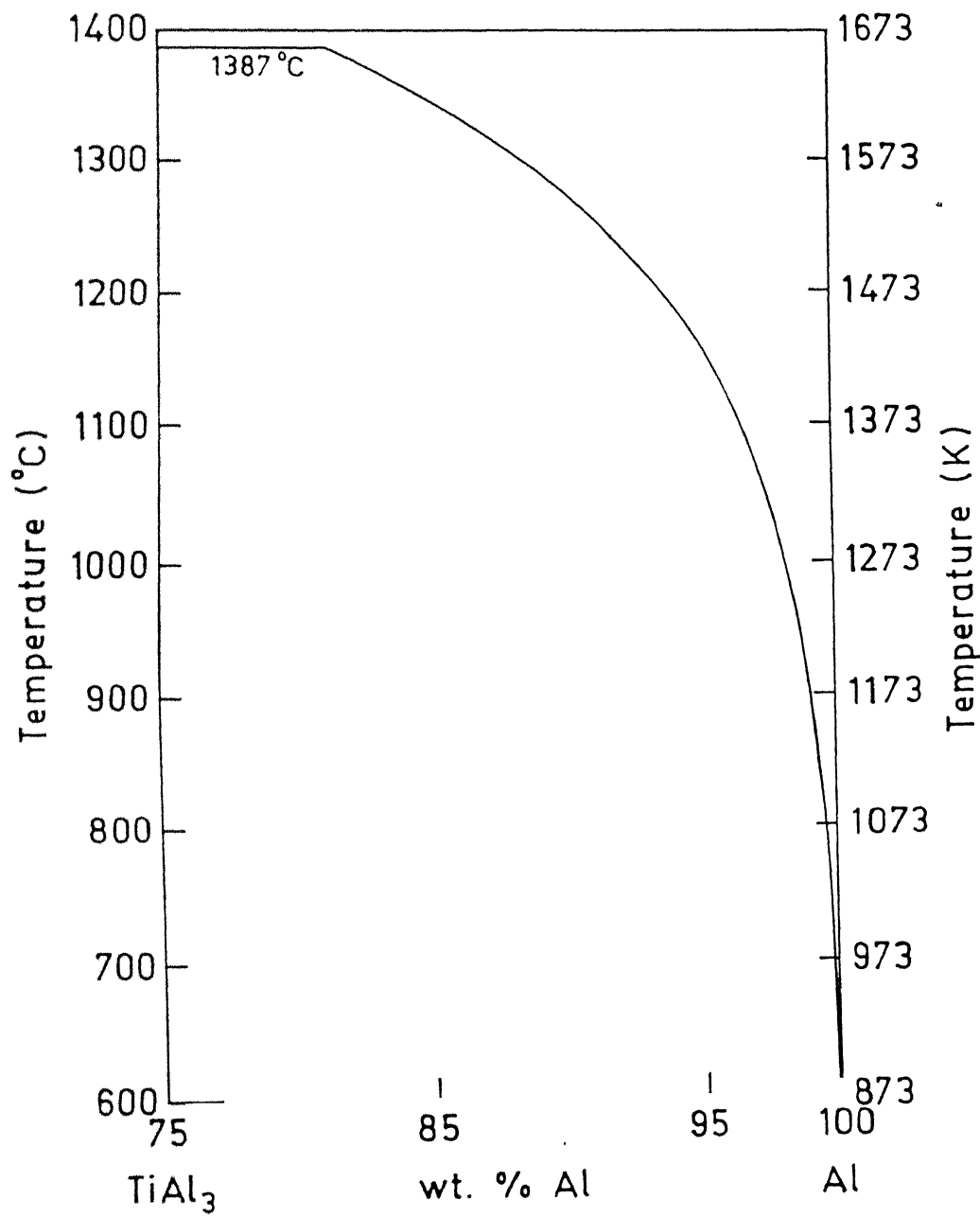


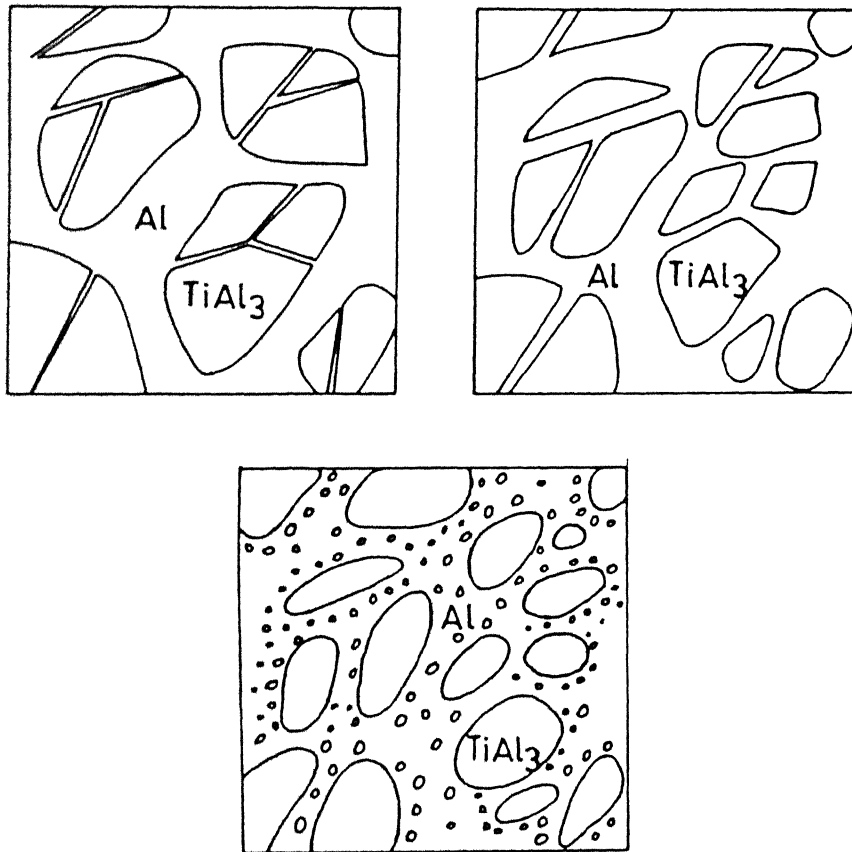
figure-6.8

The Al-rich portion of the Ti-Al phase diagram showing the variation of solubilities of Ti in liquid Al

173 K). Thus whenever the composition of liquid Al exceeds the respective solubility limit, the excess Ti is rejected from the liquid Al in the form of $TiAl_3$ particles giving rise to reprecipitation. Reprecipitation process can take place in two different ways. In the first case, reprecipitation can occur by homogeneous nucleation throughout the liquid Al whenever the Ti content exceeds the solubility limit at that particular temperature [Figure-6.9(c)]. Alternatively, reprecipitation can also occur by heterogeneous nucleation on the existing larger particles of $TiAl_3$.

6.3.5 Neck formation by solid state sintering:

As soon as the entire amount of liquid Al provided for reaction is consumed, solid state sintering mechanisms become operational leading to development of necks between the contacting particles. The driving force for material transport under this pressure less sintering is the surface energy. Depending on the size of the particles or the amount and distribution of porosity, the surface energy varies. Also the grain boundary energy is also known to provide driving force for sintering [140]. Since the surface energy is reduced when the concave regions are filled in, the grain boundary regions act as sinks for material source [140]. The convex particle surfaces such as solid-pore interfaces act as material source.



Schematic Diagram Showing Dissolution and Reprecipitation of TiAl_3 in Liquid Al.

ure-6.9

Showing the process of particle disintegration along the preexisting cracks.

6.4 MICROSTRUCTURAL VARIATIONS OBSERVED IN THE DISPERSED REACTION DOMAIN:

6.4.1 Effect of reaction time and temperature on the reaction zone thickness and the amount of reaction product:

The variation of the average volume fraction of $TiAl_3$ particles in the dispersed reaction domain with respect to time was shown in Figure-5.35. Similarly, the variation of reaction zone thickness as a function of reaction time at different reaction temperature was shown in Figure-5.2.

The procedure for estimation of total mass " $m_p(i)$ " of aluminide formed per unit area of the reaction interface has been described in Chapter-4. The results thus obtained for the variation of $m_p(i)$ with reaction time at different reaction temperatures are shown in Figure-6.10.

As explained in sections-6.2.1 and 6.2.2, the amount of $TiAl_3$ in the reaction zone of couples reacted under specific time and temperature conditions is governed by two factors, (i) formation of $TiAl_3$ by chemical reaction at the reaction interface and (ii) growth of the reaction layer by the diffusion of Al towards the reaction interface through the DO_{22} lattice of $TiAl_3$. As both kinetics of chemical reaction, as well as diffusion of Al through $TiAl_3$ lattice, increase with reaction temperature the reaction product formed at a given time increases with reaction temperature. Obviously, the amount of $TiAl_3$ formed at a given temperature increases with reaction time.

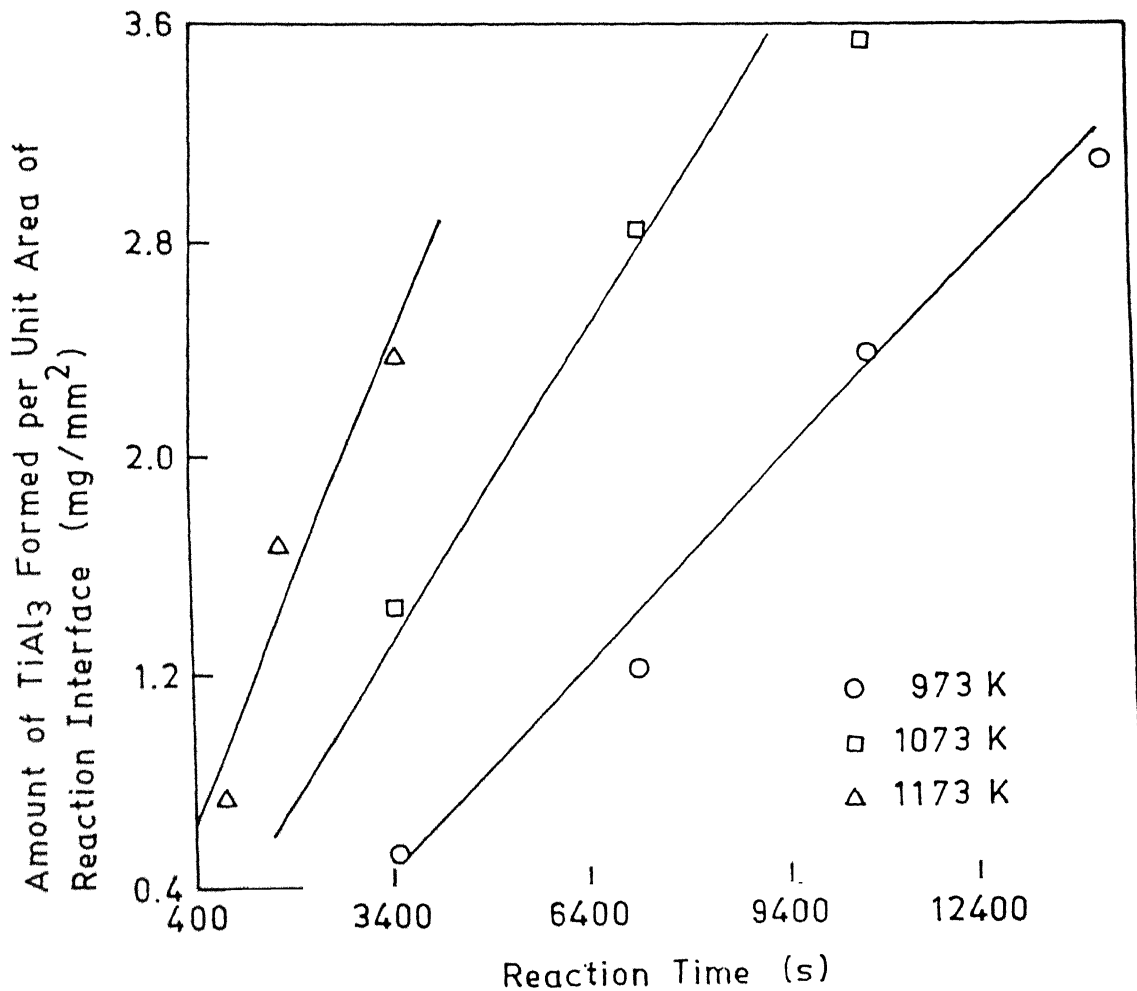


Figure-6.10 Variation of total amount reaction product formed per unit area of the reaction interface with time at different reaction temperatures.

As discussed earlier, the reaction layer after its fragmentation and separation, gave rise to $TiAl_3$ particles which were carried away far from the reaction interface under the influence of convective currents and thus resulted in the formation of the dispersed reaction domain. The thickness of the reaction zone is therefore expected to be strongly influenced by the distance over which convective currents persist. A brief background of the circumstances under which convective currents are generated is given in 6.3.2. The distance over which thermal currents persist is governed by the temperature gradient set up in liquid Al ahead of the reaction interface. The temperature gradient, in turn, depends on the interface temperature, T_I , which as explained in section-6.3.1, attains an equilibrium value at a given reaction temperature such that $T_R < T_I < T_{ad}$. Therefore, at a given reaction temperature, the distance over which the convective currents persist remains roughly constant. The linear variations of reaction zone thickness with reaction time at a given reaction temperature can thus be understood.

Further, it is clear that a higher reaction interface temperature (T_I) will be attained at higher reaction temperatures leading to a steeper temperature gradient. Thus the distance over which convective current carry aluminide particles away from the reaction interface increases with increase in reaction temperature. Therefore, it is expected that the slope of reaction zone versus reaction time plots increases as the reaction temperature increases. This indeed was observed in the present study and has been shown in Figure-5.2.

6.4.2

Variations of volume fraction of $TiAl_3$ particles with distance from the reaction interface:

As presented in the section-5.3.3.5 (Figures 5.31 and 5.32), the volume fraction of $TiAl_3$ showed a systematic variation with distance from the reaction interface going through a maximum under each reaction condition. In addition, the distance at which maxima in the volume fraction occurred was also found to be characteristic of specific reaction condition. Both maximum and minimum volume fractions increased with reaction temperature and reaction time (Figure-5.33). This increase can be understood in terms of the total amount of $TiAl_3$ formed after longer reaction time and enhanced kinetics of $TiAl_3$ formation at higher reaction temperatures. It was also shown in section-5.3.3.5 that the distance at which maxima in the volume fraction occurred increases with reaction time at a given reaction temperature.

It should be recalled that the volume fraction, V_v at a given distance, x from the reaction interface was measured by quantitative metallography. As shown in Figures-5.42 and 5.46, particles of smaller size were found near the reaction interface and the particle size increased up to the mid regions of the dispersed reaction domain. As shown in Figure-5.33, minimum and maximum volume fractions in a given Ti/Al couple had a difference of about 15%. The maxima in V_v versus x curves occurred because of larger number of coarser particles/unit volume in those regions of the dispersed reaction domain. On the other hand, in regions near the reaction interface, larger number of particles were found to be in the size range of 0-8 μm . The presence of these finer

particles lead to smaller volume fraction of aluminide particles near the reaction interface. In contrast, coarse particles were observed in regions at the farther end of the dispersed reaction domain but they dispersed more sparsely. The variation in v_v versus x curve mainly occurred because of the particle size distribution present in the dispersed reaction domain.

As discussed section-6.3, the particle size variation in dispersed reaction domain of reaction couples arises due to the following factors:

- (i) transportation of particle separated from the fragmented reaction layer under the influence of convective currents,
- (ii) disintegration and smoothening of particles by their dissolution in liquid Al,
- (iii) reprecipitation of newer particles from the supersaturated liquid and
- (iv) particle coarsening by Ostwald ripening.

At the beginning of the reaction there are no particles in the liquid, and therefore, it's viscosity is low. Particles formed initially are thus easily carried away from the reaction interface over the larger distances. This was clear from micrographs of Ti-Al-V alloy/Al and Ti-Al-Mo-Zr-Si alloy/Al couples near the end of the reaction dispersed domain, which showed particles with flat surface, sharp edges and corners and internal and surface cracks [Figures-5.28(a)-5.28(d)] indicating early stages of their formation by separation from the reaction

layer. However, with the progress of the reaction, the population of aluminide particles separating from the reaction layer increases, leading to the formation of a mushy zone near the reaction interface. The effective viscosity of the liquid, therefore, increases with reaction time making transportation of aluminide particles more and more difficult. Thus particles formed during subsequent stages of reaction could not easily move to larger distances and were pinned down to the mid region of the dispersed reaction domain. The fall in the velocity profile after reaching a maxima, as shown in Figure-6.6, also played a role in inhibiting the transportation of particles to far of distances leading to their lesser number in those regions.

As far as the dissolution of particles in liquid Al is concerned, it's extent is governed by their solubility in the liquid, which increases with their reaction temperature and higher chemical potential arising from sharp edges and corners and the local concentration of defects such as grain boundaries and other defects such as dislocations. The dissolution rate is also influenced by the presence of alloying elements. The microstructural examination of particles by SEM and TEM indeed showed the presence of sharp edges, grain boundaries and highly dislocated areas in $TiAl_3$ particles (Figures-5.20, 5.21 and 5.24-5.28).

Since the temperature was highest near the reaction interface, the extent of disintegration of particles and smoothening of their surface by dissolution was expected to be

more prominent in those regions. Particles of finer size ($< 8 \mu\text{m}$) and smoother surface were indeed observed in regions near to the reaction interface (Figure-5.42).

In order to understand the effect of reaction time and temperature on the maxima with respect to the reaction zone thickness in case, normal distance of peak position with respect to reaction zone thickness were calculated from the data shown in Table-5.9a and Table-5.9b. Results obtained for different reaction temperatures are shown in Figure-6.11. These results indicate that the normalized distance at which volume fraction occurs has a tendency to go through a minimum (around the mid region) with respect to reaction time. Such a behavior can again be understood in terms of convective current present in the dispersed reaction domain. Thus, when the reaction time is small, the number of particles present in the liquid is relatively lower leading to an effectively less viscous liquid. The majority of particles can therefore move over larger distances creating the peak beyond mid region of the dispersed reaction domain. However, with increase in reaction time, the number of aluminide particles in the liquid increases making it more viscous. If the reaction time is not high enough to cause disintegration and smoothening of the particles, they experience more difficulty in being transported over larger distances. The normalized peak position for their volume fraction thus falls. In contrast when the reaction time increases further, their transportation becomes easier due to their disintegration and smoothening of surfaces.

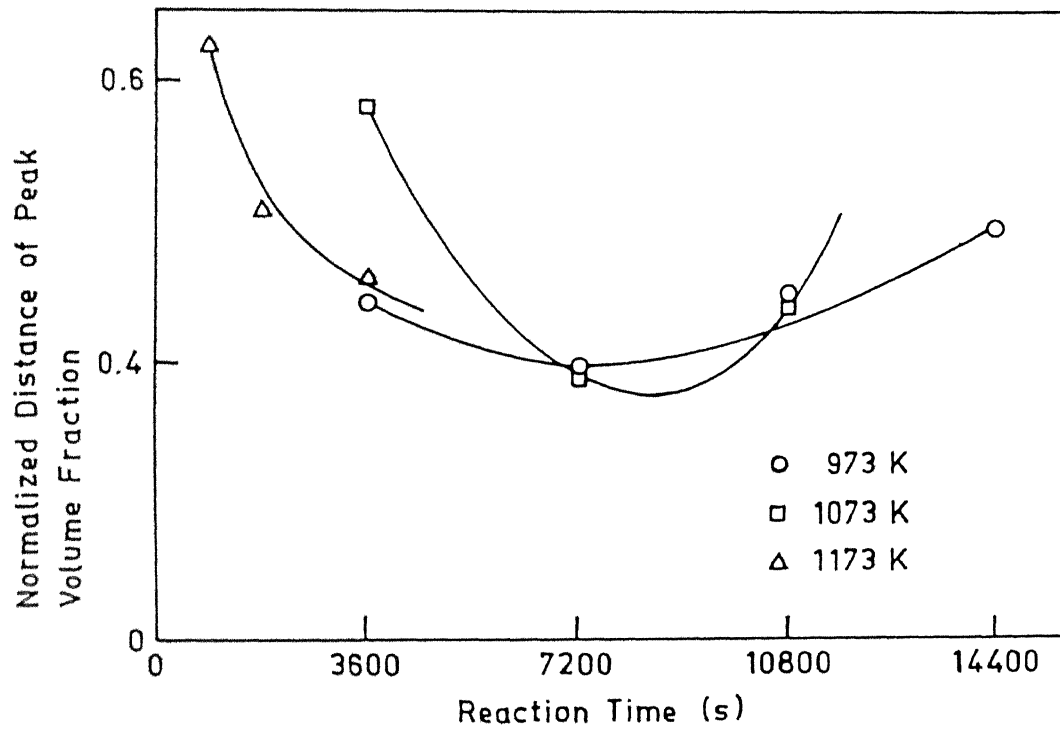


Figure 6.11

Variation of normalized distance of peak volume fraction with reaction time at different reaction temperature.

6.4.3

Variation of particle shape in the dispersed reaction domain:

Results shown in Figures-5.24 of chapter-5 clearly showed that a variation in particle shape occurred in the dispersed reaction domain of Ti/Al, Ti-Al-V alloy/Al and Ti-Al-Mo-Zr-Si alloy/Al couples. While the particles were more or less equiaxed in case of Ti/Al couples, particles in Ti alloy/Al couples showed elongated shapes of largely varying aspect ratio as function of distance from the reaction interface (Figure-5.29). In general, the particle surface smoothness in pure Ti/Al as well as Ti alloy/Al couples decreased with increasing distance from the reaction interface.

In terms of physical phenomena explained section-6.3, the morphology of aluminide particles must be understood in terms of (i) their fragmentation from the reaction layer, (ii) their disintegration into finer particles and (iii) their selective dissolution from sharp corners and grain boundaries. As far as fragmentation reaction layer is concerned, numerous cracks, perhaps in preferred crystallographic orientations were readily observed in the reaction layer as well as very large number of particles. The TEM micrograph shown in Figure-6.12, indicates the nature of cracking inside $TiAl_3$ particle leading to their angular morphology.

As discussed in the previous section, particles fragmented from the reaction layer had the driving force for their transportation away from it under the influence of convective

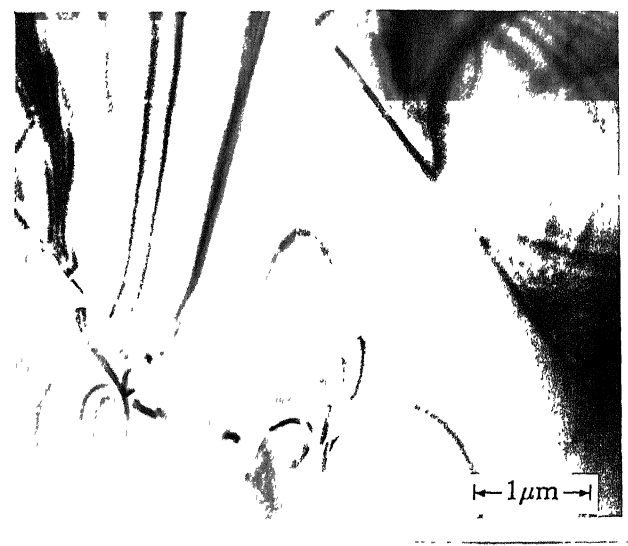


Figure-6.12 TEM micrographs showing the process of particle disintegration leading particles of sharped corners.

currents. These particles, further underwent disintegration during their stay in liquid by selective dissolution at preexisting cracks/grain boundaries/other defect regions. The tendency to undergo such changes however decreased as the temperature of liquid Al surrounding them decreased. Therefore, particles farther away from the reaction interface, being at lower temperatures retained their size and sharp corners and preexisting cracks. On the other hand, particles near the reaction interface more readily went through such changes. Results of the present study show that the presence of the alloying additions viz. V in $TiAl_3$ phase particles formed in Ti-Al-V alloy/Al couple and (Mo + Zr + Si) in Ti-Al-Mo-Zr-Si alloy/Al couple, had a mark influence on the dissolution rate in the liquid. It appears that the rate of dissolution of $TiAl_3$ base alloy in liquid Al considerably decreases by the presence such alloying addition. Due to lesser dissolution rate, the particles retained their sharp edges and angularity. This lead to a wider change in their morphology across the dispersed domain. This influence was more prominent in Ti-Al-Mo-Zr-Si alloy/Al couples in which a variation of the aspect ratio from 1.2 to 4.5 was observed across the dispersed reaction domain.

6.4.4 Variation of particle size distribution and mean particle size with distance from the reaction interface:

As shown in section-5.3.3.7 (Figure-5.42), the local particle size distribution varied with distance from the reaction interface. It was observed that while most of the particles near to the interface belonged to the finer size range (0-8 μm), those

at distances away from the reaction interface showed a more uniform distribution with more or less equal population in all the size ranges. In contrast, the mid regions showed a bimodal size distribution.

The existence of a size distribution of $TiAl_3$ particles in the dispersed reaction domain can be understood in terms of motion of different size particles under convection current and reprecipitation and particle coarsening processes which have already been explained. Figure-5.46 shows the local mean particle size as a function of distance from the reaction interface. Since a roughly bimodal type of distribution existed near the mid regions of the dispersed reaction domain (Figure-5.42), and large number of particles were found to be $< 4 \mu m$ in size, the mean size was also calculated for particles lying the range of $4-24 \mu m$ in size. Such a variation has been represented by curve B in Figure-5.46. These results clearly indicate that the particle size does not increase beyond the mid region of the dispersed reaction domain. While as explained earlier, particles farthest from the reaction interface have the least tendency to disintegrate and therefore retain their coarser size, those present at mid regions undergo these changes. Therefore, the presence of larger particles in mid regions can be explained in terms of particle coarsening. On the other hand, presence of the large number of finer particles near the reaction interface can be explained in terms of the higher dissolution rate in these regions.

6.4.5

Variation of average particle size with reaction temperature and time:

It was shown in Figure-5.40 and 5.41 that the particle size distributions in the dispersed reaction domain of Ti/Al reaction couples also varied with reaction temperature and time. As shown in Figure-5.41, the fraction of the finer particles in the size range of 0-4 μm gradually decreased with reaction time. At the same time the number of particles in higher size ranges increase. These observations clearly bring out the role of particle coarsening occurring in the dispersed reaction domain with respect to the reaction time. Further, the presence of roughly a bimodal size distribution highlights the role of simultaneously operating dissolution, reprecipitation and coarsening phenomena. The role of temperature in the evolution of particle size distribution can also be understood.

6.4.6

Particle Coarsening in Fully Reacted Couples:

When the liquid Al is still present, the TiAl_3 particles grow by the process similar to those occurring in conventional liquid phase sintering which have been explained in sections-6.4.2 - 6.4.4. Thus, the smaller TiAl_3 particles which are the result of the secondary disintegration processes are expected to dissolve preferentially and reprecipitate on larger TiAl_3 particles. This is similar to the grain growth occurring during final stages of conventional liquid phase sintering [140]. On the other hand, the microstructures of reaction zones formed in fully reacted couples, i.e. the entire Al provided in the couple is consumed, are shown in Figure-6.13(a) to 6.13(c). Figure-6.13(b) clearly shows the

particle coarsening. Similar to characteristic features of rapid grain growth during high temperature solid state sintering by the particle coalescence, higher reaction temperature in the present case also lead to increase in the average size of the resulting $TiAl_3$ particles by grain growth. This is clearly demonstrated in Figure-6.13(a) which shows that the reaction product consisted of $TiAl_3$ particles having several necks due to the sintering occurring between them.

6.5 FORMATION OF Ti_9Al_{23} IN PURE Ti/Al COUPLES AT THE REACTION TEMPERATURE OF 1373 K:

As discussed earlier in Section 6.1, the XRD patterns obtained from pure Ti/Al couples reacted at different temperatures revealed that (i) $TiAl_3$ was the only Ti-Al intermetallic compound formed during reaction synthesis in the temperature range of 973 K - 1273 K ($700^\circ C$ - $1000^\circ C$) and (ii) $TiAl_3$ as well as Ti_9Al_{23} phases formed at the reaction temperature of 1373 K ($1100^\circ C$). Reasons for the formation of $TiAl_3$ at lower reaction temperatures and the mechanism for its formation have already been discussed in Sections 6.1.1 and 6.1.2 respectively. Reasons and mechanisms of Ti_9Al_{23} formation at 1373 K ($1100^\circ C$) and its consequence on microstructural evolution in the reaction zone of couples will be discussed in the present section.

6.5.1 Mechanism of Formation of Ti_9Al_{23} :

It has already been discussed that the chemical reaction leading to the formation of $TiAl_3$ is exothermic in nature. Thus, when the exothermic reaction begins at the reaction interface, the

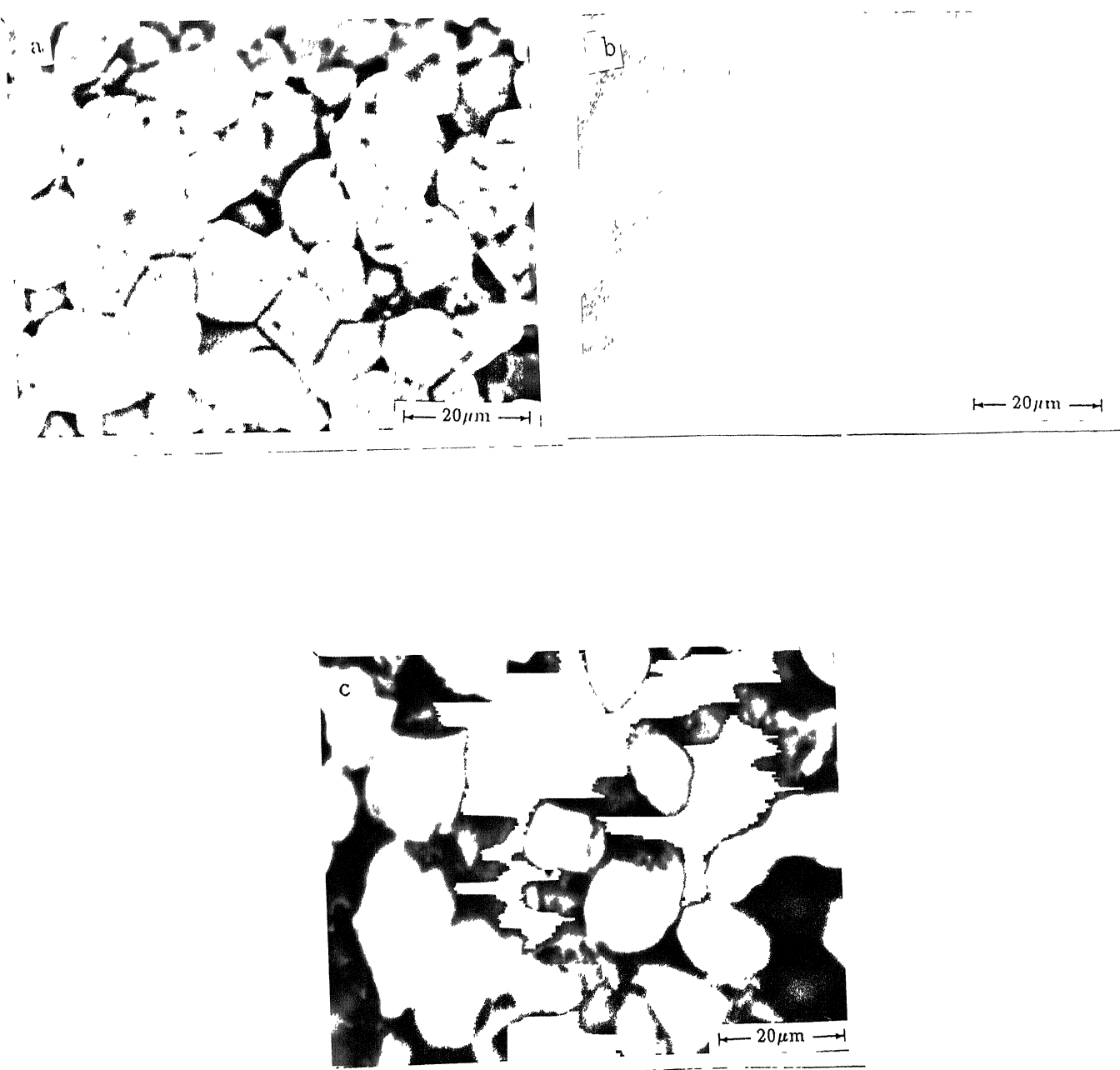


Figure 6.13 SEM microstructures of TiAl₃ particles in fully reacted couples; reacted at (a) 1073 K (800°C) for 14400 sec (4 hour), (b) 1173 K (900°C) for 7200 sec (2 hour) and (c) 1273 K (1000°C) for 3600 sec (1 hour).

exothermic energy released at the reaction interface may be consumed in increasing the temperature of (i) the reaction product itself, i.e. $TiAl_3$, (ii) conductive dissipation through solid Ti and (iii) conductive and convective dissipation through liquid Al. Subsequently, as the reaction layer grows and its thickness increases the heat dissipation also involves the conductive heat transfer through the reaction layer of $TiAl_3$.

In calculations made for the estimation of the adiabatic temperature during reaction synthesis, as shown in Section 6.3.1, it is generally assumed that the entire exothermic energy is absorbed by the reaction product itself [141]. However, it is more realistic to assume that a part of the heat generated is dissipated by conduction through solid Ti and a part also by conduction as well as convection through liquid Al.

The nature of the convective heat transfer through liquid aluminium, however, is a quite complex. As discussed in Section 6.3.2, the exothermic reaction occurring at the Ti/Al reaction interface increases the interface temperature which, in turn, establishes thermal gradients in liquid Al. The presence of thermal gradients is expected to trigger thermal currents in the liquid Al carrying the adjacent liquid, which is at a higher temperature, away from the reaction interface. The presence of such thermal currents will be increasing the effectiveness of the convective heat transfer. However, the dispersion of $TiAl_3$ particles in liquid Al, which arises from the fragmentation of thin separated layer of the reaction product, creates a mushy zone

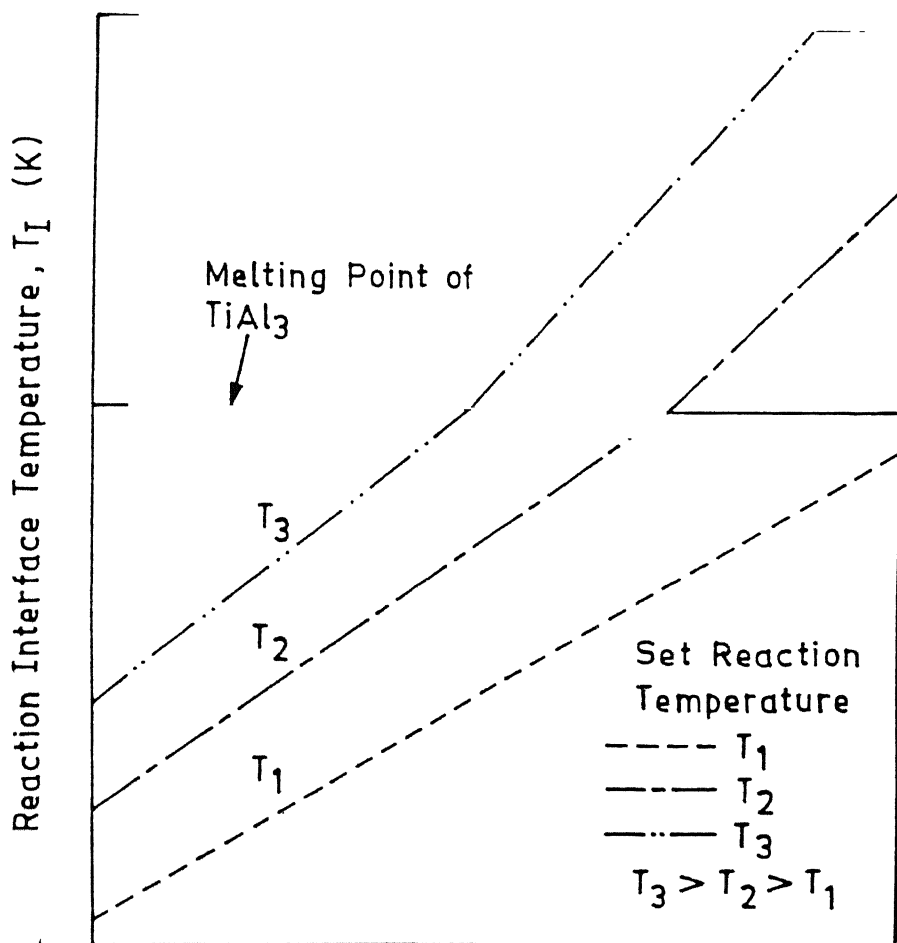
in the liquid ahead of the reaction interface. These $TiAl_3$ particles start flowing along the paths of thermal currents and get transported away from the reaction interface. Due to the simultaneously operating physical phenomena involving (i) particle transportation along thermal currents, (ii) dissolution and reprecipitation of $TiAl_3$ particles in liquid Al and (iii) particle coarsening, the population, the size distribution and the morphology of particles in the mushy zone continuously change as a function of the distance from the reaction interface. Thus the mushy zone in liquid Al is not homogeneous in terms of population of particles and their sizes and shapes. Obviously, the presence of a mushy zone in liquid Al causes some resistance against the convective heat transfer through liquid Al.

The analysis of heat transfer under such complex conditions requires considerable computational efforts and, due to the non-availability of the reliable data regarding heat transfer coefficient in the liquid/mushy zone, it could not be undertaken in the present study. However, by assuming that a finite fraction of the exothermic energy released at the interface is consumed in conductive and convective heat transfer through solid Ti and liquid Al, the situation shown schematically in Figure-6.5 results. It can be seen from this figure that the reaction temperature T_R is maintained uniformly through solid Ti and liquid Al at $t = 0$. Once the reaction begins and if we assume that the entire exothermic energy is utilized by the reaction product, the temperature of the reaction interface may shoot up to the adiabatic temperature T_A . However, in reality this is not the

case and due to the heat losses from the reaction interface to the surroundings the temperature of the interface reaches T_I , at time $t = t'$ which is lower than T_A . Therefore, due to the temperature rise of the reaction interface from T_R to T_I , the next stage of reaction, say at $t = t''$, occurs at the new reaction temperature T_I . Since T_I , is greater than T_R a higher amount of exothermic energy is released during this stage of reaction due to which the interface reaction temperature rises to T_I'' . The sequence of these events continues with subsequent stages of reaction occurring at higher and higher temperatures till an equilibrium stage is reached.

A schematic variation of the reaction interface temperatures for various starting reaction temperatures has been shown in Figure-6.14. It can be seen that the melting of the reaction product, i.e. $TiAl_3$, may occur at some specific temperature as the reaction temperature increases.

The reason for the formation of Ti_9Al_{23} at the reaction temperature of 1373 K can be understood in terms of the exothermic nature of the chemical reaction and the mechanisms involved with the heat transfer of the exothermic energy from the reaction interface. It has also been explained that the actual temperature of the reaction interface, T_I , is always higher than the set reaction temperature, T_R , and the fraction of the exothermic heat utilized in increasing the temperature of the reaction product increases with the progress of reaction, i.e. with the increase in thickness of the $TiAl_3$ reaction layer as well as that of the mushy

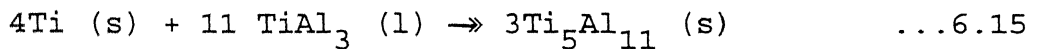


Fraction of Exothermic Energy Utilized in Rising Reaction Interface Temperature

Figure 6.14 Schematic variation of reaction interface temperature for various starting reaction temperatures.

zone established in the dispersed reaction domain. Therefore, if the reaction temperature is high enough and heat-transfer characteristics of the reaction interface to its surroundings are such that the reaction interface temperature is increased beyond the melting point of $TiAl_3$, the freshly formed reaction product would be expected to undergo an incipient melting. However, due to the poor thermal conductivity of $TiAl_3$ the temperature of the adjacent $TiAl_3$ film is not expected to rise beyond its melting temperature throughout its width.

Therefore, after the progress of the reaction for some time the newly formed $TiAl_3$, due to its inability to efficiently dissipate away the released exothermic energy, undergoes melting and separates out the initially formed and grown film of $TiAl_3$ from the Ti interface. The Ti interface thus gets wetted by the liquid $TiAl_3$. As an interaction of liquid $TiAl_3$ with solid Ti, the following chemical reaction leading to the formation of Ti_5Al_{11} may undergo



As shown in the Al rich portion of the Ti-Al phase diagram according to Raman and Schubert [60], Figure-6.15, and listed as eutectoid and peritectoid reactions (reactions 4 and 5) in Table-6.4, the formation of Ti_9Al_{23} can be explained due to the presence of Ti_5Al_{11} . The formation of Ti_9Al_{23} at the reaction temperatures of 1373K and possibly temperatures higher than 1373 K can thus be explained in terms of the incipient melting of freshly

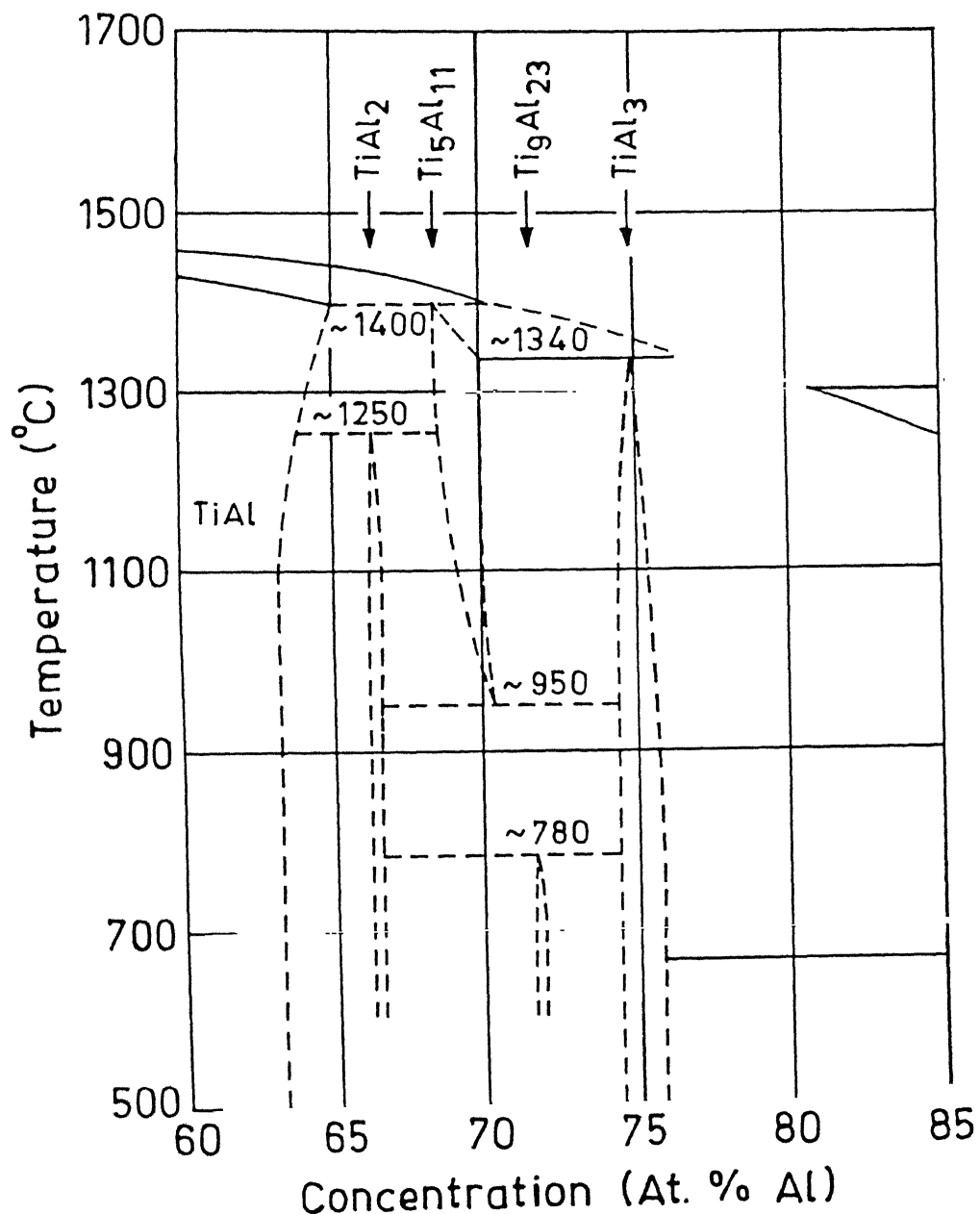


Figure 6.15 The Al-rich portion of the Ti-Al phase diagram [60].

Table 6.4 : Reactions occurring in the Al-rich portion of the Ti-Al phase diagram according to Raman and Schubert [60]

	Reaction	Temperature (K)	Nature of reaction
1.	$TiAl + liquid_1^a \rightarrow Ti_5Al_{11}$	~1673	Peritectic
2.	$Ti_5Al_{11} + liquid_2^b \rightarrow TiAl_3$	~1673	Peritectic
3.	$TiAl + Ti_5Al_{11} \rightarrow TiAl_2$	~1523	Peritectoid
4.	$Ti_5Al_{11} \rightarrow TiAl_2 + TiAl_3$	~1223	Eutectoid
5.	$TiAl_2 + TiAl_3 \rightarrow Ti_9Al_{23}$	~1053	Peritectoid

^aLiquid₁ of composition Ti-70.34 at.% Al.

^bLiquid₂ of composition Ti-76.88 at.% Al.

formed $TiAl_3$. The fact that the formation of this phase requires the availability of Ti_5Al_{11} which, in turn, requires the availability of liquid $TiAl_3$ and Ti_9Al_{23} is not found to be forming in samples reaction synthesized at lower reaction temperatures, suggests that at these reaction temperatures the rise in reaction interface temperature is not sufficient to cause melting of $TiAl_3$. This observation, in turn, suggests that a sufficiently large fraction of the exothermic energy is indeed dissipated through conductive and convective heat transfer and, therefore, simple calculations for estimating the adiabatic temperature are inadequate.

6.5.2 Effect of Reaction Conditions on the Morphology of the Aluminide Particles:

Figures-5.25(a) - 5.25(e) show the scanning electron micrographs at the mid region of the dispersed reaction domain in couples reacted for 3600s (1hr) at 973K ($700^\circ C$), 1073K ($800^\circ C$), 1173K ($900^\circ C$), 1273K ($1000^\circ C$) and 1373 K ($1100^\circ C$) respectively. Particles of titanium aluminides in the matrix of Al can be seen in all the cases. It can also be seen that while the particles of titanium aluminide had average sizes of $6\mu m$, $8\mu m$, $10\mu m$ and $12\mu m$ respectively at the reaction temperatures of 973K ($700^\circ C$) to 1273K ($800^\circ C$) respectively, those obtained in samples reacted at 1373 K ($1100^\circ C$) had an average size of $93\mu m$ [Figure-5.(e)]. This large difference in the average size of the aluminide particles occurs due to the different mechanisms of aluminide layer separation from the solid titanium at different reacture temperatures.

As explained previously, at lower reaction temperatures the exothermic heat released from the chemical reaction is not sufficient to cause the melting of the $TiAl_3$ film formed and, therefore, the separation of the reaction product occurs by its fragmentation which, in turn, is caused by its cracking and fissuring. On the other hand, at higher reaction temperatures, e.g. 1373 K ($1100^{\circ}C$), at which the local melting of the freshly formed $TiAl_3$ can occur the aluminide film (already having some cracks and fissures, as schematically shown in Figure-6.16) separates out from solid Ti due to the incipient melting of the freshly formed reaction product at the reaction interface. The $TiAl_3$ film separated out from solid Ti may subsequently undergo its fragmentation under thermal currents. In this case, since not much severe cracking is preceded, the aluminide particles remain coarse. The larger grain growth at higher reaction temperatures is also expected to cause large size particles at higher reaction synthesis temperatures.

6.6. KINETICS OF $TiAl_3$ FORMATION:

Analysis of kinetics of aluminide formation is important from the point of view of selecting proper reaction conditions. For example, the reaction conditions can be chosen so as to make the synthesis reaction go to its completion/partial completion depending on the demand for different end products. Additionally, the processing conditions such as optimum combination of reaction temperature and time, alloying additions etc., can be selected for the synthesis of the product.

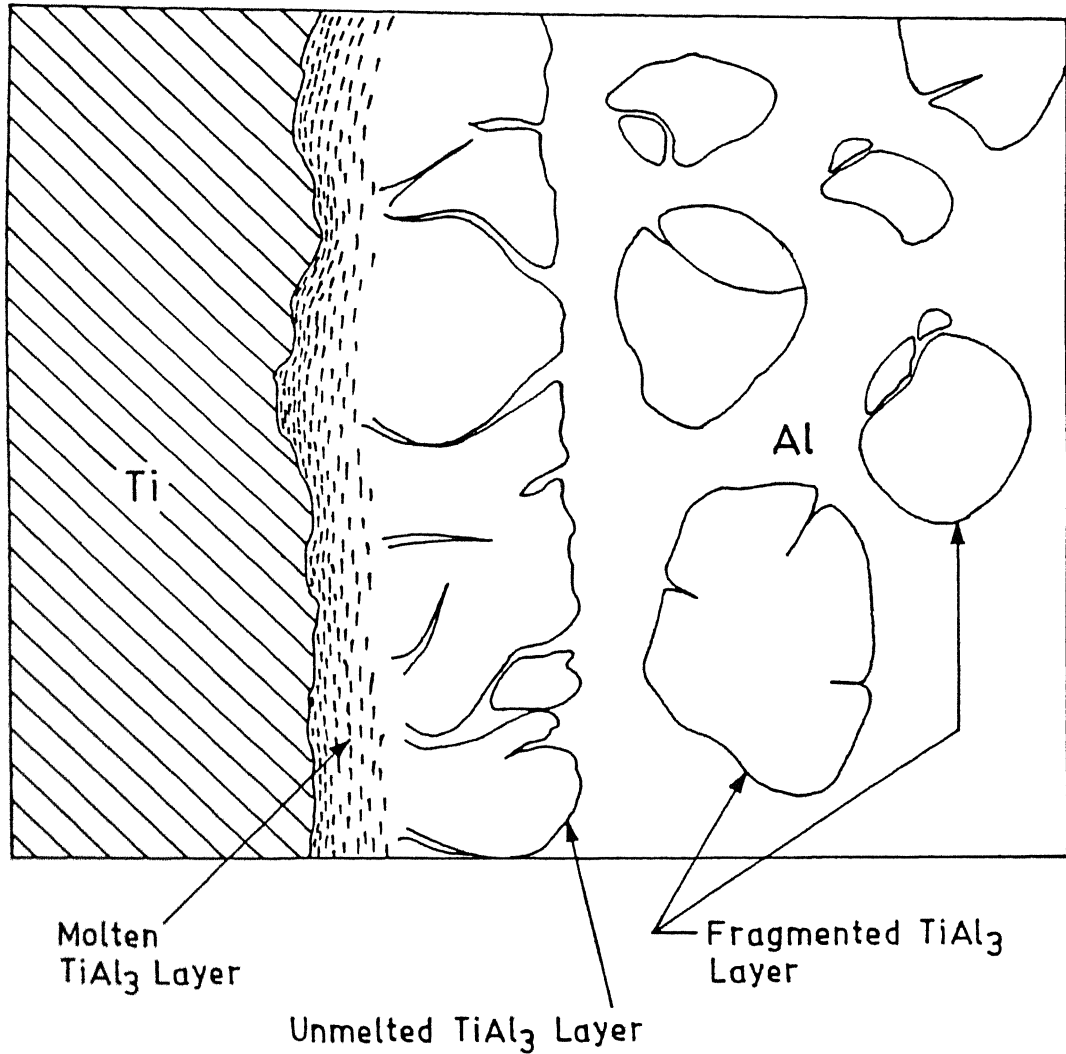


Figure 6.16 Nature of separation of TiAl_3 layer from Ti surface due to incipient melting of TiAl_3 at higher reaction temperature.

Apart from giving the idea about the effect of processing conditions, knowledge of kinetics of reaction is important for understanding the physical processes occurring during reaction synthesis. Estimation of activation energy of reaction is possible from the kinetics data which, in turn, helps in assessing the reaction mechanism.

In several of the investigations carried out in the past on the $TiAl_3$ formation, the kinetics of $TiAl_3$ formation were evaluated on the basis of data obtained on the interaction layer thickness versus time. As discussed in Section-6.2.1 and 6.2.2, the microstructural evolution during the reaction synthesis of $TiAl_3$ suggests that the formation of $TiAl_3$ occurs by chemical reaction, and the reaction zone (referred to as the "interaction layer", or "thickness of the $TiAl_3$ layer" in the literature) in partially reacted couples consists of some amount of Al in addition to the reaction product, $TiAl_3$. Thus the thickness of the reaction zone with time does not give exact idea about the effect of reaction time on the extent of reaction. Hence, the amount of $TiAl_3$ formed per unit area of the reaction interface was assumed to give an the exact estimate of the extent of reaction taken place in a known time interval. Kinetics of $TiAl_3$ formation, thus in the present study have been evaluated from the data obtained on the total amount of $TiAl_3$ formed per unit area of the reaction interface ($m_p(i)$) as a function of the reaction time 't'. Since the reaction occurs at $Ti(s)/Al(l)$ interface, the total amount of the reaction product formed per unit area of the reaction interface has been considered as the parameter that gives an

estimate of the extent of reaction that has taken place after a known time interval. The details of the procedure followed in the estimation of $m_p(i)$ have been described in section-4.4.4. The average values of $m_p(i)$ as a function of the reaction time 't' are presented in Table-6.5.

The data of $m_p(i)$ versus 't' for couples reacted at different temperatures are shown in Figure-6.10. As seen, Figure-6.10 reveals that the variation of $m_p(i)$ with reaction time was more or less linear. The plots of $m_p(i)$ versus 't' did not pass through the origin indicating that the aluminide formation occurred after an incubation period in case of couples reacted at lower temperatures, 973K (700°C) and 1073K (800°C), whereas at 1173K (900°C), the reaction seemed to start as soon as the couples were inserted in the reaction zone of the furnace. The delay in the start of the reaction at the lower temperatures may be attributed to the slower atomic processes for chemical reaction at these temperatures. In addition, enhanced wetting of liquid Al on Ti at higher temperatures as a result of decrease in the liquid Al viscosity is expected to play a prominent role in initiating the reaction faster. The growth rate constant 'k' was evaluated from the slopes of the straight lines of $m_p(i)$ versus 't'. As shown in the figure (Figure-6.17), the growth rate increased with increase in reaction temperature in the range of 973K (700°C) - 1273K (1000°C). Figure-6.17 shows the experimentally determined values of $\log k$ as a function of $\frac{1}{T}$ for the Ti/Al reaction couples. The slopes of the linear best fit line of the data points gave the value of activation energy, Q . The activation energy was

Table 6.5 : Effect of reaction temperature and time on the amount of $TiAl_3$ formed per unit area of the reaction interface in Ti/Al couples.

Reaction Temperature (K)	Amount of $TiAl_3$ formed (mg/mm^2)					
	0.9	1.8	3.6	7.2	10.8	14.4
973	--	--	0.51	1.19	2.38	3.12
1073	--	--	1.44	2.83	3.34	--
1173	0.74	1.66	2.37	--	--	--

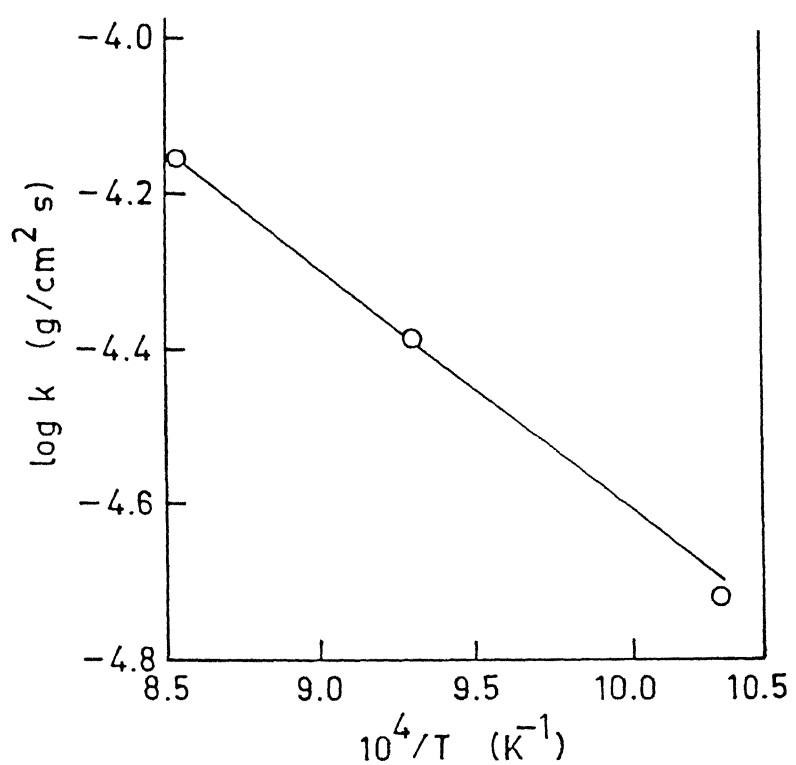


Figure 6.17

$\ln k$ vs. $1/T$ for the data obtained on total amount of reaction product per unit area of the reaction interface.

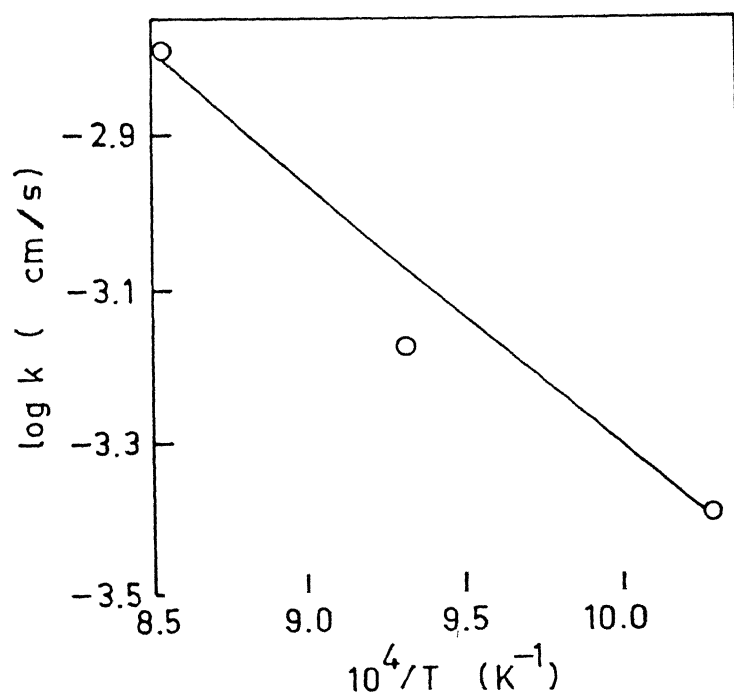


Figure 6.18

$\ln k$ vs. $1/T$ for the data obtained from the variation of reaction zone thickness with time.

calculated using the equation

$$\ln(k) = \exp(-Q/RT)$$

... 6.16

As noted, the value of Q obtained is 14.9kcal/mole

As presented in Chapter-2, activation energy (Q) reported in the literature for various studies on $TiAl_3$ form [121-127] are related to the growth of the $(TiAl_3 + Al)$. Though each of these studies deal with different aspects of aluminide formation, the growth kinetics of $TiAl_3$ formation in each of these studies were evaluated on the basis of the thickness of $(TiAl_3 + Al)$ layer obtained for different reaction times. Activation energy values obtained in these individual studies have been listed in Table-6.6 along with the respective temperature ranges of investigation.

In order to compare the kinetics of aluminide formation evaluated in the present study with those reported in the literature, $\log(\text{growth rate})$ versus $\frac{1}{T}$ have been plotted. The variation of reaction zone thickness with time (Figure-6.18) shows that the activation energy (Q') value of 15.7kcal/mole has been obtained. A comparison of this value with those obtained in the literature shows that the results obtained in the present study match fairly well with the reported data (Table-6.6) within the limits of experimental accuracies possible. However, the Q' do not represent the activation energy for the growth of $TiAl_3$. This value in fact represents the activation energy for the formation of the $(TiAl_3 + Al)$ layer.

Table - 6.6

Activation energy obtained during studies
interaction of Ti with liquid Al.

Studies on	Temp. Range (°C)	Ti and Al Composition	Act. Energy kCal/mole	Ref.
.Solid state Diffusion of Al in Ti (Thin film deposit)	460	Ti and Al layer	-----	Thuillard [136]
.Ti/Al thin films	350-500	Ti and Al -0.25 at% Cu	38.6 to 49.9 (in case of Cu)	Tardy and Tu [137]
.Inter- diffusion between Ti and Al	516-642			Van Loo & Reick [135]
.Growth Kinetics of (Al+TiAl ₃) layer	700-920	Ti in liquid Al Ti99.75%	22 ± 2	Mackowiak and Sheir [121]
—do—	700-900	Ti99%-	23 ± 2	
		Ti in Ti saturated Al	30.48 ± 7.2	Ermenko [128]
Brazing of Ti with Al	680	Al contains some alloying elements	39.7	Takemoto Okomoto [126]
Hot Dip Aluminide Coatings	700-800	Commercial pure Al	45.75	Abdel- Hamid [127]
		Super refined Al	19.70	

development of the two phase ($TiAl_3$ + Al) microstructure. As discussed in section-6.3, the two phase mixture evolved as a consequence of thermal currents inside liquid Al.

It is to be noted here that the kinetic steps involved in the formation of the aluminide include the following important factors:

- (a) exothermic chemical reaction at the Ti/liquid Al interface leading to the formation of $TiAl_3$ and
- (b) flow of fragmented particles away from the reaction interface due to thermal currents inside liquid Al.

In step (a), for continuous chemical reaction to occur, supply of Al to the reaction site by diffusion through the already formed $TiAl_3$ is essential. This is possible only by diffusion of Al through $TiAl_3$ to the Ti/ $TiAl_3$ interface. In view of this, activation energy for the formation of $TiAl_3$ is equal to the sum of the activation energies for chemical reaction between Ti and Al and for the diffusion of Al through the $TiAl_3$ layer.

Chapter 7

Conclusions

Examination and analysis of the reaction product obtained by reaction synthesis between Ti/Al, Ti-Al-V alloy/ Al and Ti-Al-Mo-Zr-Si alloy/ Al reaction couples, as conducted in the present study, give the following conclusions.

1. Results of phase analysis by X-ray diffraction and selected area diffraction under TEM and compositional analysis by energy dispersive spectroscopy (EDS) reveal that as long as an excess amount of liquid Al is present, $TiAl_3$ is the only aluminide formed by reaction synthesis carried out between pure Ti and liquid Al in the reaction temperature range of 973K - 1273K ($700^{\circ}C$ - $1000^{\circ}C$).
2. Similarly, $TiAl_3$ base compounds of compositions Ti-62.8Al-1.6V and Ti-62.8Al-1.4Mo-0.7Zr-0.1Si (all in wt.%) form when the reaction synthesis is carried out between Ti-6Al-4V and Al and Ti-6.5Al-3.2Mo-1.8Zr-0.3Si and Al (all in wt.%) respectively. Results of the present study show that a decrease in the lattice parameter of $TiAl_3$, i.e. a and c , occurs as a result of its alloying with V as well as (Mo + Zr + Si).

3. The intermetallic compound Ti_9Al_{23} forms in addition to $TiAl_3$ when the reaction synthesis between solid Ti and liquid Al is carried out at the reaction temperature of 1373K ($1100^{\circ}C$).
4. Formation of $TiAl_3$ as the only reaction product formed in Ti/Al copuples reacted in the temperature range of 973K ($700^{\circ}C$) to 1273K ($1000^{\circ}C$) can be explained in terms of its lowest free energy of formation when compared to that of Ti_3Al and $TiAl$.
5. Formation of $TiAl_3$ occurs by an exothermic chemical reaction between solid Ti and liquid Al. However, after the direct contact between solid Ti and liquid Al ceases due to the formation of $TiAl_3$, further growth of $TiAl_3$ reaction layer occurs mainly by the diffusion of Al to the reaction interface through the lattice of $TiAl_3$.
6. The reaction zone ahead of the reaction interface consists of a thin continuous reaction layer of $TiAl_3$ and a dispersed reaction domain. The reaction layer contains numerous cracks. The dispersed reaction domain, in turn, consists of $TiAl_3$ particles in an Al-rich matrix.
7. Sub-structural features of the reaction layer and $TiAl_3$ particles present in the dispersed reaction domain, as observed under TEM, reveal that the $TiAl_3$ formed

possesses heavily deformed regions consisting of planar defects, such as stacking faults and superdislocations, as well as cracks along well defined orientations.

8. Both, the mass of the reaction product as well as the reaction zone thickness, as estimated from quantitative metallographic measurements, increase linearly with reaction time at reaction temperatures of 973K (700°C), 1073K (800°C) and 1173K (900°C). Activation energy calculations based on such data gave its value to be in the range of 14.9 - 15.7 kJ/mole.
9. The analysis of measurements made by the quantitative metallography shows that the volume fraction of $TiAl_3$ particles in the dispersed reaction domain varies with the distance from the reaction interface and goes through a maximum. The distance at which the peak in volume fraction occurs increases with reaction time as well as reaction temperature. However, distance of the maximum volume fractions of the particles when normalized with respect to reaction zone thickness initially decreases and then increases with increase in reaction time.
10. The particle size distribution in the dispersed reaction domain varies with distance from the reaction interface. The number of particles in the size range of 0-4 μm is found to be the largest near the reaction interface and it gradually decreases as the distance from the reaction

interface increases. On the other hand, coarse particles are almost non-existent near the reaction interface and their number gradually increases as the distance from the reaction interface gradually increases.

11. Mean $TiAl_3$ particle size varies across the dispersed reaction domain. Starting from a fine particle size near the reaction interface, it gradually increases up to the mid-region of the dispersed reaction domain and stabilizes thereafter.
12. Increase in reaction temperature as well as reaction time result in an increase in the number of coarser particles with a corresponding decrease in that of finer particles. Particles exhibit a bimodal size distribution as the reaction temperature and time increase initially and attain more or less a uniform size distribution with a further increase in reaction temperature and time.
13. The shape of $TiAl_3$ base alloy particles formed in $Ti-Al-V$ alloy/Al and $Ti-Al-Mo-Zr-Si$ alloy/Al couples varies considerably with distance from the reaction interface. As the distance from the reaction interface increases, the aspect ratio of particles increases. Moreover, particles near the reaction interface posses smoother surfaces while those at distances away from it are found to have angular turns and sharp edged corners. These shape variations are observed to be less prominent in $TiAl_3$ particles formed in Ti/Al reaction couples.

14. Microstructural features observed in dispersed reaction domains of reaction couples can be explained in terms of convective currents persisting in liquid Al ahead of the reaction interface and several other physical phenomena such as secondary disintegration of $TiAl_3$ particles, surface smoothening of particles by dissolution, reprecipitation and particle growth.

12. B.H. Rabin and R.N. Wright, Metall. Trans. A, Vol. 22A (1992), 277.
13. H.C. Yi and J.J. Moore, in 'Combustion and Plasma Synthesis of High Temperature Materials', Z.A. Munir and J.B. Holt (eds.), VCH, New York (1990), 122.
14. Chemical Technology and Metallurgy, ed. A.G. Merzhanov, Chernogolovka (1975).
15. Z.A. Munir, Ceramic Bull., 67 (1988), 342.
16. V.I. Itin, d A.D. Bratchikov, V.N. Doronin and G.A. Pribytkov, Sov. Phys. J., 24 (1981), 1134.
17. H.C. Yi and J.J. Moore, J. Mater. Sci., 24 (1989), 3455.
18. H.C. Yi and J.J. Moore, J. Mater. Sci., 24 (1989), 3462.
19. A.P. Hardt and R.W. Holsinger, Comb. Flame, 21 (1973), 91.
20. A. Bose, B.H. Rabin and R.M. German, Powder Metall. Int., Vol. 20, No. 3 (1988), 25.
21. B.H. Rabin and R.N. Wright, Metall. Trans. A, dVol. 23A, January (1992), 35.
22. J.L. Murray, Met. Trans., 19A (1988), 243.
23. J.L. Murray, in 'Binary Alloy Phase Diagrams', T.B. Massalski (ed.), ASM, Metals Park, Ohio (1986), p. 173.
24. J.C. Shuster and H. Ipseer, Z. Metallkd., Vol. 81 (1990), 389.
25. D. Banerjee, T.K. Nandy and A.K. Gogia, Scripta Met., 21 (1987), 597-600.
26. A.K. Gogia et al., Mater. Sci. Engg., A159 (1992), 73-86.
27. A.J. Williams, Can. Metall. Quart., Vol. 4, No. 3 (1965), 181-203.
28. T. Hamajima, G. Luetjeering and S. Weissmann, Metall. Trans., Vol. 3, No. 11 (1972), 2805-2810.
29. D. Banerjee, R.V. Krishnan and K.I. Vasu, Metall. Trans. A, Vol. 11A, No. 7 (1980), 1095-1105.
30. H. Boehm and K. Loehberg, Z. Metallkd., Vol. 49 (1958), 173-178.
31. R.C. Hansen and A. Raman, Z. Metallkd., Vol. 61, No. 2 (1970), 115-120.

32. V.N. Eremenko, S.A. Sukhaya and L.A. Tretyachenko, Izv. Vyss. Uchebn. Zaved. Tsvetn. Metall., Vol. V (1988), 97-100 (in Russian).

33. M.A. Volkova and I.I. Kornilov, Russ. Metall., Vol. 5 (1970), 148-151.

34. C.B. Jordan and P. Duwez, Trans. Am. Soc. Met., Vol. 48 (1956), 783-794.

35. A. Raman, Z. Metallkd., Vol. 57, No. 7 (1966), 5335-540.

36. K. Hashimoto, H. Doi and T. Tsujimoto, Trans. Japan Inst. Met., Vol. 27, No. 10 (1985), 741-749.

37. D.R. Sandlin and H.A. Klung, Jr., Master Thesis, Institute of Technology, Wright Patterson Air Force Base, Ohio (1961).

38. D. Li, Y.Y. Liu and X.J. Wan, Jinshu Xuebao, Vol. 20, A375-A382 (in Chinese).

39. L.P. Luzhnikov, V.M. Novikhova and L.P. Marsev, Metallovl. i Term. Obrabotka Metall., Vol. 2 (1963), 13-16 (in Russian).

40. T.T. Nartova and O.N. Andreev, 2nd Mater. Symp., 1972, Nauka Ed., Moscow (1974), 194-197 (in Russian).

41. C. Bruklo, H. Nowotny, O. Schob and F. Benesovsky, Monatsh. Chem., Vol. 88, (1957), 494-501.

42. K. Schubert, K. Frank, R. Gohle, A. Maldonado, H.G. Meissner, A. Raman and W. Rosstentscher, Naturwissenschaften, Vol. 50 (1963), 41.

43. A. Raman and K. Schubert, Z. Metallkd., Vol. 56 (1965), 44-52 (in German).

44. K. Kamei, T. Ninomiya and S. Hayashi, Met. Abstrss. Light Metals and Alloys, 1964-1966 (1968), 67-70.

45. A.M. Zakhrov, I.T. Guldin, A.A. Arnold and Yu. A. Matsenko, Russ. Metall., Vol. 4 (1988), 185-189.

46. C. Vahlas, P.Y. Chevalier, E. Blanquet, CALPHAD, Vol. 13 (1989), 273-292.

47. C. McCullough, J.J. Valencia, C.G. Levi and R. Mehrabian, Acta Met., Vol. 37, No. 5 (1989), 1321.

48. K. Kaltenbach, S. Gama, D.G. Pinatti and K. Schulze, Z. Metallkd., Vol. 80 (1989), 511.

49. U.R. Kattner, J.C. Lin and Y.A. Chang, Met. Trans. A, 23A (1992), 2081.

50. M. Yamaguchi and H. Inui, in "Intermetallic Compounds", J.H. Westbrook and R.L. Fleischer (eds.), John Wiley & Sons Ltd. (1994), 147.

51. M. Yamaguchi, Y. Umakoshi and Y. Yamane, Phil. Mag., Vol. 55 (1987), 301.

52. C.L. Fu, J. Mater. Res., Vol. 5, No. 5 (1990), 971.

53. M. Nakamura and K. Kimura, J. Mater. Sci., Vol. 26 (1991), 2208.

54. S.F. Pugh, Phil. Mag., Vol. 45 (1954), 823.

55. M. Yamaguchi and H. Inui, in "Intermetallic Compounds", J.H. Westbrook and R.L. Fleischer (eds.), John Wiley & Sons Ltd. (1994), p. 147.

56. V.K. Vasudevan, R. Wheeler and H.L. Fraser, High Temperature Ordered Intermetallic Alloys III

57. D.G. Morris, S. Günter, R. Lerv and J.C. Joye, in "Structural Intermetallics", R. Darolia, J.J. Lewandowski, C.T. Liu and P.L. Martin, MMM Society (1993), p. 87.

58. J.P. Nic, S. Zhang and D.E. Mikkola, Mater. Res. Soc. Symp. Proc., Vol. 213 (1991), p. 1697.

59. M. Khantha, same as above, p. 229.

60. A. Raman and K. Schubert, Z. Metallkd., Vol. 56 (1965), 44.

61. V. Ya. Markiv, V.V. Burnashova and V.P. Ryobov, Metallofizika, Vol. 46 (1973), 103.

62. A. Seibold, Z. Metallkd., Vol. 72 (1981), 712.

63. D.G. Pettifor in "Intermetallics - Structure and Mechanical Properties", O. Izumi (ed.), The Japan Institute of Metals (1991), p. 149.

64. D.M. Nicholson, G.M. Slocks, W.M. Temmerman, P. Sterne and D.G. Pettifor, in High Temperature Ordered Intermetallic Alloys III, Vol. 133, C.T. Liu, A.I. Taup, N.S. Stoloff and C.C. Koch, Mater. Res. Soc. (1989), p. 17.

65. M.E. Eberhardt, K.S. Kumar and J.M. MacLaren, Phil. Mag. B, Vol. 61 (1990), 943.

66. K.S. Kumar, Int. Mater. Rev, Vol. 35 (1990), 293.

67. M.H. Yoo and C.L. Fu, *ISIJ International*, Vol. 31 (1991), 1049.

68. E.P. Jeorge, D.P. Pope, C.L. Fu and J.H. Sniebel, *ISIJ International* Vol. 31 (1991), 1063.

69. D.E. Mikkola, J.P. Nic, S. Zhang and W.W. Mittigan, *ISIJ International*, Vol. 31 (1991), 1076.

70. H. Mabuchi et al., *Scripta Met.*, Vol. 24 (1990), 1553.

71. S. Zhang et al., *Scripta Met.*, Vol. 24 (1990), 57.

72. C.T. Turner, W.O. Power and J.A. West, *Acta. Met.*, Vol. 37 (1989), 2635.

73. E.P. George, W.D. Poter, H.M. Hansen, W.C. Oliver and B.F. Oliver, *J. Mater. Res.*, Vol. 4, No. 1 (1989), 78.

74. Z.L. Wu, D.P. Pope and V. Vitek, *Scripta Met.*, Vol. 24 (1990), 2187.

75. J.R. Rice and R. Thomson, *Phil. Mag.*, Vol. 29 (1974), 73.

76. D. Banerjee, A.K. Gogia, T.K. Nandy, K. Muraleedharan and R.S. Mishra, in 'Structural Intermetallics', R. Darolia, J.J. Lewandowski, C.T. Liu, P.L. Martin, D.B. Miracle and M.V. Nathal, The MMM Society (1993), 19.

77. D. Banerjee, A.K. Gogia, T.K. Nandy and V.A. Joshi, *Acta. Met.*, Vol. 36 (1988), 871.

78. A.K. Gogia, S. Kamat and D. Banerjee (submitted for publication, 1993).

79. E.S. Bumps, H.D. Kessler and M. Hansen, *Trans. AIME*, Vol. 194 (1952), 609.

80. P. Duwez and J.L. Taylor, *J. of Metals* (1952), 70.

81. S.C. Huang, E.L. Hall and M.F.X. Gigliotti, in 'High Temperature Ordered Alloys II', Materials Research Society Symposia Proceedings, Vol. 81, N.S. Stoloff, C.C. Koch.

82. S.C. Huang and E.L. Hall, *Met. Trans. A*, Vol. 22A (1991), 427.

83. Blackburn and H.A. Lipsitt, *Meet. Trans. A*, Vol. 5 (1974), 1373.

84. K. Vedula and J.R. Stephens, *Metal Powder Report*, Vol. 42, No. 2 (1987), 84-89.

85. L.S. Apgar and D. Eylon, *ISIJ International*, Vol. 31, No. 8 (1991), 915.

86. J.C. Beddocs, W. Wallace and M.C. de Malherbe, Int. J. of Powder Metallurgy, Vol. 28, No. 3 (1992), 313.

87. C.F. Yolton, T. Lizzi, V.K. Chandhok and J.H. Moll, 'Progress in Powder Metallurgy', Vol. 42, MPIP, Princeton, (1986), p. 479.

88. V.S. Moxson and G.I. Friedman, Metal Powder Report, Vol. 43, No. 2 (1988), 88.

89. J.F. Gider, Ceram. Engg. Sci. Proc., Vol. 3 (1982), 519.

90. A.G. Merzhanov, V.M. Shkiro and I.P. Borovinskaya, "Synthesis of Refractory Inorganic Compounds", Noyes, New Jersey (1985).

91. J.B. Holt, MRS Bull., Vol. 12 (1987), 60.

92. Z.A. Munir, Ceram. Bull., Vol. 67 (1988), 342.

93. Z.A. Munir and V. Anselmi-Tamburini, Mater. Scis. Rep., Vol. 3 (1989), 277.

94. H.C. Yi and J.J. Moore, J. Mater. Sci., 25 (1990), 1159-1168.

95. J. Subrahmanyam and M. Vijayakumar, J. Mater. Sci., Vol. 27 (1992), 6249.

96. V.M. Maslov, I.P. Borovinskaya and A.G. Merzhnov, Combustion Explos. Shock Waves, 12 (1976), 631.

97. Y.S. Naiborodenko and V.I. Itin, Comb. Explos. Shock Wave, Vol. 11 (1975), 293.

98. A.P. Savitskii, L.S. Marcunova, N.N. Burtsev, M.A. Emeljanava in 'Proc. VII. Int. P/M Conf.' DDR, Dresden (1981) p.169

99. Z.A. Munir, Metall. Trans. A, 23A, No. , Jan (1992), 7-13.

100. D.R. Gaskell, Introduction to Metallurgical Thermodynamics, McGraw-Hill, New York (1973), p. 26.

101. K.A. Philpot, Z.A. Munir and J.B. Holt, J. Mater. Sci., 22 (1987), 159.

102. Y.S. Naiborodenko, V.I. Itin and K.V. Savitski, Sov. Phys. J., 11 (1968), 293, 626.

103. A. Bose, B. Moore, R.M. German and N.S. Stoloff, J. Metals, Setember (1988), 14.

104. C. Nishimura and C.T. Liu, Acta. Metall. Mater., Vol. 41, No. 1 (1993), 113-120.

105. Z.A. Munir, Ceram. Bull., 67 (1988), 342.

106. H.C. Yi, A. Petric and J.J. Moore, J. Mater. Sci., Vol. 27 (1992), 6797.

107. V.I. Itin, d A.D. Bratchikov and L.N. Portnikova, Societ Powd. Metall. Ceram., Vol. 209, No. 5 (1980), 315.

108. Y.S. Naiborodenko, V.I. Itin and K.V. Savitskii, ibid, Vol. 91, No. 7 (1970), 562.

109. W.R. Wrzesinski and J.C. Rawers, J. Mater. Sci. Lett., Vol. 9 (1990), 432.

110. G. Wang and M. Dahms, J. Metals, No. 5 (1993), 52.

111. Y.D. Hahn and Y.T. Lee, Advances in Powder Metallurgy and Particulate Materials - 1992, Vol. 9, MPIF, New Jersey (1992), p. 309.

112. J.C. Rawers and W.R. Wrzesinski, E.K. Roub and R.R. Brown, Mater. Sci. and Techno., Vol. 6, Feb. (1990), 187.

113. J.C. Rawers and W.R. Wrzesinski, J. Mater. Sci., Vol. 27 (1992), 2877.

114. G.X. Wang and M. Dahms, Powder Metall. Int., Vol. 24, No. 4 (1992), 219.

115. K. Shibne et al., in 'Intermetallic Compounds - Structurre and Mechanical Properties', O. Izumi (ed.), (1991), 833.

116. G.X. Wang and M. Dahms, Scripta Met., 26 (1992), 717.

117. D.C. Dunand, Materials and Manufacturing Processes, Vol. 10, No. 3 (1995), 373.

118. J.C. Murray and R.M. German, Advances in Powder Metallurgy and Particulate Materials - 1992, Vol. 9, MPIF, New Jersey (1992), p. 295.

119. Mackowiak and Shreir, Acta. Met., Vol. 4 (1956), 556.

120. Mackowiak and Shreir, J. Less. Com. Metals, Vol. 1 (1959), 456.

121. Mackowiak and Shreir, J. of Less Com. Metals, Vol. 15 (1968), 341.

122. A.A. Abdel-Hamid, Z. Metallkd., Vol. 81 (1990), 601.

123. A.A. Abdel-Hamid, Z. Metallkd., Vol. 81 (1991), 383.

124. K. Venishi, d A. Sugimoto and K.F. Kobayashi, Z. Metallkd., Vol. 83 (1992), 241.

200

125. J.H. Abboud and D.R.F. West, *J. Mater. Sci.*, Vol. 27 (1992), 4201.

126. T. Takemoto and I. Okamoto, *J. Mater. Sci.*, Vol. 23 (1988), 1301.

127. A.A. Abdel-Hamid, *Z. Metallkd.*, Vol. 82 (1981), 921.

128. V.N. Eremenko, Ya. V. Natanzon and V. Ya. Petrishschev, *Soviet Powder Met. and Metal Ceramics*, (1987), 118.

129. Slama and Vignes, *J. of Less Com. Metals*, Vol. 24 (1971), 1.

130. A.P. Savitski and N.N. Burtsev, *Soviet Powder Met. and Metal Ceramics*, Vol.18., No.2 (1979) 96

131. V.G. Khrooav, *Soviet Powd. Met. and Metal Ceramics*, Vol.18, No.1 (1979), 16.

132. Rhines and Dehoff, 'Quantitative Microscopy', McGraw-Hill Book Company, New York, 1968.

133. G. Thomas, John Wiley & Sons Inc., New York (1962) p 195.

134. J. Tarnaki and Y.W. Kim, *Scripta Met.*, Vol. 22 (1988), 329.

135. F.J.J. van Loo and G.D. Reick, *Acta. Met.*, Vol. 21, No. 1 (1973), 61.

136. M. Thuillard, L.T. Tran, C.W. Nieh and M.A. Nicolel, *J. Appl. Phys.*, Vol. 65, No.6 (1989) 2553.

137. J.Tardy and K.N. Tu, *Physical Review B*, Vol. 32, No.4 (1985) 2070.

138. C. Wagner and W. Schottky, *Z. Phys. Chem.*, Vol. B11, 163.

139. B. Sundman and J. Agren, *Z. Phys. Chem. Solids*, Vol. 42 (1981) 297.

140. R.M. German, in " Liquid Phase Sintering ", Plenum Press, New York (1985).

141. J.B. Holt and Z.Z. Munir, *J. of Mater. Sci.*, Vol. 21 (1986) 251.

142. Y. Umakoshi, M. Yamaguchi, T. Yamane and T. Hirano, *Phil. Mag. A.*, Vol. 58 (1988), 651.

143. O. Kubasweskii and W.A. Dench, *Acta. Metall.*, Vol.3 (1955) 339.

144. J. Szekely and N.J. Themelis, "Rate Phenomena in process Metallurgy", John Wiley & Sons. Inc., New York (1971) 219.

APPENDIX

SPEKTOR'S METHOD

Spektor considers the penetration of a polydispersed system of spheres by a straight line, or secant (as in Fig. 6-1c). First, he assumes that there are many spheres of diameter D , the centers of which are distributed in space with statistical uniformity. Figure 6-7 illustrates the geometry

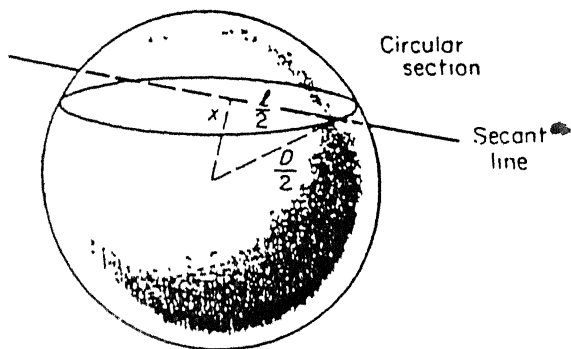


Fig. 6-7 Geometrical relationships in the method of chords.

involved when a chord is produced by the intersection of a straight line with a sphere of diameter D .

The distance from the center of the sphere to the intersecting chord is

$$x(i,j) = \sqrt{\left(\frac{D}{2}\right)^2 - \left(\frac{\ell_i}{2}\right)^2} \quad (6-28)$$

where ℓ_i is the length of the chord.

The number of chords per unit length of the secant having lengths between ℓ_i and D is calculated next. These chords must belong to only those spheres whose centers lie within a cylinder of unit length and radius x . This situation is depicted schematically for spheres of diameter D , in Fig. 6-8.

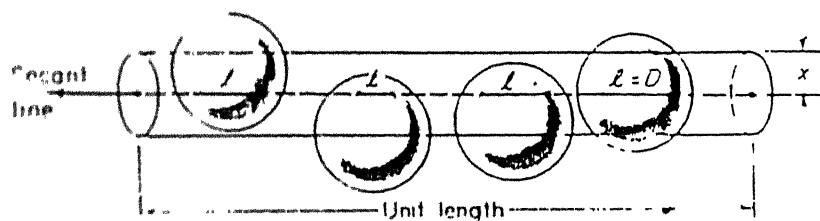


Fig. 6-8 Penetration of spheres of diameter D with centers within a distance x of a random secant line

If there are $N_V(j)$ centers of spheres per unit volume of the structure, then the number of chords (ranging in length from ℓ_i to D_i) per unit length of the secant will be

$$N_L(i,j) = \pi x^2(i,j) N_V(j) = \frac{\pi}{4} (D_i^2 - \ell_i^2) N_V(j) \quad (6-29)$$

For a polydispersed system let the spheres be classified into groups with diameters

$$D_1, D_2, D_3, \dots, D_n, \dots, D_k$$

and numbers per unit volume

$$N_V(1), N_V(2), N_V(3), \dots, N_V(j), \dots, N_V(k)$$

Per unit length of secant line, the number of intercepts greater than ℓ_i is obtained by summing over all size classes of particles having diameters greater than ℓ_i :

$$N_L(i,k) = \frac{\pi}{4} \sum_{j=1}^k (D_j^2 - \ell_i^2) N_V(j) = \frac{1}{4} \sum_{j=1}^k \pi D_j^2 N_V(j) - \frac{\pi \ell_i^2}{4} \sum_{j=1}^k N_V(j) \quad (6-30)$$

It can be recognized that $\sum_{j=1}^k \pi D_j^2 N_V(j) = S_V(i,k)$, the total surface area

of the v particles, and $\sum_{j=1}^k N_V(j) = N_V(i,k)$, the number of particles with diameters greater than ℓ_i . Substituting in Eq. (6-30) gives

$$N_L(i,k) = \frac{1}{4} S_V(i,k) - \frac{\pi \ell_i^2}{4} N_V(i,k) \quad (6-31)$$

Thus, the number of chords per unit length of test secant with lengths between ℓ_i and D_{\max} is expressed in terms of the surface area and number of particles having diameters greater than ℓ_i .

Continuous distribution. If the distribution is assumed to be continuous, Eq. (6-31) can be differentiated, giving

$$dN_L(i,k) = \frac{1}{4} dS_V(i,k) - \frac{\pi \ell_i^2}{4} dN_V(i,k) - \frac{\pi}{2} N_V(i,k) \ell_i d\ell_i \quad (6-32)$$

Since, for particles with diameters between ℓ_i and $\ell_i + d\ell$, $dS_V = \pi \ell_i^2 dN_V$, the first two terms on the right-hand side of Eq. (6-32) drop out, giving

$$dN_L(i,k) = -\frac{\pi}{2} N_V(i,k) \ell_i d\ell \quad (6-33)$$

considering that

$$\begin{aligned} dN_L(i,k) &= -dN_L(0,i) \\ dN_L(0,i) &= \frac{\pi}{2} N_V(i,k) \ell_i d\ell \end{aligned} \quad (6-34)$$

where $N_L(0,i)$ is the number of chords smaller than ℓ_i . Hence, the desired relationship is obtained between the integral distribution of particle diameters and the distribution function of chords

$$N_V(i,k) = \frac{2}{\pi} \frac{1}{\ell_i} \frac{dN_L(0,i)}{d\ell} \quad (6-35)$$

with $N_V(i,k)$ defined as the number of particles with diameters greater than ℓ_i , and $dN_L(0,i)/d\ell$ is equal to the distribution function of chords determined experimentally.

For finite differences, it is possible to use Eq. (6-35) in the form

$$N_V(i,k) = \frac{2}{\pi \Delta} \frac{N_L(i)}{\ell_i} \quad (6-36)$$

where $N_L(i)$ is the number of chords in the interval, $\ell_i \pm \Delta/2$. The narrower the fractional interval Δ , the greater the accuracy.

Discontinuous distribution. The analysis of the distribution of spherical particles may be simplified if a continuous function is not required. Usually it is sufficient to represent the distribution of particle sizes as a discontinuous function with a limited number of class intervals. Some modifications of the formulas must be introduced in this case.

The following expressions can be written by analogy with Eq. (6-36):

$$N_V(i,k) = \frac{2}{\pi \Delta} \frac{N_L(i)}{\ell_i} \quad (6-37)$$

$$N_V(i+1, k) = \frac{2}{\pi\Delta} \frac{N_L(i+1)}{\ell_{(i+1)}} \quad (6-38)$$

where $N_L(i)$ and $N_L(i+1)$ are the number of chords in the intervals $\ell_i \pm \Delta/2$ and $\ell_{(i+1)} \pm \Delta/2$, respectively. Subtracting Eq. (6-38) from Eq. (6-37) gives

$$N_V(i) = \frac{2}{\pi\Delta} \left[\frac{N_L(i)}{\ell_i} - \frac{N_L(i+1)}{\ell_{(i+1)}} \right] \quad (6-39)$$

where $N_V(i)$ is the number of particles with diameters between ℓ_i and $\ell_{(i+1)}$.

Let the entire range of chords be broken down into class intervals of equal length Δ , as shown in Fig. 6-9. Using this system of nomenclature,

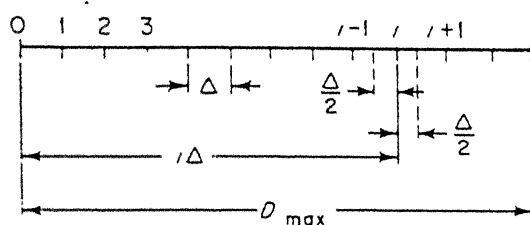


Fig. 6-9 Breakdown of chords and particle diameters into class intervals.

Eq. (6-39) can be written as

$$N_V(i) = \frac{2}{\pi\Delta} \left[\frac{N_L(i)}{\Delta(i - \frac{1}{2})} - \frac{N_L(i+1)}{\Delta(i + \frac{1}{2})} \right] \quad (6-40)$$

where $N_V(i)$ is the number of particles with diameters in the interval $i\Delta - \Delta/2$ to $i\Delta + \Delta/2$, whose mean diameter is $i\Delta$. The working formula is obtained by rearranging Eq. (6-40):

$$N_V(i) = \frac{4}{\pi\Delta^2} \left[\frac{N_L(i)}{2i - 1} - \frac{N_L(i+1)}{2i + 1} \right] \quad (6-41)$$

An additional advantage in Spektor's method of chords is that the total surface area of the particles can be obtained readily. For separate particles, regardless of their planar shape, it is known that the surface area per unit volume is equal to twice the number of boundaries intersected per unit length of test secant [see Eq. (4-3)]; that is,

$$S_V = 2\bar{N}_L \quad (4-3)$$

Since each chord represents two intersections, if the particles are not contiguous, the expression above becomes

$$S_V = 4\bar{N}'_L \quad (6-42)$$